CRANFIELD UNIVERSITY

Nuhu Abdullahi

Oil-Water Separation Phenomenon Due to Corrosion Cavity and Scale Sediments Build-Up in Horizontal Pipeline

School of Engineering

PhD thesis

Academic Year: 2011 - 2012

Supervisor(s): Dr. László Könözsy, Dr. Al Savvaris

September 2012

CRANFIELD UNIVERSITY

School of Engineering

PhD thesis

Academic Year 2011 - 2012

Nuhu Abdullahi

Oil-Water Separation Phenomenon Due to Corrosion Cavity and Scale Sediments Build-Up in Horizontal Pipeline

Supervisor(s): Dr. László Könözsy, Dr. Al Savvaris

September 2012

This is thesis is submitted in fulfilment of the requirements for the degree of Doctor of Philosophy

ABSTRACT

The concurrent flow of two immiscible liquids (Oil-Water) in pipelines is usually encountered in oil production and pipeline transportation. Water is present in crude oil and separation facilities. The aim of this thesis is to investigate the effect of pipe deformations caused by corrosion cavity and scale sediments build-up on the water cut at the pipe wall. An extensive literature review survey on both experimental and numerical investigation has been performed on oil-water flows in horizontal pipelines. Two multiphase flow models (Mixture and Eulerian models) were formulated and presented with the corresponding conservation equations. The three major turbulent modelling approaches to capture turbulent phenomenon were described; Reynolds Averaged Navier-Stokes Equations (RANS) was selected as an appropriate turbulence model for turbulent flow simulations.

Preliminary runs were performed for two of the validation cases in order to estimate the pipe entrance length and establish the parameters of the reference state corresponding to pure oil and oil-water. Validation studies were performed to choose the appropriate multiphase model. The results showed that Eulerian multiphase model was fairly more accurate and acceptable in comparison to the mixture model. A further Validation studies was also conducted to select the droplet diameter, whereby appropriate droplet diameter of 3×10^{-5}mm was selected. The corrosion cavity and scale sediments were modelled with rectangular cavity and cubical obstacle respectively oriented perpendicular to the pipe flow. The model geometries and computational mesh were generated with GAMBIT (2.4) and exported to FLUENT (6.3). The simulation was conducted for input water volume fraction of 0.1 and 0.3, Reynolds number of 18,500 and 22,000. Configurations of 16 cases were considered because of computational requirements.

Numerical simulation of oil-water pipe flow with corrosion cavity and cubical obstacle were performed and analyses of flow features have been described. Effect of aspect ratio, input water volume fraction and Reynolds number on the

amount of water volume fraction at the pipe wall, cavity and around cubical obstacle have been analysed. Quantitative data of maximum and minimum water volume fractions in the pipe, cavity walls and around the cubical obstacle have been computed and compared. The results indicated that around the cavity, turbulence was produced resulting to recirculation, mixing and separation of water from oil. Similarly, oil-water separate from the front, sidewalls and behind the cubical obstacle which lead to formation of different types of vortices. It was observed that water segregated faster with increase in input water fraction and decrease in Reynolds number. However, more water settled to the bottom of deep cavity than shallow cavity and the area of pipe wall wetted by water reduced as the Reynolds number increases. Parametric study on cavity flow has been conducted with the new adjusted turbulent viscosity with damping functions. The results showed improvement on water volume fraction distribution behaviour in pipe and cavity wall surfaces.

ACKNOWLEDGEMENTS

I would like to thank my former supervisor Dr. Evgeniy Shapiro for his kind help and excellent guidance during the course of this study. He was always available to attend to me with his tight schedule whenever I needed an advice and I really appreciate that.

My special thanks also go to my present supervisors Dr. László Könözsy and Dr. Al Savvaris that intervened during the course with all the special encouragement, support and help they passed were valuable.

Finally, I would like to thank my sponsor Petroleum Technology Development Fund (PTDF) Abuja Nigeria, my family and friends that gave me support during the academics years.

Nuhu Abdullahi

TABLE OF CONTENTS

LIST OF FIGURES

LIST OF TABLES

NOMENCLATURE

C_D	drag coefficient
d	cavity depth (m)
D	Pipe diameter (m)
f	friction factor
f_{drag}	Drag function
$F_{lift,\ q}$	lift force (N)
$F_{vm,\ q}$	virtual mass force (N)
g	acceleration due to gravity (m/s^2)
G_o	mass fluxes of oil (Kg/m2.s)
G_w	mass fluxes of water (Kg/m2.s)
K	turbulent kinetic energy (m^2/s^2)
K_{dc}	fluid-fluid exchange coefficient
L	cavity length (m)
P	pressure ($N/m^{2)}$
R_e	Reynolds number
Re_o	Reynolds numbers for oil
Re_r	relative Reynolds number
Re_w	Reynolds numbers for water
T	temperature (k)
t	pipe thickness (m)
u'_c	fluctuating velocity of continuous (m/s)
u'_d	fluctuating velocity of dispersed phase (m/s)
v	velocity (m/s)
w	cavity width (m)
ε	dissipation rate (m^2/s^3)
μ	dynamic viscosity (N s/m^2)
ρ	density (kg/m^3)
ϕ	dispersed phase concentration

$\widetilde{U}_m$	mixture velocity (m/s)
$\overrightarrow{v_m}$	Average velocity (m/s)
L_e	entrance length (m)
Re_t	turbulent Reynolds number
X_{tt}	Lockhart-Martinelli factor
f_m	mixture coefficient of friction
f_μ	damping function
u_τ	Friction velocity (m/s)
y^+	non-dimensional distance from the wall
y_τ	viscous length (m)
α_o	Volume fraction for oil
α_p	Volume fraction for dispersed phase
α_w	Volume fraction for water
μ_m	Mixture viscosity (N s/m^2)
μ_t	turbulent viscosity (N s/m^2)
ρ_m	Mixture density (kg/m^3)
τ_p	Particle relaxation time (s)
ϵ_r	roughness height (m)

1 INTRODUCTION

1.1 Motivation and problem description

The concurrent flow of two immiscible fluids/liquids, such as oil and water in pipelines has received great attention in process engineering and pipeline transportation. Water is obtained from underground formation in large quantities with crude oil, particularly in older oil wells. Water is injected to oil well to increase pressure and thereby stimulate oil production also small quantity of water is added with oil to reduce pressure drop during oil transportation in pipeline. Therefore, oil and water may exist inside the oil well as well as in distribution and transportation pipelines. During the simultaneous flow of oil-water in pipeline, water may separate from oil to form base at the bottom of the pipe. At low water cuts, corrosion is not significant or can even be neglected, because the water is entrained by the moving oil, but with a high water cut, the water break-out may occur leading to separation of water at the bottom of the pipe and increasing the likelihood of internal pipeline corrosion which generally affects the structural integrity of pipelines. The water cut has a significant effect on the critical oil velocity for water entrainment. In this case, corrosion will be increased by increasing in water cut or presence of free water in steel pipe.

Consideration of the internal corrosion rate is a very important issue, because it depends on flow regime of oil-water; and is severe, where the phases are separated at low flow rate. Furthermore, there is no corrosion risk under oil wetting of pipe wall and highly turbulent flows at low water cuts are linked with insignificant corrosion risk, whereas low flow rate with higher water cuts has been linked with high corrosion risk. Pipeline corrosion is a serious problem in oil and gas industries, the total annual cost of corrosion in the oil and gas production industry is estimated to be $1.372billion, broken- down into $589million in outside pipelines and $463million for facilities cost and $320million for capital expenditure (Mathew, 2008). Pipeline failure data for the year 2001 in USA indicates that 29% pipeline failure in oil pipeline is caused due to corrosion and data from Western Europe on onshore transmission

pipeline failure from 1970 to 1997 indicate 17% of failure that results in loss of oil products is caused due to corrosion (Hopkins, 2004).

Understanding the flow behaviour of oil-water mixture is indispensable in pipelines and oil-water separation facilities. It is also important in predicting the percentage of free water close to the pipe surface. The oil-water mixture flow is a complex problem in the field of hydromechanics, because it is difficult to develop reliable computational models due to the difference in densities, free boundaries of the phases, the presence of interface among the phases, the mass and heat transfer rate mechanism, and due to the fact that separate phases can move with different mean velocities (Govier and Aziz, 1977). In multiphase flow, it is important to understand the interaction between the oil and water phase and the way they are distributed over the cross sectional area of the pipe, the analysis can indicate which phase wets the pipe wall and the position of the oil and water phase. The separation and distribution of the oil-water phases depend on the gravity and turbulence, with lower flow rate, the two phases will separate due to gravity acting at right angle to the direction of flow while in the case of dispersed flow, the gravity moving normal to pipe axis (Hussaini et al., 2008).

During the flow of oil and water in pipeline, the water can separate from oil and wet the internal base of pipe wall which may result to general corrosion or localise corrosion known as pitting, cavities of holes of different sizes and shapes are formed at the pipe base. The initiation of corrosion cavities in the pipeline can be dangerous by acting as a stress riser, consequently leading to stress corrosion cracking in the pipe wall. The corrosion cavities are more dangerous than uniform corrosion damage, because one corrosion cavity is enough to produce the catastrophic failure of the entire pipeline system as shown in figure1-1.

Figure 1.1: Corrosion cavities shapes in pipe (NACE, 2005)

The oil-water turbulent dispersed flows in the horizontal pipeline past open corrosion cavity in the internal base of the pipe leading to unsteady flow fluctuation. The large scale flow fluctuations entrain the mainstream flow in to boundary layer and induce pressure fluctuations at the impingement corner of the cavity result to recirculation and separation of water from oil and formation of vortices as demonstrated in figure 1.2. Knowledge of the flow field inside the cavity is fundamentally important to show the influence of corrosion cavity in changing the flow features. Numerical simulation can be used to predict the flow field and explain the behaviour of flow features in the presence of cavities and the amount of water volume fraction and it distribution in contact to the cavity and pipe wall.

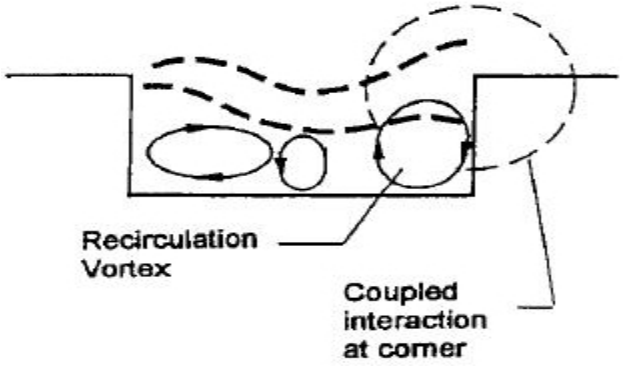

Figure 1.2: Schematic of flow in a cavity (Rockwell and Linj, 2001)

The corrosion cavity geometry shapes are not easy to describe because of the irregular shape of the cavity geometry in horizontal and circumferential direction

of the pipe which extend to the cavity depth. Corrosion cavity may appear as a single or a group of neighbouring cavities divided by the thickness of the pipe wall materials, the corrosion cavity geometry can be in the form of hemisphere or cup shape pattern depending on seriousness of corrosion damaged. However, there are no clear corrosion cavity geometry patterns as shown in figure 1-3.

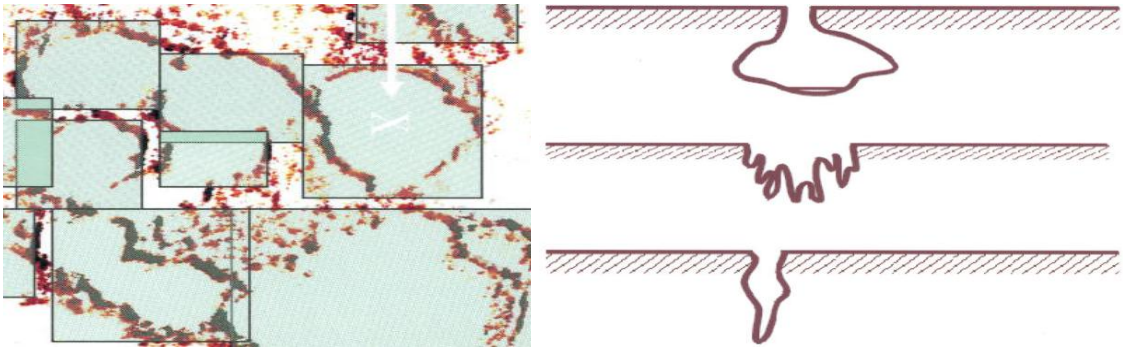

Figure 1.3: Corrosion cavities geometry patterns (NACE, 2005)

Practically, since no exact corrosion cavity shape and no data available from literature or published papers for the shape of corrosion cavities, even if it was available the complexity of the corrosion cavity makes it impossible to analyse numerically the physics of flow and separation of water from oil. We are interested in the fundamental physics of investigation should focus on model geometries. In addition, geometry must be restricted in terms of parameters to enable investigation of range of Reynolds numbers and water volume fractions. It is proposed to model the corrosion cavity using rectangular cavity, oriented perpendicular to the flow as presented in figure 1-4(a).

The rectangular shape will limit the number of geometrical parameters, hence simplifying the analysis. On the other hand rectangular shape represents the worst case scenario for phase separation. The control parameters are:

- The ratio of cavity length and width to pipe diameter (L/D and W/D)
- Ratio of cavity depth to pipe diameter (H/D)

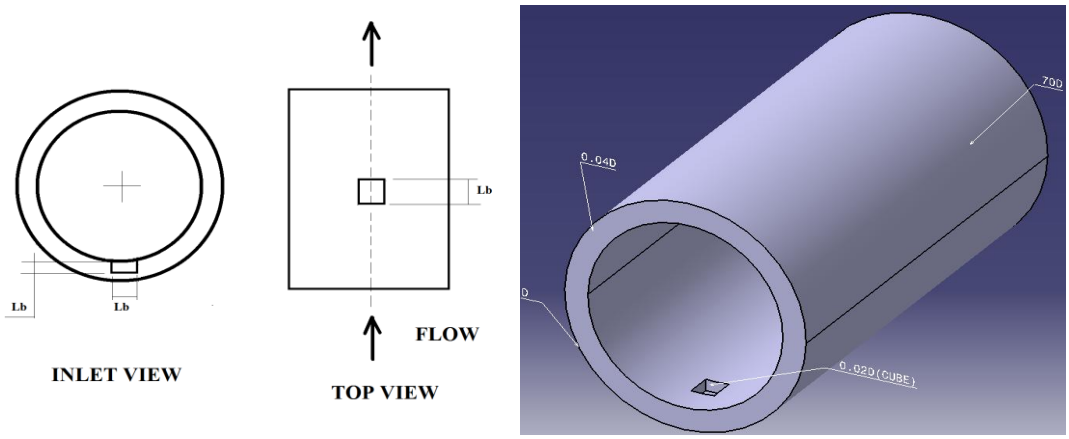

(a) (b)

Figure 1.4: Schematic of corrosion cavity model (a) Deep cavity (b) Isometric view

Determination of these parameters would take into account the pipe wall thickness of production pipes. A survey of onshore and offshore pipeline was performed and it indicated that the pipe wall thickness is typically of 1-4% of pipe diameter (Hebei, 1997). Therefore, the cavity depth will be restricted to 2% of the pipe diameter. Also the study will be limited on rectangular cavities with length equal to width (L=W). Then the only parameter left is the ratio of the cavity length to depth (L/H). These have to be selected to represent deep and shallow cavities. The typical range of Reynolds number of oil-water turbulent dispersed flow ranged from 5,000 to 100,000 and the range of water volume fraction between $\alpha_w = 0.1$ and $\alpha_w = 0.3$ based on the summary of published literature results reviewed of Reynolds number, mixture velocity, density and viscosity ratio as presented in table 1.1.

Authors	Pipe d (cm)	μ_o/μ_w	ρ_o/ρ_w	Range of mix.velocity (m/s)	Range of Reynolds No
Oglesby (1979)	3.81	0.828	1.000	1.0-1.5	7922-11883
Trallero (1995)	5.08	29.6	0.850	0.25-3.0	340-4076
Angelli et al (1996)	2.43	1.6	0.801	1.7-4.3	23454-59325
Soleimani et al (1999)	2.43	1.6	0.801	2.1-3.0	28963-41376
Angelli& Hewit (2000a)	2.43	1.6	0.801	0.3-4.0	41375-55167
Simmon et al (2001)	6.3	1.125	0.684	0.8-3.1	24936-96629
Elseth (2001)	5.63	1.6	0.790	0.75-3.0	23173-92694
Lovick et al (2004)	3.8	5.25	0.828	0.8-3.0	5492-20596

Table 1-1: Experimental data of oil-water dispersion in horizontal pipes

The scale sediments formation represents serious challenges for the operation and maintenance of multiphase pipelines. Scale build-up a hill like structure in the interior pipe base, scale sediments protect the underlying pipe steel from damage at the same time result to surface irregularities and changes in internal diameter of pipeline resulting in obstructing cleaning and pigging operation as well as increasing pressure loss, this situation affect the distribution capacity of the entire pipeline system and has consequence on increasing maintenance cost and down time. Typical service scale sediments deposits are shown in figure1-5.

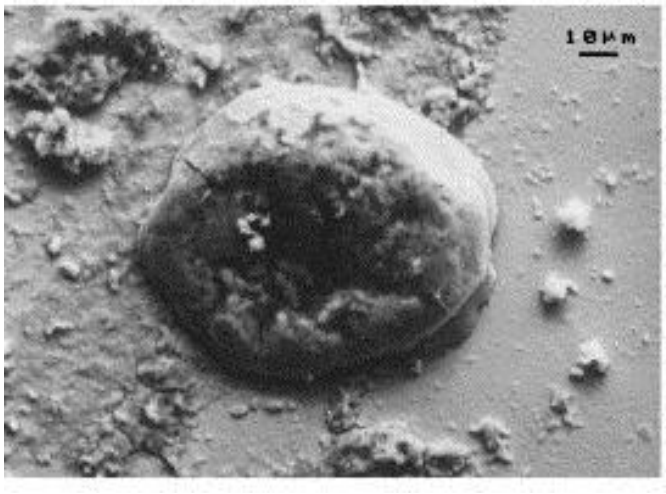

Figure 1.5: Corrosion scale deposits (Cavaleiro et al., 2000)

Oil-water flows over scale sediments (cubical obstacle) on the internal base of horizontal pipeline can generate flows recirculation, separation and reattachment with complex flow field and high turbulent flow intensity. The turbulent features near the ground surface of the scale sediment (cubical obstacle) approaching the top of the side results to flow recirculation, separation and formation of vortices. At the ground surface behind the build-up there will be recirculation, vortices formation and separation. The vortices formation may enhance further separation of water from oil due to the reduce velocity in the area, as a result localise corrosion may initiate at the base of the pipe surface as presented in fiqure1-6 (a). Presence of scale sediments in the internal base of pipe wall will increase pressure drop significantly across the pipe. In general, this pipe deformation can enhance mixing in pipeline flows; they enhance mixing by promoting turbulence and forming unsteady flow structures. Numerical simulation can be used to visualise and study the influence of scale sediments in changing the flow features as well as to measure the amount of water fraction at the pipe wall in the present of non-uniform corrosion or scale sediment build-up which may cause localised water break-out and have a marked effect on pipeline corrosion damage.

The analyses of flow field around the model cubic surface shown in figure1-6(b) clearly define the complex nature of flow passing over a cubic geometry, the flow field shows separations in front of the cube which consists of primary and secondary vortices, up to four separation vortices were classified. The main vortex curved around the cube into the wake as a horse-shoe vortex. The flow separates at the side wall, and at the front corner of the roof, whereby reattachments was observed on the side walls. Behind the cube, a large separation region interacts with horse-shoe vortex, initiate from the ground plate; an arch vortex develops behind the cube. The common fluctuation frequencies were identify sideways behind the cube, which were initiated from the vortex shedding of the flow past the side walls. Furthermore, flow separation behaviour was detected, particularly of the vortices in front and on the roof (Martinuzzi and Tropea, 1976).

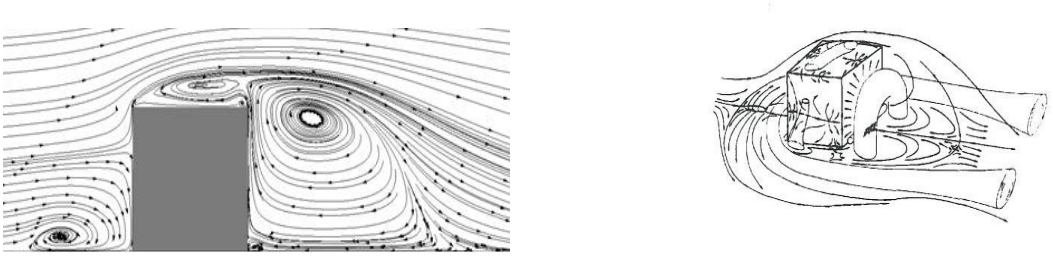

(a) (b)

Figure 1.6: Typical flow over a cubical geometry (Martinuzzi and Tropea, 1993)

Similarly for scale sediments geometry patterns, no exact shape of scale sediment deposits available from literature because of the irregularity profile of scale deposit. In order to quantify the amount of water volume fraction around the scale sediment and analyse the physics of separation of oil-water flows, the investigations will consider scale sediment model geometry (cubical obstacle). The cubical obstacle will be placed in the centre of the bottom wall of the pipe oriented perpendicular to the flow as shown in figure 1.7. The cubical shape will also favour separation. The only geometrical parameter left is then the linear dimension of the cube; this has to be 10% and 20% of the pipe diameter since we are interested in initial stages of sediment formation.

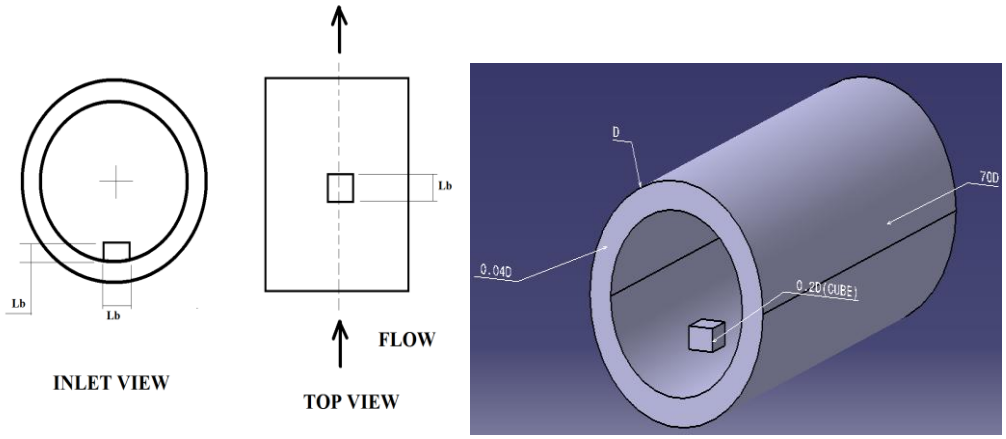

(a) (b)

Figure 1.7: Schematic of scale sediments model (a) higher aspect ratio (b) Isometric view

The investigation of oil-water dispersed flow through horizontal pipeline with corrosion cavity and scale sediments will focus on the water volume fraction at the pipe wall, particularly in the recirculation region. The main properties of interest are:

- Value of the maximum water volume fraction
- Position of the maximum water volume fraction
- Distribution of the water fraction in the area of the cavity and the cubical obstacle

The results will be interpreted in terms of the effect of the Reynolds number, inlet water volume fraction and geometrical parameters. Trends will be explored resulting in improved understanding the effect of pipe wall deformation under a range of flow conditions on the amount of water in contact with the wall which is directly linked to internal corrosion.

Analysis of oil-water turbulent flow in the presence of corrosion cavity and scale sediments will help to explain the contribution of these pipe deformation geometries in accelerating further corrosion damaged. The analysis will further present matrix of data showing relationship of Reynolds numbers or mixture velocity to the amount of in-situ water fraction and distribution at the pipe wall in the presence of pipe deformation (corrosion cavity and scale sediments). The investigations will have application in pipeline design particularly in enhancing the corrosion prediction models and consequently will further improve the performance and safety of pipeline operation.

1.1.1 Aims and Objectives

The interest is on evaluating the effects of pipeline roughness induced by corrosion cavity and scale sediments formation on pipe wall during the flow of oil and water in horizontal pipeline. The pipeline roughness (Corrosion cavity and scale sediments) on pipe wall occurs due to change in flow conditions, geometry and operating conditions which may lead to water break out and settle at the bottom of the pipe wall leading to internal pipeline corrosion. The prediction of these flow characteristics for oil-water flows in pipe is still limited or incomplete. However, understanding turbulent multiphase dispersed flow remains difficult and challenging. There are few publications on computational modelling of dispersed flows of oil and water in horizontal pipeline; most of the studies were on stratified flows. The aim of this project is to determine the effect of pipe deformation induced by corrosion and scale sediments formation at the pipe wall in accelerating further corrosion damage. The main objectives of this project are:

- Validation of CFD modelling of oil-water flows in stratified and turbulent dispersed flow regimes.
- Numerical investigation of corrosion-related wall-roughness effects (corrosion cavity model) on oil-water immiscible fluid flows in pipes. These investigations include detailed analysis of the different water cuts close to the pipe wall surface, which is caused by corrosion cavity.
- Numerical investigation and CFD modelling of the scale build-up sediments effect (cubical obstacle model) which induces roughness on the pipe wall in the oil-water flow. These investigations include analysis of different water cuts around the cubical obstacle region.

The ANSYS FLUENT 6.3 solver will be used as computational environment. The solver has the capability to resolve flow features through the solution of conservation equations. It is also intended to investigate the potential of FLUENT software in resolving important flow features such as turbulence dispersed flow of oil-water in pipe with deformations.

1.2 Physics of oil-water flow and literature review

A good understanding of physical properties of fluids such as viscosity, density and drops size and distribution and how they interact in horizontal pipeline are important in describing and predicting flow regime or flow behaviour. The viscosities of fluids increase with decrease in temperature and viscosity are higher at low shear rates compared with higher shear rates, hence flow encountered low resistance at higher shear rate resulting to decrease in oil-water mixture viscosity. Viscosity of oil is low at higher shear rate; this means at higher shear rate the flow encountered less resistance, in addition at higher shear rate the viscosity of dispersion show Newtonian behaviour, while at low shear rate, the viscosity display Non-Newtonian behaviour. Thus the turbulence within the fluid decrease as the viscosity increase which has overall effect on pressure drop.

Viscosity ratio for liquid-liquid flow can vary greatly depend on the liquids, viscosity ratio varies in the range of 0.3 to 10^4 for oil-water flow in horizontal pipeline (Valle, 1997). In multiphase flow, the viscosity of oil-water mixture depends on the viscosity of primary phase, viscosity of secondary phase, volume fraction of primary phase and temperature. Oil viscosity affects the formation of annular flow pattern. In case of oil annulus annular flow pattern, the size of the annulus reduces as the oil viscosity decrease (Arrichakran, 1989). Furthermore, flow of oil-water with low viscosity ratio lead to much instability in interface, the relative movement of interface can lead to disturbance and formation of droplets close to the oil-water interface, it has been noticed that oil-water mixture viscosity was higher than the oil viscosity when flowing alone in pipe, the increases in mixture viscosity lead to increase in pressure drop.

Density of liquids describes the mass of fluid system; the value can vary widely between liquids. During the flow of oil and water in horizontal pipe, the less dense fluid flows on top of the denser fluid. Hence, when the density ratio is high, the formation of dispersed flow patterns becomes difficult. The density ratio of oil-water flow varies between 0.7 and 1.1 (Valle, 1997). A typical

example of change of density with temperature of heptane's oil and water are illustrated in figure 1-8.

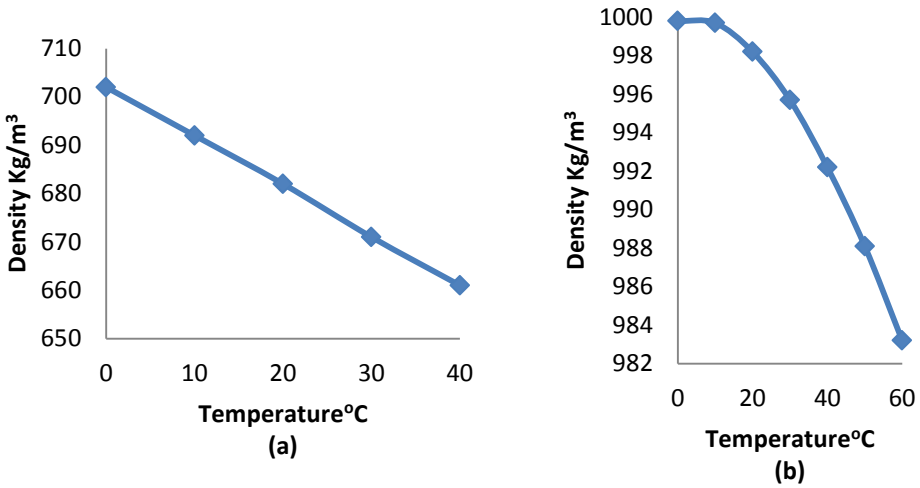

Figure 1.8: Variation of density with temperature (a) Heptane oil (b) Water

During the dispersed flow of oil and water in pipe, oil phase wets the pipe wall, the water phase flows as a fine droplet, the interaction of water small droplets merge into bigger droplets, bigger water droplets tend to separate from oil phase due to gravity in horizontal flow and form a water layer at bottom of the pipe, the distribution of droplet size in the cross sectional area of pipe depend on the turbulence intensity and force acting on the drop such as lift force.

Hinze (1956) conducted studies on drop size distribution, the author compute maximum drop diameter and the associated forces inspire the drop break up of immiscible fluid. He discovered that the dynamic motion of turbulent flow is responsible for the sizes of the largest droplets. In another investigation of oil-water flows, the author stated that the drop size distribution is a function of fluid properties, flow condition and pipe geometry. This idea of droplets size was used for predicting transition to fully dispersed flow pattern in liquid-liquid flow. Brauner (2002) modified Hinze's (1956) investigation to a high dispersion system where droplet coalescence takes place, the flow rate of oil phase should have enough turbulent energy to unsettle the tendency of water droplets to merge, he arrived at proportionality between the rate of turbulent energy supply by the flowing oil phase and the rate of surface energy production in the water

phase. The rate of drop break-up in turbulent dispersion depends on the critical Weber number (We_{crit}), which is the ratio of hydrodynamic stress to surface tension.

$$We_{crit} = \frac{\tau d_{max}}{\sigma} \quad \textbf{(1-1)}$$

Where,

$\tau = \text{Hydrodynamic stress}$

$d = \text{diameter of droplet}$

$\sigma = \text{surface tension}$

The bigger the critical Weber number, the more difficult to break droplet in two-phase dispersion but when the dispersion droplets greater than the critical Weber number, it tend to separate from immiscible flow dispersion to the bottom of pipe, which is commonly phenomenon obtained in oil-water flow in horizontal pipeline.

The simultaneous flow of immiscible fluids in long horizontal pipelines can have different distribution referred to as flow patterns or flow regimes, and in each flow pattern, the flow can also have specific hydrodynamic characteristics. The flow regimes can be described with superficial velocities of the phases, volume fraction, geometry of the pipe (e.g. diameter and orientation) and physical properties such as density and viscosity of the corresponding phases. Another property affects the flow pattern, which are the wetting characteristics of pipe wall (Angeli and Hewitt, 1998). During the horizontal flow of oil-water in pipe different flow patterns were identified, the main flow regimes are:

- Stratified flow can be defined as the flow occurs at lower mixture flow rate, which means that the mixture velocity is low; where the oil-water flow in clear separate phases relying on their densities; and where oil flow at upper part of the pipe and the water flow at the bottom lower part of the pipe are leading to a well define interface.

- Dispersed flow can be defined as the flow occurs at higher mixture flow rate, which means that the mixture velocity is high, where one fluid as dispersed drops and the other fluid as continuous phase. The changes in flow conditions determine the distribution of dispersed and continuous phase within the pipe. The dispersed drops can occupy portion of the pipe or uniformly distributed.
- Annular flow: Annular flow occurs in oil-water flow when one phase flow at the centre of the pipe and the other flow at the pipe wall forming an annular film. This flow pattern is common when one phase has higher viscosity than the other phase.

Trallero et al. (1997) performed comprehensive and well acknowledge experimental investigation on oil-water flow patterns and its transition on transparent horizontal test section of diameter 50.13 mm and 15.54 m long. Mineral oil and water were used as test fluid with viscosity ratio, density ratio and surface tension of 29.6, 0.85 and 36 dyne/cm respectively. The aforementioned authors also observed and classified six oil-water flow patterns under segregated and dispersed flow patterns. According to Trallero et al. (1997), the classification can be described as:

- Segregated Flows:
    - Stratified flow (ST);
    - Stratified flow with mixing at the interface (ST&MI).
- Dispersed Flows:
    - Water-dominated:
        - Dispersed of oil in water and water (Do/w&w);
        - Oil-in-water emulsion (O/w).
    - Oil-dominated:
        - Dispersion of water in oil and oil in water (Dw/o, Do/w);
        - Water-in-oil emulsion (W/o).

According to Trallero et al. (1997): “The stratified flow (ST) occur at low oil-water flow rate while the oil and water layer flow separately without any mixing

at the interface, with increase in flow rate, resulting to mixing between oil and water at the interface then stratified flow with mixing at interface occurs (ST&MI). With higher water flow rate, a single layer of water is flowing at the bottom part of the pipe while the dispersion of oil-in-water is flowing at the top, leading to a dispersion of oil- in- water over a water layer (Do/w&w), with further increase in water flow rate, oil-in-water dispersion is observed (O/w). Lowering the water flow rate at a small rate and increasing the oil flow rate, the two types of dispersion coexist, one at the top and the other at the bottom, the resulting flow pattern is dispersion of water- in- oil and oil- in- water (Dw/o, Do/w), with the additional increase in oil flow rate water-in-oil dispersion occurred (W/o)". The oil-water flow patterns in a horizontal pipeline are shown in figure1-9.

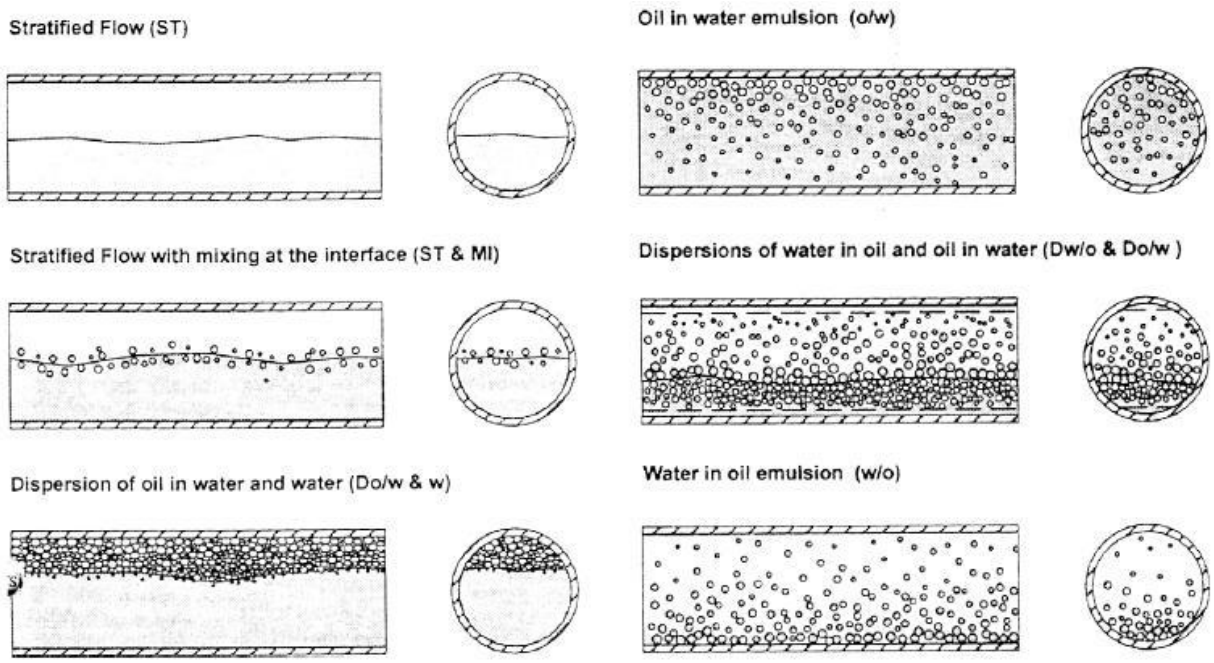

Figure 1.9: Classification of oil-water flow patterns in horizontal pipeline (Trallero et al., 1997)

Studies also demonstrated that at the lowest water volume fraction of 40%, the water would be dispersed in oil and at the highest water volume fraction of 60%; the oil would be dispersed in water. The dispersion of oil-water flows will change under different flow conditions, oil continuous flow will change to water

continuous flow and hence the phase wetting the pipe wall change from water phase to oil phase, this phenomenon in literature is refer to as “phase inversion” and is associated with change in pressure gradient and mixture viscosity (Xu, 2004; Brauner , 2002).

The quantitative measurements of flow conditions were stated in another experimental studies of oil-water wetting in horizontal pipe flow (Ayello et al., 2008) which show that at low velocity of 0.5m/s, with water cut lower than 10% water flows as droplets, but with water cut ranging from 10-15%, the water droplets become a single layer flowing at the bottom of the pipe, this condition leads to stratified flow. At this velocity of 0.5m/s, increased in water cut up to 15% leads to a clear stratified flow with water at the bottom of pipe wall and this condition is susceptible to internal corrosion damage. With water cut lower than 7% and further increase in velocity up to 1.0m/s, the flow turbulence increase, two different kinds of water drops are formed, the small and the big water droplets, the big wet the pipe wall. With further increase of water cut from 7% to 10%, when the flow velocity remain constant at 1.0m/s, the condition create a continuous water layer and some water is pulled in to the oil phase and the flow pattern becomes stratified flow with mixing at the interface, with further increase of water cut up to 15%, water is formed at the bottom of the pipe wall. When the mixture velocity is further increase to 1.5m/s and water cut to 20%, dispersed flow prevails and oil wets the pipe wall, therefore the pipe is free from internal corrosion.

1.2.1 Experimental studies of oil-water flows

In this section previous work on experimental studies of two-phase liquid-liquid flow in horizontal pipe is briefly reviewed, attention is given to different flow patterns observed and their classification and the effect the flow pattern on flow characteristics such as pressure gradient, hold up and drop size distribution. Experimental data will be selected from the review papers for numerical validation studies.

The determination of geometric distribution of two-phase flow in pipeline known as flow patterns and its parameters like pressure gradient, water holdup, phase inversion has been the subject of intensive research and measurement in past five decades (Russell et al., 1959; Charles et al., 1961; Guzhov et al., 1973; Oglesby, 1979; Arrichakaran et al., 1989; Nadler and Mewes, 1997; Angeli and Hewitt, 1998 etc). The study of oil-water flow pattern is very important because it has great influence in pipeline pressure drop and the analysis of oil-water flow patterns can provide information on position and distribution of oil and water phase, the phase that wet the pipe wall.

The flow patterns encountered in oil-water flows in horizontal pipeline are more difficult to identify and measure than the oil-gas flow pattern due to the effect of gravity and buoyancy which tend to separate the lighter fluid from the denser fluid as well as the dynamic flow behaviour of oil-water flow mixture, oil physical properties and rheological behaviour can be Newtonian or non-Newtonian also the viscosity ratio of oil-water can be wide-ranging from million to less than one (Xu, 2007). The recent improvement in instruments and measuring techniques, significant progress has been achieved in understanding oil-water flow patterns; different flow pattern have been identified and measured.

Russel et al. (1959) performed experiment of oil-water flow in a horizontal pipe to study the flow behaviour of oil-water flows, flow patterns, liquid holdup and pressure gradients with pipe of diameter 20.5mm and 8.5m long. The oil and water viscosity and density ratio are 20.13 and 0.84 respectively. The fluid characteristic inside the pipe were observed over the range of input-water

volume fraction from 0.1 to 10 at varying superficial water velocity from 0.035m/s to 1.08m/s. The observed flow patterns were stratified flow, mixed flow and bubble flow. The flow patterns were observed in laminar and turbulent flows, at low water input ratio, the continuous phase appears as elongated bubbles, with increase in input water volume fraction, stratified flow prevailed and with further increase in input ratio, the flow become mixed (dispersed). In similar investigation performed by Charles et al. (1961) who studied oil-water mixture of equal density in horizontal pipeline of 7.3m long and 26.4mm internal diameter, the authors investigate flow patterns and its parameters. The flow data used during the experiment are presented in table 1.2.

Oil viscosities	6.29, 16.8 and 65.0mPa s
Oil density	988kg/m^3
Range of oil velocity	0.015m/s to 0.9m/s
Range of water velocity	0.03m/s to 1.05m/s
Range of Input oil-water ratio	10% to 100%

Table 1-2: Input flow data of oil-water flow by Charles et al. (1961)

The flow patterns observed during the flow of equal density of oil-water mixture in horizontal pipeline are:

- Water-drops-in-water
- Concentrates-oil-in-water
- Oil-slugs-in-water
- Oil bubbles-in-water
- Oil-drops-in-water

With high oil-water ratios, oil is in the continuous phase and water-drops-in-oil was observed, with decrease in oil-water ratios, the observed flow patterns are the concentrates-oil-in-water, oil-slugs-in-water and oil bubbles-in-water, but when the water flow as continuous phase, oil-drops-in-water was observed. The authors related the flow patterns observed to flow patterns described by Russell

et al. (1959). The bubble flow of Russell et al. (1959) appeared corresponds to oil-drop-in-water, oil-slugs-in-water and oil bubbles-in-water, while the stratified flows correspond to the concentric-oil-in-water flow pattern and the mixed flows correspond to water-drops-in-water flow pattern. The schematic of flow patterns observed are shown in figure1.10

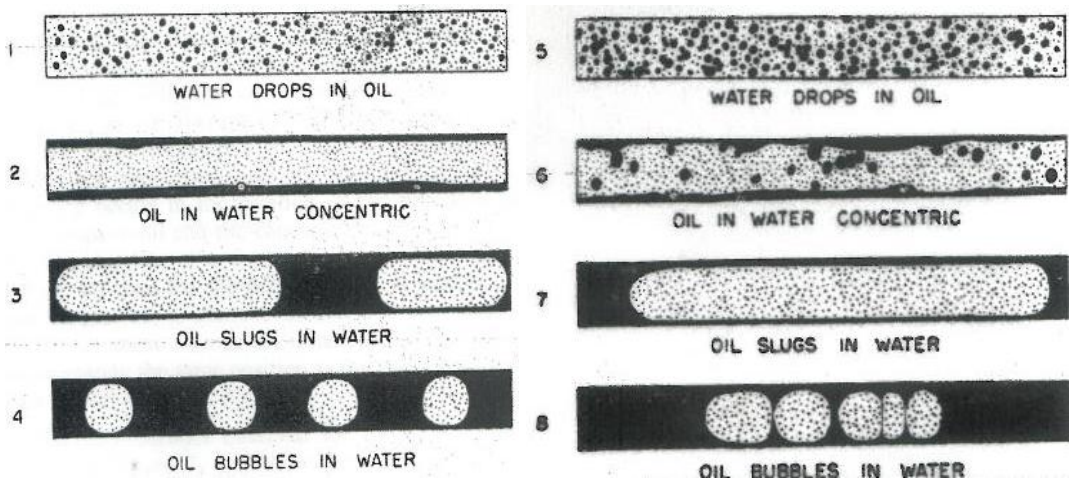

(a) (b)

Figure 1.10: Flow patterns observed for oil density 985kg/m^3 and oil viscosity of 16.8mPa s (a) water velocity=0.03m/s, (b) water velocity=0.20m/s by Charles et al. (1961)

More detailed experimental investigations of oil-water flow was conducted by Guzhov et al. (1973) to observed flow patterns in horizontal pipeline steel of internal diameter of 40mm. the ratio of oil and water viscosity and density are 21.8 and 0.898 respectively, the mixture velocity ranged from 0.2m/s to 1.7m/s. Eight flow patterns were observed and reported as:

- Stratified flow
- stratified flow with mixing at interface and a water layer
- stratified flow with mixing at interface and water layer of oil in water dispersion
- water in oil and oil in water emulsion
- water in oil emulsion
- oil in water emulsion and a lower water

- oil in water emulsion and a lower layers of oil in water dispersion
- oil in water emulsion

Annular flow pattern was not observed in the experiment. Most of the flow patterns observed by the authors are in good agreements with the flow patterns reported by (Trallero et al., 1997; Oglesby, 1973; Malinowski, 1975).

Malinowski (1975) investigates oil-water flow behaviour in horizontal acrylic pipeline of 38.4mm internal diameter and 30m long. The ratio of oil and water viscosity and density are 4.6 and 0.850 respectively while the surface tension measured as 22.3dyne/cm. The mixture velocity ranged from 0.19m/s to 1.36m/s. Flow patterns of stratified and dispersed flow were observed as segregated flow, dispersion of oil in water, dispersion of water in oil and dual dispersion. The flow pattern transition to dispersed flow occurred at oil superficial velocity from 0.3m/s to 0.61m/s. The measured experimental data were related with oil-water models of stratified flow model which show good agreements with experimental data. It is observed that pressure gradient is a function of oil viscosity and superficial velocity of oil.

The pressure gradient as a function of fluid properties and flow conditions was also observed and reported by Oglesby (1979) who conducted extensive experimental studies on liquid-liquid flows in horizontal pipeline with three classes of oils. The fluid physical properties and experimental data are shown in Table1.3

Ratio of oil and water viscosity	32, 61, 167
Ration of oil and water density	0.859, 0.863, 0.870
Surface tensions	30.1, 29.4, 35.4
Range of mixture velocity	0.61m/s, 3.66m/s

Table 1-3: Fluids properties and experimental case data by Oglesby (1979)

The authors observed and reported 14 different flow patterns, but Trallero et al. (1997) reclassified them in to six flow patterns namely: segregated, semi-segregated, semi-mixed, mixed, semi-dispersed and homogeneous flow patterns. In separate experiment studies with the same experimental facilities of equal pipe internal diameter of 50.8mm and the fluids with the same fluid physical properties. Cox and Scott (1985) carried out a detailed investigation of oil-water flow in a pipe to observed flow patterns and to resolve the flow characteristics features. The mixture velocity used varied from 0.88m/s to 1.08m/s with viscosity and density ratio of 1.38 and 754 respectively. The observed flow patterns reported are stratified flow, dispersion of oil- in- water and dispersion of oil- in- water in water layers. The study also revealed that as the mixture velocity increase from stratified flow and stratified flow with mixing at interface, the amount of phase dispersion also increases.

Arirachakaran et al. (1989) carried out experimental analysis on oil-water flows in horizontal pipelines with a wide range of oil viscosities and under two different pipe materials of internal diameters of 41mm and 26.6mm. The investigation includes bringing together 1200 experimental data to identify flow patterns and its transition. The water volume fraction varied from 5% to 90%. The viscosities of oil used in 41mm diameter pipe are 4.7, 58, 84 and 115mPa s while the viscosities of oil in 26.6mm internal diameter are 237mPa s and 2116mPa s.

Five flow patterns were observed in terms of stratified flow with mixed in interface, mixed flow with separated flow of dispersion and free layer phase, annular flow pattern and dispersed flow of oil in water and water in oil flow pattern. The following conclusions are obtained; the oil viscosity from the experiment has negligible effect on flow pattern, when water is the continuous phase, the oil annular flow pattern decreased in size as the oil viscosity decrease. During the flow of oil phase as continuous phase, the water annulus flow pattern was not observed because the oils used in the studies were not heavy viscous to maintain oil core in water annular flow. The flow pattern under this study has good agreements with flow pattern observed by Trallero et al. (1997). Flow patterns characteristics of oil-water were also investigated by Valle

and Utvik (1995) in a horizontal pipe of 120m long with inner diameter of 72.6mm. The two observed flow patterns are; stratified flow and dispersed flow. For all the flow rates, dispersed flow was observed when the water volume fraction is less than 45%, while stratified flow occurred when the water volume fraction is greater than 45%.

In another study of oil-water flow characteristics by Valle et al. (1997) who performed experimental studied of oil-water stratified flow to investigate pressure drop, local holdup and flow patterns characteristic using water and D80-oil with viscosity and density ratio of 2.55 and 0.792 respectively. The flow patterns reported are stratified flow, stratified flow with mixing at interface, dispersion of oil in water over a water layer and dispersion of water in oil over water layer. The experimental results showed that when the superficial velocity of the phase greater than 0.7m/s, higher in-situ dispersed phase fraction was formed at the pipe base or at the top of the pipe and water bubble films were observed in the pipe wall for all the reported flow patterns. Flow patterns were identified and reported with the aid of modern measuring instruments by Nadler and Mewes (1997) investigated the flow of oil-water in 48m long horizontal steel pipe of 59mm diameter. The measurements were performed for oil viscosities of 22, 27 and 35mPas. The observed flow patterns look similar to the flow patterns reported by Trallero et al. (1997), as compared in Table1-4. The results are also reported for the effect of emulsification and phase inversion on the pressure drop of different flow regimes.

Trallero et al. (1997)	Nadler and Mewes (1997)
Stratified flow	Stratified flow of separated phases
Stratified flow with mixing at interface	Stratified flow with mixing at interface
Dispersion of oil in water and water	Oil-in-water dispersion above a water layer
Oil- in- water emulsion	Unstable oil-in-water emulsion
Dispersion of water in oil and oil in water	Layers of dispersion water in oil and oil in water& water
Water- in- oil emulsion	Unstable water-in-oil emulsion
	Layers of water in oil dispersion and water

Table 1-4: Comparison between flow patterns of Trallero et al. (1997) and Nadler and Mewes (1997)

The authors differentiated between dispersion and emulsions of flow, dispersion flows are those flows in which there are two phase, one primary layer is continuous with secondary layer disperse non-equal droplets, while the secondary phase is a pure liquid. Emulsion is defined as one primary phase is flowing in the whole pipe cross-section while the secondary phase is completely dispersed in the whole cross-section of pipeline in uniform size droplets.

Andreini et al. (1997) conducted an experiment on two-phase flow of oil-water flows in a transparent horizontal pipe of 30mm internal diameter, 1m long to observed flow patterns and its transitions. The physical properties of oils used in the experiment are shown in table 1.5. The mixture velocity varied from 0.12m/s to 0.3m/s. Flow patterns were observed and classified as dispersed flow, slug flow, bubble flow, plug flow and annular flow.

Viscosity at 25^{o}C $10^{-4}m^2/s$	Density at 25^{o}C Kg/m^3	Interfacial tension at 25^{o}C
71.170	866.48	31.5
51.325	866.25	36.0
9.874	865.50	37.4

Table 1-5: Experimental oil physical properties by Andreini et al. (1997)

Angeli and Hewit (1998) studied pressure gradient and flow patterns during the simultaneous flow of oil-water in horizontal acrylic and steel pipes of 24mm and 24.3mm respectively. The mixture velocity varying from 0.3m/s to 3.9m/s while input water volume ranging from 0% to 100%. The oil physical properties are presented in table 1.6

Density	801kg/m^3
Viscosity at 25^{o}C	1.6mPa
Interfacial tension oil-water at 25^{o}C	0.017N/m
Interfacial tension air-oil at 25^{o}C	0.027N/m

Table 1-6: Oil physical properties by Angelli and Hewitt (1998)

The observed flow patterns ranging from stratified flow, three layers flow pattern, stratified/mixed flow pattern to fully dispersed flow pattern. Stratified flow pattern occurred at a lower mixture velocity for steel pipe than the acrylic pipe, with increase in mixture velocity, drop of one liquid form within the layer of other, but with higher flow rate, drops tend to appear in the oil-water interface, three layer flow pattern observed. Stratified/ mixed flow pattern occurred during the dispersed flow of oil and water, one liquid is continuous while the other forms dispersed drops, at a lower velocity, under this regime; the dispersed phase occupied the top and bottom part of the pipe while the centre is a clear of continuous layer. The stratified flow pattern occurred in steel pipe at 0.3m/s while in acrylic pipe at about 0.6m/s. The three layer flow pattern appeared in steel at a lower velocity ranging from0.7m/s to 1.03m/s than the acrylic which ranging from 0.9m/s to 1.7m/s. The dispersion in steel pipe (1.3m/s) is more homogeneous than the acrylic pipe (1.7m/s). It was found that using equal mixture velocity and water volume fraction, the flow patterns in steel pipe is more unstable than the acrylic pipe and oil phase have a tendency to remain more continuous in acrylic pipe than the steel pipe. These were ascribed to different wettability characteristics of the two pipe materials.

The influence of mixture velocity in determines different flow patterns in oil-water flow were extensively study by Soleimani et al. (2000). The authors performed experiment to investigate the spatial distribution of oil and water in

horizontal pipeline for varying mixture velocity and input water volume fraction. The oil and water distribution experiment was conducted with input water volume fraction of 24%, 32%, 34%, 36%, 46% and 60% and at varying mixture velocity of 1.25m/s, 2.2m/s and 3m/s. The results showed at low mixture velocity stratified flow prevailed, while the higher the mixture velocity the higher the degree of mixing, the dispersed phase mixed with continuous phase to form homogeneous mixture, this occurred at mixture velocity of 3m/s. At mixture velocity of 1.2m/s and input water volume fraction of 46%, three layer flow pattern was observed, this flow pattern was also observed and reported by Lovick and Angeli (2004) as dual continuous flow.

Fairuzov et al. (2000) conducted experiment to investigate flow patterns and its transition in oil-water flow mixture in 16 inch horizontal steel pipeline carrying light crude oil. Mixture velocities varied from 0.05m/s to 2.11m/s, water volume fraction ranged from 1.5% to 50%. Flow patterns of oil-water were identified and then categories to two major types; stratified and dispersed flow pattern. The full-scale experimental data were used to plot flow pattern map. The transition boundary was related with theoretical flow transitional line, the authors found that stratified and non-stratified transition have good agreements with viscous Kelvin-Helmholtz analysis reported by Trallero et al. (1997). The results revealed that in stratified flow total phase separation does not occur; small amount of water droplet always present in oil continuous phase.

Lovick et al. (2000) performed experiment on oil and water flows in horizontal stainless steel to study stratified and dispersed flow patterns to calculate the pressure gradient. During the stratified flow, mixture velocity was varying from 0.021m/s to 0.35m/s. Pressure drop, in-situ hold-up and velocity ratios were measured at two oil volume fraction of 61.5% and 76.9%. For dispersed flow experiment, mixture velocity varying from 2m/s, 2.5m/s, 3m/s and 3.5m/s while for the input oil volume fraction ranging from 0% to 100%. The investigations started with single phase (oil), the pressure gradient decreased as oil volume fraction increase up to 60%, with increase in oil volume fraction, there is small increase in pressure gradient before it achieve minimum at 72% to 80%, then

pressure gradient increase as the oil volume fraction decrease and these correspond to the phase inversion region. The flow patterns observed during the dispersed flow are the dispersion of oil or water as continuous phase. The investigation of flow structure was conducted by Angeli and Hewitt (2000a) during the concurrent flow of oil and water in two different pipe materials of 24mm (acrylic) and 24.3mm (steel) inner diameter. Different flow patterns were observed and reported in both the acrylic and steel pipe. The flow patterns are, stratified wavy flow pattern, stratified wavy with drops, three layer flow pattern, stratified mixed flow pattern and fully dispersed or mixed flow pattern.

The mixed flow pattern occurred in the same mixture velocities as the three layer flow pattern, at below 30% input water volume fraction and above 50% of input water volume fraction in steel and acrylic pipe. The mixed flow pattern occurred in steel pipe at a lower velocity than the acrylic pipe. This was attributed to the differences in pipe wall roughness of the two pipe materials. In stratified mixed and three layer flow patterns, the oil continuous phase flow over a large range of mixture velocity in acrylic pipe than the steel pipe, this is because oil tend to wet and stick to acrylic pipe wall over a long time than the steel pipe. The flow structure in steel pipe was more disturbed than the acrylic pipe and this was ascribed to the pipe roughness. The authors concluded that the results of the transparent pipe or acrylic pipe cannot be used for the steel or any pipe materials in the design of oil-water pipe flow system.

Simmons and Azzopardi (2001) studied drop size distribution in dispersed liquid-liquid pipe flow in order to investigate the flow condition or flow pattern at which the dispersion occurred. The experiments were performed on both horizontal and vertical pipe. Mixture velocities ranging from 0.8m/s to 3.1m/s while the viscosity and density ratios are 1.125 and 0.684 respectively. Over the range of flow condition on horizontal flow, different flow patterns were identified and classified as; stratified flow, stratified flow with mixing at the interface, continuous dispersion of water in oil with water layer and water in oil dispersion. The flow patterns observed were in good agreements with flow patterns observed by Trallero et al. (1997), the oil droplets in water layer was not

observed under this experiments because the oil phase dominate the whole cross section of the pipe wall as a continuous phase with only present of dispersion of water at a water layer. The flow patterns transition from stratified to dispersed flow were well predicted by the flow patterns map as shown in figure1-11 but it over predicted the transition to complete dispersion.

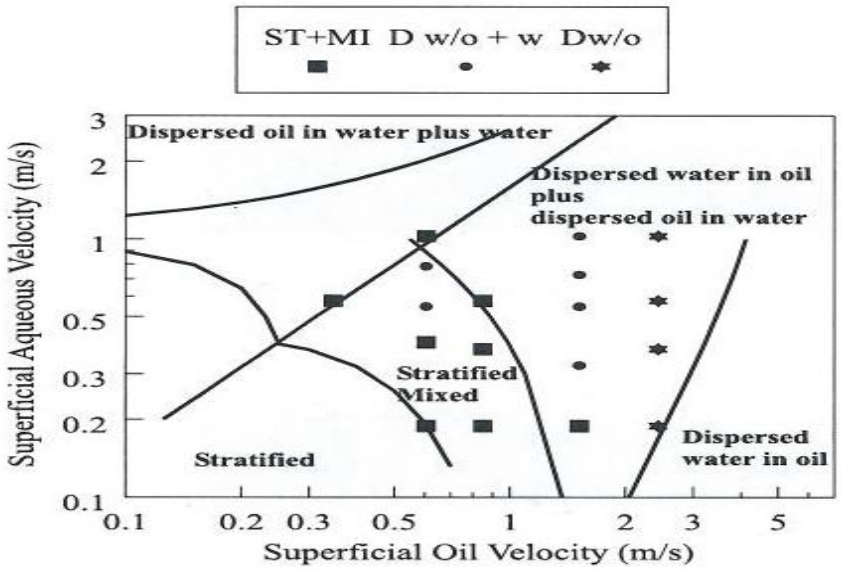

Figure 1.11: Flow pattern map of oil-water flows as compared with map of Trallero et al. (1997)

Brauner (2002) performed detail experimental and modelling and control of liquid-liquid two phase system. Flow patterns characteristics were described and classified and transition from stratified to fully dispersed flow were model together with effect of curve interface. According to the author the flow conditions, pipe geometry and operational condition are the control parameters in determination of flow pattern or flow structure during the flow of oil-water in horizontal pipeline. Eighteen (18) different flow patterns were identified in liquid-liquid systems which were classified under four categories: stratified flow pattern with smooth interface or stratified flow pattern with wavy interface, slug flow pattern, annular flow pattern and dispersed flow pattern.

At low flow rate, stratified flow may exist due to the effect of gravity, with increase in flow rates, the phases interface becomes wavy, with drops at interphase, the entrainment increase with additional increase in flow rate, the

two phases are continuous at the bottom and top with drop at the interface, forming a three phase layers. For high water flow rate, the water phase becomes continuous, while the oil phase is discontinuous result to oil dispersed in water. Similarly for high oil flow rate, the water phase may become discontinuous leading to water dispersed in oil. The oil and water may form annular-core composition, the oil flows in a core while the water forms the annulus. The annular flow is commonly found in small internal diameter pipe with small density difference between the two phases (Charles et al., 1961; Arrichakran et al., 1989).

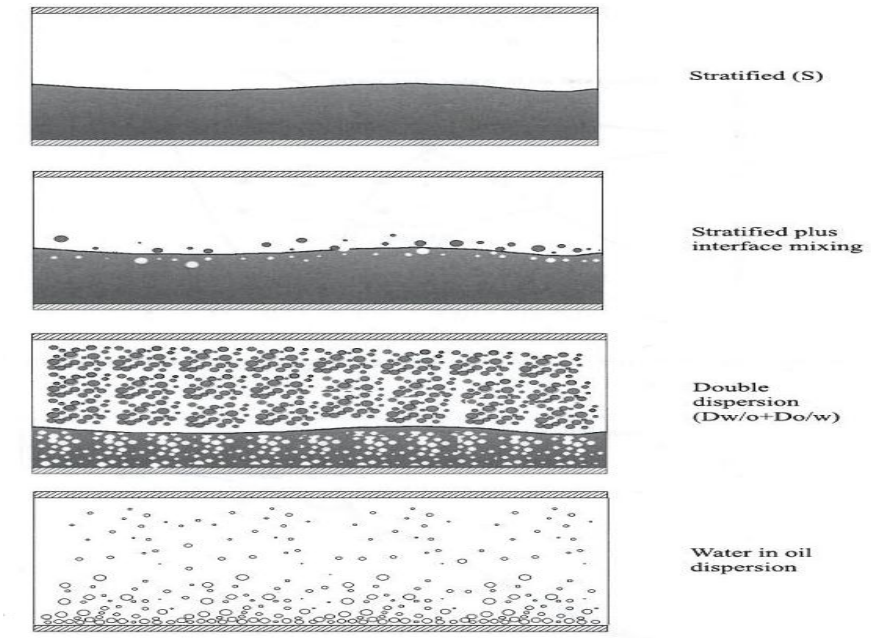

Figure 1.12: Oil-water flow patterns classification by Simmons and Azzopardi (2001)

Lovick and Angeli (2004) investigate three layers flow pattern during the flow of oil-water in horizontal pipe. The oil volume fraction ranged from 10% to 90%. The dual continuous flow was observed at 1.5m/s mixture velocity but with further increase in mixture velocity, the dual continuous flow pattern was only observed in 50% input oil volume fraction. However, the lower the flow rate or mixture velocity, the closer dispersed drops concentrate at the interface at high mixture velocity, the dispersed phase tends to move from the pipe wall to the centre of the flow. At lower mixture velocity, stratified flow occurred and the

denser phase wet the pipe wall. However, three reasons were given by Soleimani et al. (2000) on dispersed phase droplets tend to move to the centre of the flow due to high mixture velocity: the boundary layer push the droplet to the centre because of boundary layer lift force, gravity helps in droplets distribution and finally the droplets in dispersed phase have equal diffusivity with the continuous phase.

Rodriguez and Oliemans (2006) conducted experimental studies on oil-water flow in horizontal and inclined pipeline to measure flow patterns, holdup and pressure gradients in 82.8mm diameter steel pipe, 15m long with mineral oil and brine as test fluids. The viscosities of mineral oil and brine are 7.5mPa s and 0.8mPa s while the densities are 830kg/m^3 and 1060kg/m^3 respectively. The mixture velocities ranged from 0.04m/s to 5.55m/s. The flow patterns were measure over pipeline inclination of -5^0, -2^0, -1.5^0, 0^0, 1^0, 2^0 and 5^0. Seven flow patterns were observed and reported which is in line with flow pattern proposed by Trallero et al. (1997) and are given in table 1.7.

Stratified smooth	ST
Stratified wavy	SW
Stratified flow with mixing at interface	ST &MI
Dispersion of oil in water and water	Do/w &w
Oil in water homogeneous dispersion	o/w
Water in oil homogeneous dispersion	w/o
Dispersion of water in oil and oil in water	Dw/o &Do/w

Table 1-7: Flow pattern classifications as observed by Rodriguez and Oliemans (2006)

Recently an experiment study was conducted by Mantal et al. (2007) to investigate the difference and similarities of oil-water flow pattern in two different pipe diameters, the diameters of the pipes are 0.012m and 0.025m. The flow pattern observed in 0.025m diameter pipe are smooth stratified, wavy stratified, three layer flow, plug flow, oil dispersed in water and the white emulsion, while

the observed flow patterns in 0.012m diameter pipe are wavy stratified, plug, slug, rivulet, churn, oil dispersed in water and white emulsion.

The flow in small diameter pipe indicated that oil flow as plug at the upper part of the pipe, while the oil flow as stratified wavy in case of large diameter pipe, with higher increase in phase velocities, the three layer flow pattern prevail with droplets at interface in 0.025m diameter pipe, also the present of surface tension lead to the formation of slug flow pattern in 0.012m diameter pipe. With additional increase in oil flow rate, rivulet flow pattern was observed in small pipe. In large diameter pipe, increase in oil flow rate lead to increase in interfacial shear stress which results to more concentration of drops at phases interface and formation of dispersed flow pattern. From experimental results, the three layer flow pattern is only common in large pipe but does not appear in small pipe. On the other hand, rivulet and churn flow patterns appeared in small pipe, these differences occurred due to the effect of increase in surface tension and contact angle between the oil-water interfaces.

Xu (2007) review the experimental studies on oil-water flow in the past decades with emphasis on flow patterns identification and transition, pressure drop prediction and phase inversion. The flow patterns transition prediction in oil-water flows is a difficult hydrodynamic challenge; there were no comprehensive flow pattern maps for immiscible fluid interaction in horizontal pipelines due to the difference in the type of oil, fluid properties and the difference in the properties of pipe material. However, Trallero (1995) flow patterns transitions criteria are given in table1-8 well recognised with the previous published flow pattern transition in oil and water flow, only one flow pattern was not reported, the dispersion of water in oil over water layer (Dw/o &w), in this flow pattern, there was free water zone, which contain the oil droplets of different diameter sizes.

Segregated flow			
Flow pattern			Transition criteria
ST			VKH
ST&MI			IKH, $U_w < U_{wmL}$ & $U_w > U_o$
Dispersed flow pattern water dominated region		Oil dominated region	
Flow pattern	Transition criteria	Flow pattern	Transition criteria
Do/w & w	$U_w < U_{wmH}$ & $U_w > U_o$, outside IHK	Dw/o & Do/w	$U_o \geq U_{ooH}$ & $U_w > U_{wwH}$, inside & outside IHK
o/w	$U_w \geq U_{wmH}$ & $U_w > U_o$, outside IHK	w/o	$U_w < U_{omH}$ & $U_w > U_o$, outside IHK $U_o > U_{omH}$, inside IHK

Table 1-8: Flow pattern transition criteria (Trallero, 1995)

Whereby U_o is the oil layer velocity; U_w is the water layer velocity; U_{omH}, U_{wmH}, U_{ooH}, U_{wwH} and U_{wmL} are transition velocities, respectively; VKH is the viscous Kelvin-Helmholtz Criteria; IKH is the inviscid Kelvin-Helmholtz Criteria.

The authors list various measurement techniques in identifying and measuring flow patterns and its boundaries. The early investigators used visual observation with combination of photography (Oglesby, 1973; Malinowski, 1975); this is achieved through a transparent pipe on the pipe wall, in addition to visual observation, a photographic or video technique and high frequency impedance probe is used to observe flow patterns and its boundaries by making use of local probes, and conductivity needle probe which is more applicable to dispersed flow regime because the continuous phase is not easily identified; the water phase was conductive while the oil phase was non-conductive, the conductivity probe was used to discover the continuous phase as also reported by Arrichakaran et al. (1989).

The average crude oil production and transportation in the world become heavier oil, and water is present during the oil recovery from oil. Vuong et al. (2009) performed experimental studied on high viscosity oil-water pipe flow in horizontal and vertical pipe. The study was conducted with 50.8mm internal

diameter steel pipe of horizontal and vertical inclination to examine the effect of viscosity on pressure gradient, water holdup and flow patterns. The experimental data were presented over the range of water and oil superficial velocity of 0.1m/s to 1m/s. The oil physical properties are given in table1-9:

Name of product	**ND50 mineral oil**
Viscosity	0.225Pa.s at 37.8^{o}C
Density	884.4kg/m^{3} at standard
Interfacial tension with water	35.75dynes/cm at 19.8^{o}C 30.4dynes/cm at 19.8^{o}C

Table 1-9: Oil physical properties as reported by Vuong et al. (2009)

Relying on the literature of Brauner (2002), flow patterns observed in horizontal direction are “stratified wavy with droplets at interface”, “dispersion of oil in water over a water layer”, and “full dispersion of oil in water and dispersion of oil in water and oil films”. The stratified wavy with droplets at interface occurred at low flow rate, this flow pattern was observed by Brauner (2002) as stratified flow with mixing at the interface (ST&MI). With increase in flow rate, the water phase becomes continuous with oil disperse as droplet at the top of the pipe cross section, this flow patterns is known as dispersion of oil in water over a water layer, with further increase in flow rate, this lead to full dispersion of oil in water. The dispersion of oil in water and oil films flow patterns occurred when the oil films was observed on the pipe wall. The oil films to the wettability of pipe wall materials as reported by Angeli and Hewit (2000b).

The experimental data of liquid-liquid flows in horizontal pipe are summarised in table1.10

Authors	Pipe D (cm)	μ_o/μ_w	ρ_o/ρ_w	σdyn/cm	Velocity Range(m/s)	Flow pattern
Russell et al. (1959)	2.03	20.13	0.840		0.04-1.08	SM, D_o/w, B_o
Guzhov et al. (1973)	4.0	21.8	0.898	44.8	0.2-1.7	SM, D_w/o, D_o/w, D_o/w&w, D_w/o & O/w
Malinowski (1975)	3.84	3.33	0.850	22.3	0.19-2.08 0.26-1.36	SM, D_o/w, D_w/o D_w/o & O/w
Laflin&Oglesby (1976)	3.84	4.12	0.830	22.3	0.17-1.16 0.17-1.16	SM, D_o/w, D_w/o D_w/o & O/w
Oglesby (1979)	4.1	32 61 167	0.859 0.863 0.870	30.1 29.4 35.4		D_o/w, D_w/o , D_w/o & O/w
Cox(1985)	5.08	1.54	0.756	30	0.05-0.64 0.05-0.64	ST, D_o/w, D_o/w&w
Scott(1985)	5.08	1.54	0.756	30	0.05-0.64 0.05-0.64	ST, O/w, D_o/w&w
Nadler&Mewes (1995)	5.9	18-35	0.848	30	0.0078-1.48 0.0143-1.44	ST, SM, D_o/w&w D_w/o, D_w/o & O/w D_o/w, D_w/o&w
Valle&Kvandal (1995)	3.75	2.25	0.792	37.3	0.2-1.2 0.25-1.15	ST, SM, D_o/w&w D_w/o & O/w
Trallero et al. (1997)	5.08	29.6	0.85	36	0.01-1.8 0.01-1.8	ST, SM, D_o/w&w D_w/o, D_w/o & O/w D_o/w, D_w/o&w
Andreini et al. (1997)	0.3 0.6	562 920 1307	0.886 0.889 0.893	31.5 36.0 37.4	Q_o =0.32 to 3.31L/h Q_w =33.9	D_o/w, SLo,PLo ANw
Angeli&Hewit (1998)	2.43 2.4	1.6	0.801	17	0.2-3.9 0.2-3.9	ST, D_o/w, D_w/o D_o/w&w, D_w/o & O D_w/o & O/w
Fairuzov et al. (2000)	36.3 5.0	5.07	0.853		0.05-2.11	ST, D_o/w&w
Lovick et al. (2000)	3.8	5.25	0.828	44.7	2.0-3.5	S_t, SM, D_o/w, D_w/o
Angeli&Hewit (2000)	2.43	1.6	0.801	17	0.2-3.9	ST, D_o/w, D_w/o D_o/w&w, D_w/o & O D_w/o & O/w
Simmon et al. (2001)	6.3	1.125	0.684	10	0.8-3.1	SM, D_w/o &w, D_w/o
Angeli et al. (2002)	3.8	5.25	0.828	44.7		SW, D_o/w, D_w/o & O/w D_w/o

Table 1-10: Experimental data of liquid-liquid in horizontal pipe flows (Angeli and Hewitt, 1998; Brauner , 2002; Xu, 2007)

The flow patterns show significant difference because of the influence of mixture velocities, density ratio, viscosity ratio; pipe wall wetting properties and the diameter of the pipe (see more details in table 1-10). The oil-water viscosity ratio varied between 1 and 1307, while the density ratio ranged from 0.7 to 0.9. The Interfacial tension also varied from 10 to 50dyn/cm, while the mixture velocity ranged from 0.05 to 3.9 m/s and from 0.0078 to 4.0 m/s.

work was done on oil-water dispersion in horizontal pipe to have better understanding of the nature of interactions between the two phases and how it affect the flow patterns (Angeli and Hewit, 1998; Suleimani et al. ,1999). The dispersed flow patterns for oil-water tend to separate to the top or bottom of the pipe depending on density in relation to the continuous phase, the two types of dispersion: oil-in-water dispersion and water-in-oil dispersion have been identified in most of the studies. The experimental results revealed flow behaviour in oil-water flow dispersion which is affected by density, viscosity of the phases and the droplets size and distribution. In some of the experiments, stratified annular flow and stratified slug appeared (Andrainel et al., 1997; Arrichakran et al., 1989). The oil viscosity has great influence in the occurrences of annular flow. The annular flow in oil-water flow can be found in low density ratio of oil and water and in small diameter pipe.

The published experimental data for liquid-liquid flow in horizontal pipeline all agreed well with the flow pattern presented by Trallero et al. (1997). One of the flow regimes such as water dispersion in oil over a clean water layer was not observed in most of the studies. Trallero et al. (1997) reported that, when water was dispersed in oil and there was a free water zone, the oil always presents in the water in the form of droplets of different diameter sizes. Some of these experimental data on stratified and dispersed flow regimes will be used for validation study against computational modelling.

1.2.2 Oil-water flow design parameter (pressure gradient)

The pipe flow design parameters are the pressure gradient, phase inversion and water hold up. This section described how the pressure gradients play a role in pipe flow design and the contribution of published work from literature in understanding pressure gradient as design parameters during the flow of oil-water in pipeline.

Early research on oil-water flow has been dedicated on pressure drop reduction through the introduction of small amount of water to the viscous oil to reduce the shear stress between the pipe wall and the fluid which may result to significant pressure loss reduction. Another approach of pressure loss reduction is by reducing the viscosity of oil by means of increasing the temperature of oil, but this method is expensive. Pressure drop reduction becomes important when transporting oil in pipeline over a long distance because of high viscosity result to high pumping power requirement and the less viscous phase wets the pipe wall while the more viscous phase form the core of the pipe. it is difficult to achieve continuous annular flow in immiscible flow due to change in pipe geometry, buoyancy force and the mixing between the phase. In addition, phase distribution is complex because of existence of different flow pattern with different hydrodynamics features, water in oil dispersion is more stable and easier to achieve than oil-core annular flow. Knowledge of hydrodynamics characteristics and measurement of water volume fraction in oil-water flow are the first step for determine the pressure gradient in pipe flow.

Russell et al. (1959) investigate pressure loss reductions in oil pipeline as a result of addition of water using mathematical analysis for segregated flows. The experimental pressure gradients were compared with analytical method for pipe and flat plate. This early experimental results of pressure gradient stimulate further investigation by Charles et al. (1961) using equal density of oil-water mixture. The experimental results obtained indicate that pressure gradient was reduced to minimum through the addition of water when the oil is in laminar flow. Pressure reduction was obtained by the addition of water when the

superficial velocity of oil is 0.3m/s, while for oil superficial velocity greater than 0.3m/s pressure loss was not observed. It can be conclude that addition of water to oil, which is not in turbulent stage, will lower the pressure gradients to minimum, after further addition of water to oil; the pressure gradient will be greater than the pressure gradient of single phase oil flow.

The experimental pressure gradient studies by Charles et al. (1961) further inspire an extensive experimental pressure gradient research by Guzhov et al. (1973) in which the authors observed a peak in pressure gradient at 60% water fraction and were ascribed to phase inversion of the oil-water mixture during oil-water dispersion. During stratified flow at low mixture velocities, with increase in oil volume fraction, the pressure drop reached maximum at 60% water volume fraction, while further increase in mixture velocities, the pressure drop reached the maximum at 10-30% water volume fraction. It has been deduced in stratified flow with oil of higher or medium viscosity, the pressure drop decreases with increasing water from single oil phase to single water phase, this observation was also reported by Nadler and Mewes (1997).

The effect of droplet size on pressure loss reduction was studied by Knudson et al. (1973) who studied theoretical and empirical relation for pressure drop during the flow of immiscible fluid in pipeline. The authors observed that the dispersed droplet size have small effect on pressure losses, the pressure drop decreases for increasing drop size with a high concentration of dispersed droplet, while Malinowski (1975) measured pressure gradient and compared the experimental data with stratified flow models and homogeneous model of Soot et al. (1971). The stratified model shows good agreements with the pressure gradient experimental data at mixture velocity greater than 0.14m/s. The author observed that pressure gradient of oil-water flow was functions of oil-water volume fraction ratio, oil viscosity and superficial velocity of oil and was supported by Arichakkran et al. (1989) who investigated pressure gradient in stratified and homogeneous turbulent dispersed flows of immiscible fluid. The authors observed pressure gradient as a function of oil viscosity, input water volume fraction, temperature and mixture velocity. For oil-in-water dispersion,

temperature and oil viscosity has negligible effect on pressure gradient which is in contrast with water-in-oil dispersion where temperature has a great influence on pressure drop because temperature affects oil viscosity. Furthermore, pressure gradient increases at phase inversion point, these increases depend on the change in oil viscosity and mixture velocity. The authors developed two models based on two different flow regimes or flow patterns known as stratified pressure gradient and homogeneous pressure gradient models.

The stratified pressure gradient model was compared with experimental data of Russell et al. (1959), the model shows good agreements with experimental data at lower mixture velocity, while deviation from the experimental data was observed at higher mixture velocity. The homogeneous pressure gradient model assumptions were considered such as no-slip condition and mixture rule which was applied with density, velocity, viscosity and friction factor were evaluated based on laminar and turbulent regimes. The authors recommended oil viscosity to be used directly when the oil is in the continuous phase and the flow is laminar, while water viscosity is applied when the water is the continuous phase and the flow regime is turbulent, in another experimental investigation with comparison with homogeneous model by Malhotra (1995). The author performed experiments on pressure gradient of oil-water dispersion and compared with mixture rules of homogeneous model. The model predicts pressure drops in good agreement with experimental data, the model failed to predict pressure drops at phase inversion point and in transition between stratified and dispersed flow pattern. The author recommended that better homogeneous model needs to be developed to tackle the hydrodynamic features of oil-water dispersion through detail study of influence of physical properties on oil-water dispersion.

Nadler and mewes (1997) studied pressure drop of emulsion and related the results to a single phase flow. The pressure drop reached the maximum for water volume fraction of 10% to 20% and also maximum for water dispersion in oil emulsion, but with highest water volume fraction, the pressure drop is twice the pressure drop of pure oil flowing alone in pipe. For an intermediate water

volume fraction, the pressure drop of two-phase flow of immiscible liquids decreased down to values in the order of pressure drop of pure water flowing alone in a pipe, these findings satisfied the results of pressure drop by Lovick and Angelli (2004).

The reduction in pressure drop is caused by continuous water layer flowing at the pipe wall. Further increase in water volume fraction leads to further increase in pressure drop to second maximum, the second maximum pressure drop result to oil in water emulsion, which is associated with phase inversion as shown in region(III) of figure1-13. The increases in water volume fraction lead to further decrease in pressure drop equal to the single phase of water phase pressure drop. The experimental results also indicate that for low water volume fraction, the pressure drop of two-phase flow of immiscible liquid in emulsion is higher than the pressure drop of the oil phase (single phase) in pipe.

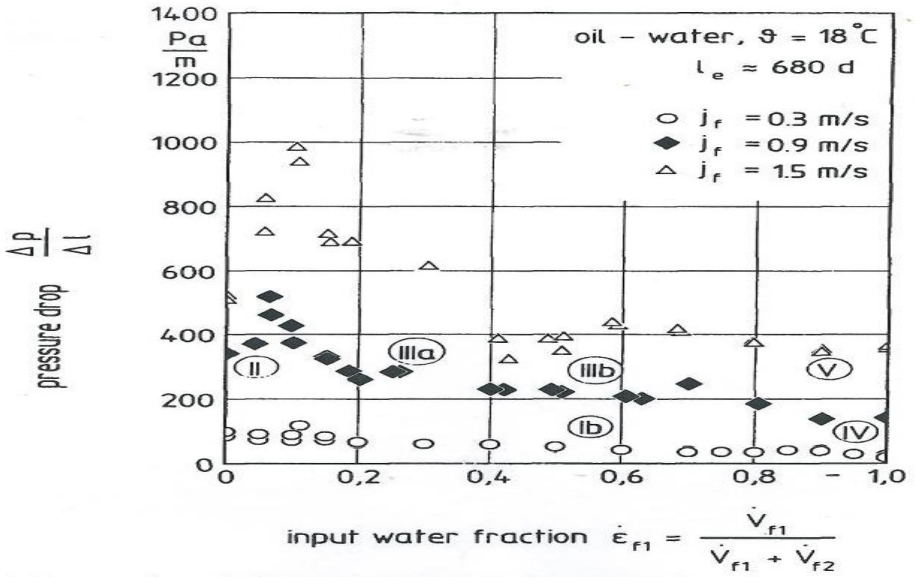

Figure 1.13: Pressure drop of oil-water flows by Nadler and Mewes (1997)

Lovick et al. (2000) investigated pressure gradient on stratified and dispersed flow patterns of oil-water flows in horizontal stainless steel pipe of 8m long and 38mm internal diameter with oil viscosity of 6.0cp and density 828kg/m^3, the interfacial tension of oil-water at 25^{0}C was given as 44.69mN/m. For stratified flow, mixture velocity was varying from 0.021m/s to 0.35m/s. Pressure drop, in-situ hold-up and velocity ratios were measured at two oil volume fractions of

61.5% and 76.9%. For dispersed flow experiment, mixture velocity varying from 2m/s, 2.5m/s, 3m/s and 3.5m/s while the input oil volume fraction ranging from 0% to 100%. The investigations started with oil single phase, in all the measurement the pressure gradient decreased as oil volume fraction increased up to 60% of oil volume fraction, with additional increase in oil volume fraction, there is small increase in pressure gradient before it reached minimum at 72% to 80% of oil volume fraction, the pressure gradient then increased as the oil volume fraction decreased and these correspond to the phase inversion region, then the pressure gradient increased as oil volume fraction increased up to 100%.

Rodriquez and Oliemans (2006) measured the pressure gradient and compared with theoretical models of two fluid models and homogeneous models. The theoretical models are applicable to flow regime with complete separation in case of stratified flow or complete mixing with regard to dispersed flow, the two fluid models is applicable to stratified and semi-stratified flow, while the homogeneous model can be compared with disperse flow regime. In case of two fluid models, the pressure gradient prediction accuracies is 35% in compared with experimental data, while in case of homogeneous model the prediction accuracies for pressure gradient is 5%. In fact the homogeneous model works best for oil-in-water dispersion and dispersion of water-in-oil flow patterns. It can be deduced from these results that the prediction accuracies varied with flow patterns while the homogeneous model has high prediction accuracies.

Comprehensive experimental pressure gradients of oil-water flow in dispersed flow were also conducted by Angeli and Hewit (1998) using acrylic and steel pipe. It was observed that the pressure gradient in steel pipe in all were higher than the acrylic pipe under the same mixture velocity and input volume fraction, it was attributed to the difference in pipe wall roughness and wettability characteristics of the two pipes. The results were compared with theoretical model of homogeneous model by means of mixture viscosity correlations of Duckler et al. (1964) and Brinkman (1952). The comparisons of experimental

data generally show poor agreement with homogeneous model when the oil is the continuous phase, the authors ascribed the problems to increase in interfacial mixing and interfacial friction factor in steel pipe and the higher drag reduction associated with oil continuous phase in two pipes. The investigation of pressure gradient with homogeneous model on oil-water dispersion was also performed by Elseth (2001). The author observed the increase in water volume fraction leads to further increase in pressure gradient up to the phase inversion point.

1.3 Two- phase flow modelling

Multiphase flows are flows consist of more than one phase or constituents, whereby fluids share a common flow field or each of the fluid may have its own flow field. The classification of two phase flows includes liquid-liquid mixture, liquid-gas mixture, and solid-liquid mixture. Modelling of these types of flows is very complicated, the main difficulties are due to the present of interface between the two phases and the discontinuities associated with the phases as well as the two phase flow interaction and mixing can increase the complexity of the flow. However, in this study, the interest is on numerical simulation of oil-water dispersion in horizontal pipeline with pipe deformation (corrosion cavity and scale sediments). In the present section, the theory and applications of multiphase models have been reviewed for two-phase oil-water flow. There are two approaches to predict the complex flow behaviour in multiphase flows: Euler-Lagrange and Euler-Euler approach in the ANSYS-FLUENT environment. These two approaches are also applicable to oil-water flow in horizontal pipelines.

Euler-Lagrange models, the approach is computational expensive and is applicable to dispersed flow of volume fraction less than 10% (ANSYS FLUENT 6.3 Documentation). The continuous phase is the continuum through the solution of the Reynolds Averaged Navier-Stokes (RANS) equations, which are time-averaged equations. The dispersed phase is solved by computing the trajectories of large number of particles, e.g. presence of bubbles or droplets

can be considered in the flow field. The phases interacted through the exchange of mass, momentum and energy.

Euler-Euler approach for stratified and dispersed flow regime is mostly used for higher volume fraction of dispersed phase typically of volume fraction greater than 10%. Two phases are handled separately, and the mean equations include additional interaction terms for drag, lift, virtual mass and turbulent dispersion. Euler-Euler method used closure assumption of Lagrange analysis of particles behaviour which used the concept of volume fraction of phases. Therefore, in this study the concentration is on Euler-Euler modelling approach which can be used to predict the flow field during the flow of oil-water in pipe with deformations (corrosion cavity and scale sediments). Within the context of Euler-Euler modelling approach, there are three Euler-Euler multiphase models present in ANSYS-FLUENT computational environment:

- Volume of fluid (VOF) Model;
- Mixture Model;
- Eulerian Model.

Volume of fluid (VOF) model was introduced by Hirt and Nichols (1981). It is a useful tool for modelling immiscible fluid flows with variable density and viscosity. Volume fractions are assumed to be continuous function of space and time, and their sum is equal to one. Application of the VOF method includes stratified/slug flows, free surface flows, motion of large bubbles in a liquid.

The Mixture model is often called the algebraic slip model, the continuity and momentum equations are both written for the mixture of continuous and dispersed phases. The volume fraction for each dispersed flow is calculated from continuity equation and there is an additional terms in momentum equation due to slip of dispersed phase relative to continuous phase. The equations in mixture model resemble the single phase flow but are represented in terms of mixture viscosity and mixture density. Mixture model has application in gravity settling, rotational flows and turbulent flows. Mixture model is more suitable for

liquid-liquid flows than liquid-gas flows. The advantage of mixture model is reduction in computational effort compared with Eulerian or volume of fluid multiphase model (Sirpa and Abo, 1996).

The Eulerian-Eulerian model is capable of modelling separate interacting phases by solving the mass, momentum and energy equations for each phase. A single pressure is shared by all the phases and the secondary phases are assumed to form droplets or bubbles. The properties of continuous phase determined the inter-phases momentum exchange coefficient between the continuous and dispersed phase. The Eulerian model can also resolve fluid-fluid; fluid-solid (e.g. granular) flows and can also be used in the analysis of separated and dispersed flow regimes (Bernard and Wallace, 2002).

In FLUENT, Eulerian model is relatively accurate model among all the multiphase models due to its nature of solving conservation equations for each phase, turbulence can be resolved easily than mixture or volume of fluid model. this study will concentrated on high Reynolds number fully dispersed flows with Reynolds number of 18,500 and 22,000, this effectively eliminated the interface tracking method (the volume of fluid method) available in FLUENT. Furthermore due to slip effects between oil and water phase, mixture model has limitation and restriction and will not be applicable, this leads us to selection of Eulerian multiphase model in FLUENT as the multiphase model to be used in this study.

1.4 Turbulence modelling

This section presents the basic background of turbulence and provides overview of turbulence modelling approaches with the aim of suggesting the appropriate turbulence model to be used during the course of this research study. A great deal of work had been done on turbulence modelling, full understanding of its mechanism is still not known. The fundamental equations of flow are still difficult to resolve, even though many turbulence features are well known. From observation of turbulent flows, it is clear that these flows are extremely complex and difficult to predict. This is shown in the increased

complexity of the turbulent flow equations. Most fluid flows encountered in daily lives are turbulent such as oil-water flows in pipelines.

Turbulent flows contain wide range of length and time scales; the large scales are transporter of conserve properties and are more energetic than the small scales. Turbulent flow can mix and transport fluids more effectively than the laminar flow as shown in the experiments first conducted by Osborne Reynolds (1883). In oil-water flow in horizontal pipeline, the turbulence is associated with continuous phase (oil), which is the dominant phase, while the dispersed phase is present in small quantities (water). Hence, the dispersed phase can only respond to continuous phase turbulence (Issa, 1989).

1.4.1 Turbulent flow characteristics

Turbulent flows have number of characteristics as reported by Ferziger (2002) and Launder and Sandham (2002):

- High Reynolds Number. The turbulent flows occurred at a high Reynolds number because the flow is dominated by inertia forces. For example the transition to turbulent flow in pipes occurs at $Re_D \approx 2300$ and it can vary between 1700 and 10^5 (Bernard and Wallace, 2002) due to wall roughness.
- Turbulent flows are unsteady, irregular and random. The flow consists of spectrum of different scales or eddies of different length and time scales, this properties makes modelling of turbulent very difficult, even though turbulent flow is unsteady, it is deterministic and is described by the Navier- Stokes Equations. Turbulent flows can be treated as continuum, because the small turbulent scales on the flow are much larger than the molecular scale.
- Turbulent flow has dissipative nature, because the kinetic energy of small eddies are transformed in to internal energy due to action of viscous shear stress as a result of mixing of fluid of different momentum.
- Diffusivity is also the nature of turbulence, because exchange of momentum is rapidly increased.

1.4.2 Turbulent modelling approaches

The approaches used in solving turbulence depending on the complexity of the problem. The three common approaches used in resolving turbulence flow are the direct numerical simulation (DNS), large eddy simulation (LES) and Reynolds Averaged Navier-Stokes (RANS). The summary of the approaches are:

Direct numerical simulation (DNS) is an approach which allows numerical simulation of turbulent flow to obtain through direct solution of Navier-Stokes equations without using any turbulence model for modelling the Reynolds' stresses (Pope, 2000). The DNS method is time-consuming, because all flow scales are considered in the simulations. The fluid flow governing equations derived by Navier and Stokes known as Navier-Stokes equations combine with continuity equation provide the full description of the motion. The governing equation is discretized, while the boundary condition is applied then iterate until the solution is converged. The DNS approach requires a very fine grids to model small eddies. DNS results are more accurate than many other turbulence modelling approaches (Bernard and Wallace, 2002).

Large eddy simulation (LES) method resolves large scales motion of the flow. The small scales are resolved by using sub-grid scale models. The method employs spatial filtering to separate the large scales from small scales. The Navier-Stokes equations for incompressible flows can be filtered in space. In terms of computational time, LES method is in between RANS and DNS methods. Large eddy simulation is more accurate and reliable than Raynolds Average Navier-Stokes (RANS) and is the best method where the Reynolds number is too high or the geometry is too complex for direct numerical simulation (DNS) application. Large eddy simulation is computationally expensive in comparison with Reynolds Averaged Navier-Stokes equation.

The model used in large eddy simulation is called sub-grid scale (SGS) models. The Smagorinsky model was the first SGS model and is still widely used and form the basis of all advanced SGS models and it employs the concept of eddy

viscosity. Smagorinsky model has some limitation especially when simulating more complex or high Reynolds number flows, sometimes there may be need to combine the Smagorinsky model with other models like scale-similarity model, this model correlate well with the actual SGS Reynolds stress, but Scale-similarity suffer from lack of dissipation (Ferziger, 2002) to correct this, it is good to combine the Smagorinsky model with scale-similarity to produce a mixed model. In FLUENT 3.6 software, the sub-grid models available are:

- Smagorinsky-Lilly model, the most dissipative model available in FLUENT. The Smagorinsky constant may need to be modified for particular flow.
- Wall- Adapting Local Eddy-Viscosity (WALE) model, more cost effective for near wall turbulence.
- Kinetic-energy transport model, this model accounts for transport of sub-grid-scale turbulence kinetic energy, improves resolution and increases computational cost.

RANS modelling is relying on the solution of the Reynolds' momentum equation modelling the additional terms called Reynolds' stress tensor. The RANS equations contain more unknown; therefore, the problem of closure has to be modelled. The Reynolds stress can be modelled using Boussinesq assumption which is based on the concept of eddy viscosity which includes algebraic model zero equation, one equation and two equation models (k-ε, k-ω). The Reynolds stress can be modelled directly by Reynolds stress transport equations (Reynolds stress model).

In this study, the Reynolds Averaged Navier-Stokes equations (RANS) is considered as turbulent flow model embedded in ANSYS FLUENT 6.3. The model is selected because it is less computational expensive than direct numerical simulation (DNS) or large eddy simulation (LES) and is the common turbulence modelling approach for simple and complex geometry and gives relatively accurate results.

1.4.3 Numerical investigation of oil-water flows

The effect of corrosion cavity and scale sediment (cubical obstacle) on oil-water flow in pipes and details of experimental or numerical measurements of volume fraction of water in the presence of corrosion cavity and scale sediments has not been reported in the literature as well as there are limited studies on the numerical investigation of oil-water flows in horizontal pipeline. Among the relevant studies from the literature are presented below:

Issa (1988) presented an Eulerian model for the prediction of dispersed two phase (liquid-liquid) flow at high volume fraction of the dispersed phase. In addition k-ε turbulence model for the mixture of two immiscible fluids has been proposed. This model was applied for two-phase flow in a pipeline where volume fractions can achieve 25%. The proposed models were tested for bubble flow while the results for the volume fraction, continuous phase velocity and turbulent kinetic energy of the old model and the proposed model have been compared with experimental data, the results of the prediction show improvement. The author concluded that, better model is required to address the effect of phase fraction on lift coefficient and another to account for droplet induced turbulence. Issa (1988) computed the stratified two-phase pipe flow, using standard k-ε turbulence model with wall function for each phase.

In related numerical investigations, GAO et al. (2003) simulated stratified oil-water two-phase turbulent flow in a horizontal pipe using VOF approach. The simulation is performed on 55.75mm diameter of 8m long horizontal pipe using oil viscosity of 1.6cP and density of 790kg/m^3, water volume fraction ranging from 10&-86%, oil and water reach maximum Reynolds number of 55000 and 110000 respectively. Correlations for liquid hold-up and pressure drop were drawn by analysis of the numerical results. Local phase fraction, slip ratio, pressure drop and the axial velocity profiles were validated with experimental data, the predicted results agree well with experimental data from published literature.

Fairuzov (2000) formulated Eulerian model for transient immiscible flow in pipeline based on two transient continuity equations and combined momentum equation to understand oil-water flow behaviour in transient manner which is important in determining the contact area of free water to the pipe wall and the time period it occurs as a result of increase and decrease in water volume fraction from the pipe entrance. The model has capability of simulating stratified and dispersed flow patterns using horizontal and inclined pipeline. From the numerical analysis, the author observed that during the stratified flow an increase in water flow rate from the entrance generates water holdup wave which spreads through the pipeline, while a decrease in water volume fraction leads to decrease in water superficial velocity which result to smoothening of water holdup wave front. The analysis of incline pipeline shows that the pipe slope has a significant influence on flow behaviour.

Yang and Azzopardi (2007) numerically simulated and performed experiment on kerosene and water flow in horizontal pipe with T-junction with equal diameter (67.4mm) to investigate detail phase separation phenomenon. The numerical simulation results do not indicate any significant difference in phase distribution. The experiment was performed for stratified wavy interface and dispersed flow. It was observed that oil and water separate at the T-junction and the degree of separation depends on the inlet phase flow rate.

Wang et al. (2008) performed numerical investigation of oil-water separation and distribution inside the T-junction, at the same time, experiments of oil and water flow inside a single T-junction was performed to validate the numerical results. The pipe geometry of straight pipe with T-junction incline pipe at an angle of 90^{o} to the main pipe. The model pipe diameter of 0.05m with each pipe segment 1.0m long. The pipe geometry model meshed with GAMBIT, the mesh density increased from the centre of the pipe to the pipe wall. The boundary conditions employed at the inlet was velocity inlet and the outlet boundary conditions are set based on experiment condition, while no-slip boundary conditions are prescribed at the pipe wall. The mesh pipe with T-junction was exported to FLUENT. The two fluid models together with mixture k-ε turbulence

model were selected to simulate oil-water flow in the T-junction. The result of the numerical simulation predicts phase splitting at main pipe and T-junction. The numerical results of phase distribution and split ratios are in good agreement with the experiment data.

Ping et al. (2009) numerically investigated “erosion-corrosion failure of reactor effluent air cooler (REAC) piping flow of oil”, gas and water in multiphase flow. The pipe was 19mm in diameter and length 500mm. The liner was 100mm length and 16mm diameter. The three dimensional mesh was generated and exported to FLUENT for numerical computation. Eulerian multiphase flow was selected, while the user defined function (UDF) was used to deal with additional stress because of the fluid-structure interaction, the simulation was based on time-averaged governing equations of turbulent flow. From the numerical results, it was revealed that the maximum water volume fraction and maximum wall shear appear at the bottom of the pipe. However, the results indicated that inlet velocity, slip velocity and pipe diameter ratio can influence the values and distribution of maximum water volume fraction and maximum wall shear in the pipe. The numerical results of pipe without the liner indicate uniform maximum water fraction all over the pipe, while the maximum wall shear stress emerged at the bottom of the pipe.

Rashmi et al. (2009) studied “dispersed oil-water turbulent flow in a horizontal pipe”. The Euler-Euler approach was selected to compute the flow of oil-water. Coupling between phases was carried out with various interface forces of drag, lift and turbulent dispersion. The interphase forces were calculated by the drag law of Kumar and Hartland (1985) with a constant lift coefficient. The turbulent dispersion coefficient of 0.75 and 7.5 were included in the study of Simonin and Viollet (1990). Turbulence in continuous phase was modelled using two equation standard k-ε multiphase model.

Abdulkadir et al. (2010) performed numerical simulation on the effect of mixture velocity and drop diameter on oil-water separator. The geometry model of cylindrical horizontal separator and meshing were generated using GAMBIT 2.2 software. The numerical simulation was carried out using FLUENT 6.2 with

Eulerian multiphase model in conjunction with k-ε turbulence model. The cylindrical separator geometry parameter was of 1.25m radius and 25m long. A weir of non-porous medium was position at 17.5m from inlet. Two outlets for separation of oil-water are located at either side of the weir at the bottom of the cylindrical separator at 16.5m and 19m from the inlet respectively. The third outlet located at 17.5m from the inlet while a weir of non-porous medium was position at 17.5m from inlet. Only half of the cylindrical separator was modelled, because of the complexity in the model geometry, tetrahedral mesh was selected and generated with an interval size of 0.12m to give the total number of cell of 181,370. The numerical simulation includes the determination of volume fraction and pressure gradient for each phase and also computation of three dimensional velocity for each phase. The water volume fraction of 50% was used for all the cases study.

From the numerical results, it was found that the phase separation strongly depend on mixture velocity and droplet diameter. These results suggest that for fixed droplet diameter, separation can be achieved at low mixture velocities, but increase in inlet velocity, the height of weir has to be increase to prevent overflowing of water in to oil section. Furthermore, results of large diameter ensured easy separation of oil and water due to the gravitational effect. The simulation results are in good agreement with published results in literature. Table1.11 reviewed the numerical simulations of oil-water flows in pipeline.

Authors	**Pipe Diameter (mm)**	**Reynolds Number**	**Multiphase model**	**Turbulence model**
Issa (1998)	50, 100	78500	Eulerian	K- ε
Gao et al. (2003)	55.75	110000	VOF	RNG k- ε
Fairuzov et al. (2000)	365.3	106850	VOF	-
Wang et al, (2008)	50	7416	Eulerian	k- ε
Walveker et al. (2009)	24	36045	Eulerian	k- ε
Ping et al. (2009)	19	63080	Eulerian	k- ε

Table 1-11: Summary of selected published numerical simulation of oil-water flow in pipe

The numerical results of oil-water flow in horizontal pipe presented in table 1.11. In most of the numerical investigations, Eulerian multiphase model in conjunction with k-ε turbulence model as selected as the multiphase turbulence modelling approach. The Reynolds number ranged from 7,416 to 78,500 and pipe diameter ranged from 19mm to 365.3mm. From the numerical investigation of oil-water flows, the Eulerian multiphase flow model with k- ε turbulence is suggested as appropriate models to resolve flow features in oil-water flow in horizontal pipe with pipe deformations (corrosion cavity and scale sediments). Therefore, Reynolds number of 18,500 and 22,000 will be selected under this study.

2 METHODOLOGY AND GOVERNING EQUATIONS

The main purpose of this chapter is to provide general review of relevant turbulence multiphase models in ANSYS FLUENT environment that are applicable to solve turbulent multiphase oil-water flow in horizontal pipe with pipe deformation (corrosion cavity and scale sediments). In other words to formulate the balance equations for turbulence multiphase models which will account for the conservation of mass and transfer of momentum, the equations will be used to solve for the velocity, pressure and volume fraction flow field for each of the fluid. The numerical methodology with solver parameters is described at the end of the chapter.

2.1 Eulerian multiphase model

Eulerian multiphase model resolves continuity, momentum equation for each phase and any number of dispersed phases, the model allows for the modelling of any number of interacting phases. The ANSYS FLUENT solution of Eulerian multiphase model is based on the single pressure which is shared by all phases and all the dispersed phases are assumed to form droplets. The K- ε models are available with several interphase drag coefficients that are suitable to all phases. The Eulerian multiphase model is the most accurate and complex multiphase model compared with volume of fluid or mixture multiphase model. The model can be used to the entire flow regimes ranging from stratified to dispersed flow. The application of Eulerian multiphase model includes droplet flow, fluidized beds and risers (ANSYS FLUENT 6.3 Documentation).

The fundamental governing equations for turbulence multiphase flow are derived from Eulerian average process which is the ensemble average and phase averaging. The Eulerian average is the most commonly used averaging method in multiphase flow and is used to derive the fundamental governing equation for turbulence multiphase flow; with a given variable Φ_q associated with phase q. The phase average $\widetilde{\Phi}_q$ is given as:

$$\tilde{\Phi}_q = \frac{\overline{\alpha_q \Phi_q}}{\overline{\alpha_q}} \quad \textbf{(2-1)}$$

The fundamental equations in oil-water flow using Eulerian frame work are given below (ANSYS FLUENT 6.3 Documentation).

Mass conservation equation for each phase is given as:

$$\frac{\partial}{\partial t}(\alpha_q \rho_q) + \nabla.(\alpha_q \rho_q U_q) = 0 \quad \textbf{(2-2)}$$

where U_q, α_q, ρ_q are respectively the velocity, volume fraction and density of phase q.

Conservation of momentum for each phase is calculated as:

$$\frac{\partial}{\partial t}(\alpha_q \rho_q U_q) + \nabla.(\alpha_q \rho_q U_q U_q) \quad \textbf{(2-3)}$$
$$= -\alpha_q \nabla p + \nabla.\tilde{\tau}_q + \nabla.\tilde{\tau}_q{}^t + \alpha_q \rho_q \vec{g} + \sum_{p=1}^{n} R_{pq}$$
$$+ \left(\tilde{F}_q + \tilde{F}_{lift,q} + \tilde{F}_{vm,q}\right)$$

The phase stress-strain tensor$(\tilde{\tau}_q)$ of phase q is calculated from:

$$\tilde{\tau}_q = \alpha_q \mu_q \left(\nabla \tilde{U}_q + \nabla \tilde{U}_q{}^T\right) + \alpha_q \left(\lambda_q - \frac{2}{3}\mu_q\right) \nabla.\tilde{U}_q \bar{\bar{I}} \quad \textbf{(2-4)}$$

where p is the pressure, g is the acceleration due to gravity, μ_q and λ_q are the shear and bulk viscosity of phase q and F_q is external body force, $F_{lift,q}$ is a lift force and $F_{vm,q}$ is a virtual mass force, while $\tilde{\tau}_q^t$ is the turbulent stress.

The interphase force between the phases is given by:

$$\tilde{R}_{dc} = k_{dc}\left[\left(\widetilde{U}_d - \widetilde{U}_c\right) - \left(\frac{\overline{\alpha_d u'_d}}{\overline{\alpha_d}} - \frac{\overline{\alpha_c u'_c}}{\overline{\alpha_c}}\right)\right] \quad \textbf{(2-5)}$$

Where u'_c and u'_d are the fluctuating velocity of continuous and dispersed phase respectively.

The fluid-fluid exchange coefficient relationship which can be written in general form:

$$K_{dc} = \frac{\alpha_c \alpha_d \rho_d f}{\tau_d} \quad \textbf{(2-6)}$$

The particulate relaxation time(τ_d) is given as:

$$t_d = \frac{\rho_d {d_d}^2}{18\mu_c} \quad \textbf{(2-7)}$$

Where $d_d$the diameter of the droplet, the friction factor f is the function of drag coefficient C_D and relative Reynolds number Re_r, which is calculated from:

$$f = \frac{C_D Re_r}{24} \quad \textbf{(2-8)}$$

The drag coefficient C_D of Schiller and Naumann (1935) model is used as a default value under this study and is commonly accepted for fluid-fluid pairs of phases and calculation with this model in oil and water flow is more stable compared with other models.

$$C_D = \begin{cases} 24\left(1 + 0.15{Re_r}^{0.687}\right) & if \quad Re_r \leq 100 \\ 0.44 & if \quad Re_r > 100 \end{cases} \quad \textbf{(2-9)}$$

The relative Reynolds number for the continuous and dispersed phase is computed from:

$$Re_r = \frac{\rho_c |\vec{U}_d - \vec{U}_c| d_c}{\mu_c} \quad \textbf{(2-10)}$$

The densities difference of the immiscible fluid is small, therefore virtual mass will be neglected. Because of the presence of drag force in the equation, lift force will be insignificant and therefore will be ignored.

2.2 Mixture multiphase model

The mixture model resolves the continuity and momentum equation for the mixture and the volume fraction equation for dispersed phase. The governing equations in oil-water flow using mixture model frame work are given below (ANSYS FLUENT 6.3 Documentation).

The continuity equation: the mixture multiphase model continuity equation for the mixture is given as:

$$\frac{\partial}{\partial t}(\rho_m) = \nabla \cdot (\rho_m U_m) = 0 \quad \textbf{(2-11)}$$

where ρ_m is the mixture density and $\overrightarrow{v_m}$ is the averaged velocity, which are defined as:

$$\rho_m = \sum_{k=1}^{n} \alpha_k \rho_k \quad \textbf{(2-12)}$$

$$\vec{v}_m = \frac{\sum_{k=1}^{n} \alpha_k \rho_k \vec{v}_k}{\rho_m} \quad \textbf{(2-13)}$$

where α_k is the volume fraction of phase k

Conservation of momentum equation, the momentum equation for mixture multiphase model is the summation of individual momentum equation for all the phases given as:

$$\frac{\partial}{\partial t}\left(\rho_m \vec{U}_m\right) + \nabla.\left(\rho_m \vec{U}_m \vec{U}_m\right) = -\nabla P + \nabla.\left[\mu_m\left(\nabla \vec{U}_m + \nabla \vec{U}_m^T\right)\right] + \rho_m \vec{g} + \vec{F}$$

$$+\nabla.\left(\sum_{i=0}^{n} \alpha_k \rho_k \vec{U}_{dr,k} \vec{U}_{dr,k}\right)$$

(2-14)

where μ_m is the viscosity of the mixture, $\vec{F}$ is body force, n is the number of phase and $\vec{v}_{dr,k}$ is the drift velocity for dispersed phase k.

Mixture viscosity:

$$\mu_m = \sum_{k=1}^{n} \alpha_k \mu_k \qquad \textbf{(2-15)}$$

Drift velocity:

$$\vec{U}_{dr,k} = \vec{U}_k - \vec{U}_m \qquad \textbf{(2-16)}$$

Relative velocity is the velocity of dispersed phase (p) relative to the velocity of continuous phase (q) given by:

$$\vec{U}_{pq} = \vec{U}_p - \vec{U}_q \qquad \textbf{(2-17)}$$

Mass fraction for any phase (k) is given as:

$$c_k = \frac{\alpha_k \rho_k}{\rho_m} \qquad \textbf{(2-18)}$$

The mixture model in ANSYS FLUENT used an algebraic slip formulation which is the algebraic relation for relative velocity is given as:

$$\vec{U}_{pq} = \frac{\tau_p}{f_{drag}} \frac{(\rho_p - \rho_m}{\rho_p} \vec{a} \qquad \textbf{(2-19)}$$

Particle relaxation time (τ_p) is defined as:

$$\tau_d = \frac{\rho_d d_d^2}{18\mu_c} \quad \textbf{(2-20)}$$

Where d_d is the droplet diameter of the dispersed phase p and $\vec{a}$ is the dispersed phase particles acceleration, while the drag function f_{drag} is chosen from Schiller and Naumanni (1935) given by:

$$\mathrm{f_{drag}} = \begin{cases} 1 + 0.15\mathrm{Re_r^{0.687}} & \text{if } \mathrm{Re_r} \leq 1000 \\ 0.0183\mathrm{Re_r} & \text{if } \mathrm{Re_r} > 1000 \end{cases} \quad \textbf{(2-21)}$$

The relative Reynolds number (Re_r) is also calculated from:

$$\mathrm{Re_r} = \frac{\rho_c |\vec{v}_d - \vec{v}_c| d_c}{\mu_c} \quad \textbf{(2-22)}$$

Where c and d is the continuous and dispersed phase respectively.

Volume fraction equation for dispersed phase (α_p) can be defined as:

$$\frac{\partial}{\partial t}(\alpha_p \rho_p) + \nabla.(\alpha_p \rho_p \vec{U}_m = -\nabla.(\alpha_p \rho_p \vec{U}_{dr,p}) + \sum_{q=1}^{n} (\dot{m}_{qp} - \dot{m}_{pq}) \quad \textbf{(2-23)}$$

2.3 Multiphase turbulence modelling (RANS)

Turbulence modelling in multiphase flow is difficult, the complexity arise because of the number of terms to model in momentum equation which becomes comparatively large compared with single phase flow. The two-equation turbulence models are used to close the RANS equations. The k-ε models are commonly used to describe the effect of velocities and scalar quantities fluctuation. The k-ε models in ANSYS FLUENT contain standard k-ε, RNG k-ε and Realizable k-ε, the standard k-ε model proposed by Launder and Spalding (1972) is widely used in industries. There are three available turbulence models in the context of k-ε models to model the effect of

turbulence in multiphase flows (FLUENT 6.3 Documentation). The choice of model is based on the range of input volume fraction and density ratio.

- Dispersed turbulence model
- Mixture turbulence model
- Turbulence model for each phase

The dispersed turbulence model is suitable for lower volume fraction of dispersed phase, and where there is an interface between the primary and the secondary phase. The turbulence motion in the primary phase which is in the continuous phase lead to random motion of the secondary phase; the primary phase has influence in the secondary phase. The oscillation motion of the particles in the secondary phase can be given in terms of mean characteristics of the primary phase.

The mixture turbulence models are appropriate when the densities of phases are close to unity. The mixture density and viscosity together with mixture velocity is sufficient to resolve turbulent flow field features. The mixture turbulence is an extension of single phase multiphase model and is appropriate for stratified or nearly stratified flows. Therefore, the standard k-ε mixture turbulence model was chosen to close the set of Reynolds Averaged Navier-Stoke equation (RANS) based on literature review.

The turbulence model for each phase is computationally expensive than the other two methods and is appropriate where the turbulence transfer among the primary and secondary phase plays vital role. The model solves sets of transport equations for each phase and two additional transport equations for each secondary phase.

The turbulent kinetic energy and dissipation rate equations under the standard k-ε mixture turbulence model are computed as follows:

$$\frac{\partial}{\partial t}(\rho_m k) + \nabla.\left(\rho_m \tilde{U}_m k\right) = \nabla.\left(\frac{\mu_{t,m}}{\sigma_k}\nabla k\right) + G_{k,m} - \rho_m \varepsilon \qquad \textbf{(2-24)}$$

$$\frac{\partial}{\partial t}(\rho_m \varepsilon) + \nabla.(\rho_m \widetilde{U}_m \varepsilon) = \nabla.\left(\frac{\mu_{t,m}}{\sigma_\varepsilon}\nabla\varepsilon\right) + \frac{\varepsilon}{k}(C_{1\varepsilon}G_{k,m} - C_{2\varepsilon}\rho_m\varepsilon) \quad \textbf{(2-25)}$$

Here k is the turbulent kinetic energy, ρ_m and $\widetilde{U}_m$, are the mixture density and mixture velocity respectively, calculated from:

$$\rho_m = \sum_{i=1}^{N} \alpha_i \rho_i \quad \textbf{(2-26)}$$

$$\widetilde{U}_m = \frac{\sum_{i=1}^{N} \alpha_i \rho_i \widetilde{U}_i}{\sum_{i=1}^{N} \alpha_i \rho_i} \quad \textbf{(2-27)}$$

The production of turbulent kinetic energy is defined as:

$$G_{k,m} = \mu_{t,m}\left(\nabla\widetilde{U}_m + (\nabla\widetilde{U}_m)^T\right)\nabla\widetilde{U}_m \quad \textbf{(2-28)}$$

While the turbulent viscosity $\mu_{t,m}$ is computed from:

$$\mu_{t,m} = \rho_m C_\mu \frac{k^2}{\varepsilon} \quad \textbf{(2-29)}$$

The phase averaging process results to appearance of turbulent dispersion in momentum equation and this has to be modelled because of the effect on volume fraction fluctuation in continuity equation. In ANSYS FLUENT turbulent dispersion is given a default value of 0.75. The constants for the k-ε mixture turbulence model used in this study are presented below:

Model parameter	**Default values**
C_μ	0.09
σ_k	1.0
σ_ε	1.3
$C_{1\varepsilon}$	1.44
$C_{2\varepsilon}$	1.92

Table 2-1: Standard k-ε mixture model constants (Launder and Spalding, 1972)

2.4 Numerical methodology

Computational fluid dynamics commercial software FLUENT 6.3 will be used for the numerical simulation of turbulent dispersed oil-water flow in horizontal pipe with pipe deformation (corrosion cavity and scale sediments) to solve the field equations. The control volume techniques included in the solver is to discretize the flow governing equations to algebraic form. The discretized equations are integrated on the individual control volumes in the grids to form algebraic equations resulting in system of linear equations that give values for dependent variables of pressure, velocity and water volume fraction. Under the Eulerian frame work governing equations of conservation of mass and momentum is resolved for each phase. The summary of models used in numerical simulation is shown in table 2.2.

Models	**Settings**
Time	Steady
Space	Three dimensional
Multiphase model	Eulerian
Viscous	K-ε turbulence
Wall treatment	Standard wall function

Table 2-2: Models used in numerical computation

Oil and water properties are described in material properties form, whereas semi-implicit method for the pressure link equation (SIMPLE) scheme is selected for solving the pressure- velocity decoupling. The second order upwind scheme is used to discretise the convective terms in momentum equation, turbulent kinetic energy and turbulent dissipation rate, while QUICK is selected to solve for volume fraction. Hydraulic diameter of 0.038m and turbulent intensity of 2% are applied at the pipe inlet due to the fact that the turbulent intensity for medium turbulence flow of pipe flow and ventilation system has value ranging from 1-4% (ANSYS FLUENT 6.3 Documentation).

Boundary conditions are prescribed for the inlet boundary condition; mixture velocity is used for the mixture of oil-water at inlet together with volume fraction of water as the secondary phase. For outlet boundary condition, outflow is specified as the outlet, no-slip boundary condition is given at the pipe wall and the pipe deformation walls (corrosion cavity and scale sediments) which give the correct condition for velocity at solid wall.

The computational simulation is monitored throughout to ensure the flow is fully developed and solution converged through observing the water volume fraction, velocity magnitude and pressure drop at the centreline of the pipe. Convergence criteria of 10^{-6} were specified and solution converged when all the residuals reach the convergence criterion after 30,000 iterations. The summary of solver parameters settings are given in table 2.3.

Variable	Scheme
Solver	Pressure based solver
Pressure-velocity coupling	Phase coupling SIMPLE
Momentum	Second order upwind scheme
Turbulent kinetic energy	Second order upwind scheme
Turbulent dissipation rate	Second order upwind scheme
Volume fraction	QUICK differencing scheme
Relative convergence criteria	1×10^{-6}

Table 2-3: Summary of solver parameters

3 NUMERICAL VALIDATION STUDY

The purpose of this chapter is to validate the numerical simulations of oil-water flows in horizontal pipeline against experimental results from published papers to support the choice of multiphase turbulence models and dispersed droplet diameter that will be used in this study. At present no published experimental paper on oil-water pipe flow with pipe deformation (cavity and scale sediments), therefore the experimental papers on oil-water flow in horizontal pipeline is considered for validation studies. The validation will include numerical computation of pressure gradients in single phase flow (oil) and two-phase flow (oil and water) against experimental pressure gradient of Angeli and Hewitt (1998). The computed pressure gradient of two-phase of oil-water in dispersed flow regimes will be compared with experimental pressure gradient data of oil and water of Lovick and Angeli (2004). Furthermore, the numerical pressure gradient in dispersed flow regimes will be compared with mixture viscosity homogeneous models and empirical correlations of Lockhart-Martinelli (1949). Finally, the work of Solaimani et al. (1999) on spatial distribution of oil-water in horizontal pipe flow is selected to validate and choose the appropriate dispersed droplet diameter that will be used in numerical modelling of effect of pipe deformation (corrosion cavity and scale sediment) in oil-water flows in horizontal pipe (Osarobo, 2010). The three experimental research papers were carefully selected to compare the results against the computational results.

3.1 Validation of stratified flow

Angeli and Hewitt (1998) pressure gradients were experimentally measured during the flow of oil-water in horizontal stainless steel and acrylic pipe. The experimental results indicated that at high mixture velocities, there is a peak in pressure gradient at phase inversion point leading to pressure drop. The mixed flow patterns appeared in the steel pipe at lower mixture velocities than the acrylic pipe. The experimental data are given as:

- Diameter of pipes: 24.3mm steel, 24mm acrylic
- Range of mixture velocities: 0.3m/s to 3.9m/s
- Water volume fraction: 0% to 100%
- Oil temperature: 20^0C

The oil used in the experiment was Exxol D80 kerosene together with tap water. The media properties are summarized in table 3.1.

Density	801kg/m^3
Viscosity	1.6mPa s
Interfacial tension oil-water	0.0017N/m

Table 3-1: Exxol D80 media properties (Angelli and Hewitt, 1998)

The steel pipe case is selected, because most of oil-water transportation around the world uses steel pipe. The schematic of the experimental section is given in figure 3.1.

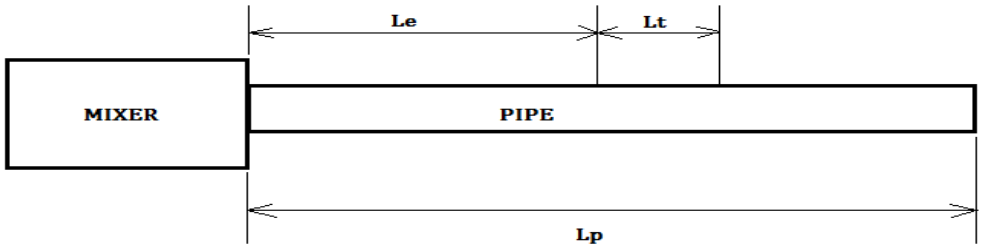

Figure 3.1: Schematic of experimental apparatus

where,

L_p is the overall length of the pipe (9m)

L_t is the length of the test section over which the pressure drop is measured (1.9m)

L_e is the entrance length which is supposed to allow the flow to develop.

Firstly, consider low mixture velocity case, stratified flow with v_m =0.6m/s (Angeli and Hewitt, 1998). The experimental results are given in figure 3.2, where by relative pressure gradient normalised by the pressure gradient without water is reported for different water volume fractions.

The notation adopted:

Q= Volume flow rate

A = $\pi \frac{D^2}{4}$ - pipe cross section

V= Volume

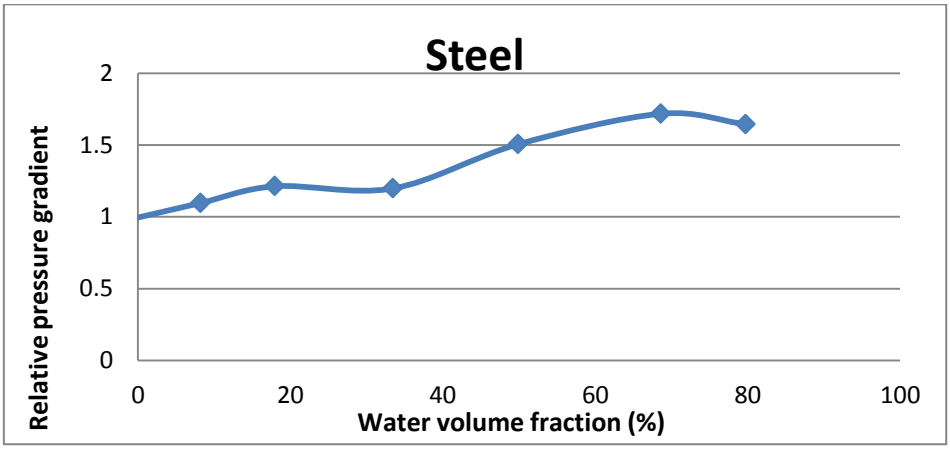

Figure 3.2: Measured pressure gradient for v_m=0.6m/s (Angeli and Hewitt, 1998)

Then the subscripts 'o' 'w' and 'm' for oil, water and mixture respectively, the superficial velocities of oil and water are given by:

$$v_o = \frac{Q_o}{A} \quad \textbf{(3-1)}$$

$$v_w = \frac{Q_w}{A} \quad \textbf{(3-2)}$$

while the volume fractions by:

$$\alpha_w = \frac{V_w}{V} \quad \textbf{(3-3)}$$

$$\alpha_o = \frac{V_o}{V} \tag{3-4}$$

Mixture velocity is based on the total flux:

$$v_m = \frac{Q_m}{A} = \frac{Q_w + Q_o}{A} = v_o + v_w \tag{3-5}$$

Volume fraction of water can be recovered from:

$$\alpha_w = \frac{Q_w}{Q_w + Q_o} = \frac{v_w}{v_o + v_w} = \frac{v_w}{v_m} \tag{3-6}$$

Hence in Angeli and Hewitt (1998), the volume fraction and mixture velocity are:

$$v_w = \alpha_w v_m \tag{3-7}$$

$$v_o = v_m - v_w = (1 - \alpha_w)v_m = \alpha_o v_m \tag{3-8}$$

The corresponding Reynolds numbers defining the flow are given by:

$$Re_o = \frac{\rho_o v_o D}{\mu_o} \tag{3-9}$$

$$Re_w = \frac{\rho_w v_w D}{\mu_w} \tag{3-10}$$

$$Re_m = \frac{\rho_m v_m D}{\mu_m} \tag{3-11}$$

The mixture properties are calculated by simple volume fraction weighting. The correlation for the entrance length determining the flow development in a pipe is given as:

$$L_e = 4.4 \times D \times Re^{1/6} \tag{3-12}$$

The friction factor for a circular pipe can be estimated using Colebrook formula (Colebrook, 1978).

$$\frac{1}{\sqrt{f}} = -2\log\left(\frac{\epsilon_r}{D \times 3.7} - \frac{4.518}{Re} log\left(\frac{6.9}{Re} + \left(\frac{\epsilon_r}{3.7 \times D}\right)^{1.11}\right)\right) \quad \textbf{(3-13)}$$

Where ϵ_r is the roughness height which in Angeli and Hewitt (1998) was equal to 7×10^{-5}m for the steel pipe case. Taking the low water volume fraction corresponding to the first three points of the diagram, the test case parameters are summarized in table 3.2.

Properties	Reference
$\alpha_o(\%)$	1
$v_o(m/s)$	0.6
$\rho_m(kg/m^3)$	801
$\mu_m(Pa.s)$	0.0016
Re_o	7299
Re_m	7299
$L_e(m)$	0.47
f_m	0.008833

Table 3-2: Experimental test cases

Once the friction factor is known, the grid requirements can be estimated from the wall law. The friction velocity is linked to the friction factor by (Pope, 2000)

$$u_\tau = v\sqrt{\frac{f}{2}} \quad \textbf{(3-14)}$$

The viscous length is given by:

$$y_\tau = \frac{\upsilon}{u_\tau} \quad \textbf{(3-15)}$$

Then the distance from the wall in the viscous length units is:

$$y^+ = \frac{y}{y_\tau} = \frac{yu_\tau}{\upsilon} = \frac{yDu_\tau v}{Dvv} = y^* Re\frac{u_\tau}{v} = y^* Re\sqrt{\frac{f}{2}} \quad \textbf{(3-16)}$$

Where y^* is the distance non-dimensional by the diameter. The pipe wall y^+ is non-dimensional number and which can be used to choose the appropriate grid formation that can lead to selection of turbulence model; turbulence models are influenced by solid wall due to the no-slip condition. In order to resolve the flow field near the wall in the boundary layer, it is important to distinguish between the three subzones:

- Viscous sub layer ($y^+ < 5$, velocity profile is laminar)
- Buffer layer ($5 < y^+ < 30$, viscous and turbulent shear dominate)
- Log-wall region ($30 < y^+$ 300, fully turbulent region)

For a turbulence model using a wall-function, the first cell must reside in the log-law layer which corresponds to $y^+ \simeq 30$ (Pope, 2000). Then the actual distance of the first cell is:

$$y = \frac{y^+ D}{Re\sqrt{\frac{f}{2}}} \qquad \textbf{(3-17)}$$

Note that the overall flow is characterised by the mixture Reynolds number as opposed to the oil and water Reynolds numbers while Re_m is used for the definition of the friction factor and the distance of the first cell from the wall. The corresponding y of the first cell for our cases is summarised in table 3.3.

	Reference (m)
$y^* = \frac{y}{D}$	0.061851
y	0.001503

Table 3-3: First cell distance (Angeli and Hewitt, 1998)

3.1.1 Pipe model and grid generation

The pipe model geometry and mesh were generated with GAMBIT 2.4. For dimensionless representation, diameter of the pipe is D and the total length of the pipe is 370D, while the length of the test section is 78D starting from 206D from the pipe inlet to achieve fully developed flow. The dimensional

representations are based on the experimental study of Angeli and Hewitt (1998). The three dimensional geometry is shown in figure 3.3.

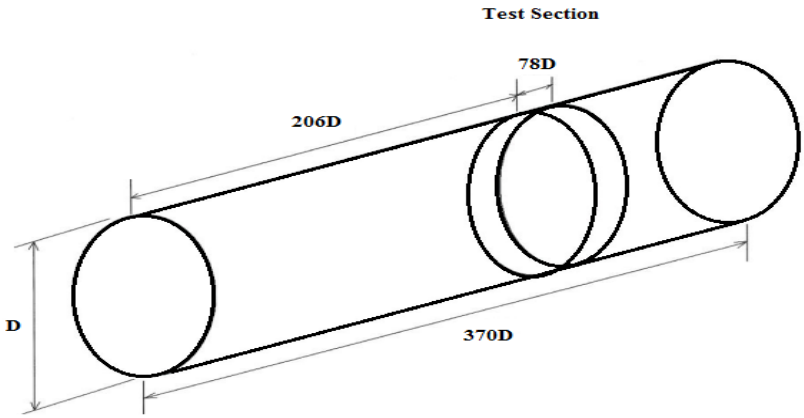

Figure 3.3: Schematic of pipe model geometry

The GAMBIT journal file generating the parametric mesh with the specified total number of elements for this case is given in the Appendix A. The inlet section of the initial mesh with 10^6 cells generated for the pure oil case is shown in figure 3.4.

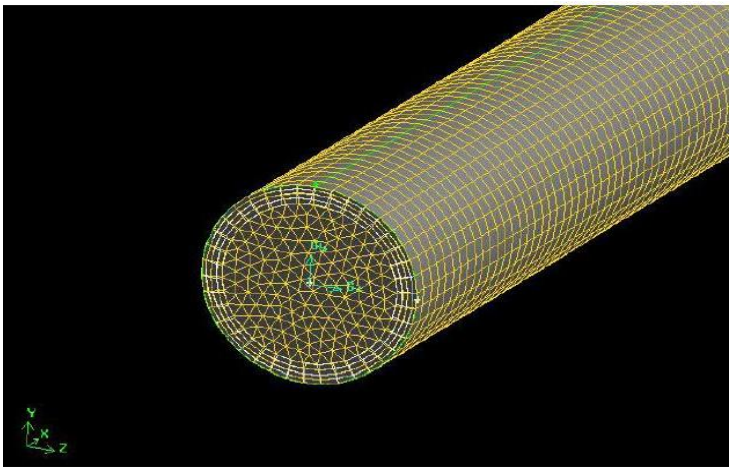

Figure 3.4: Initial mesh for pure oil flow

Preliminary computations were performed with RANS k-ε model with second order of accuracy. The inlet condition is set to constant velocity and the wall roughness is specified corresponding to the experimental case. Distribution of

pressure and velocity magnitude on the centreline of the pipe for pure oil flow is given in figure 3.5.

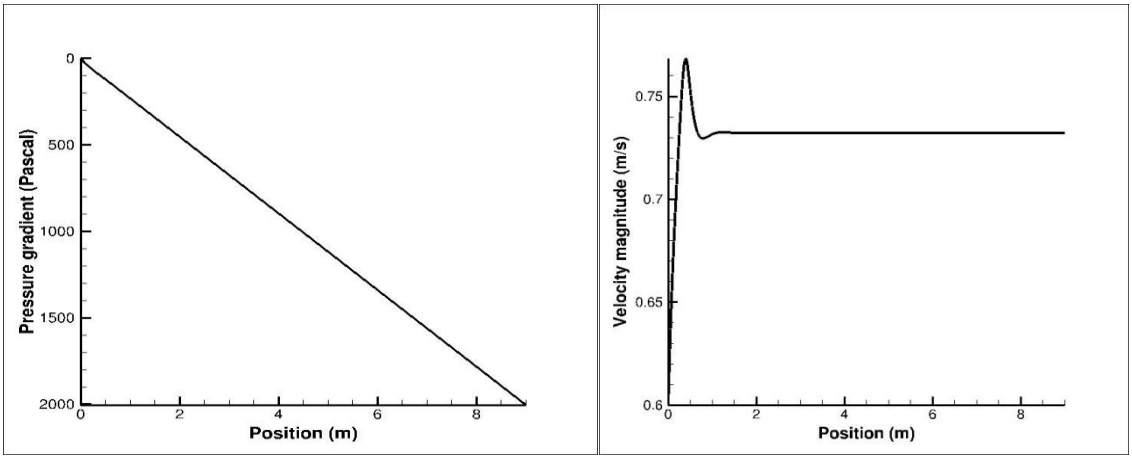

Figure3.5: Pressure and velocity magnitude at the centre of pipe

The entrance length of 1m apparent from the velocity magnitude distribution indicates that the analytic formula under predicts the entrance length by a factor of 2. However, still the test section located between x=5m and x= 6.9m is removed from the entrance zone. The computed pressure gradient in the test section is equal to $\frac{dP}{dx} = 221.6Pa$ (Figure3.6).

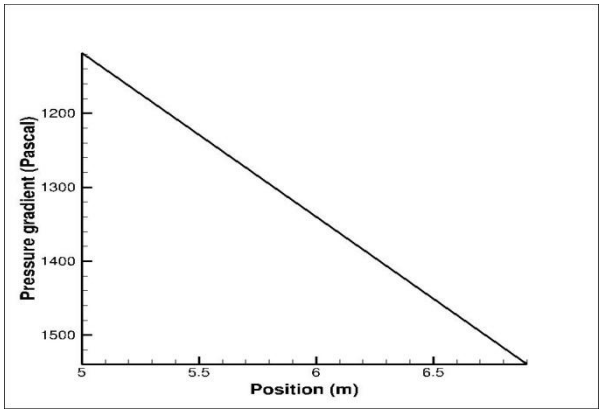

Figure 3.6: Pressure drop of pure oil flow in the test section

The validation study performed for the first pressure gradient for v_m=0.6m/s shows the computed pressure gradient in the test section to be 221.6Pa/m while the experimental measured pressure gradient gives 250Pa/m (Angeli and Hewitt, 1998), which over the test section length yields pressure drop of 475Pa.

the deviation of 11.3% observed between the experimental and computational data can be related to coarse grids and this inspire further grid study.

Six simulations were conducted for the test section varying the number of grid cells in the domain. The results are summarised in table 3.4.

Cells on the inlet face	Total cells	Sizes along the pipe	DP/DX	% Error
152	0.5×10^{6}	2.7×10^{-3}	220.23	10.3
152	1×10^{6}	1.37×10^{-3}	221.20	11.3
152	1.8×10^{6}	7.6×10^{-4}	221.50	11.4
294	0.5×10^{6}	5.2×10^{-3}	220.30	11.9
294	1×10^{6}	2.64×10^{-3}	222.40	11.0
294	1.8×10^{6}	1.47×10^{-3}	222.60	11.04

Table 3-4: Grid independence results

The figure 3.7 illustrates the graph of grid independence of pipe with total inlet face of 152 and 294 while the distance along the pipe varies depending on the total number of cell. The numerical pressure gradients are presented in table 3-4 above. The results indicate the deviation from the experimental data does not decrease with the increase of the number of cells. Therefore the error might deem to depend on solver variables and turbulent models used.

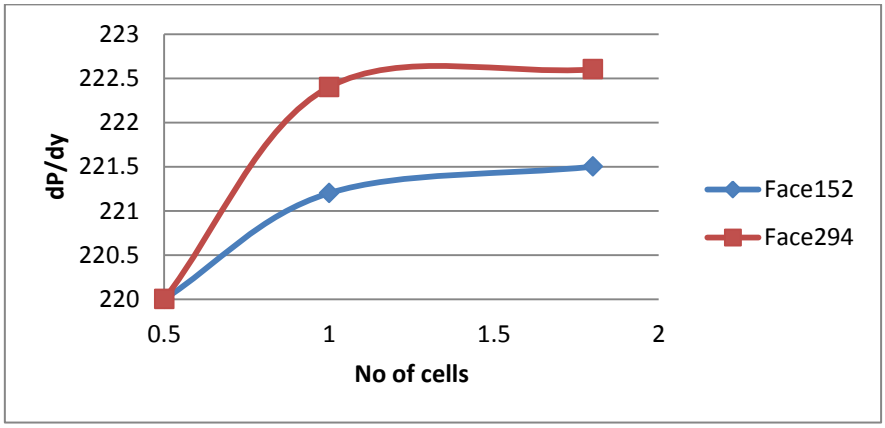

Figure 3.7: Graph of grid independence study

preliminary multiphase study (oil-water flow) of stratified flow was conducted with mixture velocity of v=0.6m/s as shown in table 3.5.

Properties	α_w	α_o	v_w	v_o	ρ_m	μ_m	Re_o	Re_w	Re_m	f_m
Reference	17.72	82.28	0.11	0.49	834	0.0015	6010	2360	6536	0.0091

Table 3-5: Experimental and test cases

The results for water volume fraction indicate that separation occurs under the action of gravity and the volume fraction changes by 12% over the length of pipe (9m).

3.2 Validation of dispersed oil-water flow in horizontal pipe

Two experimental pressure gradient data of oil-water flows in horizontal pipeline conducted by Lovick and Angelli (2004) were considered for numerical validation of dispersed oil-water flows. The pressure gradients were measured at mixture velocity of 2.5m/s and 3.0m/s, the dispersed flows regime has been observed to fall within these mixture velocities which are the range of Reynolds number of 18500-22000 under this study. Mixture multiphase model and Eulerian multiphase model were selected to validate the numerical pressure gradient against experimental pressure gradient of Lovick and Angelli, (2004). The numerical and experimental data will be compared with pressure gradient mixture viscosity of homogeneous models of Duckler etal. (1964) and Brinkman (1952). Furthermore, the numerical and experiment results will be compared with pressure gradient empirical correlations of Lockhart-Martinelli (1949).

Lovick and Angelli (2004) performed experimental study of oil-water flow to measure pressure gradient and distribution in horizontal pipe of diameter 0.038m using water and petroleum oil of density 828kg/m^3 and viscosity of 6 mPa s, with range of mixture velocity from 0.8m/s - 3.0m/s. The test-pipe consists of two eight metres (8m) sections of 38mm diameter stainless tube connected by U-turn, at the end of the first test section, 540mm transparent acrylic pipe was connected through which the flow can be observed. The test sections start from 5.5m to 7.0m of pipe length. The flow patterns observed are

stratified wavy, dispersion of oil in water, dispersion of water in oil and dual continuous flows. The measured pressure gradient corresponding to 2.5m/s and 3.0m/s mixture velocities with input oil volume fraction ranging from 0% to 100% are shown in table 3.6.

Oil %	**Pressure gradients (N/m^2)**	
	Vel. (3.0m/s)	**Vel. (2.5m/s)**
0	1600	2240
10	1642	2559
20	1688	2403
30	1605	2378
40	1422	2257
50	1361	2064
60	1278	1943
70	1261	1992
80	974	1670
90	1584	2437
100	1630	2538

Table 3-6: Experimental data of pressure gradients by Lovick and Angeli (2004)

3.2.1 Validation of dispersed flows at mixture velocity of 2.5m/s

Numerical simulation of dispersed flow (oil-water) of mixture velocity of 2.5m/s in horizontal pipe is conducted with mixture multiphase model and Eulerian model in conjunction with standard k-ε turbulence model to compute pressure gradients. The numerical results are compared with experimental data of Lovick and Angeli (2004). The computational domain presented in three dimensions with dimensionless parameter of diameter D and total pipe length of 210D, the length of test section is 40D. The model pipe geometry is shown figure 3.8. Grid independence study is performed to choose the appropriate total number of grid cells.

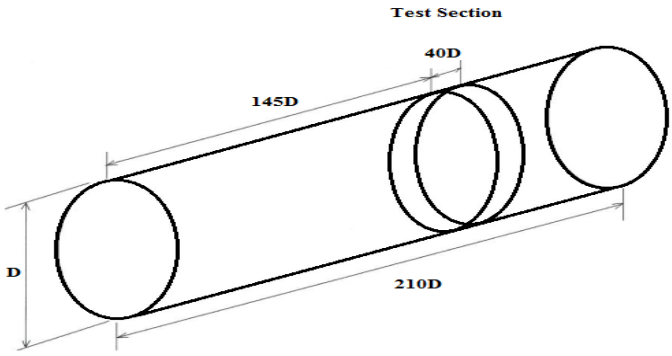

Figure 3.8: Schematic of pipe model geometry

The grids are produced with GAMBIT 2.4, hexahedral and tetrahedral cells were created for grid independence studies. The value of y^+ is calculated from equation (3.16). Therefore, the first cell distance (y) will correspond to $y^+ \simeq 30$, which is estimated from equation (3.17), while cell growth factor of 1.2 is used to connect the mesh toward the wall.

The grid independence studies were performed with mixture velocity of 2.5m/s and 3.0m/s where meshes are examined until the numerical solution is independent of additional mesh enhancement. The results of grid independence studies are shown in table 3.7.

Cells on the inlet face	**Total cells**	**Distance along pipe (m)**	**Mixture Velocity (2.5m/s)**		**Mixture Velocity (3.0m/s)**	
			DP/DX	Error (%)	DP/DX	Error (%)
915	0.5×10^{6}	3.66×10^{-3}	1214	24.3	1680	13.8
915	0.75×10^{6}	2.44×10^{-3}	1270	20.1	1760	11.7
915	1.0×10^{6}	1.83×10^{-3}	1362	15.1	1813	9.9
915	1.5×10^{6}	1.22×10^{-3}	1371	14.6	1815	9.84

Table 3-7: Grids independence study (Mixture velocity of 2.5m/s and 3.0m/s)

The optimum grids of $1\times\ 10^{6}$ cells are selected for mixture velocity of 2.5m/s and 3.0m/s and applied based on computational cost consideration. The model geometry is produced and mesh generated with inlet boundary condition as velocity inlet, the outlet boundary condition as outflow while the pipe wall boundary condition as wall. The mesh is exported to FLUENT 6.3. Mixture

multiphase model together with standard k-ε turbulent model is selected. Fluid properties are described for all the constituents. SIMPLE is selected for solving the pressure-velocity decoupling. Under relaxation factors of pressure is increased to 0.5 while the momentum reduced to 0.4. Turbulent intensity of 2% is considered with convergence criterion of 10^{-6}.

The initial solution of the simulation is obtained by using the first-order accuracy, and then final solution obtained with second order accuracy. The analysis is performed at mixture velocities of 2.5m/s and 3.0m/s with the percentages of oil volume fraction ranging from 0% to 100%. The results of numerical pressure gradients using mixture model and Eulerian model at mixture velocity of 2.5m/s are shown in table 3.8.

Pressure gradients (N/m^2)					
	Experiment	**Mixture model**		**Eulerian model**	
Oil%	Dp/dx	CFD	% Dev.	CFD	% Dev.
0	1600	1374	16.4	1403	14.0
10	1642	1298	26.5	1451	13.1
20	1688	1306	29.2	1541	9.5
30	1605	1321	21.5	1326	21.0
40	1422	1260	12.8	1256	13.2
50	1361	1181	15.2	1262	7.8
60	1278	1194	7.0	1194	7.0
70	1261	1346	-6.7	1421	-12.6
80	974	1471	-51	1490	-52.9
90	1584	1848	-16.6	1697	-7.1
100	1630	1870	-14.7	1748	-7.2

Table 3-8: Results of pressure gradient results at mixture velocity of 2.5m/s

Results of numerical pressure gradients with mixture multiphase model and experimental pressure gradient data were plotted against the percentage of oil volume fraction as shown in figure 3.9. From the results, it is observed that at lower oil volume fraction from 0% to 60%, the numerical results under-predict the experimental data with average deviation of 10.8%, while for oil volume fraction ranging from 70% to 100%, the numerical pressure gradients over-predict the experimental data with average deviation of 19.3%.

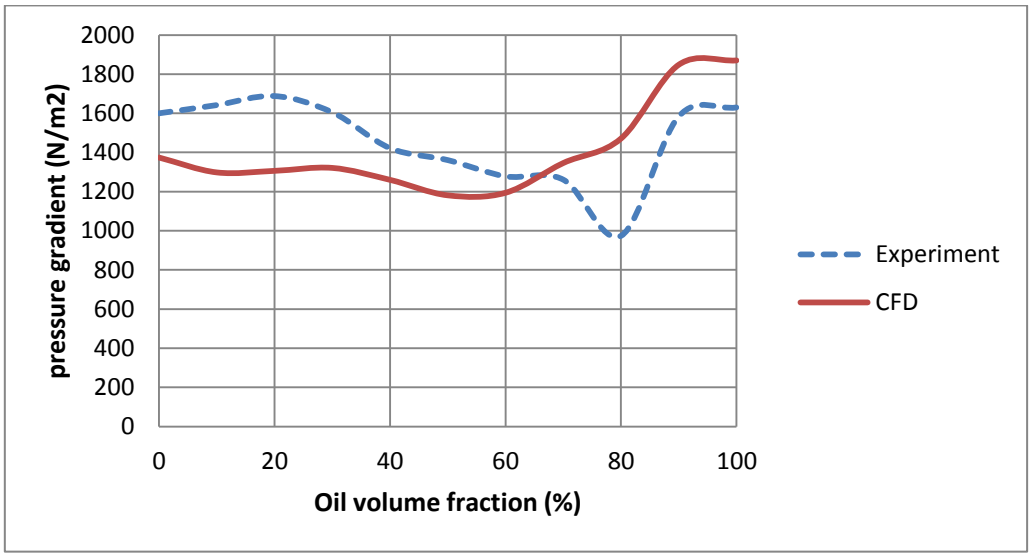

Figure 3.9: Comparison of numerical pressure gradient with experimental data at mixture velocity of 2.5m/s (Mixture multiphase model)

The pressure gradient from numerical simulations shows poor agreement with regards to pressure gradient of the experimental measurement. The discrepancy could be due to selection of mixture multiphase model.

The numerical results with Eulerian multiphase model are computed and compared with experimental data as shown in figure 3.10. The results of pressure gradient from Eulerian model shows good agreement with experimental pressure gradient, the results indicates that at lower oil volume fraction from 0% to 60%, the numerical results under-predicted the experimental while there is appearance of phase inversion at 66% oil volume fraction, the numerical results over-predicted experimental data at range of oil volume fraction from 70% to 100%.

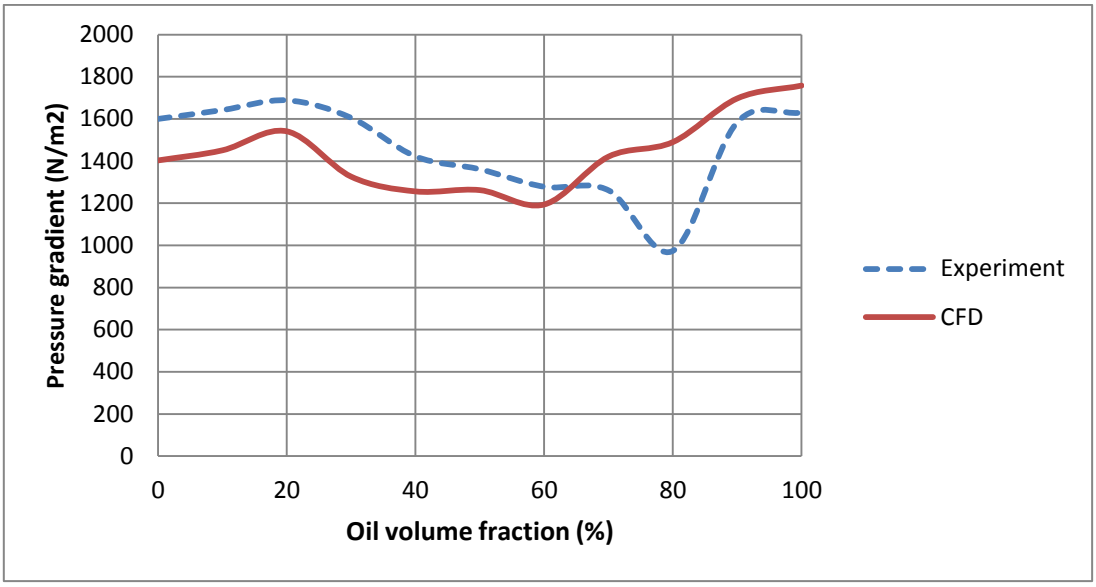

Figure 3.10: Comparison of numerical pressure gradient with experimental data at mixture velocity of 2.5m/s (Eulerian multiphase model)

3.2.2 Validation of dispersed flows at mixture velocity of 3.0m/s

Numerical simulation of pressure gradient for dispersed oil-water flows are conducted to compute pressure gradient in horizontal pipe with mixture and Eulerian multiphase model at mixture velocity of 3.0m/s. The same pipe geometry and media properties are used as reported by Lovick and Angeli (2004). Analysis of grids independence study was done as shown in table 3.3. An optimum grid cell of 10^6 cells is selected. The computed pressure gradients with mixture multiphase model and Eulerian model at mixture velocity of 3.0m/s are compared with experimental data as presented in table 3.9.

Pressure gradients (N/m^2)					
	Experiment	**Mixture model**		**Eulerian model**	
Oil%	dp/dx	CFD	% Dev.	CFD	% dev.
0	2240	1964	14.0	2002	11.8
10	2559	2143	19.4	2245	13.9
20	2403	2032	18.2	2067	16.2
30	2378	1710	39.8	1826	23.2
40	2257	1625	38.8	1780	26.6
50	2064	1649	23.5	1795	14.9
60	1943	1800	7.9	1746	11.2
70	1992	1827	9.0	1813	9.8
80	1670	2167	-29.7	2005	-20.1
90	2437	2658	-9.0	2743	-12.5
100	2538	2934	-15.6	2832	-11.6

Table 3-9: Results of pressure gradients at mixture velocity of 3.0m/s

Figure 3.11 shows the comparison of the results of numerical pressure gradient (mixture model) against experimental pressure gradient data at mixture velocity of 3.0m/s. The numerical results slightly under-predict experimental data from 0% to 70% oil volume fraction while above 70% it slightly over-predict the experimental data, from the water single phase, the addition of oil, results to increases in pressure gradient up to 20% oil volume fraction while after, the pressure gradient decreases. The computed and experimental results show the same pressure gradient curve behaviours as reported by Lovick et al. (2000). However, the phase inversion appears at 66% oil volume fraction as reported

by (Angelli and Hewit, 1998). The mixture multiphase model show fairly agreements with regard to measured data at mixture velocity of 3.0m/s (within the range of Reynolds number of 18,500- 22,000).

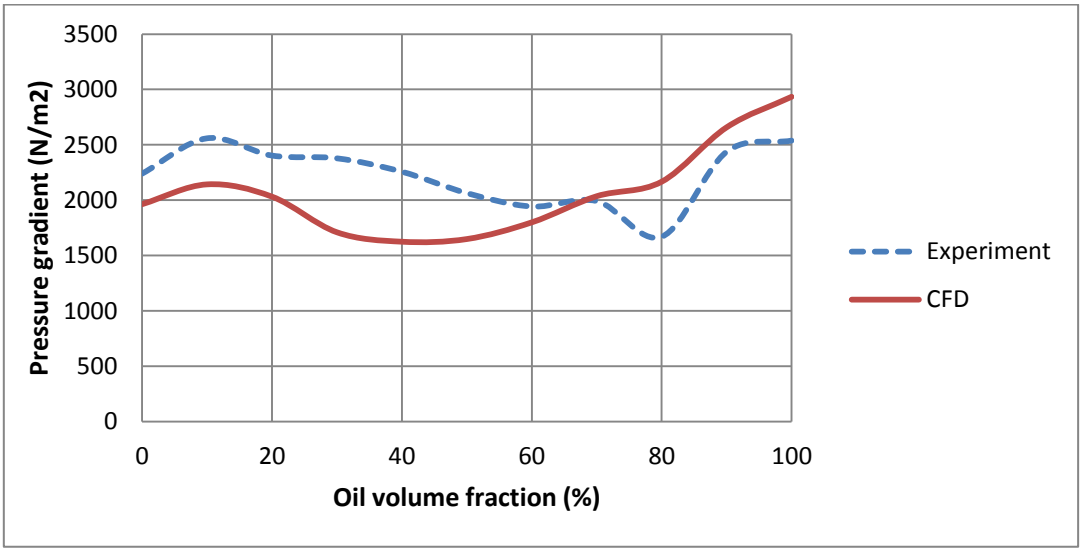

Figure 3.11: Comparison of numerical pressure gradients with experimental data at mixture velocity of 3.0m/s (Mixture multiphase model)

In figure 3.12, the Eulerian multiphase model pressure gradients are computed and compared with experimental results at mixture velocity of 3.0m/s. The numerical results fairly predicted the measured data at the range of oil volume fraction from 0% to 76% while it quite well predicted the measured data at oil volume fraction range of 76% to 100%, the phase inversion appears on 70% oil volume fraction, after the phase inversion the pressure gradient increases sharply. The same experiment and numerical result profile trends also reported by Angeli and Lovick (2004). Therefore, the Eulerian multiphase model shows more acceptable agreements with experimental data at mixture velocity of 3.0m/s and which falls under the range of Reynolds number of 18,500 to 22,000. Hence, the Eulerian multiphase model will be selected in the analysis of oil-water pipe flow with deformation (corrosion cavity and scale sediments).

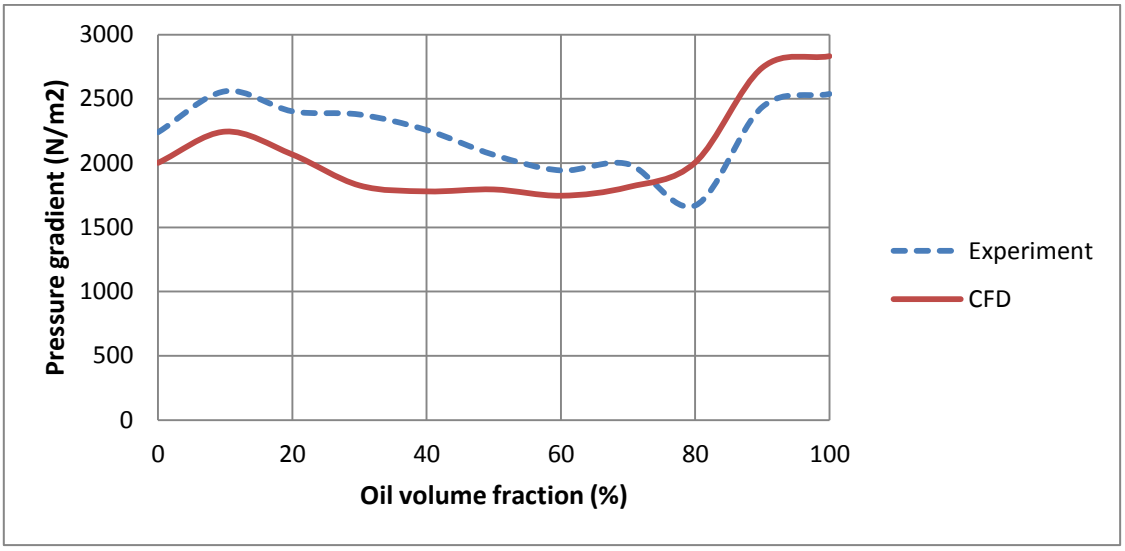

Figure 3.12: Comparison of numerical pressure gradient with experimental data at mixture velocity of 3.0m/s (Eulerian multiphase model)

3.3 Validation of oil-water dispersed flows with homogeneous models

The pressure gradient numerical results and experimental data at mixture velocity of 3.0m/s were considered for comparison with calculations from mixture viscosity homogeneous models of Brinkman (1952) and Duckler et al (1964). The homogeneous models considered the two-phase flow as a single-phase flow with average flow properties which assume to form a mixture. The pressure gradient for homogeneous models is calculated from:

$$\frac{dP}{dX} = \frac{f_m \rho_m U_m}{2D} \qquad \textbf{(3-18)}$$

where f_m is the mixture friction factor, ρ_m is the mixture density, U_m is the mixture velocity and D is the pipe internal diameter. The mixture density from homogeneous model is computed from volume averaged densities of the phases given by:

$$\rho_m = \alpha_o \rho_o + \alpha_w \rho_w \quad \textbf{(3-19)}$$

Here α_o is the volume fraction of oil, ρ_o is the density of oil, α_w is the volume fraction of water and ρ_w is the density of water.

The mixture viscosity correlations of the phases in dispersed flows are proposed by Brinkman (1952) and Duckler et al. (1964) which form two different approaches for homogeneous models. The correlation of Duckler et al.(1964) is based on averaging in term of flow volume fraction of phases, which is calculated from:

$$\mu_m = \alpha_o \mu_o + \alpha_w \mu_w \quad \textbf{(3-20)}$$

where $\alpha_o \; and \; \alpha_w$ are the oil and water volume fractions respectively and $\mu_o \; and \; \mu_w$ are the oil and water viscosities respectively, while Brinkman (1952) mixture viscosity correlation is given by:

$$\mu_m = \mu_c (1 - \phi)^{-2.5} \quad \textbf{(3-21)}$$

Here μ_m andμ_c are the viscosity of mixture and continuous phase respectively; $\boldsymbol{\phi}$ is the dispersed phase concentration. The mixture coefficient of friction f_m is calculated from modified Colebrook (1978) formula which is given by:

$$\frac{1}{\sqrt{f_m}} = -2.0 log \left\{ \frac{\varepsilon}{3.7D} + \frac{2.51}{R_m \sqrt{f_m}} \right\} \quad \textbf{(3-22)}$$

where ε is pipe wall roughness which is given as 7×10^{-5}m from experimental data (Lovick and Angelli, 2004)), while R_m is the mixture Reynolds number that can be calculated from equation (3.11). The results of the calculated homogeneous models of pressure gradient at mixture velocity of 3.0m/s based on Brinkman (1952) and Duckler et al. (1964) mixture viscosity correlations were presented with numerical and measured data as shown in table 3.10.

Oil%	Pressure gradients at mixture velocity (3.0m/s)					
	Experiment	CFD	Brinkam	% Dev.	Duckler	% Dev.
0	2240	2002	2896	-29.3	2896	-29.3
10	2559	2245	2898	-13.3	2930	-14.5
20	2403	2067	2921	-21.6	2957	-23.1
30	2378	1826	2971	-25.3	2979	-25.2
40	2257	1780	3066	-35.8	2995	-32.7
50	2064	1795	3237	-56.8	3007	-45.7
60	1943	1746	4236	-118.0	3015	-55.2
70	1992	1813	3800	-90.8	3020	-51.6
80	1670	2005	3474	-108.0	3021	-80.1
90	2437	2743	3220	-32.1	3019	-23.9
100	2538	2832	3015	-18.8	3015	-18.8

Table 3-10: Results of pressure gradients with homogeneous models (N/m^2)

The calculated pressure gradients (homogeneous models) at mixture velocity of 3.0m/s is selected for comparison with numerical and experimental pressure gradient results as shown in figure 3.13. The two homogeneous models over-predicted the experimental and numerical data. The Brinkman correlation has the highest over-prediction of data especially in oil continuous flow where there is appearance of phase inversion at 60%-70% of oil volume fraction and this can attributed to drag reduction in oil continuous flow as reported by Angeli and Hewitt (1998).

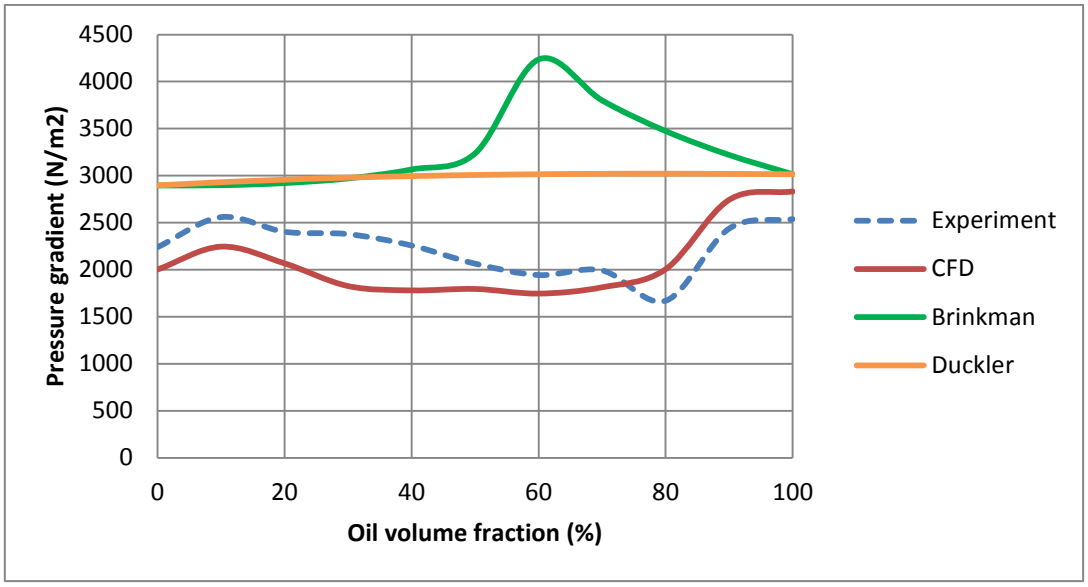

Figure 3.13: Comparison of numerical and experimental data with homogeneous models of Brinkman and Duckler at mixture velocity of 3.0m/s

3.4 Validations of oil-water dispersed flows with Lockhart-Martinelli empirical correlations

The numerical pressure gradients with experimental data were also compared with Lockhart-Martinelli pressure gradient correlations (Lockhart and Martinelli, 1949) at mixture velocity of 3.0m/s. Based on two- phase multiplier for the liquid phase and vapour phase, the correlation can be used for liquid-liquid flow and for all flow regimes, calculations of pressure gradient with Lockhart-Martinelli correlations, the following steps were required.

Calculation of mass fluxes of oil and water phase:

Water mass flux,

$$G_w = \rho_w V_w \qquad \textbf{(3-23)}$$

Oil mass flux,

$$G_o = \rho_o V_o \tag{3-24}$$

Here the subscripts ‘o’ and ‘w’ stand for oil and water, this follows by calculation of Reynolds numbers of oil and water phase:

Water phase Reynolds number,

$$Re_w = \frac{\rho_w V_w D}{\mu_w} \tag{3-25}$$

Oil phase Reynolds number,

$$Re_o = \frac{\rho_o V_o D}{\mu_o} \tag{3-26}$$

where $\mu_w and\ \mu_o$ are the water and oil viscosity respectively. The friction factors for oil and water phase are calculated with the Colebrook equation from equation (3.13) and the iterative process is used to solve for friction factor. To start with calculations of individual phase pressure gradients:

Water phase pressure gradient:

$$\frac{dP_w}{dx} = \frac{f_w G_w^2}{2\rho_w D} \tag{3-27}$$

Oil phase pressure gradient:

$$\frac{\mathrm{dP_o}}{\mathrm{dx}} = \frac{\mathrm{f_o G_o}^2}{2\rho_o \mathrm{D}} \tag{3-28}$$

The total pressure gradient can now be calculated using the two-phase multiplier. The two-phase multiplier is a function of mass flow rate, density and viscosity and can be calculated using the Lockhart-Martinelli (1949) correlation.

Lockhart-Martinelli factor:

$$X_{tt} = \sqrt{\frac{dP_w}{dP_o}} \quad \textbf{(3-29)}$$

Where d$P_w and\ dP_o$ are water phase and oil phase pressure gradients respectively. The two-phase multiplier can be calculated for each of the phase:

Water two-phase multiplier:

$$\emptyset_w = \left(1 + 12{X_{tt}}^{-1} + {X_{tt}}^{-2}\right)^{0.5} \quad \textbf{(3-30)}$$

Oil two-phase multiplier:

$$\emptyset_o = \left(1 + 12X_{tt} + {X_{tt}}^{2}\right)^{0.5} \quad \textbf{(3-31)}$$

The water and oil two-phase multipliers are used to calculate the total pressure gradient, the value of the two should be the same and hence the total pressure gradients are:

Water phase= Water phase pressure gradient × Q_w^2 **(3-32)**

Oil phase = Oil phase pressure gradient× Q_o^2 **(3-33)**

The calculated pressure gradients with Lockhart and Martinelli correlations at mixture velocity 3.0m/s are presented in table 3.11.

Oil%	Pressure gradient at mixture velocity (3.0m/s)			
	Experiment	**CFD**	**Martinelli**	**% deviation.**
0	2240	2002	2896	-29.3
10	2559	2245	1712	33.0
20	2403	2067	2233	7.1
30	2378	1826	2543	-6.9
40	2257	1780	2800	-24.
50	2064	1795	2848	-38.0
60	1943	1746	2746	-41.3
70	1992	1813	2502	-25.6
80	1670	2005	2110	-26.3
90	2437	2743	1582	35.0
100	2538	3026	3015	-18.8

Table 3-11: Results of pressure gradients with Lockhart and Martinelli correlations (N/m^2)

The results of pressure gradient with Lockhart and Martinelli correlations at 3.0m/s mixture velocity are compared with numerical and measured data as shown in figure 3.14.

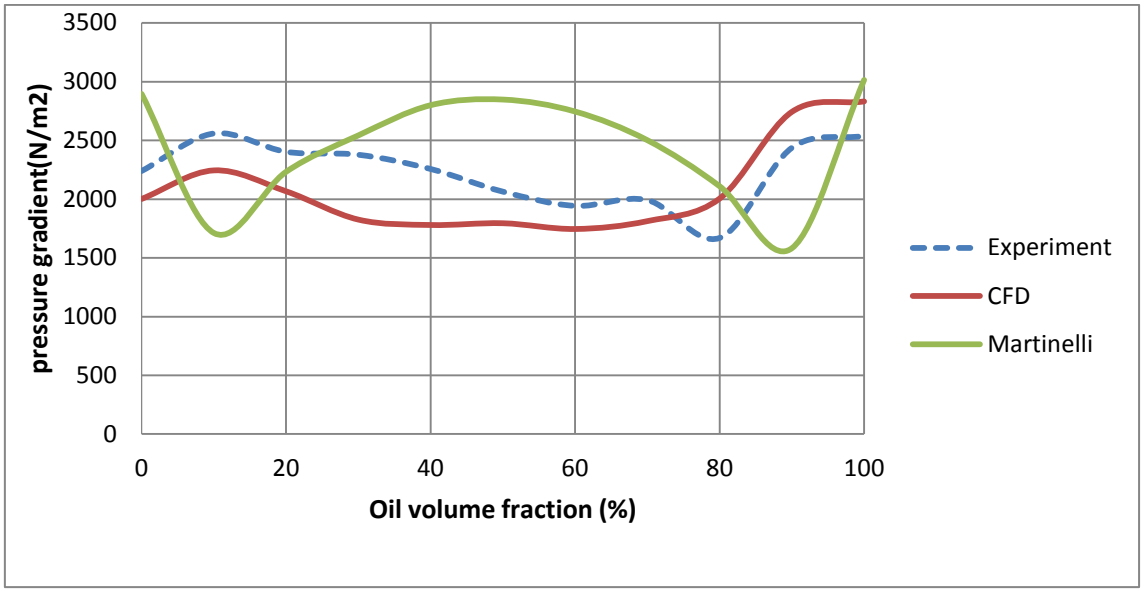

Figure 3.14: Comparison of Lockhart- Martinelli correlation of pressure gradient with numerical and experimental Data at mixture velocity of 3.0m/s

Figure 3.14 shows comparative results of numerical simulation and experimental data with Lockhart-Martinelli correlations of pressure gradient. The correlations under-predict the numerical simulation results and experimental data below 5% to 20% and above 80% of oil volume fraction, while it over-predict the pressure gradient between 20% and 80%, hence Lockhart-Martinelli correlation show poor agreements with numerical simulation results and experimental data. This can be attributed to flexibility of the correlations, which cannot be applied to all flow patterns. The correlation can perform well under annular flow and in low pressure flow.

To conclude this section, numerical validation of two phase flow of oil-water in horizontal pipe were compared with experimental data (Lovick and Angelli, 2004) at mixture velocities of 2.5m/s and 3.0m/s which fall under the range of Reynolds number of 18,500-22,000. The numerical simulation is performed with two multiphase models, the Eulerian multiphase model and mixture multiphase model in conjunction with k-ε turbulence model; the two numerical pressure gradient results were compared with experimental data and calculations of homogeneous models and empirical correlations. The following main conclusions are derived.

- The mixture multiphase model failed to accurately predict the pressure gradient under the range of Reynolds number of 18,500-22,000 as compared to experimental measurement; it shows large deviation in both the continuous and dispersed flows. Hence, the model cannot be used under this study.
- Eulerian multiphase model shows an acceptable agreement with experimental data at the range of Reynolds number of 18,500-22,000, hence the model can be used in CFD analysis of dispersed multiphase of oil-water flows in horizontal pipe with pipe deformation (corrosion cavity and scale sediments).
- The calculation of homogeneous models (mixture viscosity correlations) of Brinkman (1952) and Duckler et al. (1964) and empirical correlations of Lockhart-Martinelli (1949) show poor agreements with the numerical and experimental measurement at both the continuous and dispersed flows.

3.5 Validation of vertical distribution of oil and water phase

Validation study on vertical distribution of oil and water phase in horizontal pipe is carried out to choose the appropriate dispersed droplets diameter that will be applicable in numerical simulation of oil-water flow in horizontal pipe with pipe deformation (corrosion cavity and scale sediments) using the work done of Rashmi et al. (2009), numerically investigated oil-water distribution during the flow of dispersed oil-water flow in horizontal pipe. The simulation conducted with ANSY FLUENT 6.3. Eulerian multiphase model is selected together with standard k-ε model to resolve the turbulence in continuous phase. The three dimensional pipe with internal diameter of 0.024m and length 9,7m, the test section started from 8m distance from the pipe inlet, total of 16×10^4 cells were used for the simulation. The oil and water properties at 46% input water volume fraction are shown in table 3.12.

The numerical result of in-situ water fraction is compared with experimental data of Soleimani et al. (1999) for input water volume fraction of 46% and 60%. The

numerical results were in better agreement with experimental data at mixture velocity of 3.0m/s (range of Reynolds number 18,500-22,000), while difference was observed for lower mixture velocity of 2.12m/s. The experimental results for water volume fraction of 46% and at mixture velocity of 3.0m/s are selected for validation against numerical results.

Properties	**Oil**	**Water**
Density (kg/m^3)	801	988.2
Viscosity (mPa.s)	1.6	1.003
Velocity (m/s)	1.62	1.38

Table 3-12: Oil and water properties at 46% water fraction (Solaimani et al., 1999)

The model pipe geometry and mesh are produced with GAMBIT 2.4. The height of the first boundary cell is 0.00015 calculated from equations (3.17); the total cells of 5×10^5 are used under this investigation. Numerical simulation is conducted against the numerical computation by Rashmi et al. (2009) and experimental work done by Soleimani et al. (1999) using Eulerian multiphase model together with k-ε model. The dispersed droplet diameter was not given in the experimental work of Soleimani et al. (1999). Therefore, Rashmi et al. (2009) calculated dispersed droplet diameter with correlation of Sauter mean drop diameter (d_{32}) proposed by Angelli and Hewitt (2000) and used the convergence criteria of 1×10^{-3}in the numerical simulation. In this study, the droplet diameter will be determine by conducting a number of simulations with different drops diameter to correlate with numerical results of Rashm et al (2009) and experimental data of Soleimani et al. (1999), the best fit curve among the different drop diameter curves will be selected as our appropriate droplet diameter to be applied throughout numerical simulation of oil-water flow in horizontal pipe with pipe deformations (cavity and scale sediments). However, the results of first order simulation of 46% input water volume fraction at mixture velocity of 3.0m/s are shown in figure 3.15.

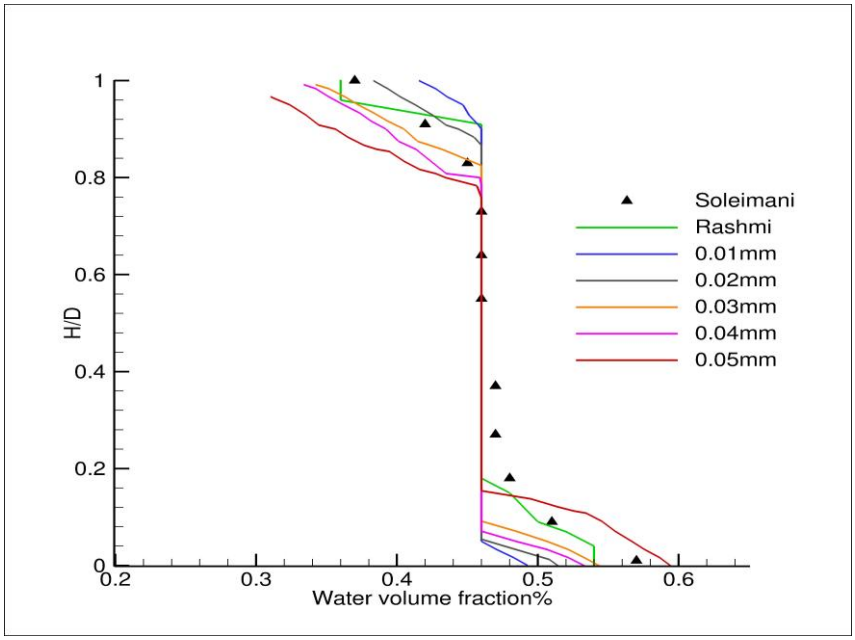

Figure 3.15: Water volume fraction droplets diameter (first order simulation)

The results from figure 3.15 show that droplet diameter of 3×10^{-5}m curve gave the correct match-curve in comparison with numerical curve of Rashmi et al. (2009) and experimental data curve of Soleimani et al. (1999). Therefore, droplet diameter of 3×10^{-5}m is selected under the first order simulation.

Numerical validation is further performed with second order simulation to compare with first order simulation results. The second order solver settings are summarized in table 3.13.

Settings	**Discretization**
Pressure-Velocity Coupling	Phase Coupled SIMPLE
Momentum	Second Order Upwind
Volume fraction	QUICK Scheme
Turbulent Kinetic Energy	Second Order Upwind
Turbulent Dissipation Rate	Second Order Upwind
Convergence Criteria	1×10^{-3}

Table 3-13: Summary of solver settings (second order simulation)

The numerical results of second order simulation at 46% water volume fraction with mixture velocity of 3m/s are shown in figure 3.16.

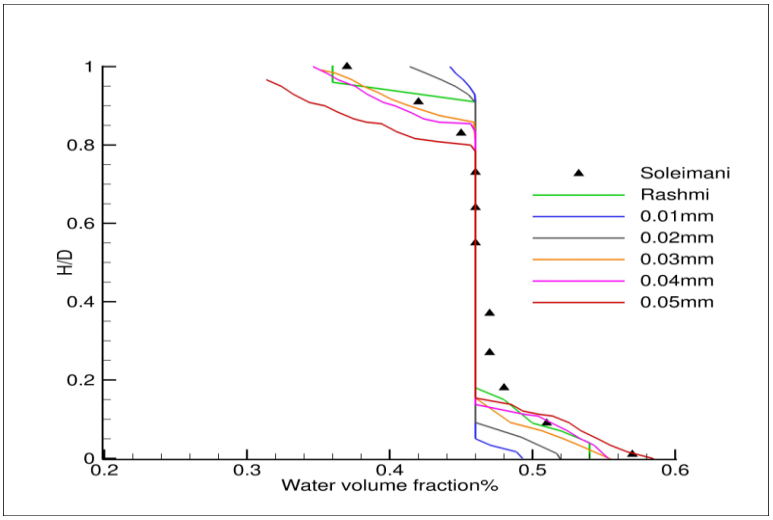

Figure 3.16: Water volume fraction droplets diameters (second order simulation)

The Results of second order simulation show the same value of dispersed droplets diameter as observed in first order simulation as the finest match-curve in comparison with numerical and experimental curve. Therefore, the value of 3×10^{-5}m droplet diameter will be used in numerical simulation of turbulent dispersed flow of oil-water in horizontal pipe with pipe deformation (corrosion cavity and scale sediments).

4 NUMERICAL MODELLING OF OIL-WATER FLOW IN PIPE WITH CORROSION CAVITY

Numerical simulation of oil-water flow in horizontal pipe with corrosion cavity is carried out to study the influence of corrosion cavity in changing the flow features and to compute the maximum and minimum water volume fraction and distribution in the pipe and cavity walls as well as to determine the contribution of corrosion cavity geometry in further accelerating oil-water separation and settlement. There are no experimental data on oil and water flow in pipe with corrosion cavity from published literatures. However, the experimental data of Lovick and Angelli (2004) of dual continuous flow of oil-water in horizontal pipeline is used as input data in this study based on validation study conducted as shown in table 4.1.

Density	828kg/m
Viscosity	6mPa.s
Oil-water interfacial tension	0.0396N/m
Pipe test length	2.66m
Pipe diameter	0.038m

Table 4-1: Pipe geometry and oil properties (Lovick and Angeli, 2004)

4.1 Pipe with cavity model geometries

The two model geometries of the pipe with cavities were produced as models for simulation of oil-water flow in horizontal pipe with corrosion cavity. The geometry parameters of pipe with cavity are presented in dimensionless quantities with reference to the experimental data of Lovick and Angelli (2004) presented in table 4.1. The length of the pipe is measured as 70D, where D is the diameter of the pipe; this is to ensure a fully developed flow. The pipe length is divided into 3 volume units, the downstream unit of the pipe has length of 55D and the upstream has the total length of 14D, while the middle volume unit of the pipe that contains the cavity has length equal to the diameter of the pipe (D). The two models geometries are generated with computer aid design

software GAMBIT 2.4. The first model of pipe with shallow cavity is rectangular in shape place at the bottom of pipe, oriented perpendicular to the flow. Cavity parameters are described in terms of ratios, the ratio of cavity length and width to the pipe diameter (L/D and W/D) and the ratio of cavity depth to pipe diameter (H/D). For rectangular cavity, the length equals the width (L=W) while the length of the deep cavity is of ratio 1/10. From investigation, the standard wall pipeline thickness is normally of 1-4% of pipe diameter (Hebei, 1997). Therefore, cavity depth is restricted to 2% of internal pipe diameter; the geometry model of pipe with shallow cavity is shown in figure 4.1.

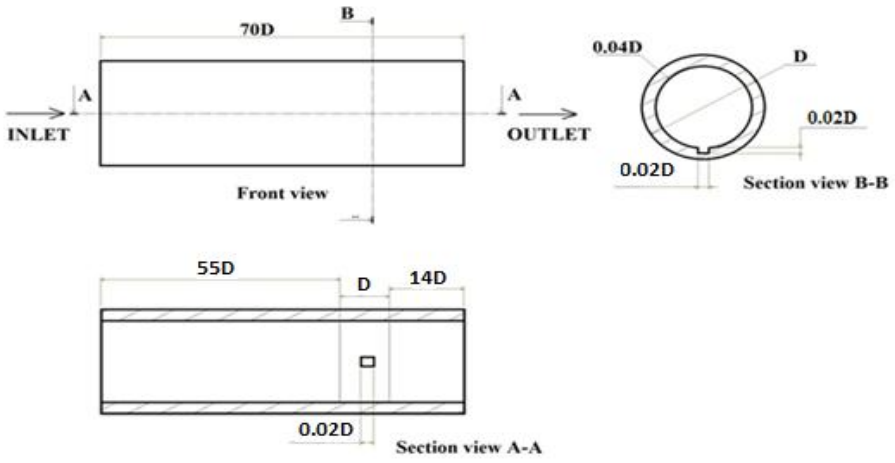

Figure 4.1: The schematic model of horizontal pipe with shallow cavity

The second model of pipe with cavity is classified as deep cavity and is cubical in shape because the cubical shape will also favor separation and is placed at the pipe base oriented perpendicular to the flow, the geometry parameters are also described in terms of ratio of length, width and depth, in other words, the controlling geometry parameters are of the ratio of cavity length and width to the pipe diameter (L/D and W/D) and ratio of cavity depth to pipe diameter (H/D). Similarly the depth of deep cavity is of 2% of pipe diameter (0.02D) which is

50% of the pipe wall thickness. Therefore, the cubical model geometry are of sides 0.02D. The model pipe with deep cavity is shown in figure 4.2.

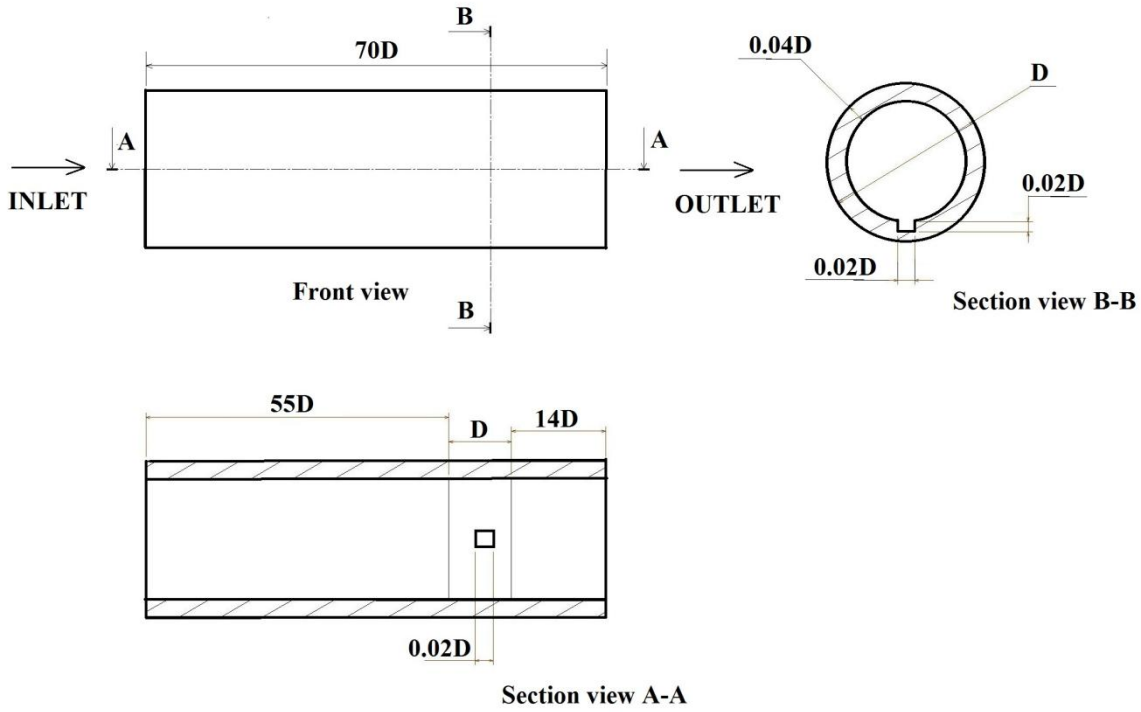

Figure 4.2: The schematic model of horizontal pipe with deep cavity

Therefore, from the above definition of cavity parameters the two model cavities are rectangular and cubical in shapes and are of shallow and deep cavity respectively. The lengths of shallow cavity and deep cavity are represented as 0.2D and 0.02D respectively, while geometry case data of pipe with cavity are given in table 4.2.

Parameters	Value
Pipe	
Diameter	0.038
Length	2.66
Cavity	
L/H Shallow	10
L/H Deep	1
H/D	0.02D

Table 4-2: Pipe with cavity case data

Based on cavity parameters ratio, the calculated cavity dimensions from Lovick and Angelli (2004) experimental case data for shallow and deep cavity are depicted on table 4.3.

Dimension	**Shallow cavity (m)**	**Deep cavity (m)**
Length	0.0076	0.00076
Depth	0.00076	0.00076
Width	0.0076	0.00076

Table 4-3: Cavity case dimensions

4.2 Grid generation

The subject of grid generation in computational fluid dynamic computation is very significant; the type of grid created for given geometry can make-up or break-up the numerical solutions (Anderson, 1995). Mesh quality affects the accuracy of the solution and ease of convergence. It is important to generate quality grids to represent the governing equations in finite form in order to achieved reasonable results. The purpose here is to mesh the two model geometries of pipe with cavity in three dimensions of reasonable mesh quality that can resolve all main flow features. However, past study has shown that the

two dimensional computations (2D) were not sufficient for the computation of local velocities and phase holdups in multiphase flows.

Mesh generating tool GAMBIT 2.4 is used to produce 3-dimensional hexahedral cells and tetrahedral cells in the pipe model with cavity; the choice of hexahedral type of mesh is for improved accuracy, flexibility of control, less computational time and to make convergence easier. In addition, it allows for good representation of the boundary layer especially at the contact region. The pipe model with cavity is divided in to three volumes, the hexahedral mesh is applied at upstream and downstream volumes of the pipe and has more coarse mesh, while the middle volume that contains the cavity, tetrahedral mesh is applied and this is the region of the cavity domain where the flow is fully developed and is the test section region where separation and recirculation of oil and water occurred.

Pipe with shallow cavity	**Elements**	**Nodes**
Pipe upstream volume	798172	706407
Pipe downstream volume	203190	180516
Middle pipe volume	274439	124755
Cavity volume	29791	27000
Total	1,302801	1,041469

Table 4-4: Number of elements and nodes for pipe with shallow cavity

The boundary layer is connected to the inner wall of the pipe; this is to ensure wall y^+ within the range for two high Reynolds numbers of 18,500 and 22,000. The height of the cell is specified and a cell growth factor of 1.2 is used to cluster the mesh toward the wall. The size functions are attached to the top of cavity in order to connect the boundary layer at the cavity surface in match with the pipe wall; the use of size function will help to generate tetrahedral cells of good quality. The number of nodes and elements for the pipe with shallow cavity are presented in table 4.4, while figures 4.3 and 4.4 give grid structures for pipe with shallow and deep cavity respectively.

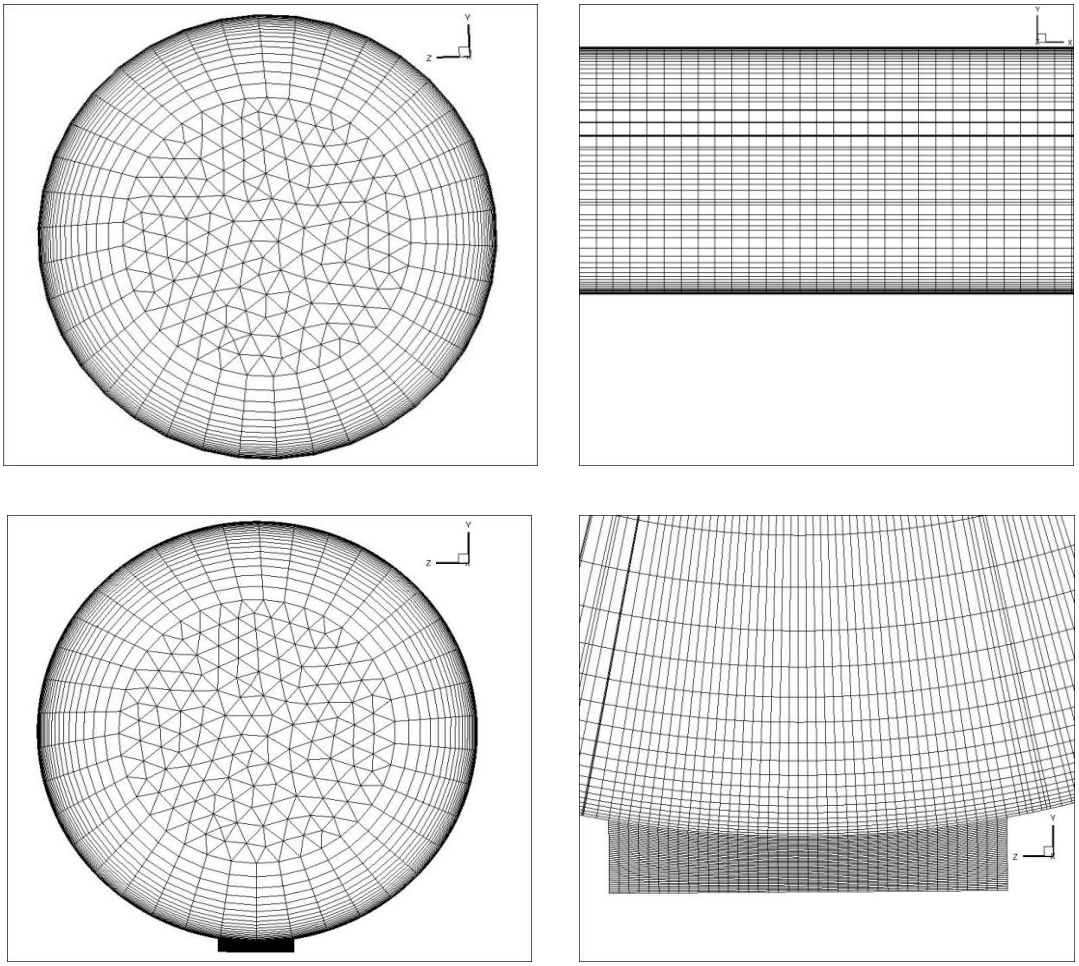

Figure 4.3: Grid structures for pipe with shallow cavity

Boundary layer is connected to the interior pipe wall to cluster the grids toward the pipe wall for the pipe with shallow cavity. The boundary layers features for the shallow cavity are given in table 4.5.

Algorithm	**First row**	**Growth factor**	**Total depth**	**No of rows**	**Int/ cont.**	**Trans/ pt**
Uniform	0.0020	1.200	0.3734	20	Yes	1:1

Table 4-5: **Boundary layers features for shallow cavity**

The size functions are applied to the volume that contain shallow cavity in order to cluster the mesh toward the top of the cavity with the same value of growth rate and maximum size of cell as 1.0.

The number of nodes and elements for the pipe with deep cavity are presented in table 4.6.

Pipe with deep cavity	**Elements**	**Nodes**
Pipe upstream volume	637704	564573
Pipe downstream volume	162552	144597
Middle pipe volume	248787	118951
Cavity volume	64000	68921
Total	1,113043	897,042

Table 4-6: Number of elements and nodes for pipe with deep cavity

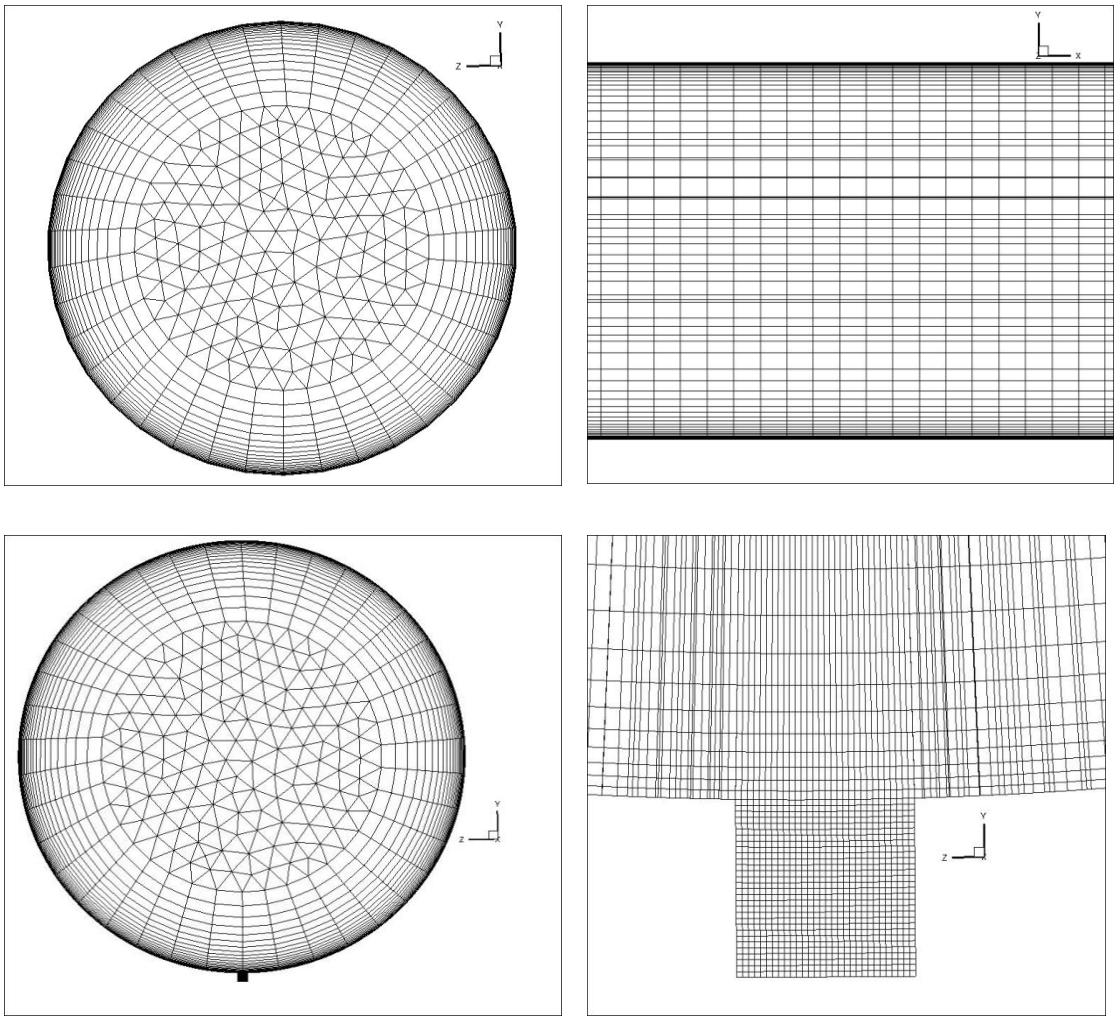

Figure 4.4: Grid structures for pipe with deep cavity

Boundary layer is connected to the interior pipe wall to cluster the grids toward the pipe wall for the pipe with deep cavity. The boundary layers features for the deep cavity are shown in table 4.7

Algorithm	First row	Growth factor	Total depth	No of rows	Int/ cont.	Trans/ pt.
Uniform	0.0022	1.200	0.3765	20	Yes	1:1

Table 4-7: Boundary layers features for pipe with deep cavity

Size function is also applied to the volume that contains deep cavity to cluster the mesh toward the top of the deep cavity with the same value of growth rate and maximum size of cell as 1.0.

4.2.1 Grid independence study

Grids independence study is performed on pipe with shallow and deep cavities at Reynolds numbers 18,500 and 22,000 to choose the appropriate total number of cells. Two meshes were produced for pipe with cavity, the height of the cell is specified and a cell growth factor of 1.2 is used to cluster the mesh toward the wall. The physical dimensions of the geometry are shown in table 4.2. Whereas the Lovick and Angeli (2004) experimental oil properties were used in grid independence studies as shown in table 4.8.

Density	828
Viscosity	6mPa.s
Surface tension	0.0276N/m
Oil-water interfacial tension	0.0396N/m

Table 4-8: Oil properties at 25^{o}C (Lovick and Angeli, 2004)

The Eulerian multiphase model and the standard K-ε turbulence model with standard wall function were selected. Boundary condition set at inlet is velocity inlet and at outlet is outflow, while no-slip is set at both the pipe and cavity walls. The followings are the solver parameters used:

- Second order double precision pressure based steady solver
- Phase coupling SIMPLE algorithm for pressure-velocity coupling
- Second order upwind discretization scheme for momentum, turbulent kinetic energy and dissipation rate
- QUICK differencing scheme for volume fraction

The convergence is achieved when the residual reaches the convergence criterion of 10^{-6}. The water volume fraction, static pressure and centreline mixture velocity are monitored and checked to ensure solution converged.

The numerical result of pressure gradients indicates that the differences between the total numbers of cells values are small. Therefore, in consideration of computational cost, the numbers of cells selected are 1×10^6 and 1.25×10^6 for deep and shallow cavity pipe respectively as shown in table 4.9.

Total cells	**Pressure gradients Plain pipe**	**Pressure gradients Deep cavity**	**Pressure gradients Shallow cavity**	**Reynolds Number**
0.75×10^6	1760	1786	1804	18,500
1.0×10^6	1817	1834	1872	
1.25×10^6	1823	1845	1912	
0.75×10^6	1779	1783	1932	22,000
1.0×10^6	1832	1845	1952	
1.25×10^6	1841	1867	1973	

Table 4-9: Mesh independence study of pipe with corrosion cavities

4.3 Numerical procedures

The pipes with shallow and deep cavity are placed at bottom of pipe oriented perpendicular to the direction of oil-water flow. Based on the literature survey, range of Reynolds numbers in oil-water pipes resulting in fully dispersed turbulent flow are identified to be between 18,000 and 25,000 and typical range of water volume fraction is between $\alpha_{w=}0.1\ and\ \alpha_w = 0.3$. Therefore, the

Reynolds numbers selected under this study are 18,500 and 22,000 with input water volume fraction as $\alpha_w = 0.1 \; and \; \alpha_w = 0.3$ in 0.038m diameter pipe of length 2.66m, because of computational requirements matrix of 8 cases will be investigated under this study as summarised in table 4.10.

The computational mesh for the pipe geometry with cavity is produced with GAMBIT2.4, the optimum number of 10^6 cells and 1.25×10^6 cells are selected for pipe with shallow and deep cavity respectively as supported in grid independence study. The mesh is exported to FLUENT 6.3 and Eulerian-multiphase flow model with standard k-ε turbulent model and standard wall function were selected. Oil and water properties are defined in material properties form whereas semi-implicit method for the pressure link equation (SIMPLE) scheme is used for solving the pressure- velocity coupling while second order upwind for discretization scheme for momentum, turbulent kinetic energy and dissipation rate with QUICK difference scheme for volume fraction. Hydraulic diameter of 0.038m and turbulent intensity of 2% are defined at the inlet. The inlet and outlet boundary conditions are specified, mixture velocity is used for the two phase at inlet and water volume fraction is used for secondary phase, no-slip boundary is given at pipe and cavity walls.

4.4 Analysis of results

This section describes the numerical simulations of oil and water flow in pipe with cavity and the analyses to improve our understanding of the change in flow features encountered during the flow of oil-water in horizontal pipe with cavity. The flow features are described in section 4.5 along with the effect of aspect ratio on the rate of water volume fraction at the pipe bottom and cavity region. The effect of Reynolds number and input water volume fraction on the flow physics is described in sections 4.6 and 4.7 respectively. Conclusion on results is outlined in section 4.8.

4.5 Simulation results and discussions

In order to investigate the influence of geometry (cavity) on the flow features during the flow of oil-water in horizontal pipe with deformation (corrosion cavity), simulations have been carried out for two different cavity aspect ratios (deep and shallow), Reynolds number (Re=18,500 and Re=22,000), and water volume fraction (0.1 and 0.3). In this analysis, the effect of aspect ratio, Reynolds number and input water volume fraction on the flow physics and separation of water from oil in the pipe with cavity will be investigated. The effect of aspect ratio on the flow features and phase separation is examined by using the same Reynolds number, the same water volume fraction but different cavity aspect ratio case. Further details into the flow physics are obtained by investigating the effect of input water volume fraction at a fixed Reynolds number and aspect ratio. Also, the effect of Reynolds number on separation rates is investigated by using a constant water volume fraction case and a fixed aspect ratio case. The flow features in flow entrance region and cavity region will be investigated. A table of simulation cases showing cases number for this analysis is shown in table 4.10. There are at least two combinations of each flow parameter which can be varied or held constant in this analysis.

Case Number	Re_m	Water Volume Fraction	Mixture Velocity (m/s)	Aspect ratio (Cavity)
1	18500	0.1	3.2	Deep
2	18500	0.3	2.5	Deep
3	18500	0.1	3.2	Shallow
4	18500	0.3	2.5	Shallow
5	22000	0.1	3.8	Deep
6	22000	0.3	2.96	Deep
7	22000	0.1	3.8	Shallow
8	22000	0.3	2.96	Shallow

Table 4-10: Simulation input data of corrosion cavities

4.5.1 Description of flow in entrance region

Eight cavity cases were simulated using ANSYS Fluent 6.3. The water volume fraction and velocity profile are monitored along the centre of the pipe for the deep and shallow cavity to ensure that the flow is fully developed and then converged. To show that the flow is fully developed plots of water volume fraction and velocity at the centre of the pipe are shown in figures 4.5 to 4.8 below. In these plots, the mixture velocity and water volume fraction at the centre of the pipe are shown to have become stable and fully developed. These plots are also used to describe the influence of cavity/aspect ratio on the flow features in the pipe. This will be done by investigating two cases with all other parameters the same but with different aspect ratios. For this analysis, Case 6 and case 8 will be considered. These two cases will be used to describe the flow in entrance and cavity region as well as the influence of cavity aspect ratio on the flow features using a combination of contour plots, line plots and

streamline plots. Cases 6 and 8 both have Reynolds number of 22, 000, water volume fraction of 0.3 and mixture velocity of 2.96m/s. The only difference is the aspect ratios of the cavities where case 6 is a deep cavity and case 8 a shallow cavity.

In figure 4.5 (deep cavity), the velocity magnitude increases around the first 20% of the pipe length. This is due to the entrance effect at the pipe inlet and the fact that the flow is still developing. About 30% into the full pipe length, the flow is fully developed and the velocity magnitude is almost constant for the rest of the pipe length. Around the location of the cavity, the velocity profile is distorted slightly suggesting that the deep cavity has an influence on the flow field up to the centre of the pipe. A similar profile is observed in figure 4.6 for shallow cavity plot. However, there is slight difference in the influence of the cavity on the velocity magnitude in the centre of the pipe for deep and shallow cavity.

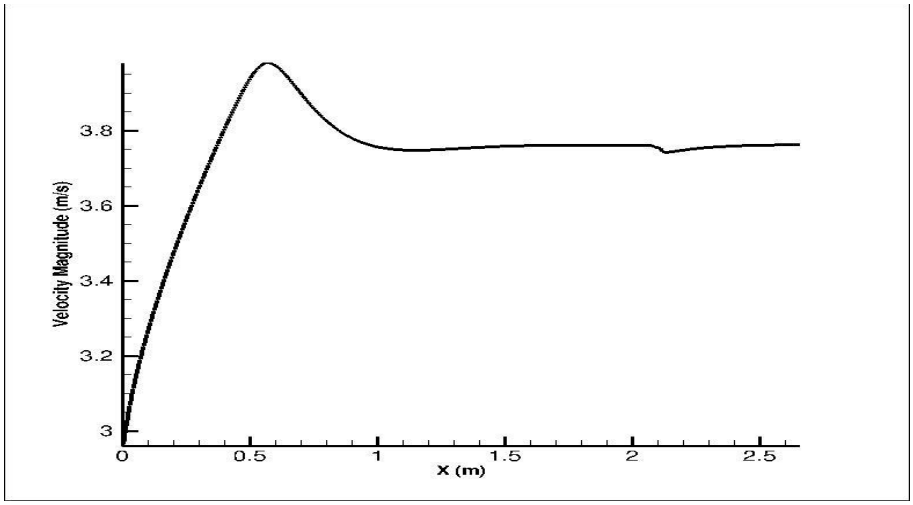

Figure 4.5: Velocity magnitude at centre of the pipe for deep cavity (case 6)

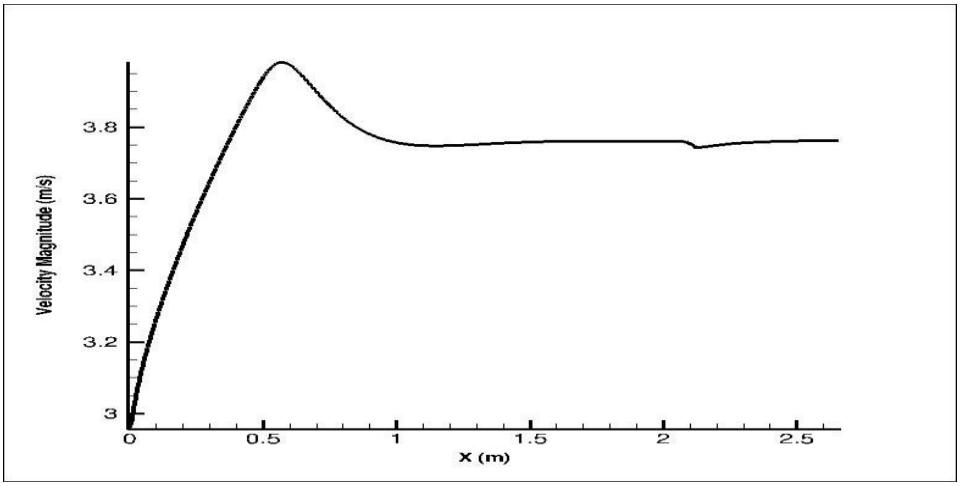

Figure 4.6: Velocity magnitude at centre of the pipe for shallow cavity (case 8)

In figures 4.7 and 4.8 below for deep and shallow cavity respectively, the water volume fraction at the centre of the pipe is constant at 0.3 throughout the entire length of the pipe. This shows that the flow is fully developed. Also the plot suggests that both the deep and shallow cavities slightly influence the water volume fraction at the position of the cavity.

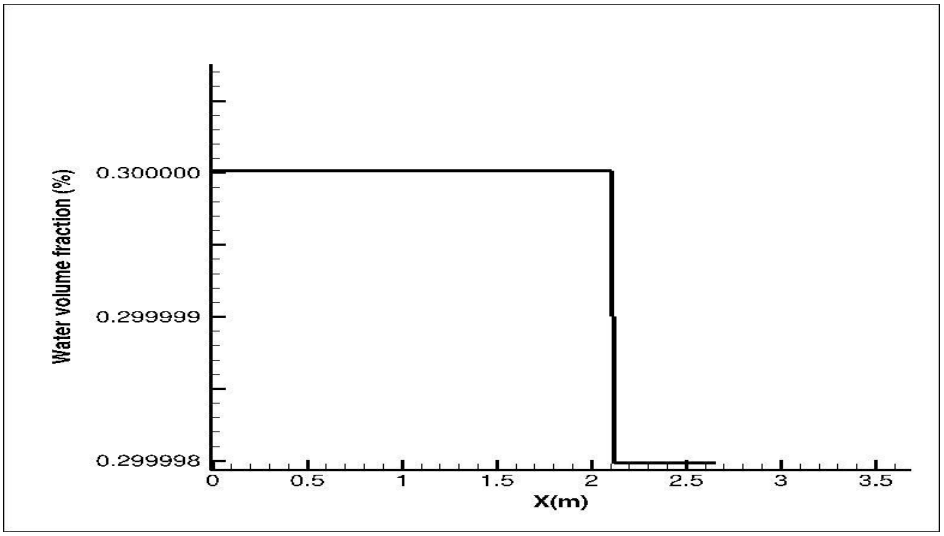

Figure 4.7: Water volume fraction at centre of the pipe for deep cavity (case 6)

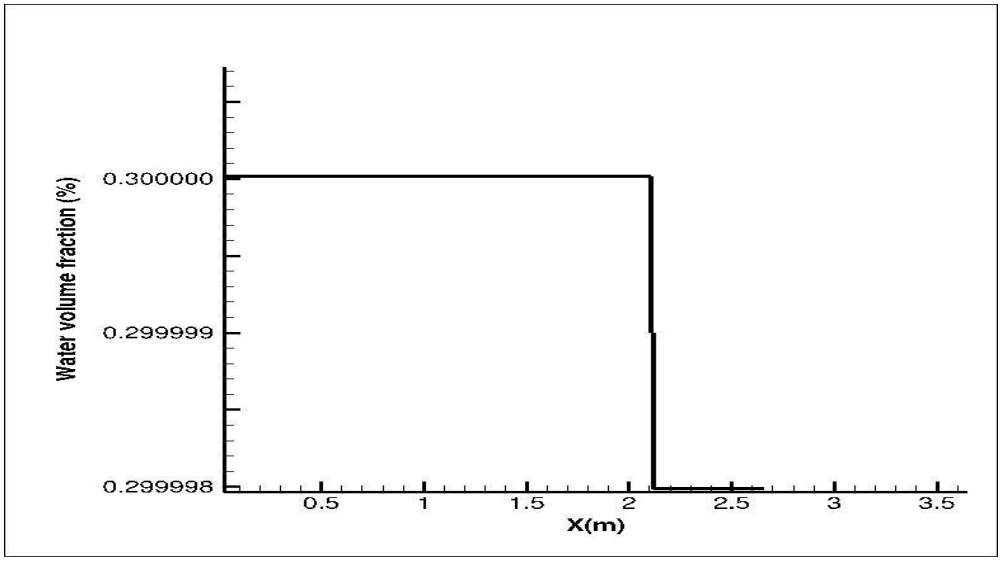

Figure 4.8: Water volume fraction at centre of the pipe for shallow cavity (case 8)

Figures 4.9 and 4.10 below show the turbulent kinetic energy plots at the centre of the pipe from inlet to outlet. In figures 4.9 and 4.10, turbulent kinetic energy increases and becomes steady at about 25% the length of the pipe when the flow is fully developed. TKE is slightly increased around the location of the cavity because of the recirculation and outward flow from the cavity.

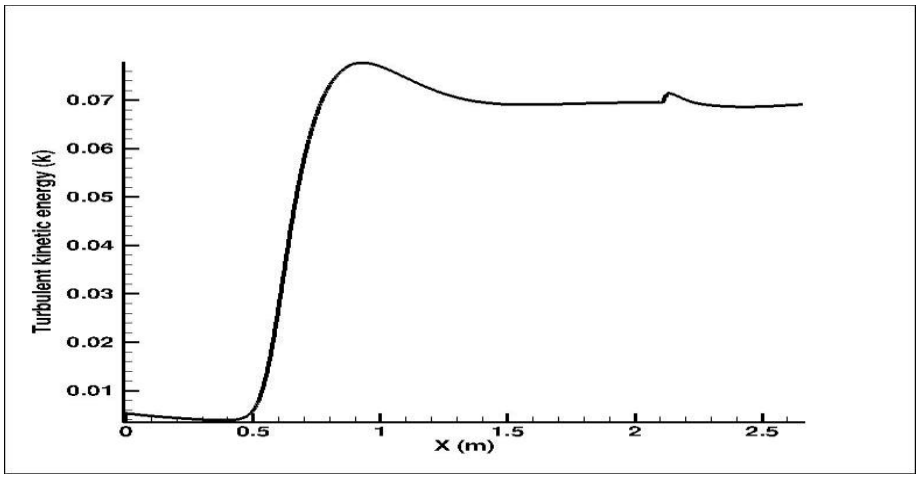

Figure 4.9: Turbulent kinetic energy at centre of the pipe for deep cavity (case 6)

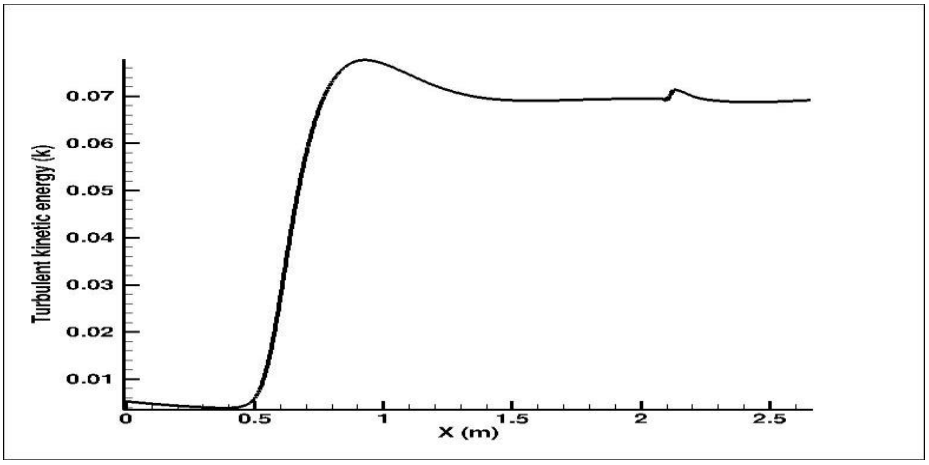

Figure 4.10: Turbulent kinetic energy at centre of the pipe for shallow cavity (case 8)

Figures 4.11 below shows the velocity profile in the perpendicular direction along the position of cavity in x direction just before deep cavity (case 6) and shallow cavity (case 8). The two plots show that the cavities do not have a significant effect on the cross-sectional velocity profile downstream of the cavity. The plots in figure 4.11 are taken at positions just before the cavity. It is taken at x = 2.10872 for deep cavity and at x = 2.10834 for shallow cavity. The plots in figure 4.12 are taken at positions just after the cavity. It is taken at x = 2.10928 for deep cavity and at x = 2.10985 for shallow cavity. The plots show that the presence of cavity does not have any significant effect on the velocity profile along the radial direction of the pipe before and after cavity.

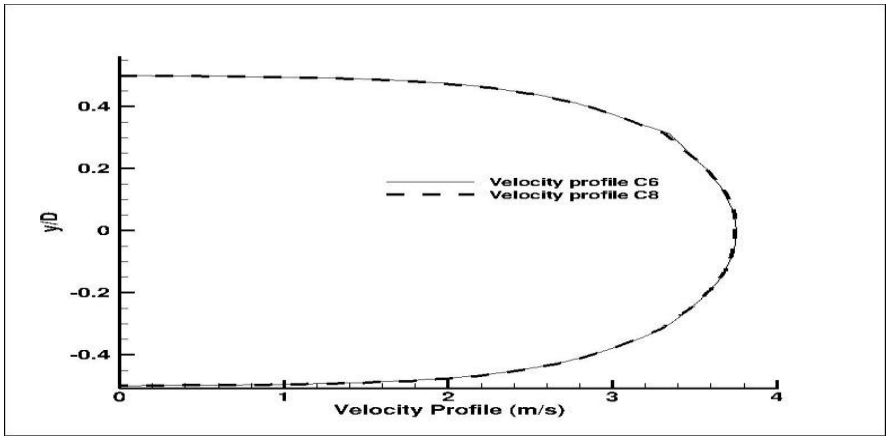

Figure 4.11: Velocity profile before deep cavity (case6) and shallow cavity (case 8)

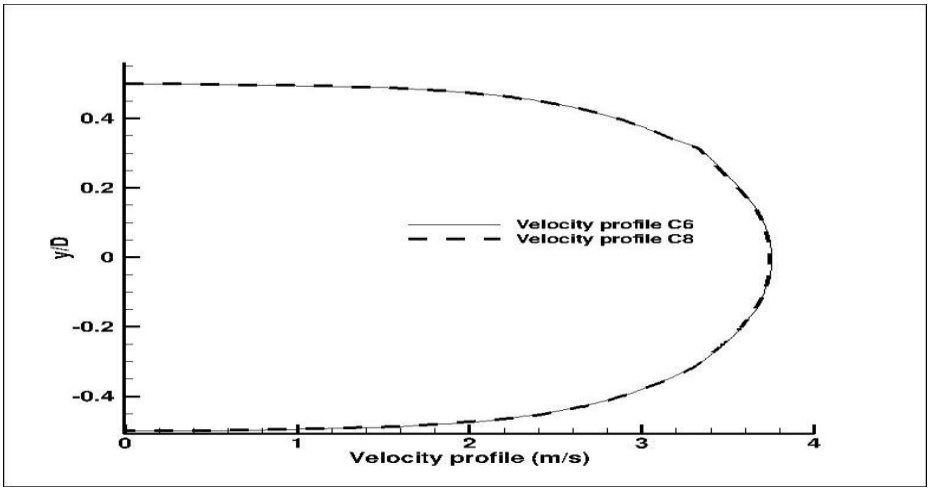

Figure 4.12: Velocity profile after deep cavity (case6) and shallow cavity (case 8)

4.5.2 Flow description inside the cavity region

During the concurrent flow of oil-water in pipe with deep and shallow cavity, the understanding of cavity flow structure is significant because it affects the distribution and position of water volume fraction at cavity entrance and cavity region. The description of the flow in open cavity regions of deep and shallow will be performed with cavity of case 6 (deep cavity) and case 8 (shallow cavity) of the same value of Reynolds number of 22,000 and water volume fraction of 0.3.

Figures 4.13 and 4.14 below show the three dimensional representation of stream traces and water volume fraction in the deep and shallow cavity regions respectively. In the deep cavity (case 6) shown in figures 4.13 and 4.17, as the flow separate from leading edge of the cavity it produce recirculation region inside the cavity, the recirculation zone is large at the centre of the cavity. This prevents the bulk flow in the main pipe from going into the cavity, where there is one large recirculation zone at the centre of the cavity; this is similar to open cavity flow structure described by Yao et al. (2000). In this type of cavity flow, the flow separating from the leading edge of the cavity does not impinge on the bottom of the cavity. A large clockwise rotating vortex is observed at the centre of the cavity, which is attached to the bottom of the cavity for about 75% of its

length. The vortex separates from the side walls and bottom walls close to the cavity bottom edges. These results in smaller vortices which form near the downstream and upstream corner causing water entrainment at corner edges, these phenomena have also been observed by Sheryl et al. (2004). Water settles to the bottom of the cavity around the four bottom edges because the large recirculation zone is around the centre of the cavity allowing water to separate and settle down close to cavity side walls at the bottom edges.

In the shallow cavity case (case 8) shown in figure 4.14 and 4.15, the flow impinges onto the bottom of the cavity around 60% length of the cavity. The flow remains attached to the bottom of the cavity until it separates around 80% of the flow over the trailing edge resulted to two recirculation zones. The first recirculation zone is just underneath the main Stream lines before the impingement position. In this zone, the turbulent kinetic energy is high compared to the second recirculation zone. The mixing in this zone is also large, resulting in more of oil-water mixture trap in leading to water separation and settlement at the bottom of cavity. The second recirculation zone is smaller and localised near the corner edges, less mixing happens here as the turbulent kinetic energy is low at this zone compared to the first recirculation zone. As a result, the rate of separation of water from the mixture is less compared to the first zone. The flow in the shallow cavity can be compared to the ‘transitional cavity flow’ ($8<L/H<11$) described by Lawson et al. (2009).

In figure 4.14 (case 8), it is clear here that the recirculation zone is just immediately after the flow separates from the bottom wall of the pipe. The recirculation looks uniform in the span wise direction. Also, the plot shows the area of high water volume fraction in contact with the pipe wall just underneath the recirculation zone. Another interesting observation from the shallow cavity plot is that the region of high water volume fraction is at the centre bottom leading edge of the cavity.

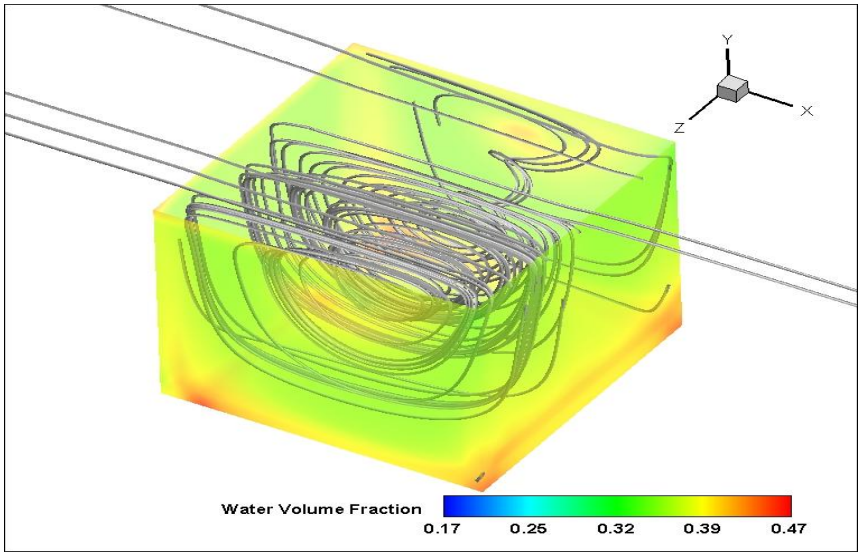

Figure 4.13: 3D view of deep cavity showing stream traces and water volume fraction (case 6)

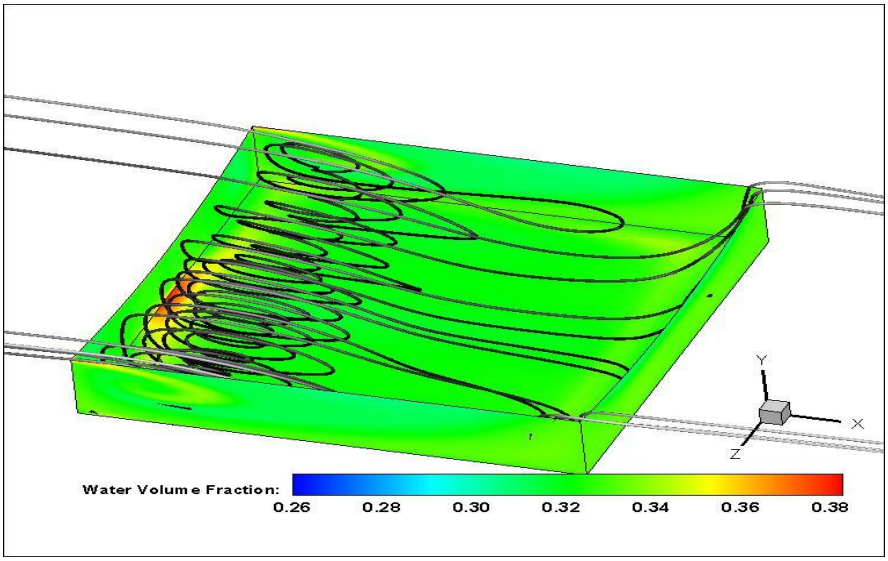

Figure 4.14: 3D view of shallow cavity showing stream traces and water volume fraction (case 8)

Figures 4.15 and 4.16 show stream traces and water volume fraction at planes perpendicular and across the flow in the shallow cavity respectively. In figures 4.15 and 4.16 below, the amount of water at the bottom of the pipe and cavity is maximum at the bottom of the pipe and at cavity leading edges. This is because of the circular geometry of the pipe and the action of gravity on water as water

is heavier than oil. It is also noticed that water has already started to settle to the bottom of the pipe just before the cavity. As the flow separates from the leading edge of the cavity, these regions of high water volume fraction flow into the cavity. As a result, when the flow leaves the cavity, there is no trace of water at the bottom of the pipe. This is an advantage because the water wetted surface area of the pipe is reduced significantly as a result of the cavity and the corrosion risk is less. On the other hand, the localized recirculation region also represents a great risk of corrosion as it is close to the sharp edge in the cavity region. Another interesting observation is that as the flow leaves the cavity, it pushes the bulk fluid upwards slightly. This does not result in any significant separation, but reduces the amount of water in contact with the pipe wall downstream of the cavity. Another important observation is that more water settles to the bottom of the pipe for the deep cavity case compared to the shallow cavity.

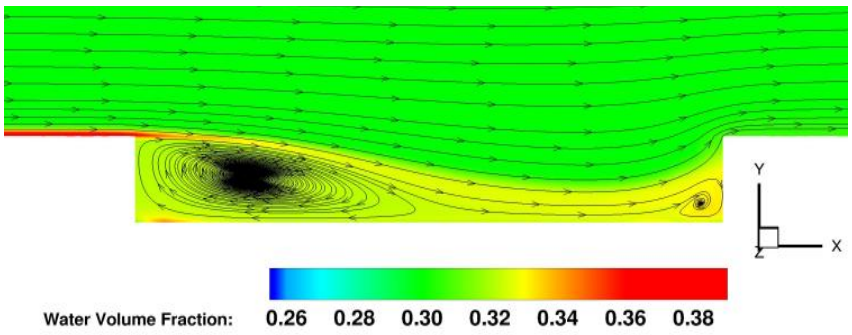

(a) 0.25 cavity width (z=0)

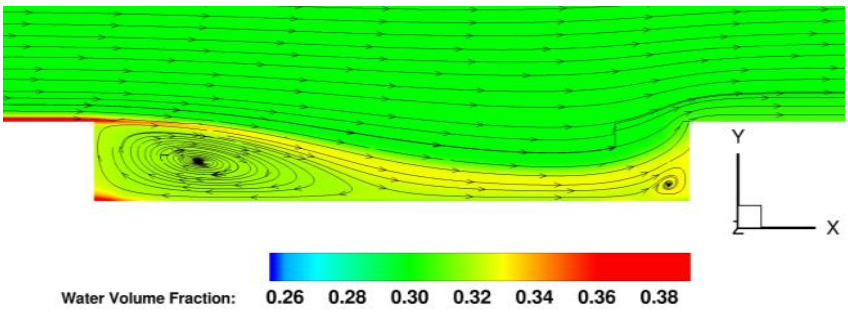

(b) 0.5 cavity width (z=0)

Figure 4.15: stream traces at various positions of x-y plane of shallow cavity

(α_w= 0.3, $U_m = 2.96m/s$)

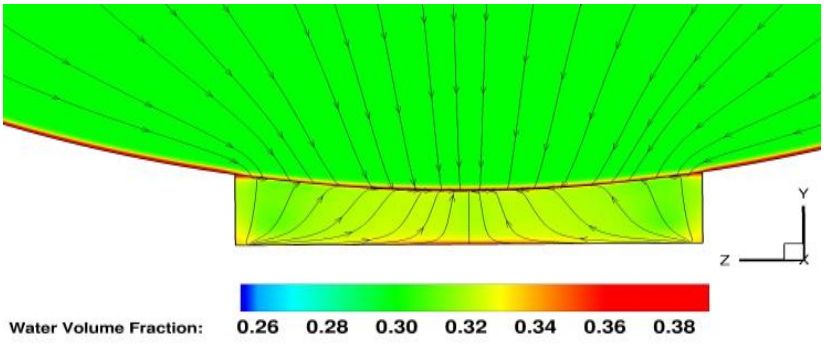

(a) 0.25 cavity length (x=2.109)

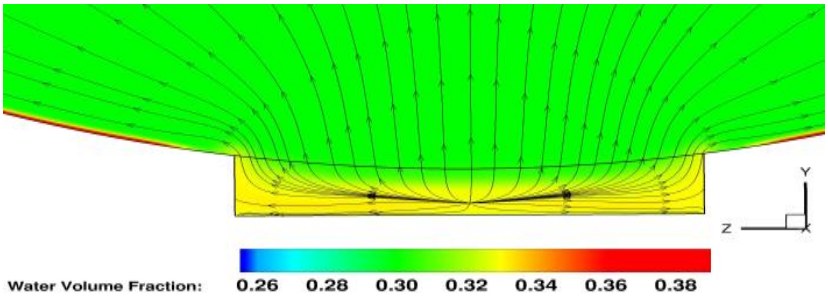

(b) 0.5 cavity length (x=2.109)

Figure 4.16: Stream traces at various positions of z-y plane of shallow cavity

(α_w= 0.3, $U_m = 2.96 m/s$)

Figures 4.17 and 4.18 depict stream traces and water volume fraction at planes perpendicular and across the flow in deep cavity respectively. In figures 4.17a and 4.17b, the maximum water volume fraction appeared at the bottom of the pipe and at cavity downstream and upstream corner edges, it happened because of action of gravity on the pipe and the appearance of recirculation region at top centre of cavity (primary vortices), water separate from the mixture at recirculation region and settles to the bottom of cavity producing another localised recirculation region near the corner edges result to formation of vortices (secondary vortices). It is observed that there is no much difference in water volume fraction distribution, position and size of primary and secondary vortices in the contour plots of figure 4.17a and figure 4.17b, while the water volume fraction and the stream traces in figure 4.18a and figure 4.18b show different flow field behaviour.

Figure 4.18a shows the plane across the flow at 0.25 cavity lengths, in this case, there are exchanges between the cavity internal flow and external flow from the shear layer leading to formation of kidney stream traces pattern inside the cavity, this leads to water being push to the two opposite side walls. The maximum water volume fraction appeared at the top sidewalls close to leading and trailing edges and at two corner edges. Figure 4.18b is the contour plots at plane across the flow for 0.5 cavity lengths, in this case, the flow structure is dominated by circulation of the inflow from the shear layer originated from pipe base to cavity floor, and the maximum water volume fraction appeared at the leading and trailing edges and at the cavity corner edges with some appearance of water bubble at the cavity mid-plane.

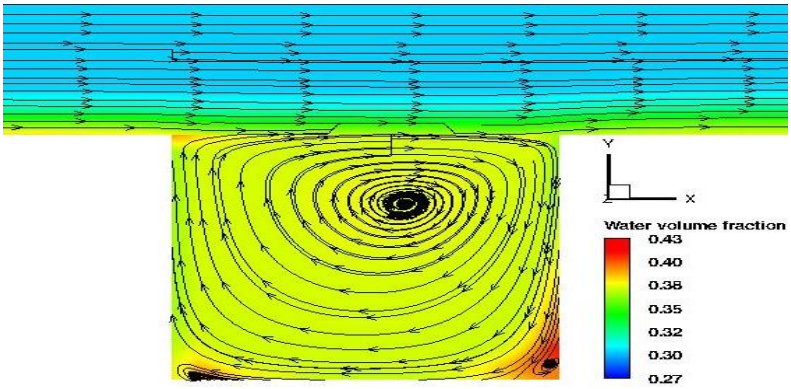

(a) 0.25 cavity width (z=0)

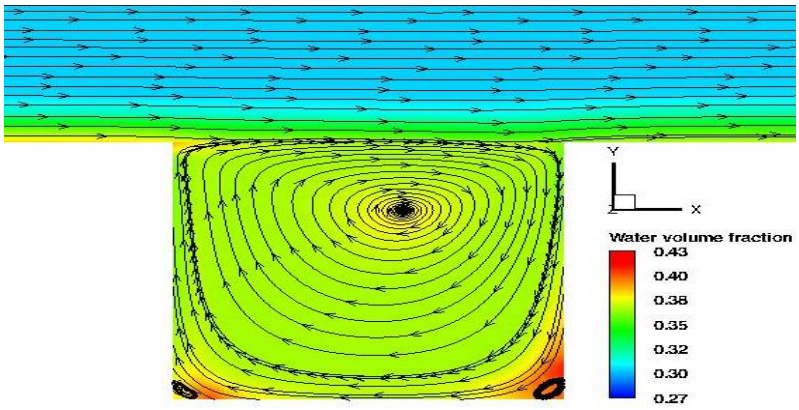

(b) 0.5 cavity width (z=0)

Figure 4.17: Stream traces at various positions of x-y plane of deep cavity (α_w= 0.3, $U_m = 2.96m/s$)

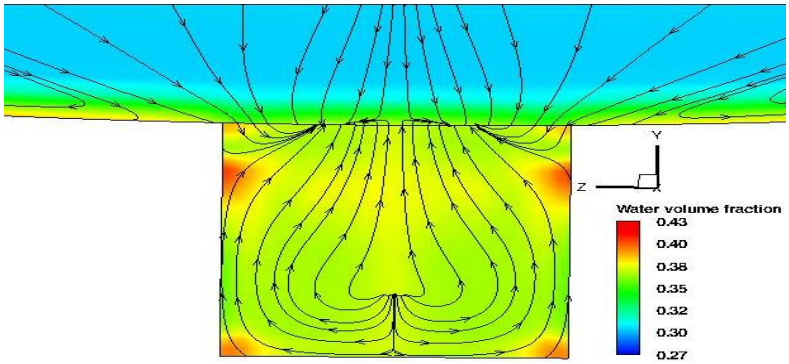

(c) 0.25 cavity length (x=2.109)

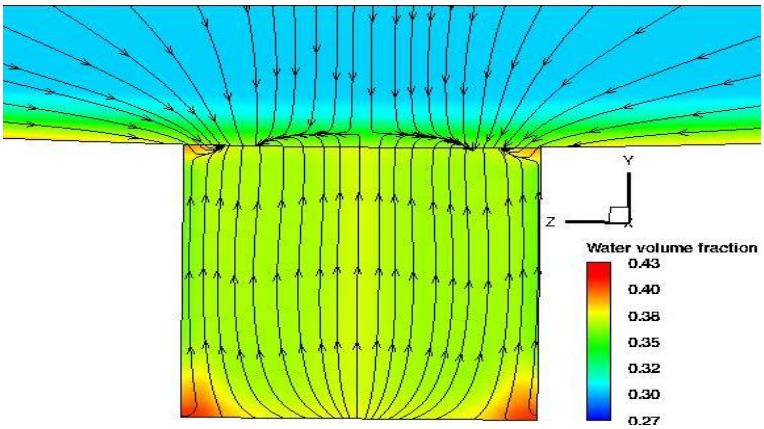

(d) 0.5 cavity length (x=2.109)

Figure 4.18: Stream traces at various positions of z-y plane of deep cavity (α_w= 0.3, $U_m = 2.96 m/s$)

Figure 4.19 below shows the velocity magnitude close to the bottom of the pipe before the deep (case 6) and shallow (case 8) cavity respectively. In figures 4.19, the velocity is seen to be high initially at the entrance of the pipe and drop rapidly afterwards. This is because at the pipe entrance, the bulk fluid separates from the pipe wall. The separation leads to acceleration of the fluid at the bottom of the pipe. Soon afterwards, the fluid is not in contact with the pipe wall and viscous effects at the pipe wall cause the fluid velocity to slow down rapidly. The velocity profile behaviour is the same for both deep and shallow cavity case. The velocity profile does not change until the cavity region is reached. Figure 4.20 shows water volume fraction close to the pipe base before the cavity for both cases. In the first 25% to 30% of the pipe length, the rate of

water settling at the bottom of the pipe is less compared to further into the pipe. This is because at the entrance region. The high flow velocity means more mixing and water is entrained more in the oil. However, when the velocity profile stabilizes, result to a steady increase in the rate of water entrainment at the bottom of the pipe.

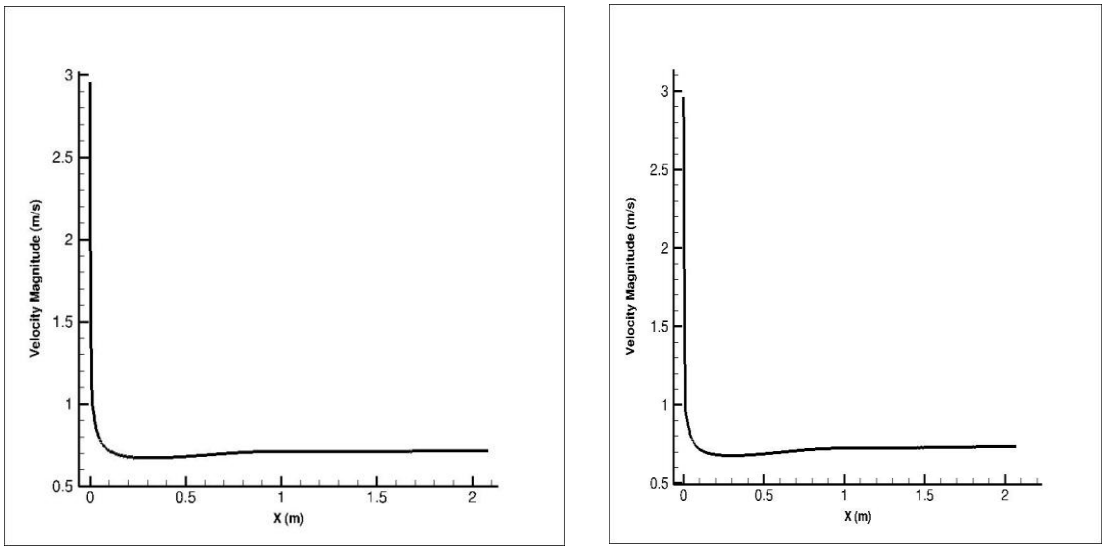

(a) Case 6 deep cavity (b) Case 8 shallow cavity

Figure 4.19: Velocity magnitude near the pipe base before cavity (Re=22,000)

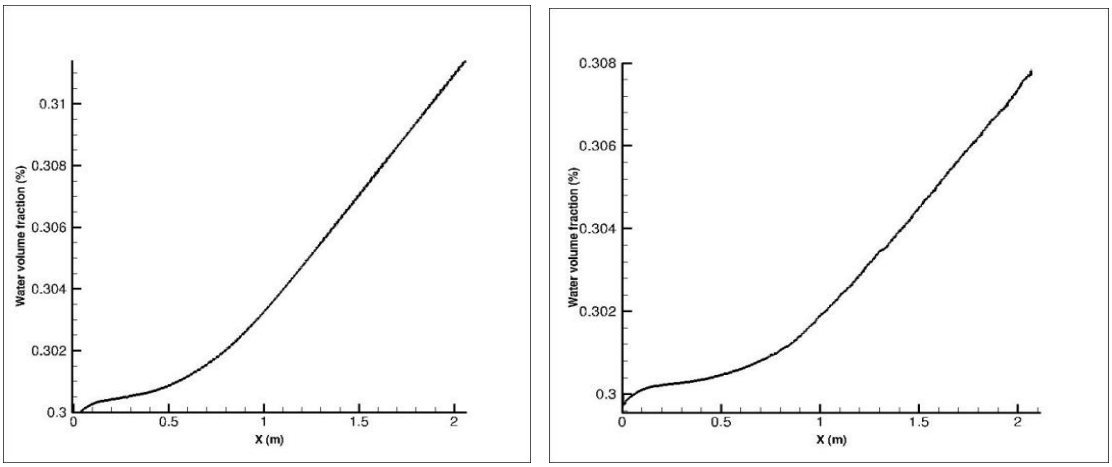

(a) Case 6 deep cavity (b) Case 8 shallow cavity

Figure 4.20: Water volume fraction near the pipe base before cavity (Re=22,000)

Figures 4.21, 4.22 and 4.23 are the line plots of water volume fraction from the top to bottom of the cavity at 0.25, 0.5 and 0.75 length of the cavity from the

leading edge to trailing edge respectively. The plots are measured on plane z = 0. Figure 4.21 shows water volume fraction line plots for deep and shallow cavity at 0.25 cavity length, in the two plots water entered the cavity at higher water volume fraction than the inlet water volume fractions for deep cavity (case 6) water increased from 0.3 to 0.376 at the bottom of cavity, and for shallow cavity water increased from 0.3 to 0.318. It can be seen that a lot of water settles at the bottom of the deep cavity (case 6) compared to shallow cavity (case 8). In figure 4.22 and figure 4.23, the results are also similar with little difference in water entrainment rates.

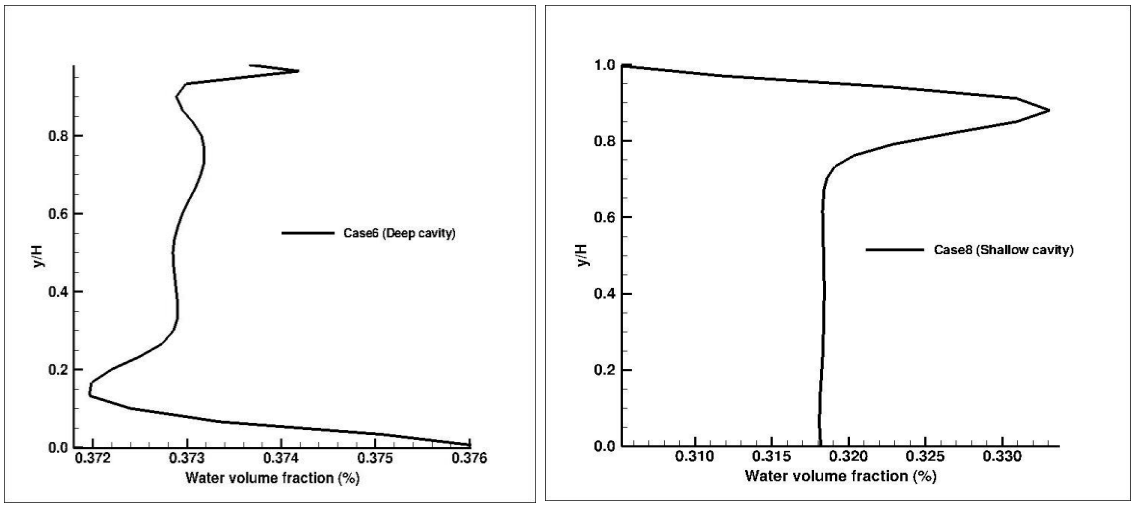

(a) Case 6 deep cavity (b) Case 8 shallow cavity

Figure 4.21: Water volume fraction at 0.25 cavity length (Re=22,000)

Figure 4.22 shows water volume fraction profile for deep (case 6) and shallow (case 8) cavity at 0.5 cavity length (Re=22,000). The deep cavity (figure 4.22a) shows the maximum water volume fraction at recirculation region at the top centre of cavity, water fraction decreased then downward to 0.370 at cavity base, while for shallow cavity (figure4.22b), the maximum water volume fraction appeared at y/H=0.3 of cavity, then water volume fraction finally decreased to 0.323 at cavity base. The results indicate that the maximum water volume fraction appeared at the top centre of deep cavity because more water separates and recirculates from trailing edge as well as influx and exchange of

flow between the shear layer and the top of cavity, also less water at centre bottom of cavity compared to bottom edges of the cavity.

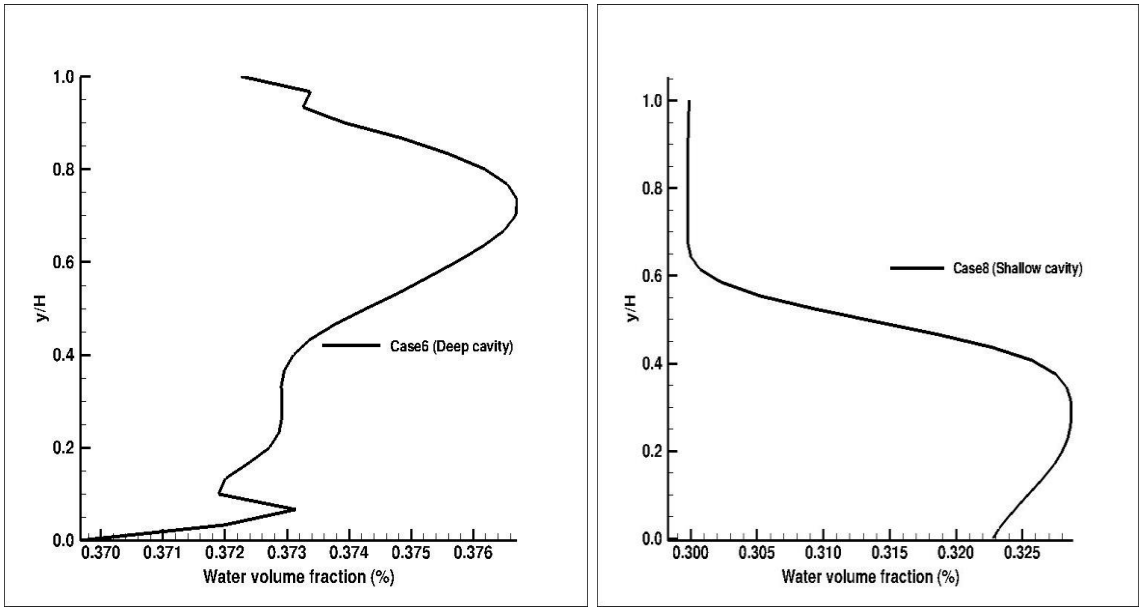

(a)Case 6 deep cavity (b) Case 8 shallow cavity

Figure 4.22: Water volume fraction at 0.5 cavity length (Re=22,000)

The distribution of water volume fraction at 0.75 cavity length for deep and shallow cavity is shown in figure 4.23. For deep cavity, water volume fraction increased from cavity inlet and reached maximum (0.379) at y/H=0.75 then water volume fraction decreased to 0.374 at cavity base, while in case of shallow cavity (figure 4.23b), the increase of water fraction starts at cavity height y/H=0.4 and then water fraction increased to 0.327 at cavity base edge. The results for deep and shallow cavity indicate that a lot of water is observed on base upstream edge than the base downstream edge of cavity.

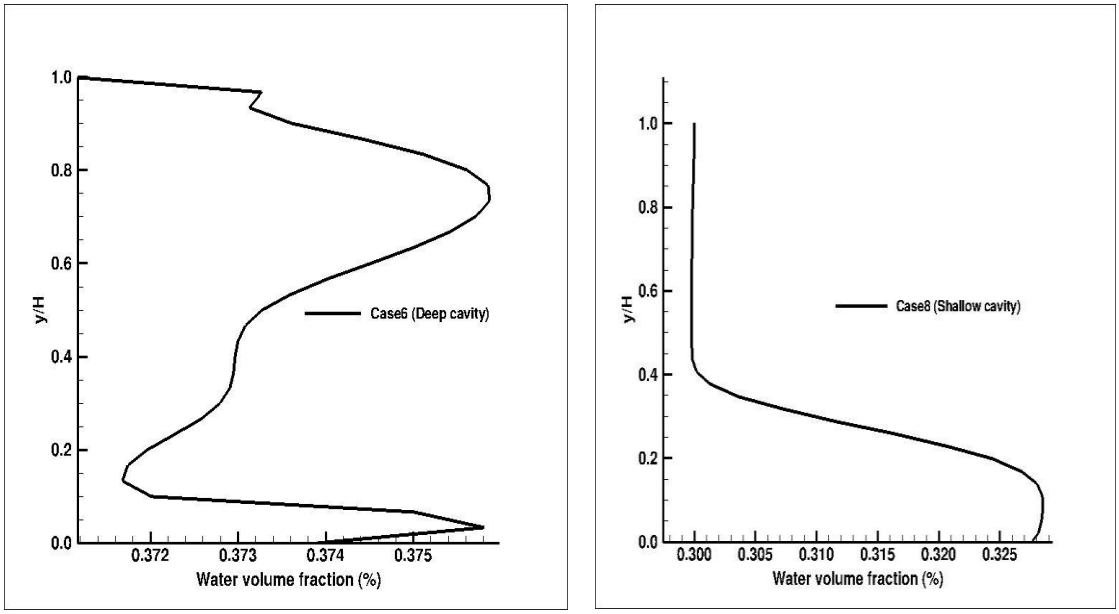

(a) Case 6 deep cavity (b) Case 8 shallow cavity

Figure 4.23: Water volume fraction at 0.75 cavity length (Re=22,000)

Figures 4.24a and 4.24b show the contour of velocity magnitude in the direction of flow in the deep and shallow cavity. The velocity magnitude is measured on along the centre plane (z = 0) for both cases. In Figure 4.24a, the region of high velocity is around the top of the cavity about 20% deep into the cavity. This is because the main vortex in the cavity centre is large and it has a pushing effect on the bulk flow in the pipe. The main vortex in this cavity is large and occupies about 80% of the cavity size compared to figure 4.24b (case 8) where the high velocity region occupies about 50% of the entire cavity. In the shallow cavity case (case 8), the flow impinges the bottom of the cavity wall at about 60% length of the cavity and separates again just before the trailing edge back into the bulk pipe flow. This shows that in the shallow cavity case, the bulk fluid velocity has a significant influence on the velocity profile in the cavity thereby resulting in lower rates of water separation from oil. In figures 4.25a and 4.25b below, the component of velocity in the upward direction is smallest at the bottom section of the cavity.

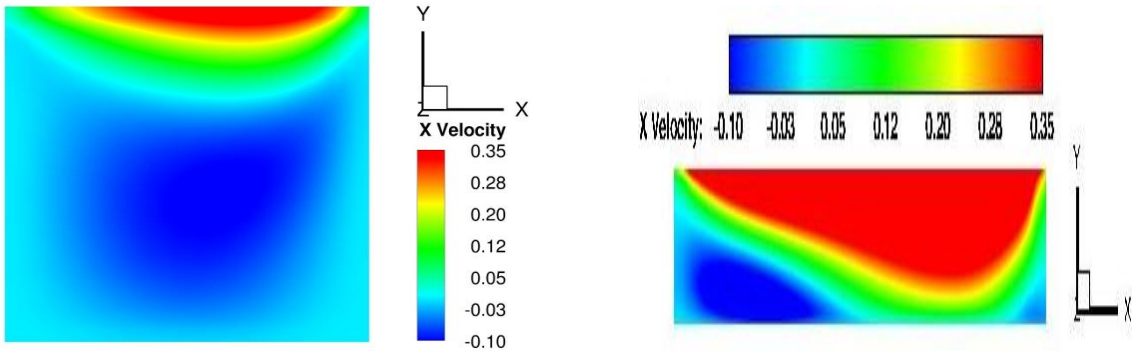

(a) Case6 **(**b) Case8

Figure 4.24: Velocity (x) at plane perpendicular to the flow (z=0, Re=22,000)

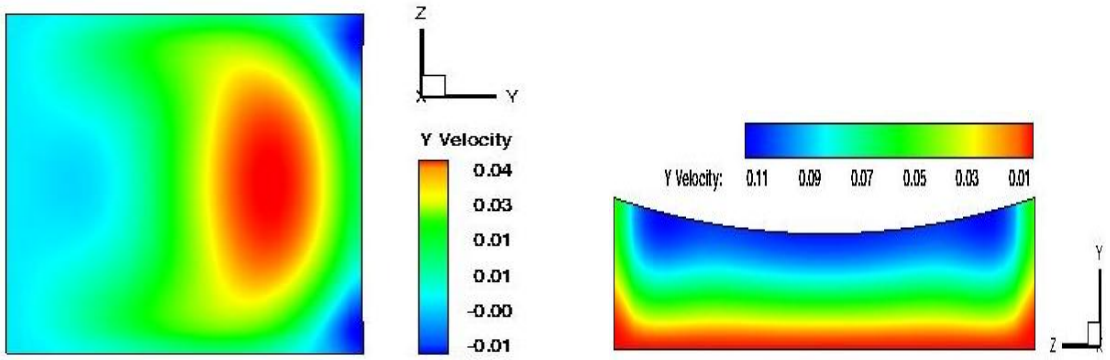

(a) (Case 6) (b) (case 8)

Figure 4.25: Velocity (Y) at plane across the flow (x=2.109, Re=22,000)

Figures 4.26a and 4.27a are the turbulent kinetic energy contour plots for case 6 (deep cavity), which indicate that turbulent kinetic energy is higher about 25% depth of the cavity from the top suggesting that there is no much mixing going on deeper into the cavity. This is not the case for shallow cavity (figures 4.26b and 4.27b) where turbulent kinetic energy is high for about 80% of the cavity suggesting that mixing is high. This mixing effect will not allow water to separate easily from the oil and settle to the cavity wall surfaces. In the deep cavity case (fig 4.26a), turbulent kinetic energy increases as the flow accelerates over the trailing edge of the cavity. Turbulent kinetic energy along plane across the flow at centre of the cavity shows that in the deep cavity case, the bulk fluid has little or no effect on the flow at this position. On the other hand, turbulent kinetic

energy is the same as the bulk fluid for about 90% of the surface for the shallow cavity case. This is because the bulks of the main pipe flow impinge on the bottom of the cavity resulting in turbulent mixing.

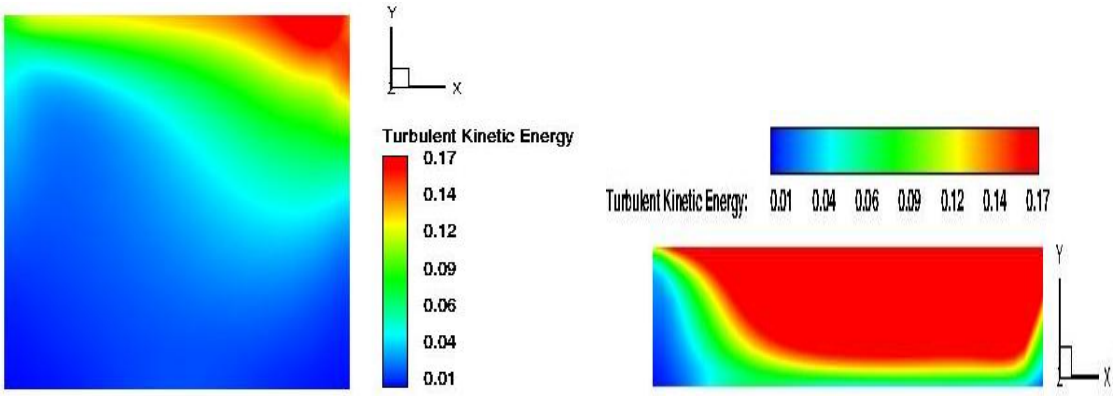

(a) (Case 6) (b) (Case 8)

Figure 4.26: Turbulent kinetic energy at plane perpendicular to flow (z=0, Re=22000)

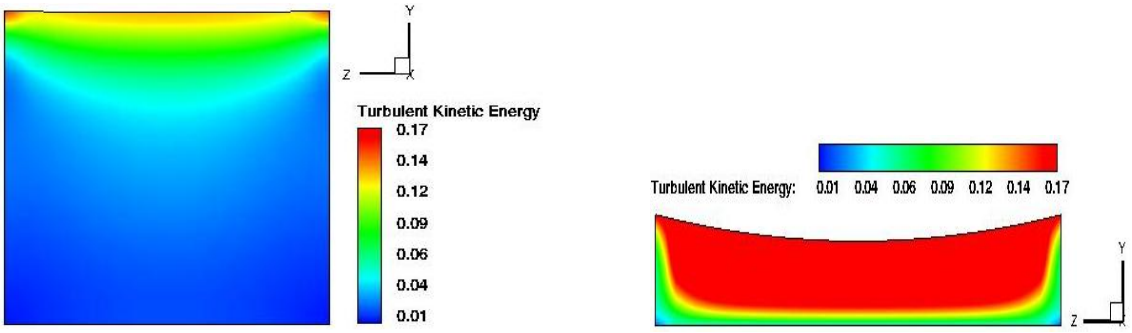

(a) (Case 6) (b) (case 8)

Figure 4.27: Turbulent kinetic energy at plane across the flow (x=2.109, Re=22000)

4.6 Effect of Reynolds number

To fully understand the effect of Reynolds number on the flow, cases with same aspect ratio and same input water volume fraction will be investigated as shown in table 4.10. This analysis will be done using deep cavity (cases 1 and 5) and shallow cavity (cases 3 and 7). A combination of contour plots and line plots will be used for the investigations. Figures 4.28a to 4.28d show contour plots of turbulent kinetic energy on plane perpendicular to flow for cases 1, 5, 3 and 7 respectively. Figures 4.28a (case 1) and 4.28b (case 5) are the deep cavity case. In figure 4.28b with higher Reynolds number the region of high turbulence activity is larger compared to case 1 (lower Reynolds number). This suggests that as the Reynolds number is increased, mixing increases in the cavity which results in lower rates of separation of water from oil in the mixture. Figures 4.29a and 4.29b also reveal that there is more turbulence in the high Reynolds number case compared to the low Reynolds number case. The increased turbulent activity in the high Reynolds number case will reduce the rate of separation of water from oil.

In the shallow cavity cases figure 4.28c and figure 4.28d, the effect of Reynolds number is not very evident. For both cases, the region of high turbulent kinetic energy is approximately the same size and occupying up to 90% of the total volume. A slight difference is observed with planes across the flow for shallow cavity case (figures 4.29c and 4.29d). The region of high turbulent kinetic energy is slightly higher for case 7 (figure 4.29d) than case 3 (figure 4.29c). From figures 4.28a to 4.28d, it is observed that more mixing goes on in the shallow cavity case than in deep cavity case. It is therefore logical to conclude that increasing the Reynolds number increases turbulent mixing which results in lower rates of separation of water. However, as the aspect ratio changes from shallow to deep cavity result to increase in the rate of separation of water from oil.

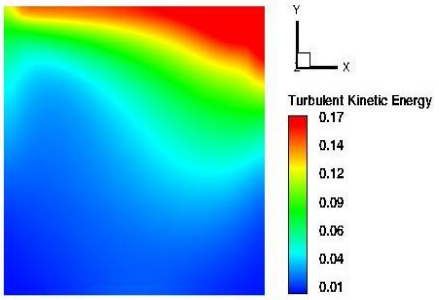

(a) Case 1, Re=18,500

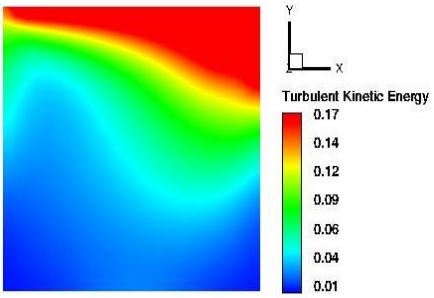

(b) Case 5, Re=22,000

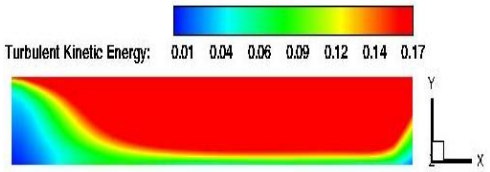

(c) Case 3, Re=18500

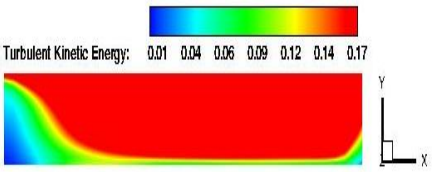

(d) Case 7, Re=22000

Figure 4.28: Turbulent kinetic energy at plane perpendicular to the flow (z=0, water fraction=0.1)

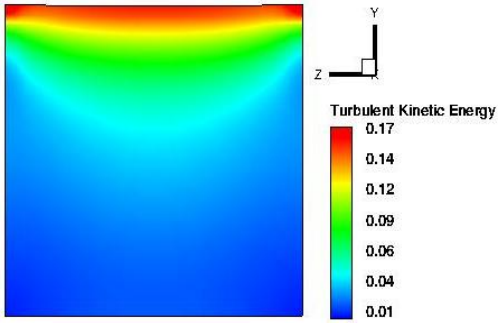

(a) Case 1, Re=18,500

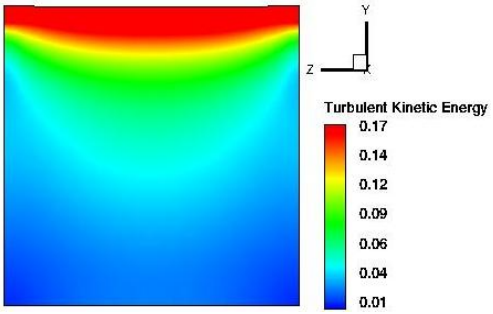

(b) Case 5, Re=22,000

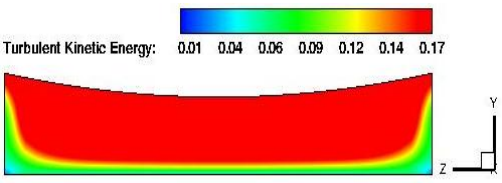

(c) Case 3, Re=18,500

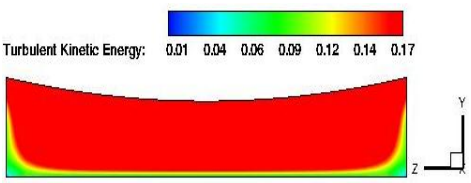

(d) Case 7, Re=22,000

Figure 4.29: Turbulent kinetic energy at plane across the flow (x=2.109, water fraction=0.1)

The contour plots of water volume fraction are shown in figures 4.30 and 4.31 below. In figures 4.30a and 4.30b, the maximum water volume fraction in contact with the pipe wall is about 0.15 for both cases. However, the water wetted area is larger for the low Reynolds number case (figure 4.30a) compared to the higher Reynolds number case (figure 4.30b). Similarly in figures 4.31a and 4.31b, the water wetted surface area is larger for the low Reynolds number case than for the high Reynolds number case. This is as a result of higher turbulence production due to higher Reynolds number. In figures 4.30c and 4.30d, which are shallow cavity cases, the water wetted surface area is smaller than that for the deep cavity cases. Also, there is difference in the maximum water volume fraction in contact with the pipe wall for the shallow cavity cases the water volume fraction in cases in figures 4.31c and 4.31d is lower than the cases in figures 4.30c and 4.30d. The water wetted surface area is larger for the deep cavity case than for the shallow cavity case because region of turbulence and recirculation is larger (relative to the cavity size) for the shallow cavity case.

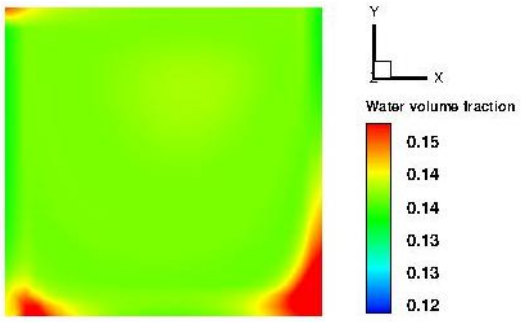

(a) Case 1, Re=18,500

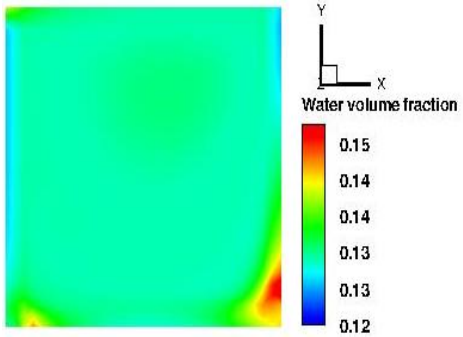

(b) Case 5, Re=22,000

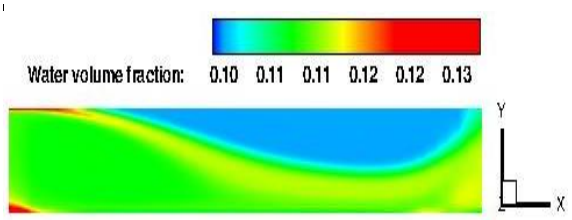

(c) Case 3, Re=18,500

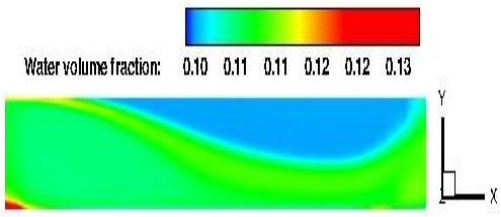

(d) Case 7, Re=22,000

Figure 4.30: Water volume fraction at plane perpendicular to the flow (z=0, water fraction=0.1)

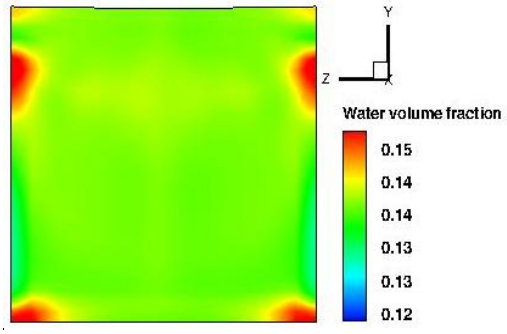

(a) Case 1, Re=18,500

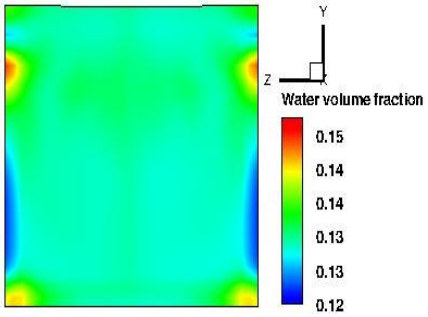

(b) Case 5, Re=22,000

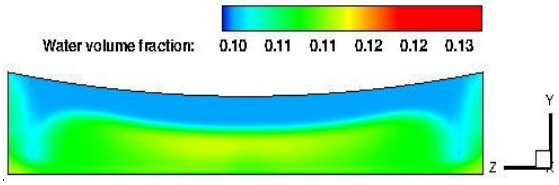

(c) Case 3, Re=18,500

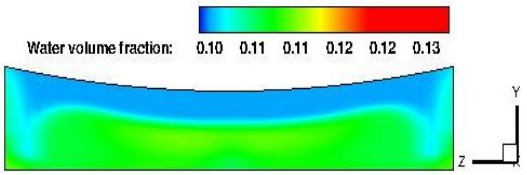

(d) Case 7, Re=22,000

Figure 4.31: Water volume fraction at plane across the flow (x=2.109, water fraction=0.1)

The velocity contour plots shown in figures 4.32a to 4.32d below relate directly to turbulent kinetic energy plots shown above. The effect of Reynolds number on the velocity profiles is not obvious in the deep cavity case. On the other hand, the region of high flow velocity is larger in the shallow cavity case than in the deep cavity case, which results in a smaller water wetted surface area in the shallow cavity compared to the deep cavity.

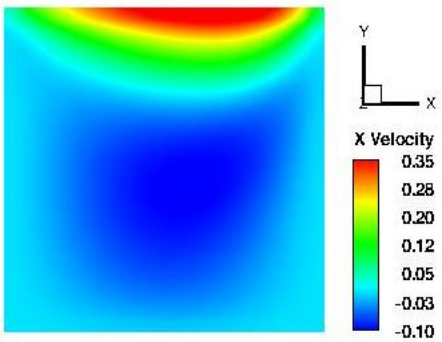

(a) Case 1, Re=18,500

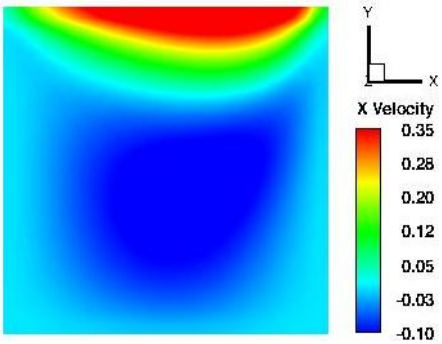

(b) Case 5, Re=22,000

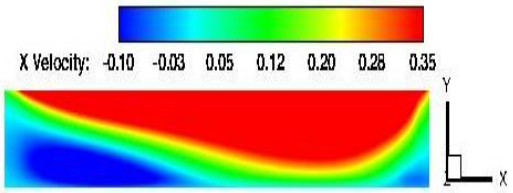

(c) Case 3, Re=18,500

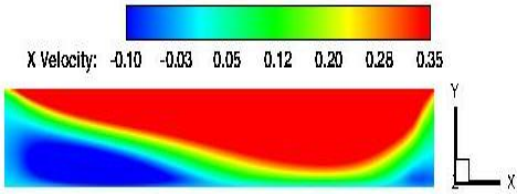

(d) Case 7, Re=22,000

Figure 4.32: Velocity (X) at plane perpendicular to the flow (z=0, water fraction=0.1)

Figures 4.33 a to 4.33 d shows stream traces along plane perpendicular to flow for cases 1, 5, 3 and 7 respectively. The effect of increase in Reynolds number is not evident between figure 4.33a (Case 1) and 4.33b (case 5). In both cases, the stream traces follow approximately the same path; however, the area of recirculation and the strength of the recirculation differ slightly for the two cases. In figure 4.33a, the recirculation zone at the bottom of the cavity is as strong as that for figure 4.33b because the stream trace easily moves up as it approaches the edges. In figure 4.33b, the recirculation is strong and the flow does not separate quickly from the wall vertical edges of the cavity. This reduces the effective area of recirculation where water could easily separate from oil. As a result less separation occurs in the high Reynolds number case compared to the low Reynolds number case. In figures 4.33c and 4.33d below and the effect of Reynolds number on the stream traces is not evident. There is area of the recirculation zone which changes slightly as the Reynolds number is increased, while secondary vortices are formed at the cavity base. It is therefore proper to conclude that the effect of change in Reynolds number is more evident for deep cavity cases than shallow cavity cases.

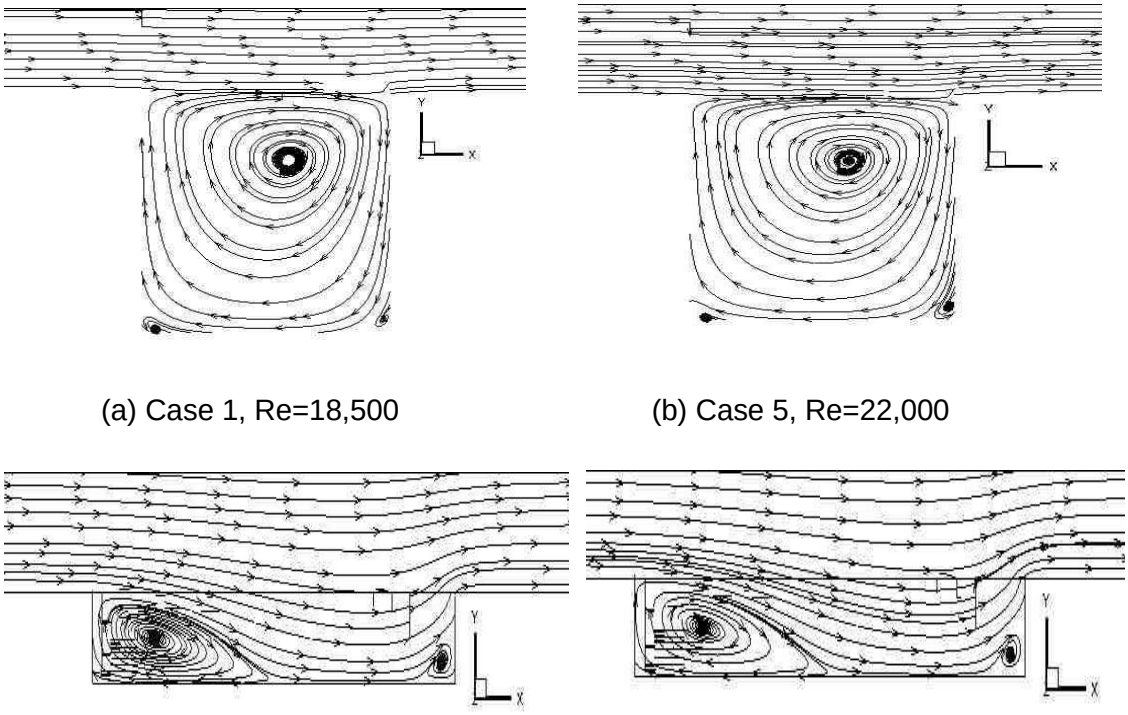

(a) Case 1, Re=18,500 (b) Case 5, Re=22,000

(c) Case 3, Re=18,500 (d) Case 7, Re=22,000

Figure 4.33: Stream traces at plane perpendicular to the flow (z=0, water fraction=0.1)

The analysis is also performed inside the cavity in stream wise direction to study the effect of Reynolds number on the cavity flow field, we shall considered how the Reynolds number affects the water volume fraction distribution, velocity and turbulent kinetic energy at cavity lengths of 0.25 and 0.75, because these are the regions of interest where secondary vortices are formed at the cavity corner edges and are in the leading and trailing edges position of the cavity. The effect of Reynolds number is observed on the line plot of water volume fraction at 0.25 cavity length as shown in figure 4.34 below. The dotted line represents case 5 (Re = 22,000), while the solid line represents case 1 (Re = 18,500). It is observed that the water volume fraction increased from 0.1 to 0.132 at the bottom for the high Reynolds number case and from 0.1 to 0.141 for the low Reynolds number case. In figure 4.35, the effect of Reynolds number on the rate of water separation at 0.75 cavity length for the deep cavity case is observed that more water settles to the bottom of the cavity for the low

Reynolds number case. This is because turbulence mixing in the cavity increases with Reynolds number.

In figure 4.36, the effect of Reynolds number is compared for the shallow cavity case at position 0.25 length of the cavity. The high water volume fraction observed at y/H = 0.8 is due to the water already settled to the bottom of the pipe before the cavity that is swept in to the cavity. At the bottom of the cavity, the water volume fraction is more for the low Reynolds number case, because turbulent mixing is less thereby allowing water to separate from oil under the action of gravity. Similarly, at position 0.75 length of the cavity shown in figure 4.37, more water settles to the bottom of the cavity for the low Reynolds number case. The values show that the high Reynolds number leads to more recirculation and turbulence thereby hindering the separation of water from oil within the cavity. Although in this case, the difference in the amount of water settling to the bottom is not much because the difference in Reynolds number in each case is small. However, as the difference in Reynolds number increases, the amount of water at the bottom of the cavity increases.

On the other hand, the differences in Reynolds number have significant effects around 0.75 the length of the cavity as shown in figures 4.35 and 4.37. In figure 4.35 for deep cavity at 0.75 cavity length, for high Reynolds number case water volume fraction increased from 0.1 to 0.32 and for low Reynolds number case water volume fraction increased from 0.1 to 0.40, similarly, in figure 4.37 for shallow cavity at 0.75 cavity length, the water volume fraction increased from 0.1 to 0.109 for high Reynolds number case and increased from 0.1 to 0.112 for low Reynolds number case. The results show that reduction in Reynolds number lead to more water settle at the bottom of cavity.

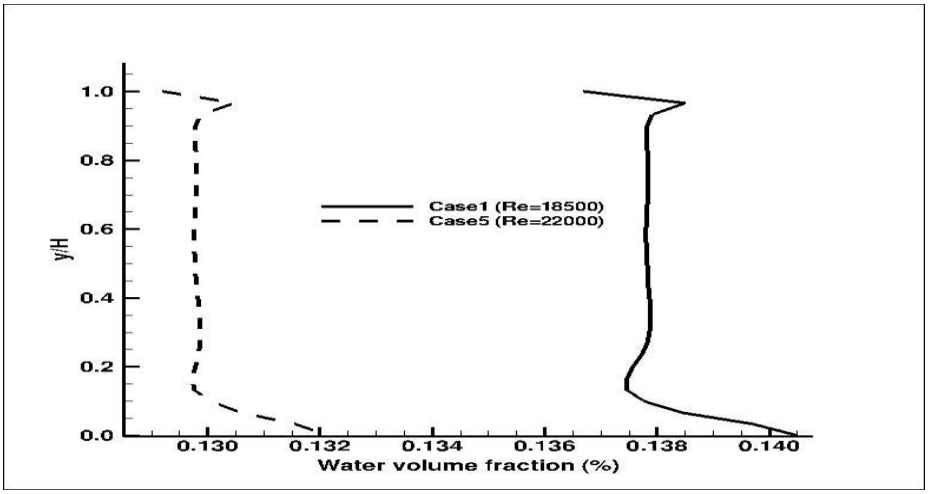

Figure 4.34: Water volume fraction at 0.25 cavity length for case 1 and 5

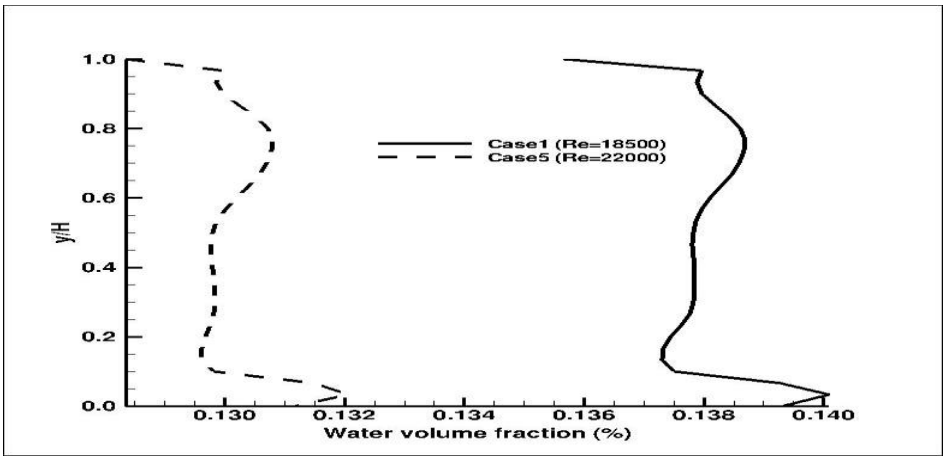

Figure 4.35: Water volume fraction at 0.75 cavity length for case 1 and 5

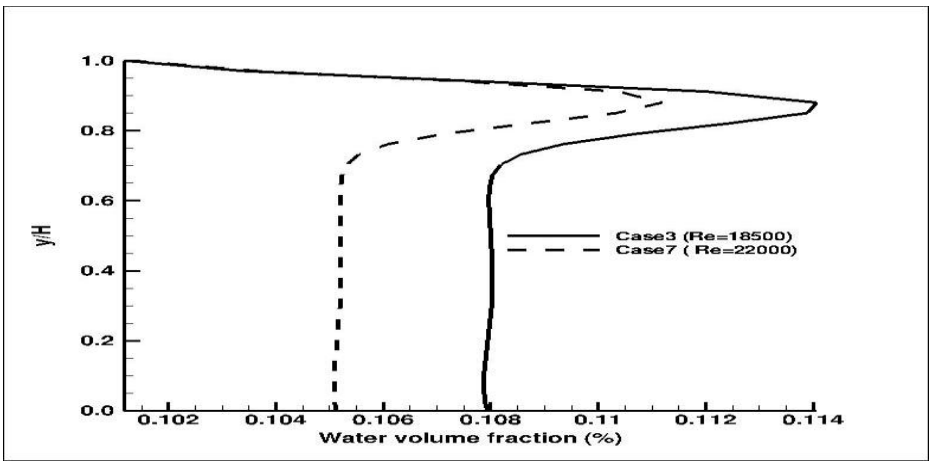

Figure 4.36: **Water volume fraction at 0.25 cavity length for case 3 and 7**

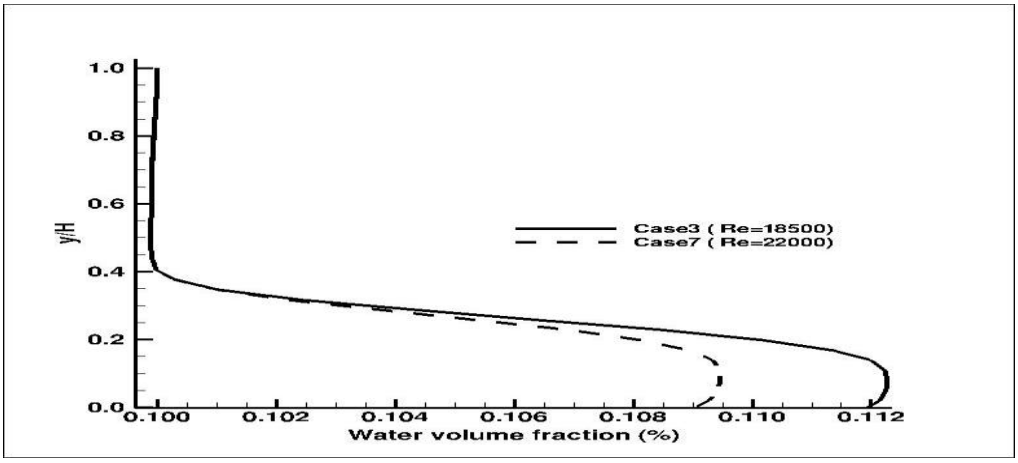

Figure 4.37: Water volume fraction at 0.75 cavity length for case 3 and 7

Figures 4.38 to 4.39 show the velocity profiles at different positions in the cavity. In figure 4.38a, the velocity profiles for the deep cavities case are shown at 0.25 lengths of the cavities. It is observed that the high Reynolds number case has higher velocity at all points along the line than the low Reynolds number case. The difference in velocity profile for each Reynolds number is not very large. The profiles also suggest that more turbulent mixing takes place towards the top of the cavity than at the bottom. In figure 4.38b (shallow cavities cases), there is not much difference in the velocity profiles for the two Reynolds numbers. The plots also suggest that more turbulent mixing takes place at the top section of the cavity than at the bottom. A quick comparison of the deep and shallow cavity cases (figures 4.38a and 4.38b) shows that more turbulent mixing occurs in the top section of the shallow cavity case as the velocity at the top is higher compared to the deep cavity case. The plots of velocity profile in the deep cavities at 0.75 cavity lengths are shown in figure 4.39a is very similar to that at position 0.25. More turbulent mixing takes place at the top section of the cavity compared to the bottom and a slight difference in velocity profile is also observed. In the shallow cavity case, the velocity magnitude increases from bottom to top of the cavity and more turbulent mixing occurs at the top section of the cavities.

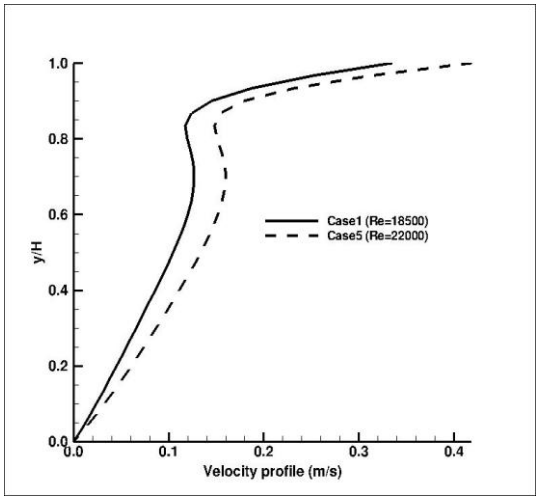

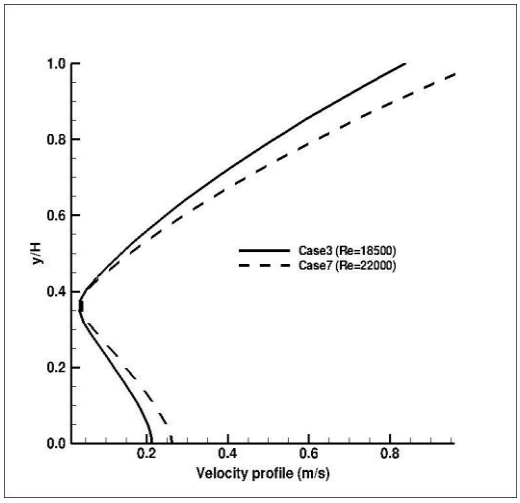

(a) Case 1 and case 5 (b) case 3 and case 7

Figure 4.38: Velocity profile at 0.25 cavity length

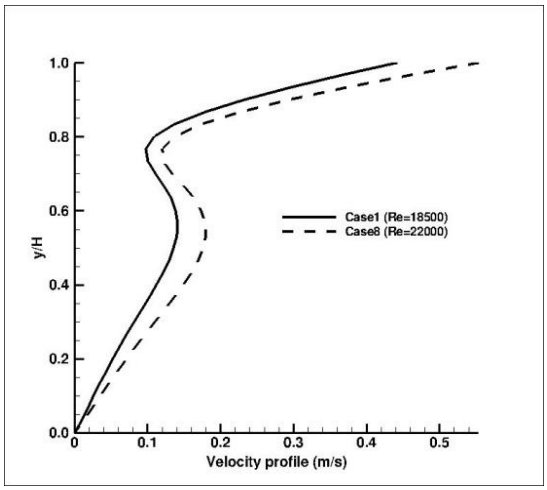

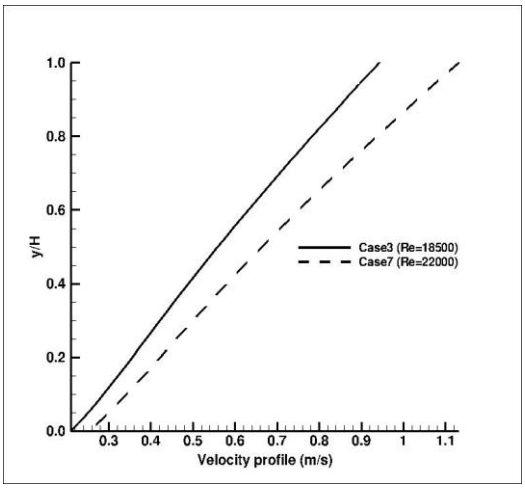

(a) Case 1 and case 5 (b) Case 3 and case 7

Figure 4.39: Velocity profile at 0.75 cavity length

From figures 4.40 and 4.41, turbulent kinetic energy is observed to increase from bottom to top for both shallow and deep cavity cases. In the deep cavity cases (figures 4.40a and 4.41a), the turbulent kinetic energy is observed to increase rapidly towards the top of the cavity because the bulk flow only has an effect on the cavity flow towards the top of the cavity. In the shallow cavity cases (figures 4.40b and 4.41b), the velocity profiles increased almost linearly from bottom to top of the cavity. The effect of Reynolds number on turbulent kinetic energy is more evident in the deep cavity case than in the shallow cavity

case. The high Reynolds number cases (case 5 and case 7) have maximum turbulent kinetic energy along the line and at top of cavity compared with low Reynolds number cases (case 1 and case 3).

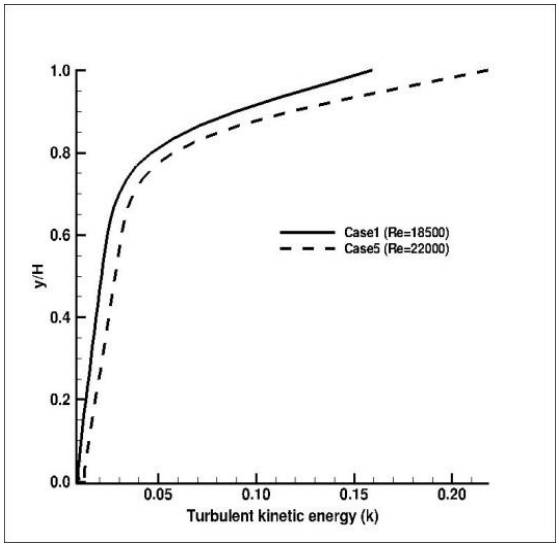

(a) Case 1 and case 5

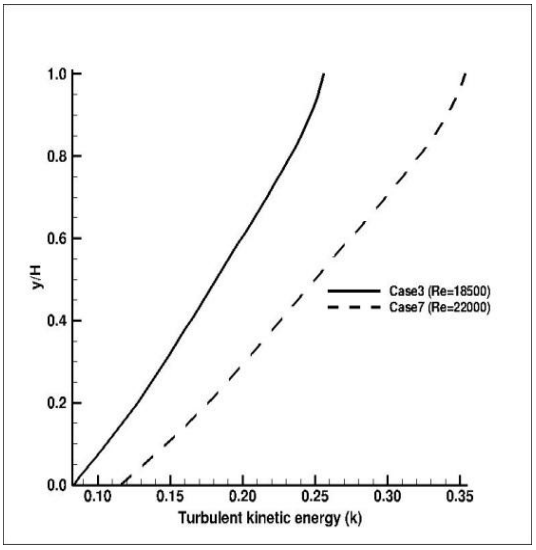

(b) Case 3 and case 7

Figure 4.40: Turbulent kinetic energy at 0.25 cavity length

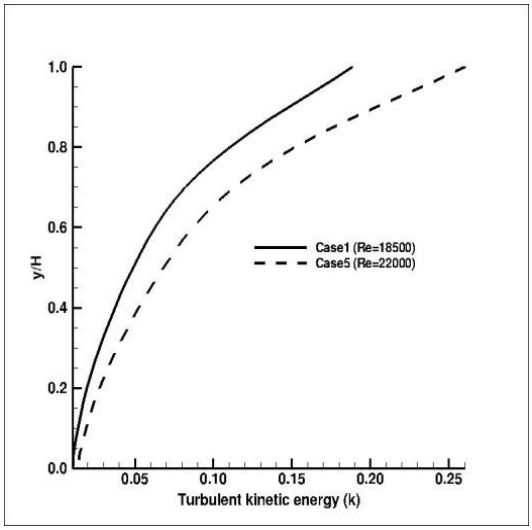

(a) Case 1 and case 5

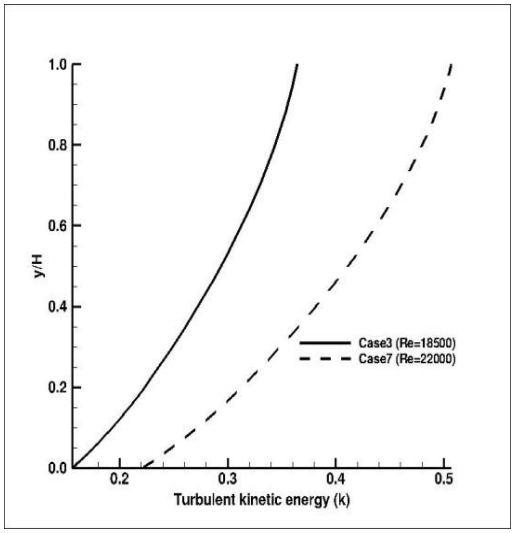

(b) Case 3 and case 7

Figure 4.41: Turbulent kinetic energy at 0.75 cavity length

4.7 Effect of input water volume fraction

To investigate the effect of input water volume fraction, two cases each of deep and shallow cavity will be compare. The analysis will be done using deep cavity (case 1 and 2) and shallow cavity (case 7 and 8) given in table 4.10. A combination of line plots and contour plots will be used for the investigations. Figures 4.42a to 4.42d below shows contour plots of turbulent kinetic energy on plane perpendicular to flow for cases 1, 2, 7 and 8 respectively. In the deep cavity (case 1 and 2), the higher the water volume fraction, the lower the turbulence production as shown in figures 4.42a and 4.42b. This is because water is heavier than oil and also has a higher inertia than oil. As a result, the mixture density of the bulk fluid is higher for the high water volume fraction case. The turbulent kinetic energy is higher for low water volume fraction case because the amount of energy required to accelerate the oil component of the multiphase fluid is lower. This is why the case with more oil results in more turbulence production compared to the case with more water. In addition, figures 4.43a and 4.43b below also reveal that less turbulence is produced when the water volume fraction is increased. Shallow cavity at plane perpendicular and across the flow (figures 4.42c, 4.42d, 4.43c and 4.43d) does not show any significant difference in turbulence production. However, in figures 4.42c and 4.42d, the area of high turbulence is slightly higher for the low water volume fraction case compared to the high Reynolds number case. This flow behaviour has an effect on the rate at which water settles to the bottom of the cavity, because less turbulence favours separation.

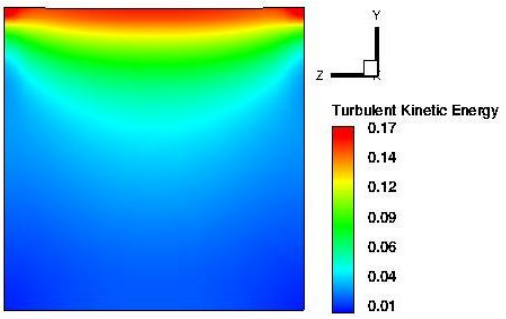

(a) Case 1, Water fraction=0.1

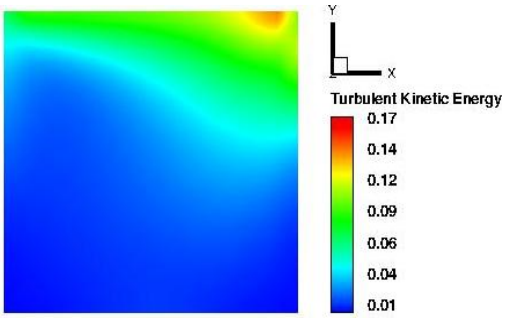

(b) Case 2, Water fraction=0.3

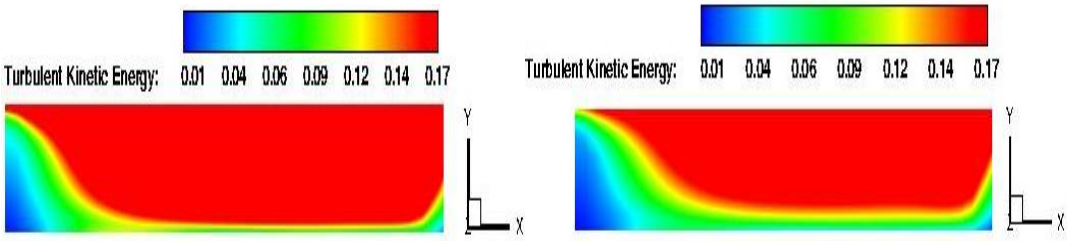

(c) Case 7, Water fraction=0.1 (d) Case 8, Water fraction=0.3

Figure 4.42: Turbulent kinetic energy at plane perpendicular to the flow (z=0)

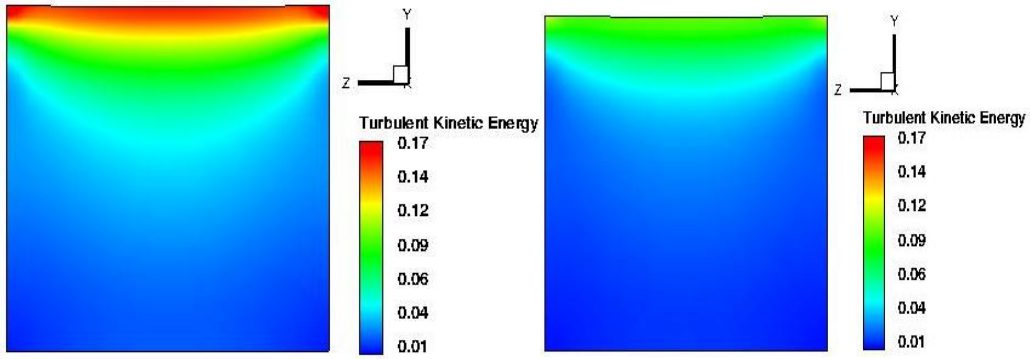

(a) Case 1, Water fraction=0.1 (b) Case 2, Water fraction=0.3

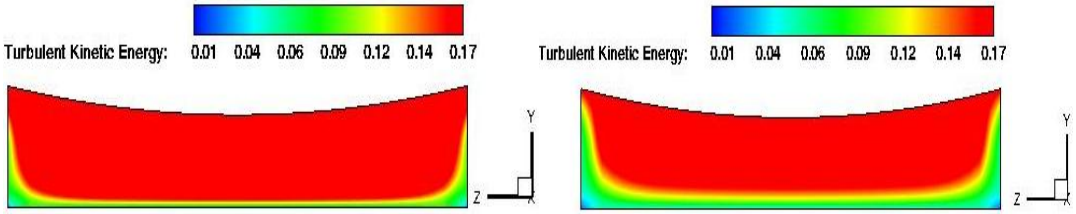

(c) Case 7, Water fraction=0.1 (d) Case 8, Water fraction=0.3

Figure 4.43: Turbulent kinetic energy at plane across the flow (x=2.109)

In figure 4.44a (deep cavity), the maximum water volume fraction in contact with the cavity wall increased from 0.1 to 0.15, resulting in an increase of 0.05. In figure 4.44b (deep cavity), the water volume fraction increased from 0.3 to 0.42, representing an increase of 0.12 compared to 0.05 in the low water volume fraction case. Similarly, in figure 4.44c (shallow cavity), water volume fraction in

contact with cavity wall increased from 0.1 to 0.13, representing an increase of 0.03. In figure 4.44d (shallow cavity), water volume fraction increased from 0.3 to 0.36, representing an increase of 0.06. From this analysis, it can be observed that as water volume fraction is increased with decrease in Reynolds number, the higher the rate of separation of water from oil. Also, by comparing the increase in water volume fraction for deep and shallow cavity cases, it can also be observed that the rate of water separation also increases as the aspect ratio is reduced.

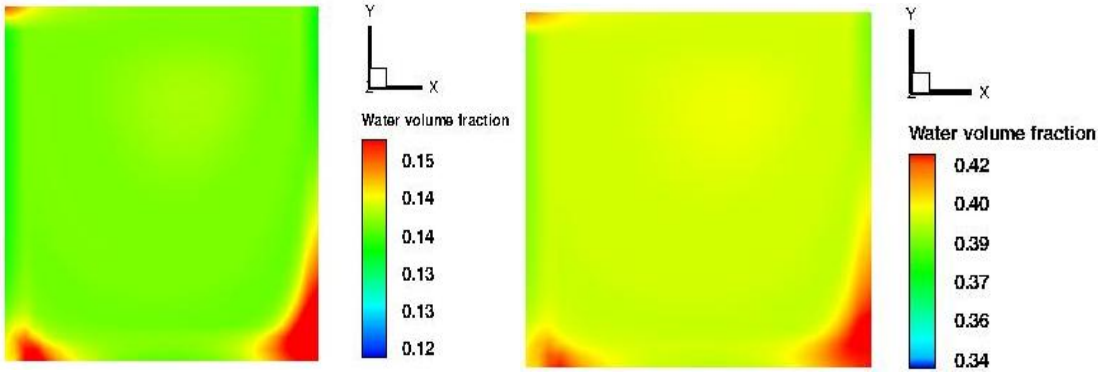

(a) Case 1, Water fraction=0.1 (b) Case 2, Water fraction=0.3

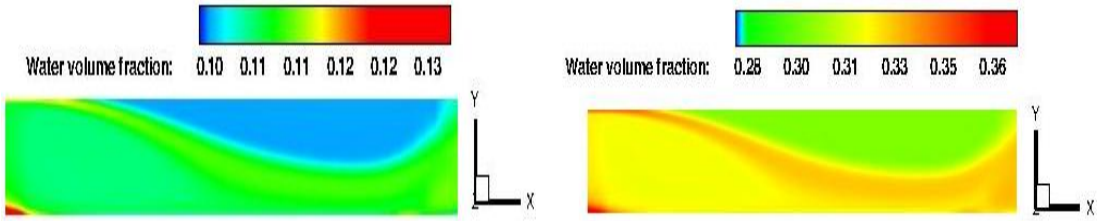

(c) Case 7, Water fraction=0.1) (d) Case 8, Water fraction=0.3

Figure 4.44: Water volume fraction at plane perpendicular to the flow (z=0)

The investigation is also performed inside the cavity in stream wise direction to study the effect of water volume fraction in the cavity domain, looking at how water volume fraction affects the water separation, velocity and turbulent kinetic energy at 0.25 and 0.75 cavity lengths. The effect of water volume fraction on the rate of water separation from oil can be observed in figures 4.45 to 4.48 below. In the line plot of 0.25 cavity length shown in figure 4.45, the rate of water separating and settling at the bottom of the cavity increases as the water

volume fraction increases. In figure 4.45 (0.1 input volume fraction) water volume fraction increased from 0.1 to 0.1405 at the bottom of the cavity representing an increase of 0.0405. In figure 4.45 for case 2 (0.3 input volume fraction) water volume fraction increased from 0.3 to 0.402 at the bottom of the cavity representing an increase of 0.102. From this analysis, the amount of water that separates increases as the water volume fraction increases. Also in figures 4.46 (line plot of 0.25 cavity length for cases 7 and 8), it is observed that the amount of water that separates from the bulk fluid increases as the water volume fraction is increased. In figure 4.46 for case 7, the water volume fraction increased from 0.1 to 0.105 representing an increase of 0.005, while it increased from 0.3 to 0.318 for case 8 representing an increase of 0.018. This also shows that more water separates from the bulk fluid and settles to the bottom of the cavity as the water volume fraction is increased.

A similar pattern is observed in the line plots of 0.75 cavity length. In figure 4.47, the water volume fraction at the bottom of the cavity increased from 0.1 to about 0.14 and from 0.3 to about 0.401, representing an increase of 0.04 and 0.104 respectively. Also in figure 4.48, the water volume fraction at the bottom of the cavity increased from 0.1 to about 0.109 and from 0.3 to about 0.328, representing an increase of 0.009 and 0.028 respectively. This also shows that the amount of water that separates from the bulk fluid and settles to the bottom of the cavity increases as the input water volume fraction increases.

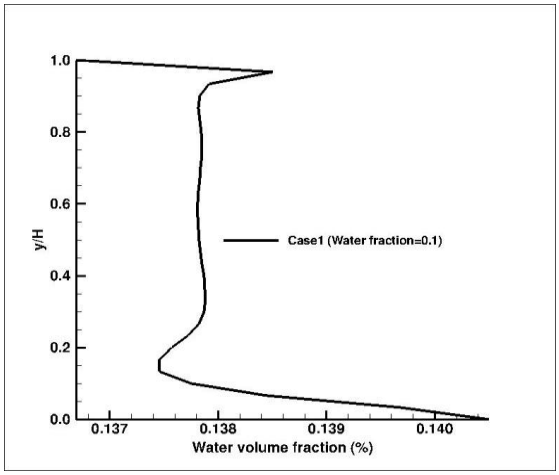

(a) Case 1, Water fraction=0.1

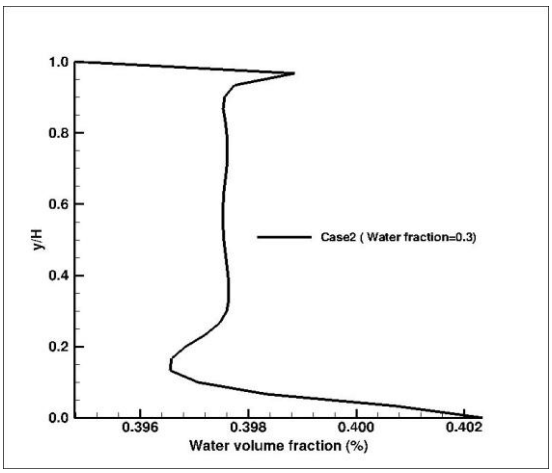

(b) Case 2, Water fraction=0.3

Figure 4.45: Water volume fraction at 0.25 cavity length (Re=18,500)

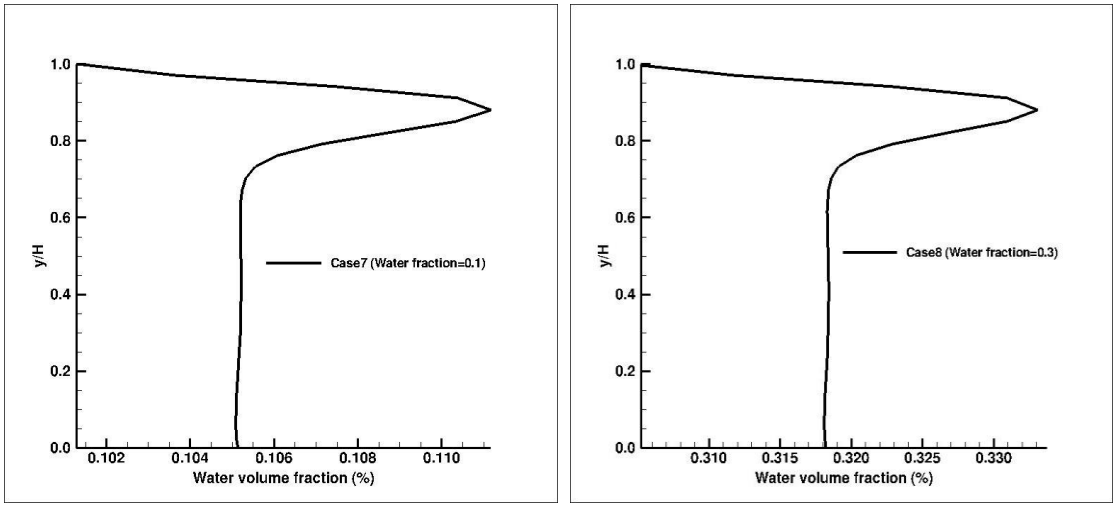

(a) Case 7, Water fraction=0.1 (b) Case 8, Water fraction=0.3

Figure 4.46: Water volume fraction at 0.25 cavity length (Re=22,000)

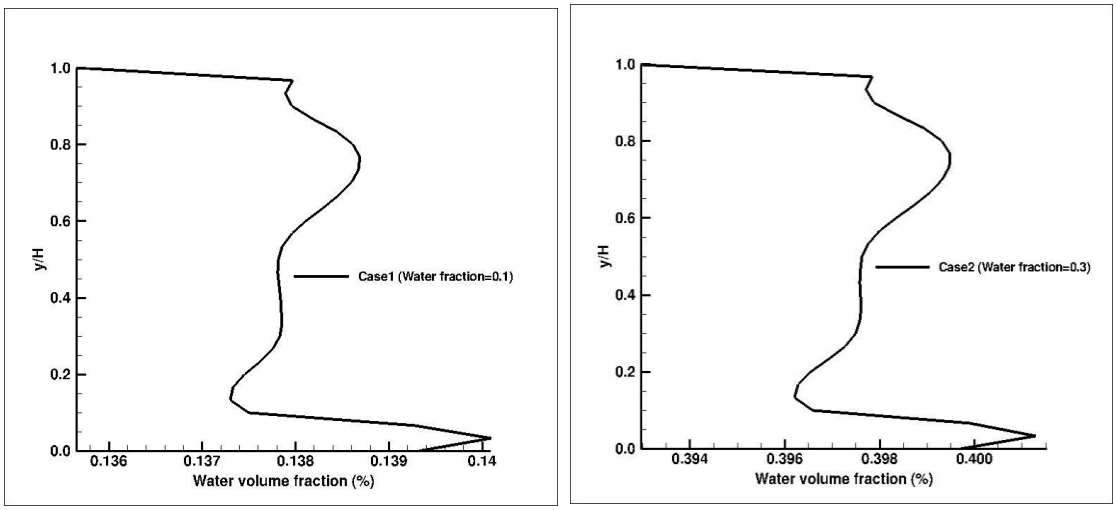

(a) Case 1, Water fraction=0.1 (b) Case 2, Water fraction=0.3

Figure 4.47: Water volume fraction at 0.75 cavity length (Re=18,500)

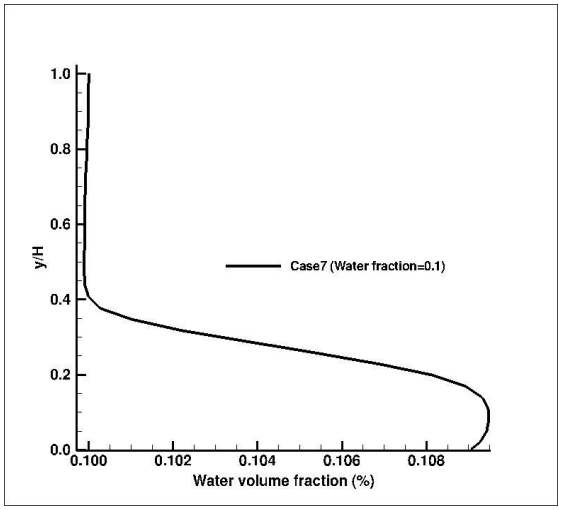

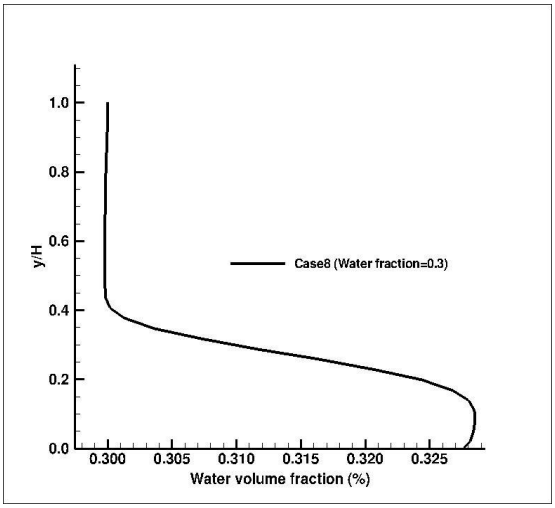

(a) Case 7, Water fraction=0.1 (b) Case 8, Water fraction=0.3

Figure 4.48: Water volume fraction at 0.75 cavity length (Re=22,000)

Figures 4.49 to 4.50 show the velocity profiles at 0.25 and 0.75 cavity lengths from top to bottom of the cavity. In figure 4.49, the velocity profile for the deep cavities case are shown at 0.25 the length of the cavities. It is observed that the flow entered the deep cavity and developed at 90% of the cavity depth, the velocity decrease downward as the mixture move from top to bottom of the cavity and the profile suggest that the case with 0.3 water volume fraction has higher velocity at all points along the line than the 0.1 water volume fraction case. The difference in velocity profile for each corresponding cases is not very large due to the difference between the two water volume fraction (0.1 and 0.3). The profiles also suggest that more turbulent mixing takes place towards the top of the cavity than at the bottom. In figure 4.49b (shallow cavities cases), there is no large difference in the velocity profile for each of the two water volume fraction of 0.1 and 0.3. A quick comparison of the deep and shallow cavity cases (figures 4.49a and 4.49b) shows that more turbulent mixing occurs in the top section of the shallow cavity case as the velocity at the top is higher compared to the deep cavity case. The plots of velocity profile in the deep cavities at position 0.75 are shown in figure 4.50a is almost similar to that at position 0.25. More turbulent mixing takes place at the top section of the cavity compared to the bottom and a slight difference in velocity profile is also observed. In the shallow cavity case, the velocity magnitude increases from

bottom to top of the cavity and more turbulent mixing occurs at the top section of the cavities. While in figure 4.50b at 0.75 cavity length of shallow cavity, the velocity magnitude is linear due to the effect of downstream movement of the two mixtures. The difference between the two velocities is relatively large because of the difference in water volume fraction.

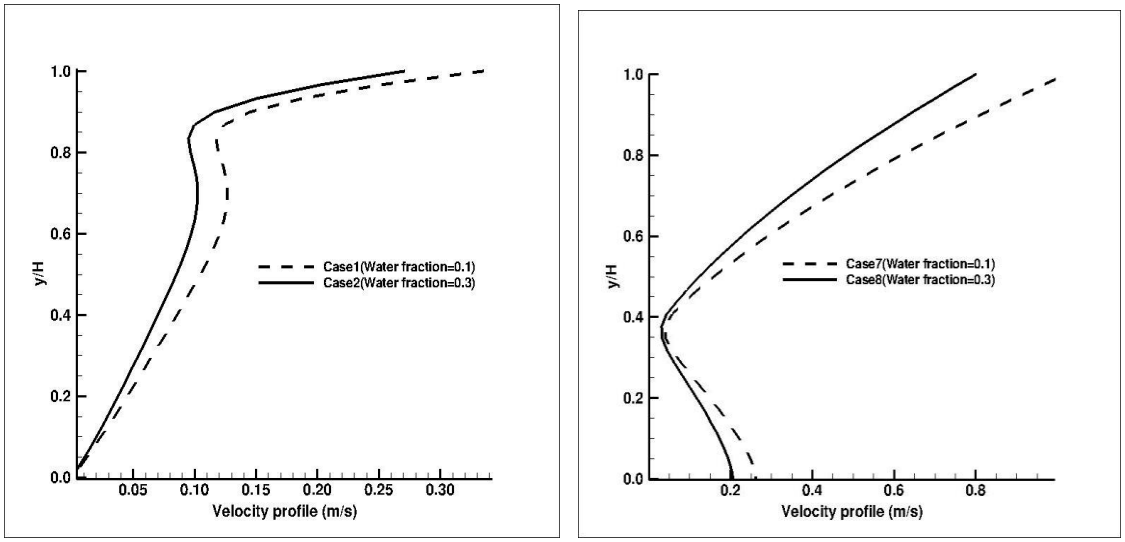

(a) Case 1& 2, Re=18,500 (b) Case 7& 8, Re=22,000

Figure 4.49: Velocity profile at 0.25 cavity length

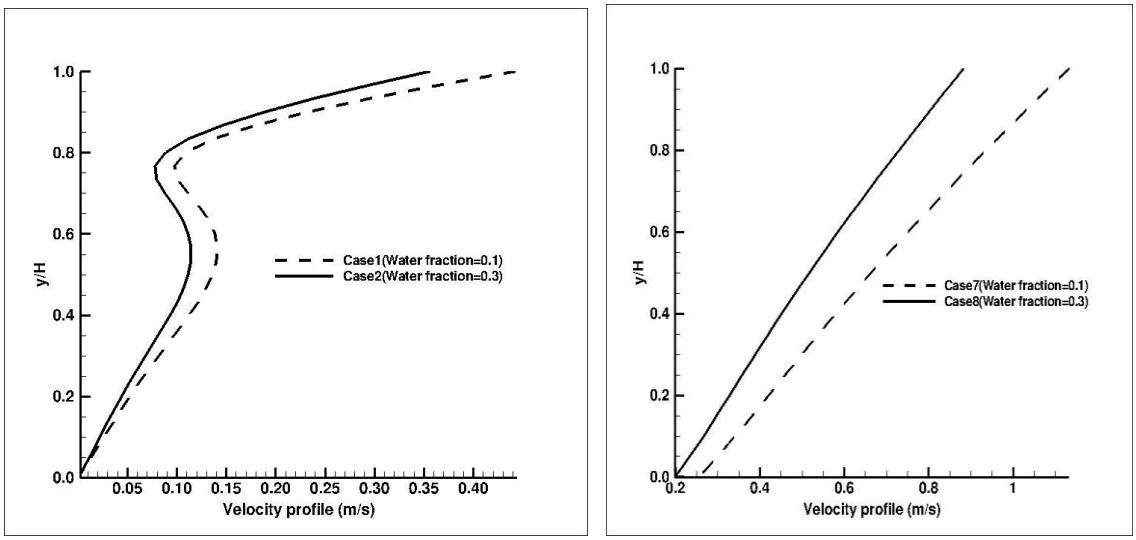

(a) Case 1 &2, Re=18,500 (b) Case 7& 8, Re=22,000

Figure 4.50: Velocity profile at 0.75 cavity length

In figures 4.51 and 4.52 show turbulent kinetic energy at 0.25 and 0.75 cavity lengths respectively. Figure 4.51 is the line plots of turbulent kinetic energy of deep and shallow cavity at 0.25 cavity length. It is observed that the turbulent kinetic energy increase from bottom to top for both shallow and deep cavity cases and the difference between the turbulent kinetic energy is relatively large because of the difference in water volume fraction. However, the case with lower water volume fraction has higher turbulent kinetic energy than the case with higher water volume fraction. In the deep cavity cases (figures 4.51a and 4.52a), the turbulent kinetic is observed to increase rapidly towards the top of the cavity because the bulk flow only has an effect on the cavity flow towards the top of the cavity. In the shallow cavity cases (figures 4.51b and 4.52b) at 0.25 and 0.75 cavity lengths, the turbulent kinetic energy increased almost linearly from bottom to top of the cavity. The effect of water volume fraction on turbulent kinetic energy is more evident in the deep cavity case than in the shallow cavity case.

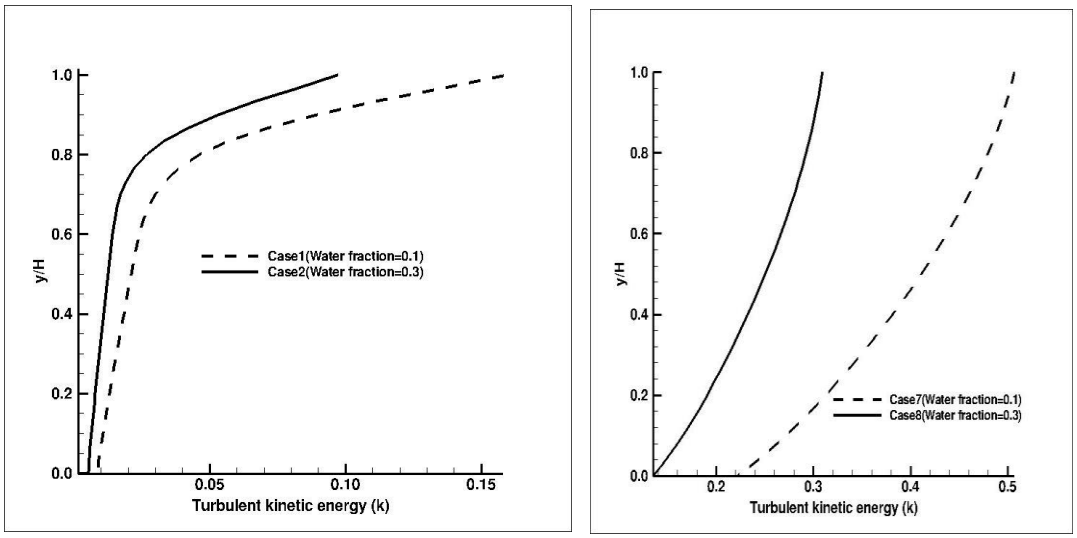

(a) Case 1& 2, Re=18,500 (b) Case 7& 8, Re=22,000

Figure 4.51: Turbulent kinetic energy at 0.25 cavity length

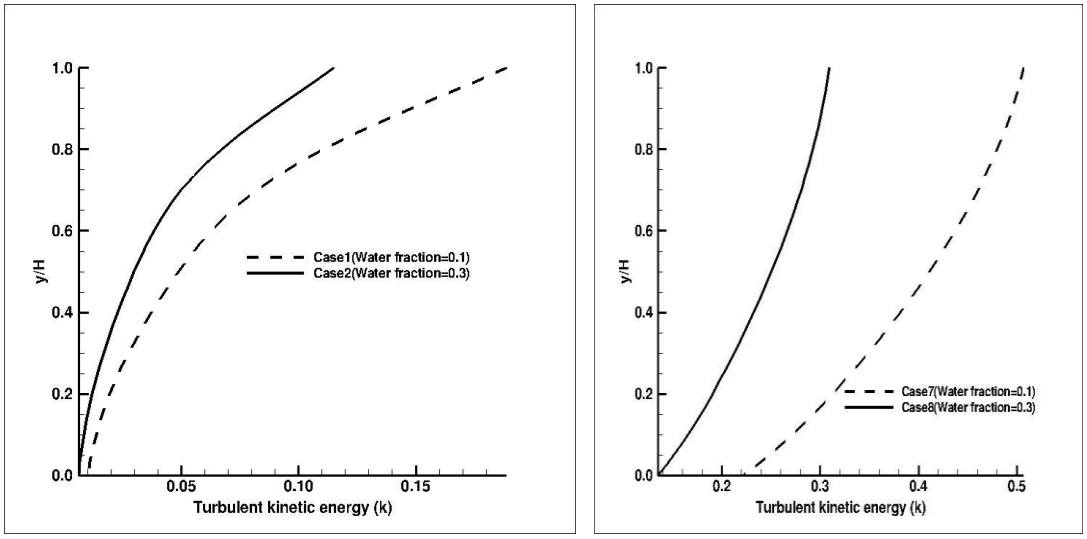

(a) Case 1& 2, Re=18,500 (b) Case 7& 8, Re=22,000

Figure 4.52: Turbulent kinetic energy at 0.75 cavity length

The figures 4.53 to figure 4.56 below show the contour plots of water volume fraction distribution at pipe and cavity walls for eight (8) simulated cases showing the position of maximum water volume fraction and the recirculation regions. The contour plots are compared base on the input water volume fraction and the cavity aspect ratio (deep or shallow cavity) whiles the flow and geometric conditions are all indicated in each figure. Figure 4.53a and 4.53b show comparison between the plots of water volume fraction of deep cavity of case 1 and case 5 of the same input water volume fraction of 0.1. It can be seen that more water is seen at leading edge of the cavity of case 1 (Re=18,500) than case 5 (Re=22,000) this is attributed to influence of gravity and the reduction of velocity at the bottom of the pipe, the more water bubbles are observed at the centre of cavity of case 1 compare with case 5 because of inflow from the shear layer and cavity leading edge. High maximum water fraction concentrates on the downstream and upstream portion corners of the cavity of case 1 (Re=18,500) compared with case 5 (Re=22,000) because of high velocity in case 5 that influences water entrainment in the moving oil. Figures 4.53c and 4.53d show the contour of water volume fraction across the flow for the two cases. For case1 (Re=18,500) more water can be seen at corner edge and top of the downstream and upstream edge of cavity than case

5 (Re=18500). This is ascribed to the difference in Reynolds number which result to differences in recirculation and separation at the cavity region. Furthermore, water bubble can be seen in the case of low Reynolds number than the case of high Reynolds number.

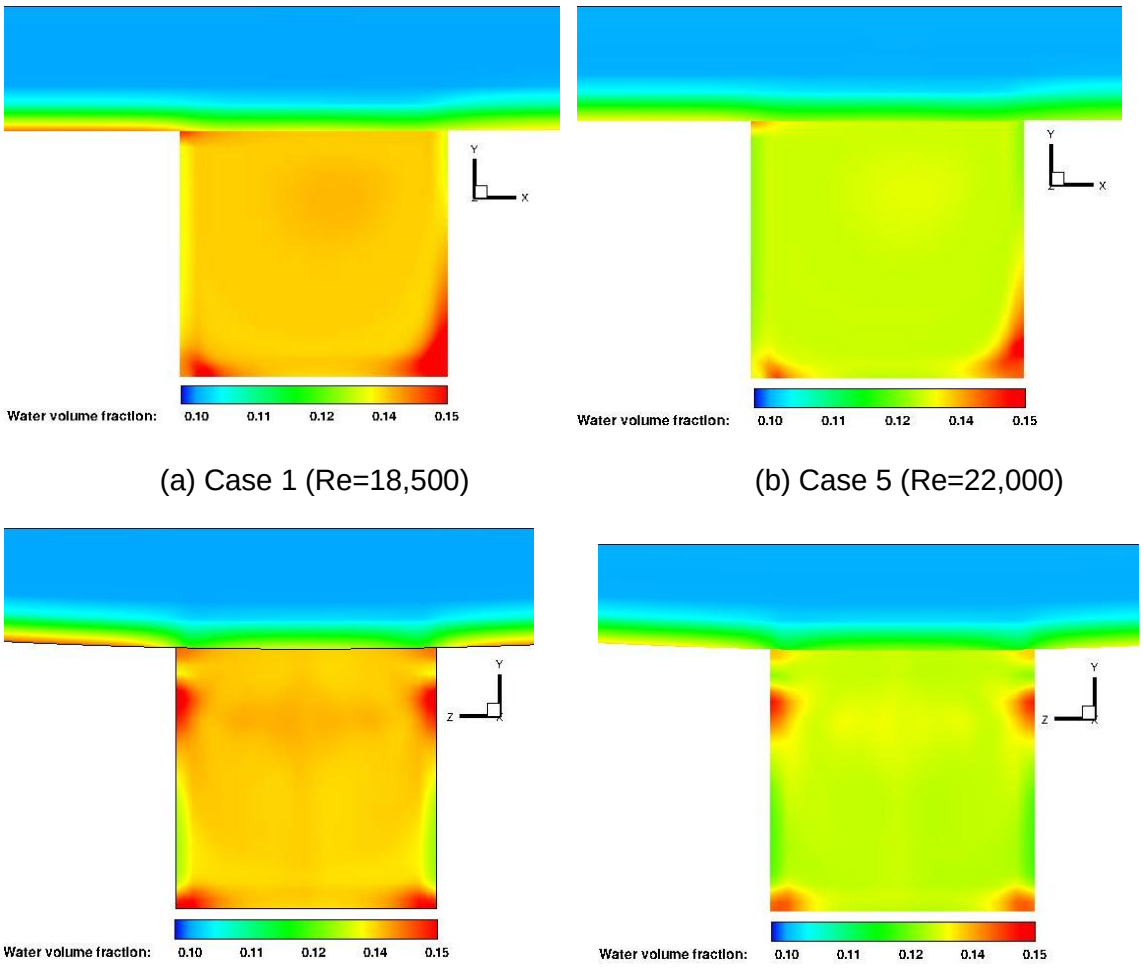

(a) Case 1 (Re=18,500)

(b) Case 5 (Re=22,000)

(c) Case 1 (Re=18,500)

(d) Case 5 (Re=22,000)

Figure 4.53: Water volume fraction at planes perpendicular and across the flow for case 1 and 5 (water fraction=0.1, deep cavity)

Figure 4.54 shows the comparison of water volume fraction distribution of deep cavity of case2 (Re=18,500) and case 6 (22,000) at high input water volume fraction of 0.3. it is observed from plane perpendicular to flow in figure 4.54a and 4.54b that maximum water fraction is concentrated more at two corners of

the cavity of case 2 compared to case 6 due to the difference in Reynolds number; more water separate from mixture and settles to the bottom of cavity for low Reynolds case. In both the two cases water bubble can be seen at the bottom of the pipe and at the shear layer. However, for the plane across the flow in figures 4.54c and 4.54d, water can be seen at leading and trailing edges and at downstream and upstream corners of the two cavities. The propensity of water settlement is more evident in cavity of low Reynolds number of case 2 (Re=18,500) than high Reynolds number of Case 6 (Re=22,000), because water separates faster from the pipe and enters the cavity for low Reynolds number case.

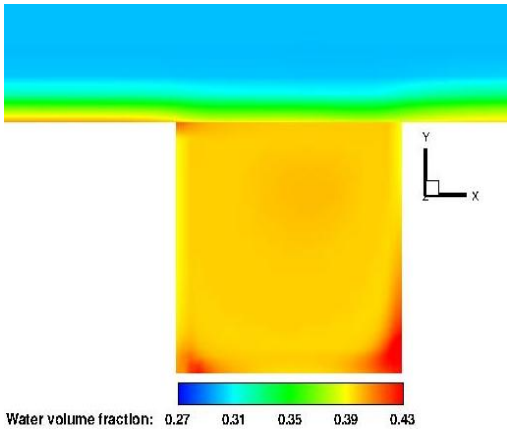

(a) Case 2 (Re=18,500)

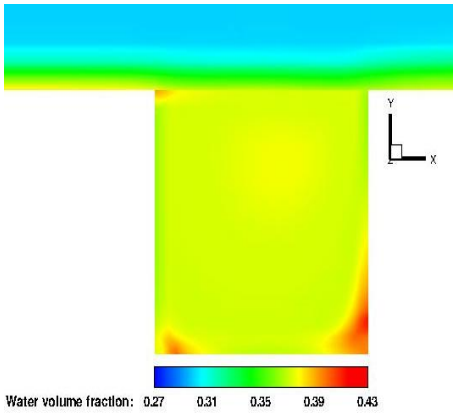

(b) Case 6 (Re=22,000)

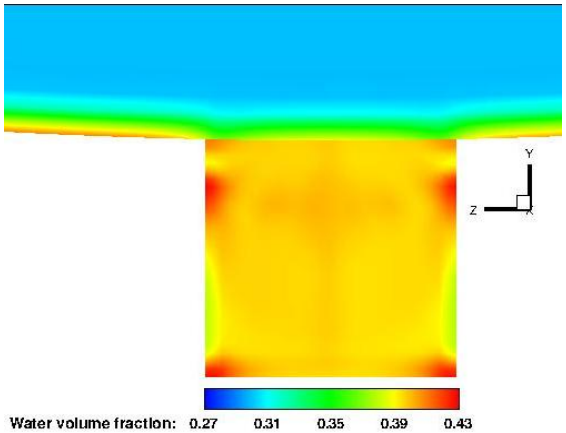

(c) Case 2 (Re=18,500)

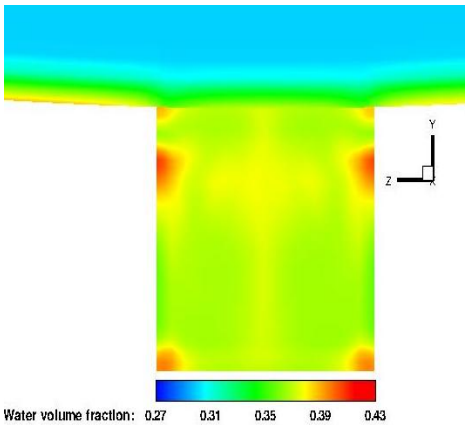

(d) Case 6 (Re=22,000)

Figure 4.54: Water volume fraction at planes perpendicular and across the flow for case 2 and 6 (Deep cavity, water fraction=0.3)

The water separation and settlement in shallow cavity can be observed in figures 4.55 and 4.56 below. Figures 4.55a and 4.55b display the water volume fraction distribution at plane perpendicular to flow of case 3 (Re=18,500) and case 7 (Re=22,000). However, in both the two cases high water fraction can be seen at bottom of the pipe and cavity leading edges with little concentration of water at downstream corner edges, also large vortices can be seen at the downstream portion of cavities results to localise water separation at the edge corner. The intensity of the turbulent activity pushes the fluid mixture to upstream wall as results of exchange of oil-water mixture between the shear layer and the cavity. For plane across the flow shown in figures 4.55c and 4.55d below, the two cases show the same water separation and settlement trends with higher propensity observed with cavity of low Reynolds number (Case 3) than cavity of high Reynolds number (case 7).

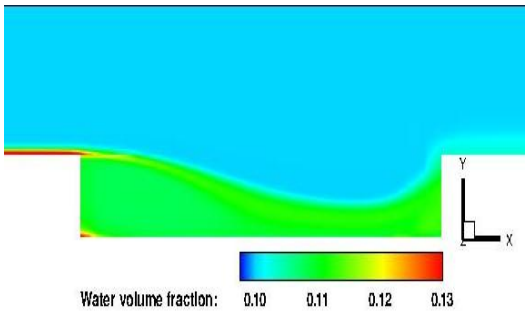

(a) Case 3 (Re=18,500)

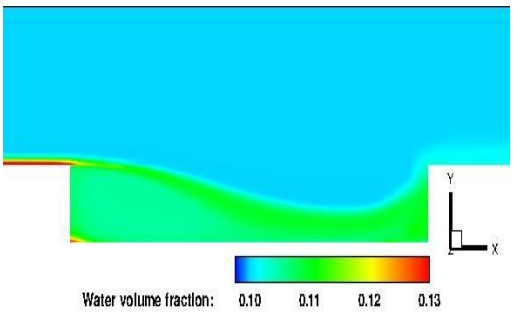

(b) Case 7 (Re=22,000)

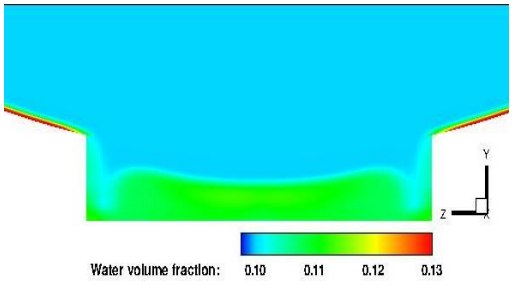

(c) Case 3 (Re=18,500)

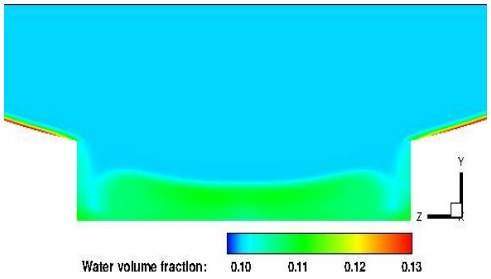

(d) Case 7 (Re=22,000)

Figure 4.55: Water volume fraction at planes perpendicular and across the flow for case 3 and 7 (Shallow cavity, water fraction=0.1)

Figure 4.56 compares the water volume fraction at plane perpendicular and across the flow of shallow cavity at water volume fraction of 0.3. The contour plots of shallow cavity provide very interesting water volume fraction distribution

behaviour. The contour plots at plane perpendicular to the flow in figures 4.56a and 4.56b show the same water fraction flow trend, whereby water can be seen at the bottom of the pipe towards the cavity leading edge with no appearance of water at cavity outlet or trailing edge. However, two vortices are generated in the two cases, the primary vortex at downstream while the secondary vortex at corner edge, this flow topology was observed in three-dimensional simulation of rectangular cavities by Yao eta al. (2004), the strength and location of the vortices can be observed, the primary vortices in case 8 (Re=22,000) is more stronger and occupied more area than the primary vortices of case 4 (Re=18,500) and this can be ascribed to the influence of difference in Reynolds number of the two cases. In both the two cases water bubbles tends to move from cavity downstream to upstream in stream wise direction and water tend to appear at tip corner downstream edge. For the plane across the flow in figures 4.56c and 4.56d, the characters of the flow field and distribution of water volume fraction in the two cases are the same.

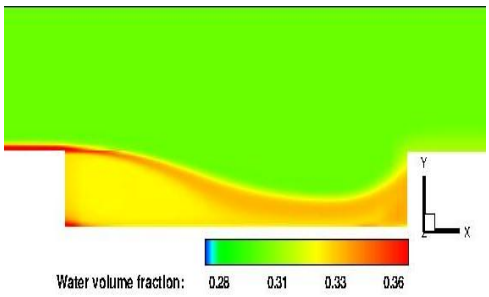

(a) Case 4 (Re=18,500)

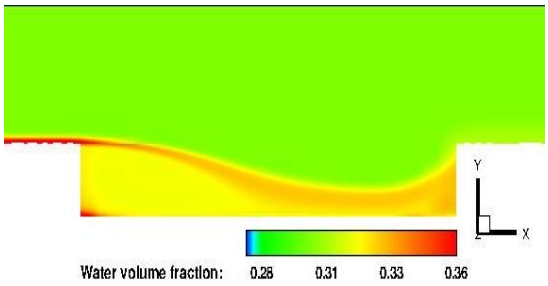

(b) Case 8 (Re=22,000)

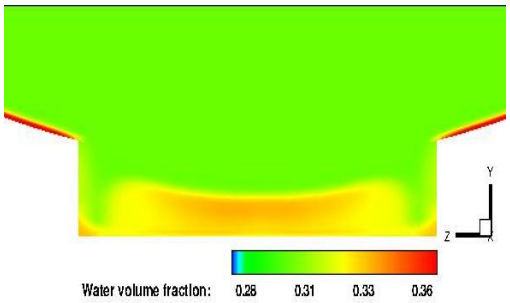

(c) Case 4 (Re=18,500)

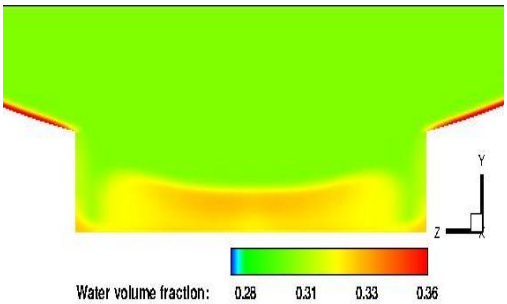

(d) Case 8 (Re=22,000)

Figure 4.56: Water volume fraction at planes perpendicular and across the flow for case 4 and 8 (Shallow cavity, water fraction=0.3)

The tables 4.12 and 4.13 below give the quantitative values of maximum and minimum water volume fraction at the cavity and pipe walls of eight (8) simulated cavity cases for input water volume fraction of 0.1 and 0.3 and Reynolds numbers of 18,500 and 22,000. The results of water volume fraction in table 4.12 and 4.13 can be interpreted in terms of effect of cavity aspect ratio, Reynolds number and input water volume fraction. Firstly, the effect of cavity aspect ratio on maximum and minimum water distribution in the cavity region shown in table 4.12 will be considered. The distribution of water volume fraction on the cavity geometry depends on whether the cavity is deep or shallow, when compare the maximum and minimum water volume fractions of case 1 (deep cavity) and case 3 (shallow cavity) of the same Reynolds number of Re=18,500 and water volume fraction of 0.1. The maximum water volume fraction of case 1 (deep cavity) and case 3 (shallow cavity) are 0.197 and 0.134 yielding percentage increase of 97% and 34% respectively. Similarly, for case 2 (deep cavity) and case 4 (shallow cavity), the maximum water volume fraction are 0.514 and 0.390 with percentage increase of 71.3% and 30% respectively. The results reveal that more water settles to bottom and surface of the deep cavity than the shallow cavity.

The same water volume fraction trend behaviour is observed with high Reynolds number cases of 22,000 and water volume fraction of 0.1, when we consider case 5 (deep cavity) and case 7 (shallow cavity) the percentage increases of water volume fraction are 76% and 30% respectively, also for deep cavity case 6 and shallow cavity case 8, the percentage increases are 55.3% and 25.3% respectively. However, the quantitative results of water volume fraction distribution revealed that deep cavity has high value of minimum water volume fraction compared with shallow cavity (case 1&3 and case 5&7). In general, the analysis discloses that deep cavity has more surface area in contact with water and more water settles at the pipe wall and bottom of the deep cavity than the shallow cavity, these situations create more potential points for initiation of internal pipeline corrosion.

The results of the maximum and minimum water fraction at cavity surface in table 4.12 also justify the effect of Reynolds number. The surface area of cavity wetted by water reduces as Reynolds number increases, when considering cases of the same cavity aspect ratio (deep cavity) and constant input water volume fraction of 0.1 for case1 (Re=18,500) and case 5 (Re=22,000). The maximum water fractions are 0.197 and 0.176 with percentages increase of 97% and 76% respectively. The other two deep cavity case of case 2 (Re=18,500) and case 6 (Re=22,000) with 71.3% and 55% increase in water volume fractions. Similarly, for shallow cavity cases, case 3 (Re=18,500) and case 7 (22,000), the water volume fraction increases by 34% and 30% respectively, the remaining two shallow cavities of case 4 (Re=18,500) and case 8 (Re=22,000) the water volume fractions increases by 30% and 25.3% respectively. The analysis for the deep and shallow cavity here revealed that with increase in Reynolds number less water settles down at bottom and surface of cavity and with decrease in Reynolds number more water settles at bottom and surface of cavity.

Case Num.	Re_m	Water Volume Fraction	Mixture Velocity (m/s)	Aspect ratio (Cavity)	Minimum Water Volume Fraction	Maximum Water Volume Fraction	% Incre.
1	18500	0.1	3.2	Deep	0.119	0.197	97.0
2	18500	0.3	2.5	Deep	0.358	0.514	71.3
3	18500	0.1	3.2	Shallow	0.100	0.134	34.0
4	18500	0.3	2.5	Shallow	0.300	0.390	30.0
5	22000	0.1	3.8	Deep	0.114	0.176	76.0
6	22000	0.3	2.96	Deep	0.339	0.466	55.3
7	22000	0.1	3.8	Shallow	0.100	0.130	30.0
8	22000	0.3	2.96	Shallow	0.300	0.376	25.3

Table 4-11: Maximum and minimum water volume fractions at cavity surface

The results in table 4.12 also exhibit water separation and distribution behaviour as the input water volume increase. The effect of input water volume fraction can be observed with case of the same Reynolds number and cavity aspect ratio. We consider case1 (input water fraction=0.1) and case2 (input water fraction 0.3), the maximum water fraction in contact with cavity surface are 0.197 and 0.514 respectively. In general, the quantitative results of water volume fraction distribution in cavity region indicate that increase in input water volume fraction will lead to reduction in mixture velocity and less water entrainment by the moving oil, so more water will separate from oil and settle to the bottom of the cavity. However, to run production oil pipeline we require less input water fraction to promote water entrainment. Similar results are observed for the remaining cases.

Case Num.	Re_m	Water Volume Fraction	Mixture Velocity (m/s)	Aspect ratio (Cavity)	Minimum Water Volume Fraction	Maximum Water Volume Fraction	% Incre.
1	18500	0.1	3.2	Deep	0.044	0.168	68.0
2	18500	0.3	2.5	Deep	0.141	0.446	49.7
3	18500	0.1	3.2	Shallow	0.043	0.171	71.0
4	18500	0.3	2.5	Shallow	0.137	0.451	50.3
5	22000	0.1	3.8	Deep	0.054	0.153	53.0
6	22000	0.3	2.96	Deep	0.173	0.419	39.7
7	22000	0.1	3.8	Shallow	0.054	0.155	55.0
8	22000	0.3	2.96	Shallow	0.169	0.422	40.7

Table 4-12: Maximum and minimum water volume fractions at pipe surface

Table 4.13 above gives the maximum and minimum water volume fractions at pipe surface, in this investigation only pipe domain is taken into account, while the cavity geometry is removed from the analysis. In this analysis, the Reynolds number and water volume fraction varied while the same pipe geometry is considered throughout the investigation. To quantify the effect of removing the cavity aspect ratio on the maximum water volume fraction at the pipe surface,

we consider case1 (deep cavity) and case3 (shallow cavity) of the same Reynolds number of 18,500 and water volume fraction of 0.1. The maximum water volume fractions of case 1 and case 3 are 0.168 and 0.171 yielding percentage increase of 68% and 71% respectively. For case 5 (deep cavity) and case 8 (shallow cavity) the maximum water fractions are 0.153 and 0.155 with percentage increase of 53% and 55% respectively. These results show the percentage increase in water volume fraction reduced from 97% to 68% for deep cavity case as well as increase from 34% to 71% for shallow cavity case in the pipe surface. The analysis revealed that reduction in water volume fraction at the pipe surface occurs because part of water is retained in deep cavity (case1), while for the increase of water fraction in the pipe surface of shallow cavity (case 3) is because little water is retained in shallow cavity. Similar water distribution trends are obtained for shallow cavity of case 5 and case7 respectively, the percentage increases in water volume fraction at the pipe surface are 53% and 55% respectively.

The effects of Reynolds number on the maximum water volume fraction at the pipe surface is shown in table 4.13. The increase in Reynolds number leads to reduction in maximum water fraction at the pipe surface evident from case 1 (Re=18,500) and case 5 (Re=22,000) of the same aspect ratio (deep cavity) and water fraction of 0.1. The maximum water fractions at the pipe surface are 0.168 and 0.153, yielding an increase of 68% and 53% respectively. Similarly, water volume fraction trends are obtained for shallow cavity cases, considering case 3 (Re=18,500) and case 7 (Re=22,000), the maximum water fraction are 0.171 and 0.155 with percentage increase of 71% and 55% respectively. The analysis shows that the higher the Reynolds number the more water is entrained by the moving oil, and the lower the Reynolds number the more water separates and settles at the bottom of the pipe wall creating suitable environment for corrosion to occur.

The effect of input water volume fraction distribution at the pipe surface is evident, the increase in input water volume fraction results to more water separate and settle at the bottom and surface of the pipe, for deep cavities case

1 (input water fraction=0.1) and case 2 (input water fraction=0.3) of the same Reynolds number of 18,500. The maximum water fractions are 0.168 and 0.446 respectively. For shallow cavities of case 7 (input water fraction=0.1) and case 8 (input water fraction=0.1) of the same Reynolds number of 22,000. The maximum water volume fractions are 0.155 and 0.422 respectively. These results show increase in input water fraction will lead to water segregates faster and settles at the bottom of pipe wall, which is consistent with observation by Konan (2009). These results can be referred to old oil-well, where by more water is produced along with oil during the exploration and transportation of crude oil, the pipeline carrying the products may contain more water, increasing the like hood of internal pipe corrosion to occur.

4.8 Parametric analysis

Parametric analysis is performed for cavity case in order to compare one of the results of cavity simulation (Case 6) conducted against the practical modified turbulence model. Turbulent models are computed by two layer turbulence approach incorporated in to computational flow field by Hui et al. (2003). The flow field is separated in two, the viscosity affected region and fully turbulent region determined by turbulent Reynolds number which was based on wall distance computed as:

$$\mathrm{Re}_{\eta} = \frac{\rho\sqrt{y^{+}}}{\mu} \qquad \textbf{(4-1)}$$

Where $\boldsymbol{y}^{+}$ is the wall distance, ρ is the density and μ is the dynamic viscosity. The damping functions are incorporated in to turbulent viscosity equation whereby the modified turbulent viscosity is calculated as:

$$\mu_{t} = {}^{f_{\mu}C_{\mu}\rho k^{2}}\!/_{\varepsilon} \qquad \textbf{(4-2)}$$

Where f_μ is the damping function given as:

$$f_\mu = \left(1 - \exp\left(-A_\mu Re_\eta\right)\right)^2 \left(1 + A_1/Re_\eta\right) \quad \textbf{(4-3)}$$

Where A_μ =0.0165, A_1 =20.5

Numerical simulations have been carried out for deep cavity cases (Case 6) which is the non-modified case and the modified case at water volume fraction of 0.3 and Reynolds number of 22,000. The modified case is the one formulated and coded using c-programme language in order to adjust the turbulent viscosity with damping functions while the non-modified is without adjustment to turbulent viscosity. The two simulation results were post-processes and analyse. Combination of contour and line plots together with table of maximum and minimum water volume fraction at pipe and cavity walls will be used for comparison.

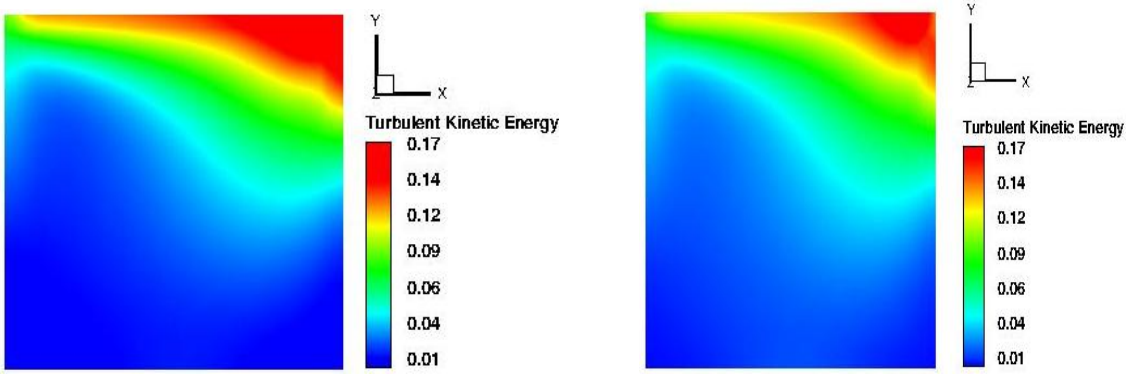

(a) Case6 (Modified) (b) Case6 (Non-Modified)

Figure 4.57: Comparison of turbulent kinetic energy distribution (Re=22,000)

Figure 5.47 displays the contour plots of turbulent kinetic energy for deep cavity cases of modified and non-modified cases. In figure 5.47a, it can be seen that the region of turbulent activity is larger for modified than the non-modified case. This suggest that water entrainment increased in modified case which leads to lower rate of separation of water from oil in the mixture, while the non-modified case in figure 5.47b has lower region of turbulent activity, the low mixing will increase the rate of separation of water from oil. However, the increases in turbulent mixing results to higher rate of water entrainment by moving oil.

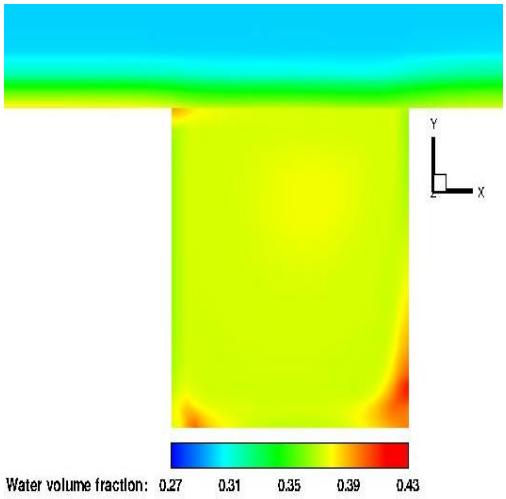

(b) Case6 (Modified)

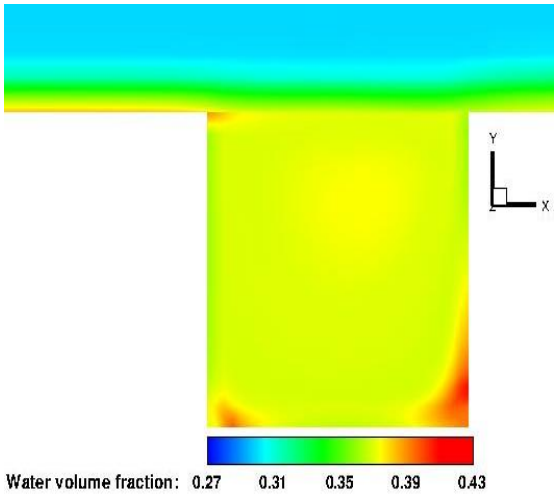

(b) Case6 (Non-Modified)

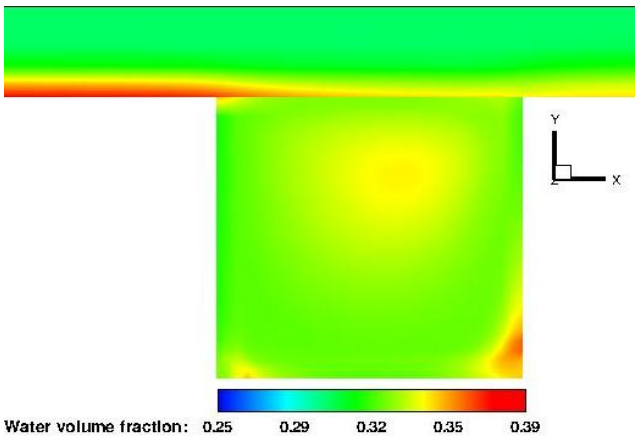

(c) Modified case with different contour level

Figure 4.58: Comparison of water volume fraction at pipe and cavity region (Re=22,000, water fraction=0.3)

The contour plots of water volume fraction for modified and non-modified case are shown in figure 5.48. When we compare figure 5.48a and figure 5.48b, the water volume fraction in modified case occupied less wetted area and water bubbles can be seen at the cavity mid-plane compare with non-modified case. in figure 5.48b of non-modified case, large water wetted area can be seen with high water volume fraction at the cavity leading edge and at the two edge corners also water bubble appeared at recirculation region. From figure 5.48a, less water distribution in cavity occurred because maximum water fraction is damped at pipe base and at upstream corner edge as evident in figure 5.48c of

modified case with different contour levels. In conclusion, figure 5.48c demonstrated the effect of damping function, which can be seen in pipe base and at shear layer; water volume fraction is smoothly distributed with bubbles at cavity recirculation region.

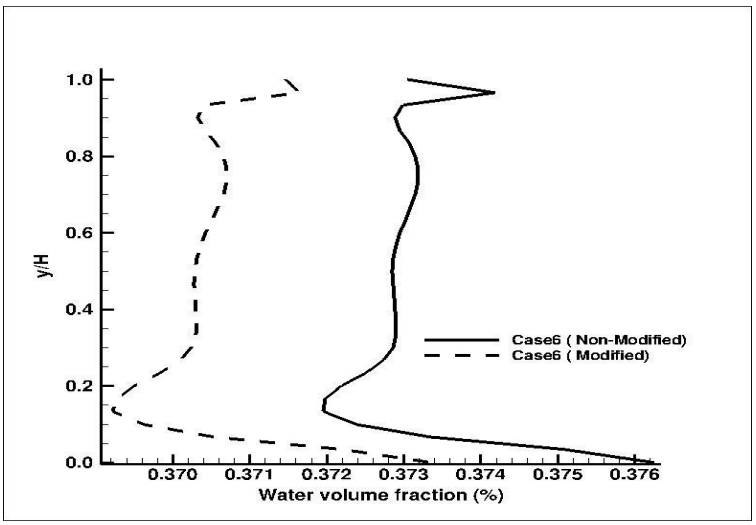

Figure 4.59: Comparison of water volume fraction at 0.25 cavity lengths

Water volume fraction distributions inside the cavity in stream wise direction were considered for comparison at 0.25, 0.5 and 0.75 cavity lengths. Figure 5.49 shows the comparison of water volume fraction at 0.25 cavity length of modified and non-modified case. For non-modified case, water entered the cavity at 0.3748 then decrease to cavity height of 0.9, this is the position of recirculation region (Primary vortex) from then water decrease to cavity height 0.25, because of the reduce velocity in cavity base from then water volume fraction increase to 0.376. The modified case follow the same water distribution trends of non-modified with differences in amount of water fraction at cavity entrance and cavity base, the modified case entered at 0.372 and settle to 0.3735 at base of cavity.

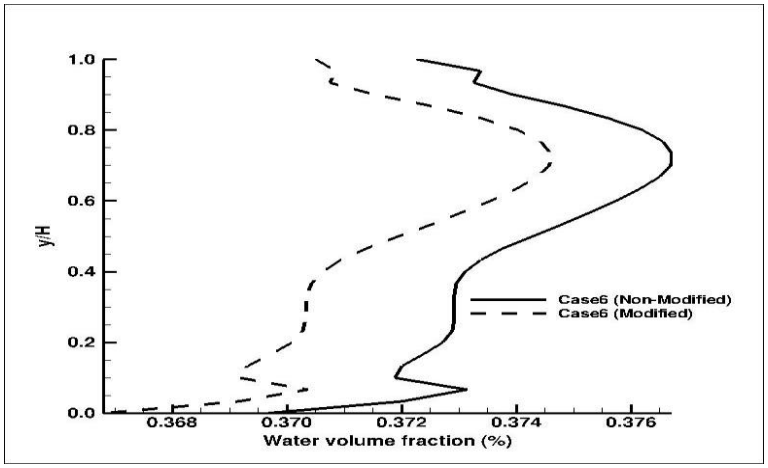

Figure 4.60: Comparison of water volume fraction at 0.5 cavity lengths

The water volume fraction distributions for modified and non-modified case at the middle of cavity (0.5 cavity length) are comparing in figure 5.50. The two profiles show the same distribution trends with differences at cavity entrance and base of cavity, the vortex core appeared at cavity height of 0.7 and more water are entrain by the moving oil because the turbulent mixing is at maximum, water separate from the vortex core by gravity and decrease down to the base of cavity, modified case settles at 0.366 and non-modified at 0.370 water volume fraction.

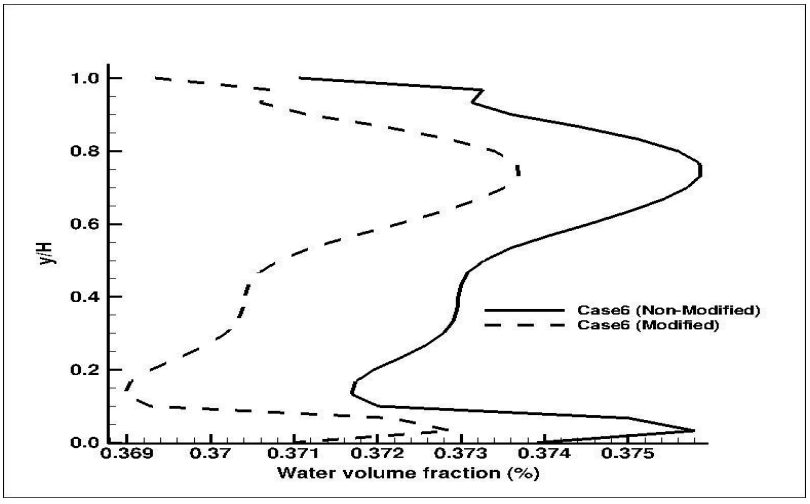

Figure 4.61: Comparison of water volume fraction at 0.75 cavity lengths

Water volume fraction distributions at the upstream region of cavity (0.75 cavity length) for modified and non-modified case are presented in figure 5.51 above.

The water profiles show the same trends, water entered the cavity and increase by 0.073 and 0.076 for modified and non-modified case respectively. The two vortices core appear at the same cavity height of 0.75, water tends to separate by gravity and decrease from vortex core to cavity height of 0.18 then water fraction increases to 0.373 and 0.376 and decreases to 0.371 and 0.374 at cavity base for modified and non-modified case respectively.

	Pipe			Cavity		
	Maximum	Minimum	% increase	Maximum	Minimum	% increase
Modified	0.4623	0.3382	54	0.4189	0.1728	39.6
Non-Modified	0.4662	0.3392	56	0.4192	0.1730	39.7

Table 4-13: Comparison of maximum and minimum water volume fraction of pipe and cavity surface (Modified and non-Modified case)

Table 5.11 gives the comparison of maximum and minimum water volume fraction in pipe and cavity wall for modified and non-modified case. In this analysis, the maximum water volume fractions in pipe walls for modified and non-modified are 0.4623 and 0.4662, yielding percentage increase of 54% and 56% respectively. The maximum water volume fractions at cavity surface for modified and non-modified cases are 0.4189 and 0.4192 with percentage increase of 39.6% and 39.7% respectively. The numerical results show that the non-modified case has the high maximum and minimum water volume fraction in contact with pipe wall compare with the modified case. Similar results are obtained for cavity region with non-modified case having high percentage increase of maximum and minimum water volume fractions in the cavity region.

4.9 Summary of results of oil-water flow in pipe with cavity

The influence of cavity geometry in changing the flow features during the flow of oil-water in pipeline with deep and shallow cavity was investigated. The effect of cavity aspect ratio on the flow physics was described; it was observed that the change in aspect ratio has influence in changing velocity, water volume fraction and turbulent kinetic energy at the centre of pipe. Small distortion appeared at the centre of pipe which depends on cavity aspect ratio, and more distortion

was observed for deep cavity case than the shallow cavity case. The cavity aspect ratio does not have any significant effect on velocity profile in radial direction before and after the cavity. In both cases, water volume fraction at the bottom of the pipe increases as the flow approaches the cavity because of the action of gravity and entrance effect. Around the cavity, turbulence is produced as the flow separates from the leading edge of the cavity, resulting in recirculation, mixing and separation of water from oil, and also it smoothens out the water volume fraction after the cavity. In the cavity region, it was observed that more water settles to the bottom of the cavity for the deep cavity case than the shallow cavity. The analysis reveals that the deeper the cavity, the more the amount of water settles at the bottom of the cavity producing potential points for initiation of internal pipeline corrosion.

The analysis of the effect of Reynolds number on the flow physics revealed that the surface area of the cavity wetted by water reduces as the Reynolds number is increased. Also, the amount of water that settles at the bottom of the pipe is reduced when the Reynolds number is increased. This result suggests that a pipeline carrying oil and water running at a high Reynolds number will less likely to corrode compared to a low Reynolds number pipeline. This is as a result of turbulence production due to higher velocities in the pipe. It has been shown before that as the Reynolds number is increased, there is reduction in the maximum water volume fraction of water in contact with the pipe wall. It is expected that when there is a large increase in Reynolds number, far less water will settle to the bottom of the pipe due to increased turbulence activity, recirculation and the entrainment of water by moving oil.

It was observed that increasing the input water volume fraction increases the amount of water that separates from the bulk fluid, thereby resulting in higher percentage of water volume fraction in contact with the pipe and cavity walls. Since water is heavier than oil, when the water volume fraction is increased, more water is available to separate from bulk fluid. It can be conclude that in a petroleum production pipeline, as the amount of water in the production pipe increases with the life of the oil well (i.e. wells that produce more water along

with crude oil), the chances of corrosion in the pipe increase thereby reducing the useful life of production pipeline. It was noticed that the cases with deep cavity and high input water volume fraction have the highest water volume fraction in contact with the cavity wall.

5 NUMERICAL MODELLING OF OIL-WATER FLOW IN PIPE WITH CUBICAL OBSTACLE

Numerical modeling of oil-water flow in horizontal pipe with cubical obstacle (scale sediments) is performed in order to study detail flow features and to quantify the maximum and minimum of water volume fractions and its distribution around the cubical obstacle region as well as to examine the contribution of cubical obstacle (scale sediments) in influencing oil-water recirculation, separation and settlement of water. However, there are no experimental results on oil-water flow in pipe with cubical obstacle from literatures. The experimental data of Lovick and Angelli (2004) of dual continuous flow of oil-water in horizontal pipeline are used as numerical input data based on the evidence of validation studies conducted as shown in table 4.1.

5.1 Pipe with cubical obstacle (scale sediments) models

The two model geometries of pipe with cubical obstacle (scale sediment) were generated with GAMBIT 2.4. The model geometries are produced in three dimensions; the purpose here is to produce mesh of high quality to resolve important flow features during the flow of oil and water in horizontal pipe with cubical obstacle (scale sediments). The scale sediments model geometries are cubical in shapes, because it will help separation. The cubical obstacle is placed at the bottom wall of the pipe oriented perpendicular to the flow. The linear dimension of the cubes is small in comparison with pipe diameter (L_b), 10% and 20% of pipe diameter is chosen as a linear dimension of the cubical obstacles of lower and higher aspect ratio respectively.

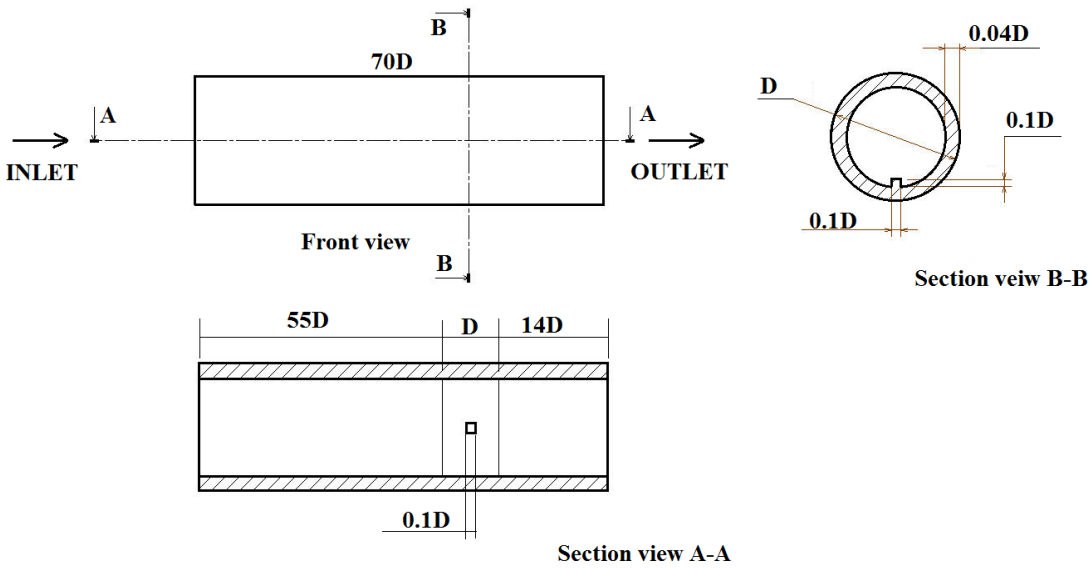

Figure 5.1: Geometry model of horizontal pipe with cubical obstacle (lower aspect ratio)

The model length of pipe is 70D in stream wise direction; the length is selected to achieve stable and fully developed flow, where D is the diameter of the pipe. The pipe length is subdivided into 3 volume sections for easy meshing and to avoid the skewness of elements in the cubical obstacle cross sectional area. The downstream section of the pipe has length of 55D and the upstream has length of 14D while the volume section of the pipe that contains the cubical obstacle has length equal to the diameter of the pipe (D). The two model geometries of horizontal pipe with cubical obstacles are of sides 0.1D and 0.2D, representing lower and higher aspect ratios as shown in figures 5.1 and 5.2 respectively.

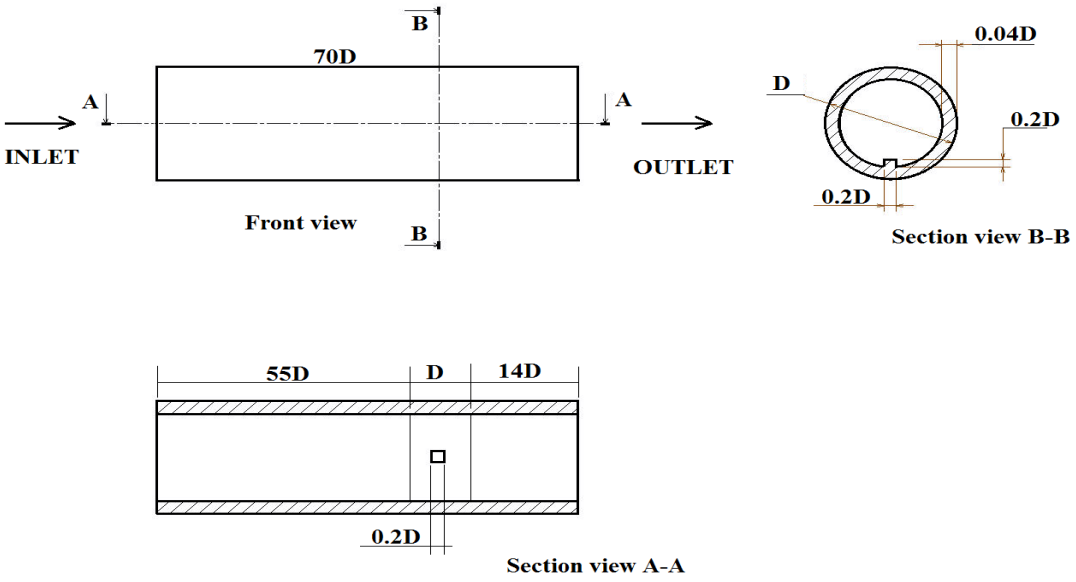

Figure 5.2: Geometry model of horizontal pipe with cubical obstacle (higher aspect ratio)

The geometry case parameters for pipe with cubical obstacle model (scale sediments) are given in the table 5.2 below.

Parameters	Values
Pipe	
Diameter	D
Length	70D
Pipe upstream	55D
Pipe downstream	14D
Cubical obstacle	
L_b	0.1D, 0.2D

Table 5-1: Pipe with cubical obstacle case data

The calculated dimensions of the cubical obstacle (scale sediment) based on the definition of cube geometry parameter ratio in table 5.2 are shown in table 5.3.

Dimension	Lower aspect ratio	Higher aspect ratio
Length	0.0038m	0.0076m
Depth	0.0038m	0.0076m
Width	0.0038m	0.0076m

Table 5-2: The cubical obstacle dimensions

5.2 Grid generation

Meshing tool GAMBIT 2.4 is used to generate three-dimensional hexahedral cells and tetrahedral cells in the pipe with cubical obstacle; the horizontal pipe model with cubical obstacle is produced in three volumes, the hexahedral mesh is applied at upstream and downstream volumes of the pipe. The two volumes have more coarse mesh, while the volume that contain the cubical obstacle has fine mesh, tetrahedral mesh is applied, this is the region of the cubical obstacle domain where the flow is fully developed. This is the test section region where separation and recirculation of oil and water occurred.

Pipe with lower aspect Bump	Elements	Nodes
Pipe upstream volume	798172	706407
Pipe downstream volume	203190	180516
Middle pipe volume with bump	263217	114854
Total	1,264,579	1,001,777

Table 5-3: Number of elements and nodes for pipe with cubical obstacle (lower aspect ratio)

The height of the cell is specified and cell growth factor of 1.2 is applied to cluster the mesh toward the wall. The boundary layer is connected to the interior wall of the pipe. The region of the pipe with cubical obstacle contains triangular mesh. The size function is attached to the top of cubical obstacle and side walls in order to connect the boundary layer at the bottom of the cubical obstacle surface, the used of size function will help to produce tetrahedral cells of good quality to resolve the important flow features. The number of nodes and

elements for the pipe with cubical obstacle (lower aspect ratio) are presented in table 5.4, while the grid structures are shown in figure 5.3.

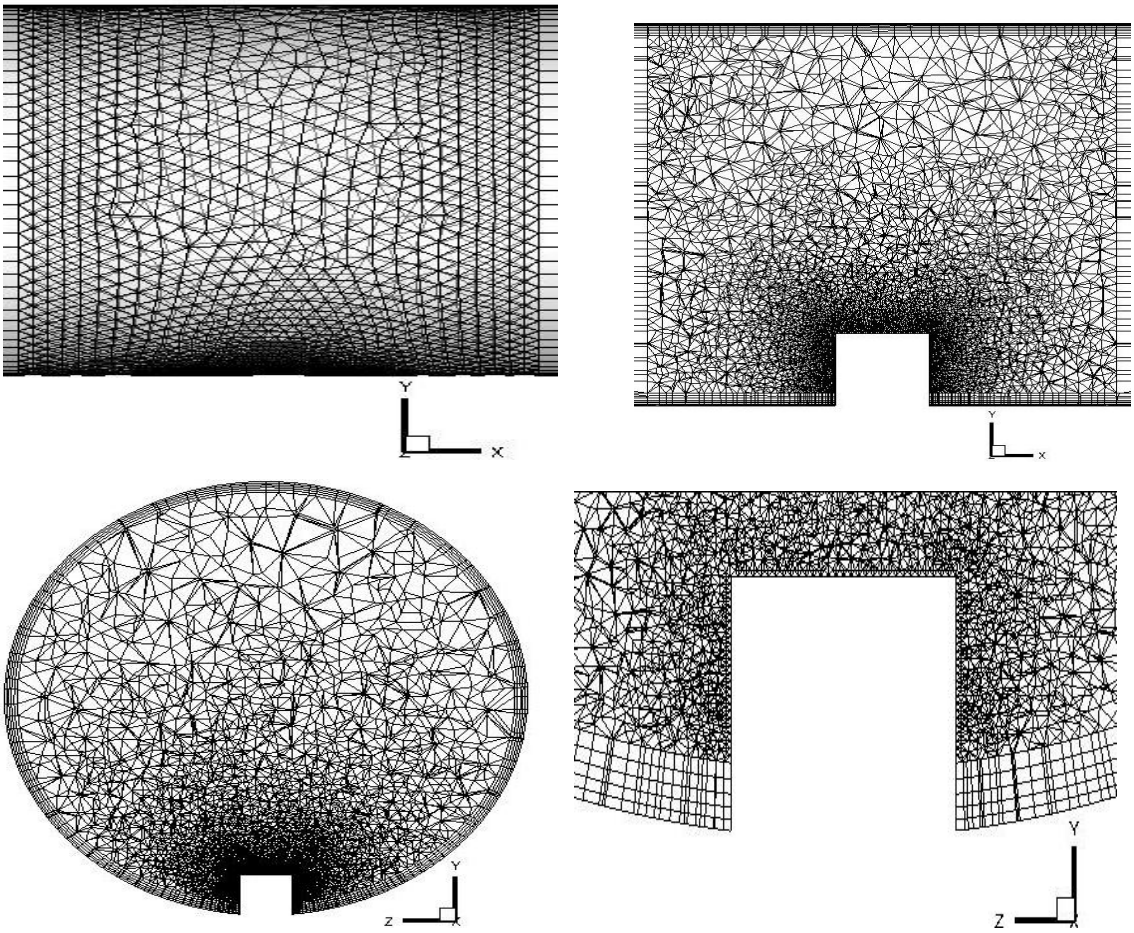

Figure 5.3: Grid structures for pipe with cubical obstacle (lower aspect ratio)

Boundary layer is connected to the interior pipe wall to cluster the grids toward the pipe wall for pipe with cubical obstacle (lower aspect ratio); the boundary layers features are given in table 5.5.

Algorithm	First row	Growth factor	Total depth	No of rows	Int/ cont.	Trans/ pt
Uniform	0.0020	1.200	0.3734	20	Yes	1:1

Table 5-4 : Boundary layers features of pipe with cubical obstacle (lower aspect ratio)

Size function is connected to the volume of the pipe that contains cubical obstacle (lower aspect ratio) to cluster the mesh toward the bottom of the cube with the same value of growth rate and maximum size of cell as 1.0.

The number of nodes and elements for the pipe with cubical obstacle (higher aspect ratio) are presented in table 5.6, while the grid structure are shown in figure 5.4.

Pipe with higher aspect ratio bump	Elements	Nodes
Pipe upstream volume	637704	564573
Pipe downstream volume	162552	144597
Middle pipe volume with bump	235612	107832
Total	1,035,868	817,002

Table 5-5: Number of elements and nodes for pipe with cubical obstacle (higher aspect ratio)

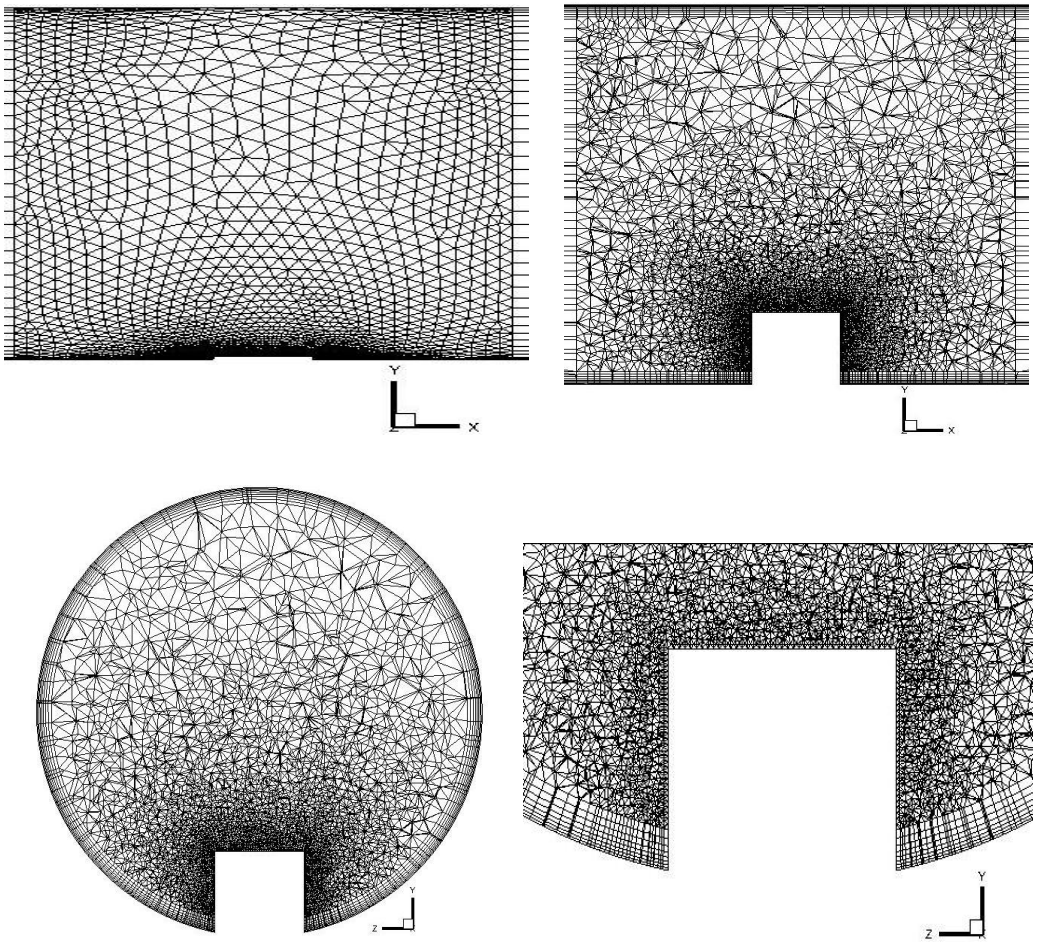

Figure 5.4: Grid structures for pipe with cubical obstacle (higher aspect ratio)

Boundary layer is connected to the interior pipe wall to cluster the grids toward the pipe wall for the pipe with cubical obstacle (higher aspect ratio); the boundary layers features are shown in table 5.7.

Algorithm	First row	Growth factor	Total depth	No of rows	Int/ cont.	Trans/ pt
Uniform	0.0022	1.200	0.3765	20	Yes	1:1

Table 5-6: Boundary layers features for pipe with cubical obstacle (higher aspect ratio)

Size function is also connected to the pipe volume that contains cubical obstacle (higher aspect ratio) in order to cluster the mesh toward the bottom of cubical obstacle with the same value of growth rate and maximum size of cell as 1.0.

5.2.1 Grid independence study

Grids independence study is conducted on horizontal pipe with cubical obstacle (scale sediments) to choose the appropriate number of cells for the numerical simulation of oil-water flow in pipe with cubical obstacle at Reynolds numbers of 15,800 and 22,000. The physical dimensions of the geometries are shown in table 5.3. Whereas the same Lovick and Angeli (2004) experimental oil properties were used in grid independence for cubical obstacles as presented in table 4.1. Two meshes of horizontal pipe with cubical obstacle of lower and higher aspect ratio were produced and then exported to FLUENT 6.3. Eulerian multiphase model and the standard K-ε turbulence model with standard wall function were selected. Boundary condition set at inlet is velocity inlet and at outlet is outflow, while no-slip is set at both the pipe and cubical obstacle walls. The followings are the solver parameters used:

- Second order double precision pressure based steady solver
- Phase coupling SIMPLE algorithm for pressure-velocity coupling
- Second order upwind scheme for momentum, turbulent kinetic energy and dissipation rate
- QUICK differencing scheme for volume fraction

The water volume fraction, static pressure and mixture velocity are monitored at the centreline of the pipe to ensure fully developed and converged solution. The residual reaches the convergence criterion of 10^{-6}. From the numerical results of grids independence study, the pressure gradient differences between the total numbers of cell values are very small. Therefore, in consideration of computational cost, cells of 1×10^{6} and 1.25×10^{6} are also selected for pipe with cubical obstacle of lower and higher aspect ratio respectively as shown in table 5.8.

Total cells	Pressure gradients Plain pipe	Pressure gradients Lower aspect ratio	Pressure gradients Higher aspect ratio	Reynolds Number
0.75×10^6	1760	1812	1844	18,500
1.0×10^6	1817	1861	1893	
1.25×10^6	1823	1884	1932	
0.75×10^6	1779	1821	1941	22,000
1.0×10^6	1832	1882	1966	
1.25×10^6	1841	1903	1987	

Table 5-7: Grids independence study of pipe with cubical obstacles

5.3 Numerical procedures

The cubical obstacles of lower and higher aspect ratio are placed at bottom of pipe oriented perpendicular to the direction of oil-water flow. Based on the literature survey, range of Reynolds numbers in oil-water pipe flows resulting in fully dispersed turbulent flow are identified to be between 18,000 and 25,000 and typical range of water volume fraction for these regimes is between $\alpha_w = 0.1 \; and \; \alpha_w = 0.3$. Therefore, the same Reynolds number were selected under this investigation as 18,500 and 22,000 with water volume fraction of $\alpha_{\,w} = 0.1 \; and \; \alpha_w = 0.3$ of the same pipe geometry and oil properties. Also matrix of 8 cases of pipe with cubical obstacles will be investigated as presented in table 5.9 below.

Based on the grid independence study, the total number of cells of 10^6 cells and 1.25×10^6 cells were selected for lower and higher aspect ratio respectively, then the mesh exported to FLUENT 6.3. Eulerian multiphase model and standard k-ε turbulent model with standard wall function were selected. Oil and water physical properties are defined in material properties forms; the same solver parameters used for cavity simulation are also applied for cubical obstacle. Turbulent intensity of 2% and hydraulic diameter of 0.038m are applied at the inlet. The inlet and outlet boundary conditions are specified,

mixture velocity is used for the two phase at inlet and water volume fraction is used for secondary phase while for pipe and cubical wall boundary conditions; no-slip boundaries conditions are given at the pipe and cubical obstacle walls.

5.4 Analysis of results

This section describes the numerical simulations that were conducted on oil-water pipe flow with cubical obstacle and the various analyses on the effect of cubical obstacle on flow features. The investigation will revealed the contribution of cubical obstacle in oil- water recirculation, separation and settlement of water. The flow features are described in section 5.5 along with the effect of aspect ratio on oil-water in pipe with cubical obstacle. The effect of Reynolds number and input water volume fraction on the flow behavior will be described in sections 5.6 and 5.7 respectively. Summary on the numerical results of pipe with cubical obstacles will be outlined in section 5.8.

5.5 Simulation results and discussions

Simulations have been carried out for two different aspect ratios of cubical obstacle. In this analysis we shall investigate the effect of aspect ratio, Reynolds number and input water volume fraction on the flow physics and separation of water from oil in the pipe with cubical obstacle. The effect of aspect ratio on the flow features and phase separation is investigated by using the same value of Reynolds number, same water volume fraction but different aspect ratio case. Further details into the flow physics is obtained by investigating the effect of Reynolds number on separation rates by using a constant water volume fraction case and a fixed aspect ratio case. Also, the effect of input water volume fraction is investigated at a fixed Reynolds number and aspect ratio. The flow features in flow entrance region and cubical obstacle (scale sediment) region will be investigated. A table of simulation input data of pipe with cubical obstacle cases is shown in table 5.9.

Case Number	Re_m	Water Volume Fraction	Mixture Velocity (m/s)	Aspect ratio Cubical obstacle
1	18,500	0.1	3.2	Lower
2	18,500	0.3	2.5	Lower
3	18,500	0.1	3.2	Higher
4	18,500	0.3	2.5	Higher
5	22,000	0.1	3.8	Lower
6	22,000	0.3	2.96	Lower
7	22,000	0.1	3.8	Higher
8	22,000	0.3	2.96	Higher

Table 5-8: Simulation input data of pipe with cubical obstacles

5.5.1 Description of flow in entrance region

Eight cases of pipe with cubical obstacle (scale sediments) were simulated using ANSYS Fluent 6.3. The water volume fraction and velocity profile are monitored along the centre of the pipe with cubical obstacle for the lower and higher aspect ratio to ensure that the flow is fully developed and the solution converged. To demonstrate that the flow is fully developed, plots of velocity at the centre of the pipe with cubical obstacle and water volume fraction are presented in figures 5.5 to 5.10. In these plots, the mixture velocity and water volume fraction at the centre of the pipe indicate stable and fully developed flow. These plots are also used to describe the influence of cubical obstacle/aspect ratio on the flow features in the pipe. This will be done by investigating two cases with all other parameters the same but with different aspect ratios. Also, for this analysis, we shall use Case 6 (lower aspect ratio) and case 8 (higher aspect ratio). These two cases will be used to describe the flow in entrance and cavity region as well as the influence of cubical obstacle aspect ratio on the flow features, a combination of contour plots, line plots and streamline plots will be used. Case 6 and case 8 both have Reynolds number of

22, 000, water volume fraction of 0.3 and mixture velocity of 2.96m/s. The only difference is the aspect ratios of the cubical obstacle where case 6 is a lower aspect ratio and case 8 is a higher aspect ratio.

In figure 5.5 case 6 (lower aspect ratio), the velocity magnitude increases around the first 23% of the pipe length. This is due to the entrance effect at the pipe inlet and the fact that the flow is still developing. About 30% into the full pipe length, the flow is fully developed and the velocity magnitude is almost constant for the rest of the pipe length. Around the location of the cubical obstacle, the velocity profile is distorted slightly suggesting that the lower aspect ratio cubical obstacle has an influence on the flow field up to the centre of the pipe, a more distortion profile is observed in figure 5.6 for higher aspect ratio. However, there is slight difference in the influence of the lower aspect ratio on the velocity magnitude in the centre of the pipe; significant difference is observed for higher aspect ratio.

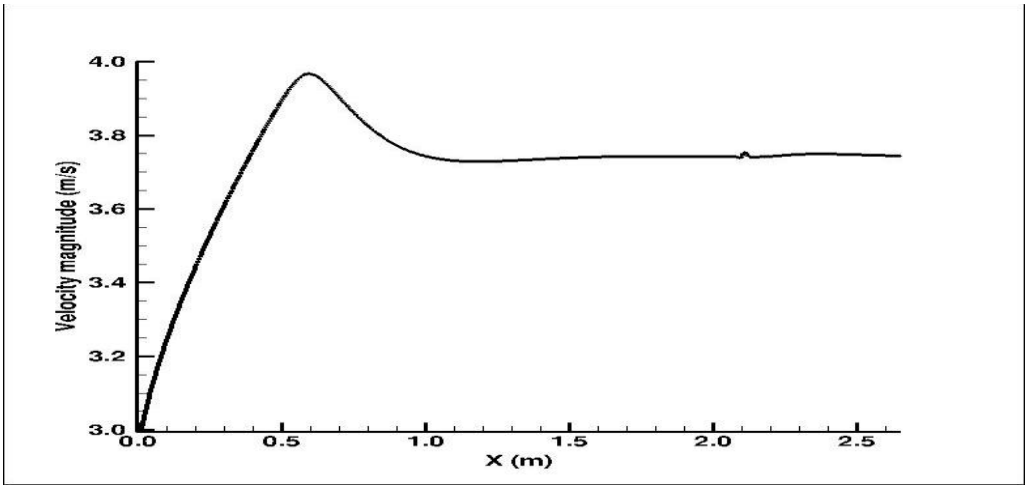

Figure 5.5: Velocity magnitude at centre of the pipe for lower aspect ratio cubical obstacle (Case 6)

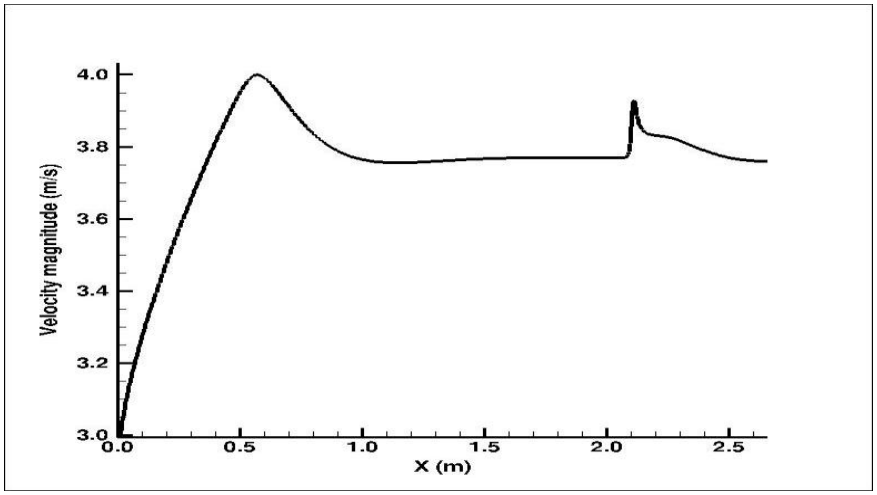

Figure 5.6: Velocity magnitude at centre of the pipe for higher aspect ratio cubical obstacle (Case 8)

In figures 5.7 and 5.8 below for lower and higher aspect ratio cubical obstacle respectively, the water volume fraction at the centre of the pipe is constant at 0.3 throughout the entire length of the pipe with a slight profile distortion at the position of cubical obstacle, this prove that the flow is fully developed and also the plot suggests that both the lower and higher aspect ratio slightly influence the water volume fraction at the position of the cubical obstacle.

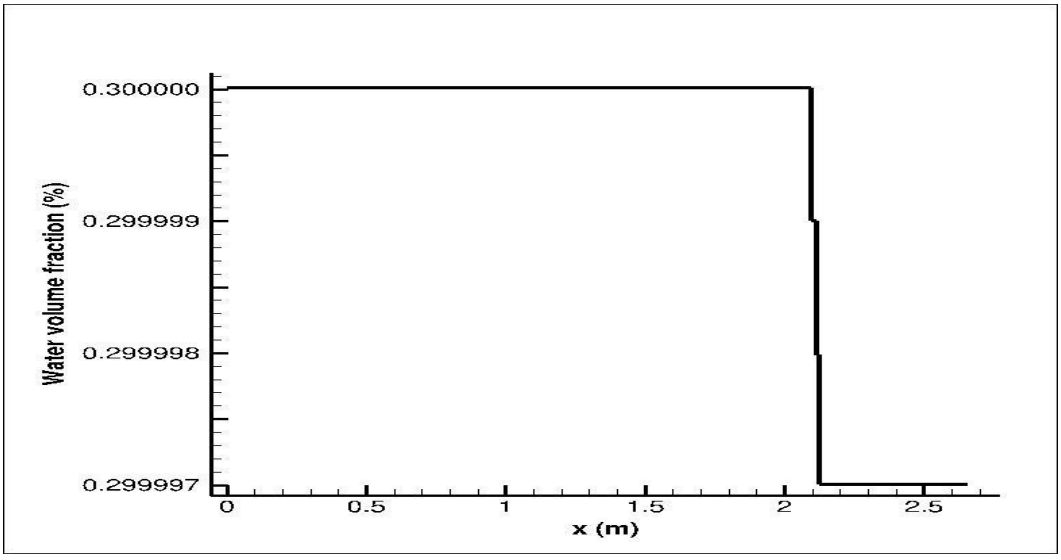

Figure 5.7: Water volume fraction at centre of the pipe for lower aspect ratio (case 6)

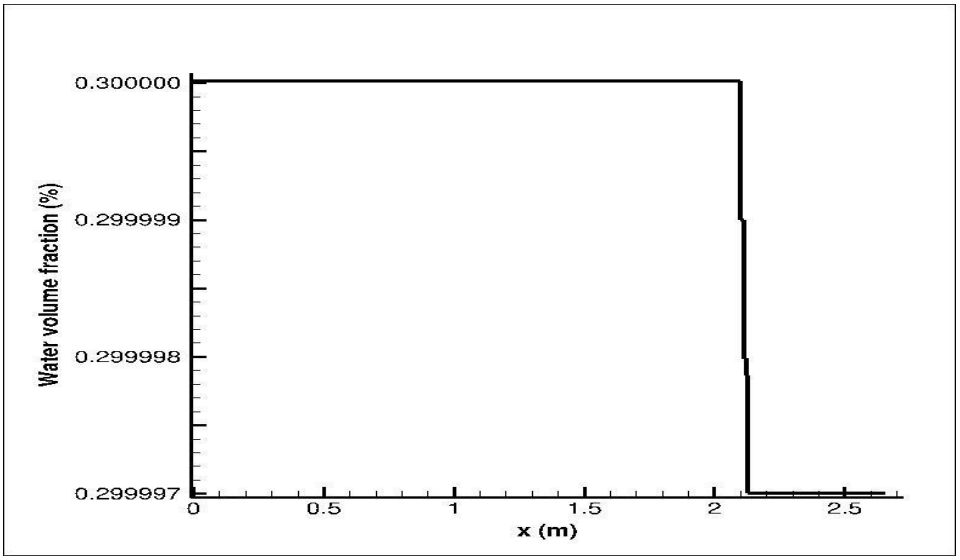

Figure 5.8: Water volume fraction at centre of the pipe for higher aspect ratio (case 8)

Figures 5.9 and 5.10 show the turbulent kinetic energy plots at the centre of the pipe from inlet to outlet. Turbulent kinetic energy increases and becomes steady at about 40% the length of the pipe when the flow is fully developed. Turbulent kinetic energy increased small around the location of the lower aspect ratio, while more increased is observed on higher aspect ratio due to the recirculation and upward flow of oil and water from the cubical obstacle region.

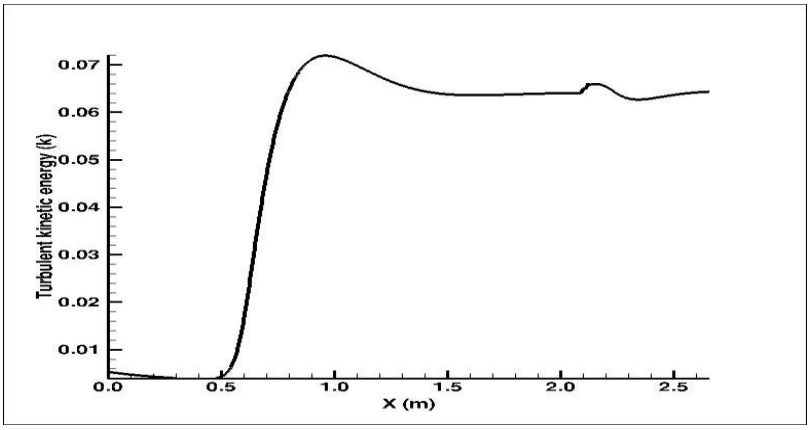

Figure 5.9: Turbulent kinetic energy at centre of the pipe for lower aspect ratio (case 6)

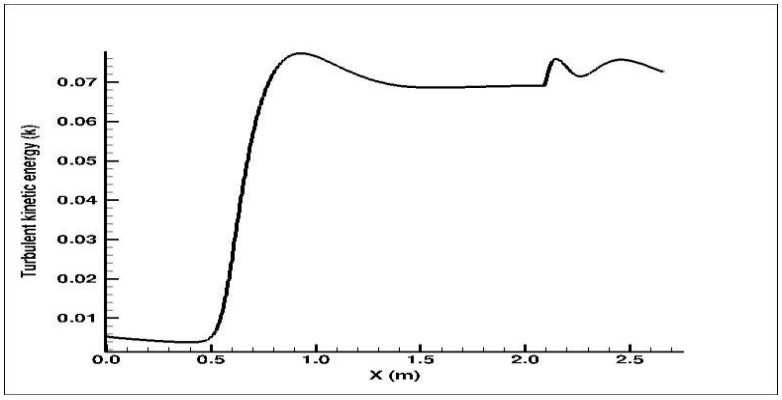

Figure 5.10: Turbulent kinetic energy at centre of the pipe for higher aspect ratio (case 8)

5.5.2 Flow description around cubical obstacle region

The oil-water flow in horizontal pipe with cubical obstacle is a simple geometry, but contains complicated flow structures. The study of flow structure in cubical obstacle is important in the analysis of oil-water entrainment, recirculation and water separation and settlement around the cubical obstacle and pipe walls. The predictions of turbulence multiphase flow of oil -water over cubical obstacle in horizontal pipe have not been reported in literature. Since no experimental results can substantiate the numerical results for oil-water flow in pipe with cubical obstacle at present, the flow structure obtained will be compared with the oil flow visualization experiments over obstacle.

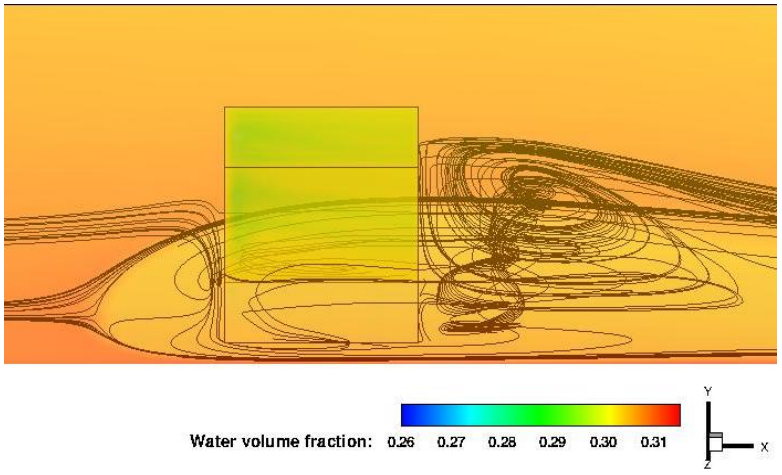

Figure 5.11: 3D view of lower aspect cubical obstacle showing stream traces and water volume fraction (case 6)

Figures 5.11 and 5.12 describe the flow structure in three- dimension of oil – water flow in horizontal pipe with cubical obstacle for lower and higher aspect ratio respectively. The oil-water flow separate in front and behind the cubical obstacle leads to formation of different type of vortices. The core vortex, which is named as horse-shoe vortex are infolds around the cubical obstacle forming a wake region, the vortex shape of the core vortex look like the horse-shoe for which the name of the vortex originated and is produced as result of effect of cubical obstacle in blocking the flow of oil-water causing the boundary layers experience an adverse pressure gradient. However, horse-shoe vortex generates high shear stress around the cubical obstacle region. As oil-water flow separate from the front corners of the cubical obstacle on the top and side walls; the flow does not reattach on the top of cubical obstacle but it appears to be reattach on the cubical side along the side walls, two vortices are detected. At the back of cubical obstacle, a large recirculation region is observed which interact with horse-shore vortex results to development of arch vortices (Martinuzzi and Trapea, 1993). It is observed that the size of recirculation region increases consistently with the size of wake as shown in figure 5.12.

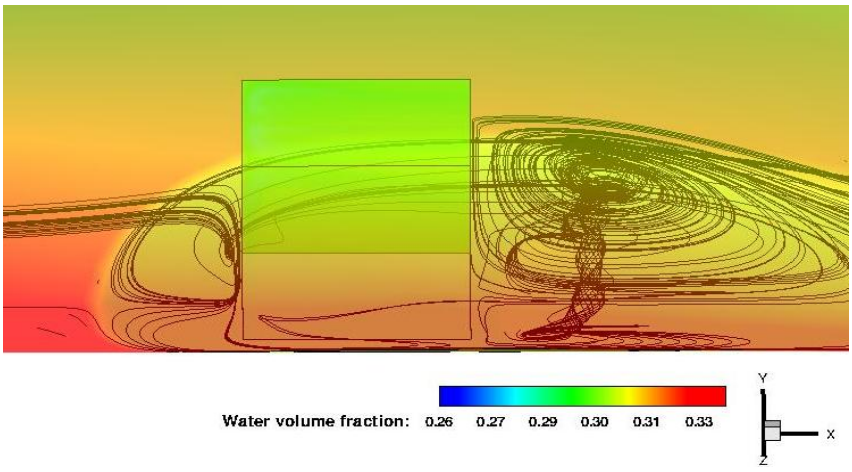

Figure 5.12: 3D view of higher aspect cubical obstacle showing stream traces and water volume fraction (case 8)

The distributions of water volume fraction at cubical obstacle regions in figure 5.11 and figure 5.12 indicate that water separate and settle in front of cubical obstacle and at pipe floor near the side walls due to effect of turbulent mixing

and action of gravity. However, more water is observed at arch vortex regions behind the cubical obstacle as a result of water separation from recirculation zone behind the cubical obstacle.

Figures 5.13 and 5.14 show the complex nature of the streamlines around the cubical obstacle floor which lead to the cubical obstacle creates an adverse pressure gradient lead to formation of horse-shoe vortex which produced converging and diverging flow pattern with the two separation regions at the front and behind the obstacle and also include the arch vortices originated from the recirculation region behind the obstacle. These near floor features resemble the experimental visualisation of Husseini and Martinuzzi (1996). In figure 5.13 for lower aspect ratio, the sizes of the vortices are small in comparison with the size of vortices of higher aspect ratio shown in figure 5.14; more water will tend to settle down in higher aspect ratio obstacle region than the lower aspect region. The wake region in higher aspect ratio cubical obstacle is larger compare with the wake in the lower aspect ratio because of difference in geometry parameters. Furthermore, the flow structures near the cubical obstacle of higher aspect ratio reveal additional vortices.

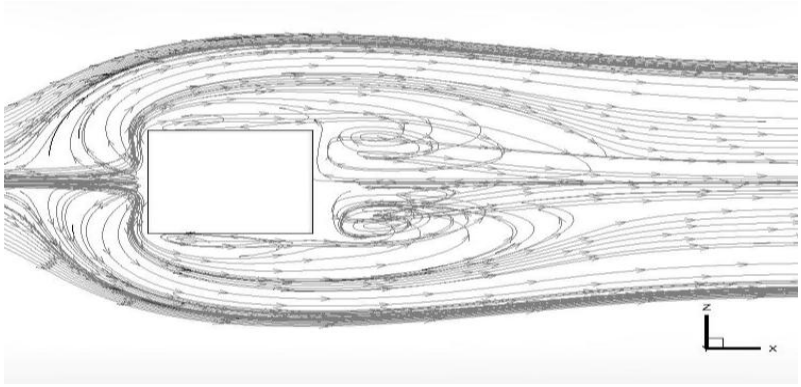

Figure 5.13: Streamlines near the pipe floor with cubical obstacle (lower aspect ratio, case 6)

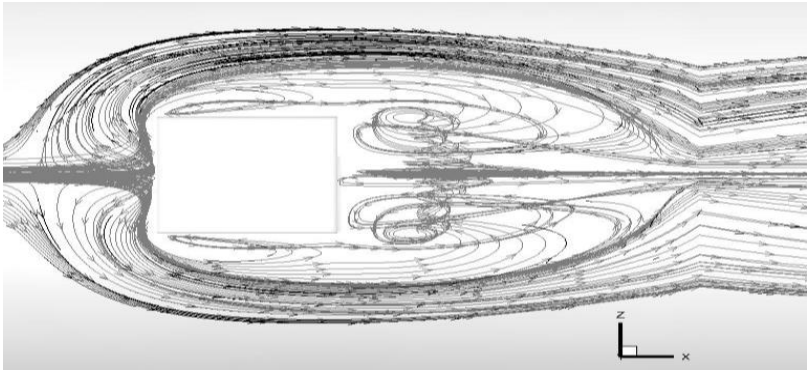

Figure 5.14: Streamlines near the pipe floor with cubical obstacle (higher aspect ratio, case 8)

Figure 5.15 depicts streamlines of lower aspect ratio cubical obstacle at a plane perpendicular to flow on x-y plane (z=0, Re=22000). The streamlines show the position of horse-shoe vortex in front base of the cube and the recirculation region behind the cubical obstacle, which is similar to experiment performed by Husseini and Martinuzzi (1996). There are two adjacent recirculation regions behind the cubical obstacle as shown in figure 5.14. To compare the streamlines of the two cubical obstacles, the regions of recirculation become more larger for the higher aspect ratio compared with lower aspect ratio, also the horse-shoe vortex in higher aspect ratio occupy large area when compared with lower aspect ratio due to difference in geometry parameters of cubical obstacles as shown in figure 5.16 below.

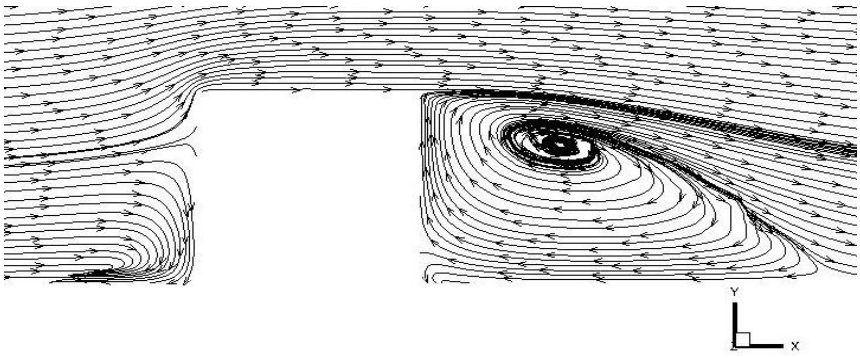

Figure 5.15: Streamlines at x-y plane perpendicular to flow (lower aspect ratio, case 6, Re=22000)

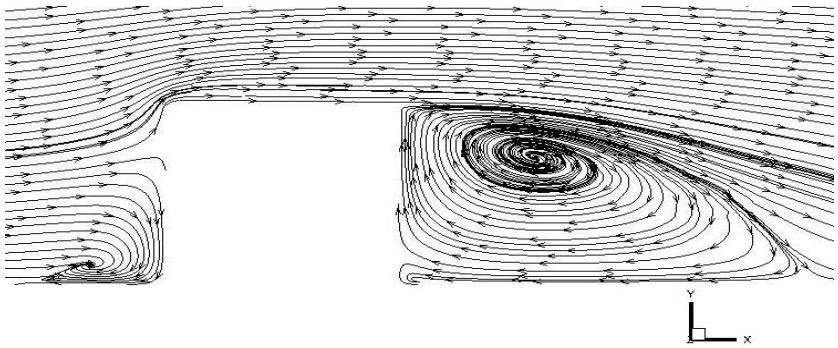

Figure 5.16: Streamlines at x-y plane perpendicular to flow (higher aspect ratio, case 8, Re=22000)

Figure 5.17 and figure 5.18 show the streamlines at z-y plane across the flow (x=2.109, Re=22000) for lower aspect ratio (case 6) and higher aspect ratio (case 8) cubical obstacle respectively. In figure 5.17, the streamlines show the flow separates at the sidewall of cubical obstacle, which leads to formation of horse-shoe vortex and vortices at sidewall. The same flow structures behaviours are observed for lower aspect ratio with only difference of eyes vortices which appear at the top of the cubical obstacle that is not present with higher aspect ratio cubical obstacle as demonstrated in figure 5.18.

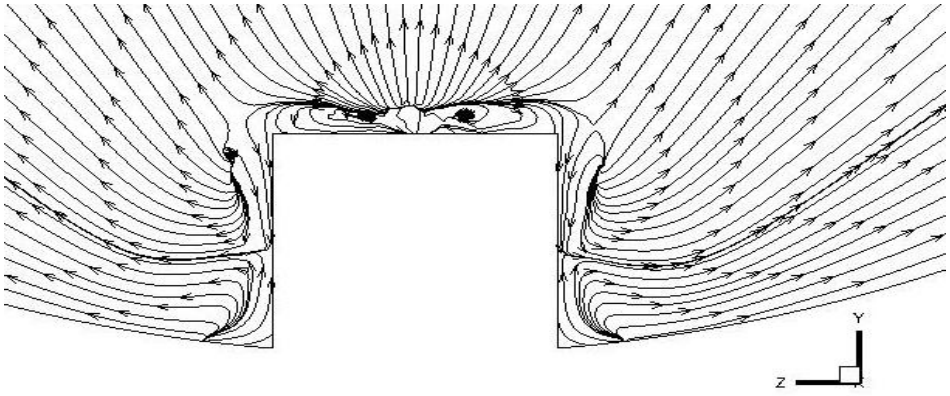

Figure 5.17: streamlines at z-y plane across the flow (lower aspect ratio, case 6, Re=22000)

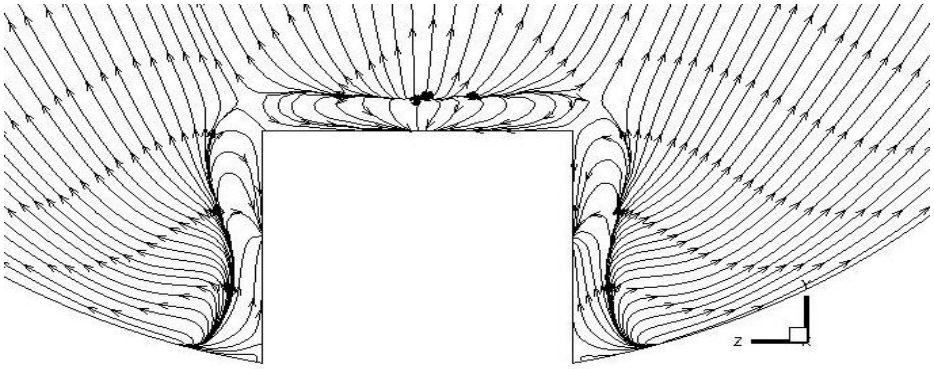

Figure 5.18: streamlines at z-y plane across the flow (higher aspect ratio, case 8, Re=22000)

The analysis of turbulent kinetic energy on oil-water flow in pipe with lower and higher cubical obstacle is presented below. Figure 5.19 shows the contour plots of turbulent kinetic energy at plane perpendicular to flow (z=0) for lower aspect ratio (case 6) and higher aspect ratio (case 8) of the same water volume fraction of 0.3 and Reynolds number of 22,000. Figure 5.19a shows the maximum turbulent intensity at the top front face of cubical obstacle and it decreases as flow move along the recirculation region behind the cubical obstacle and this indicate the area of maximum velocity, while in figure 5.19b, the maximum turbulent intensity occupied a large area at top front face of higher aspect ratio cubical obstacle and more turbulent intensity is observed and decreases along the recirculation region.

Figure 5.20 displays the contour plot of turbulent kinetic energy at plane across the flow (x=2.109) for lower aspect ratio (case 6) and higher aspect ratio (case 8). Figure 5.20a shows less turbulent intensity is observed at two opposite faces and at shear layer on top of the cubical obstacle, whereas more turbulent intensity is observed with higher aspect ratio in figure 5.20b.

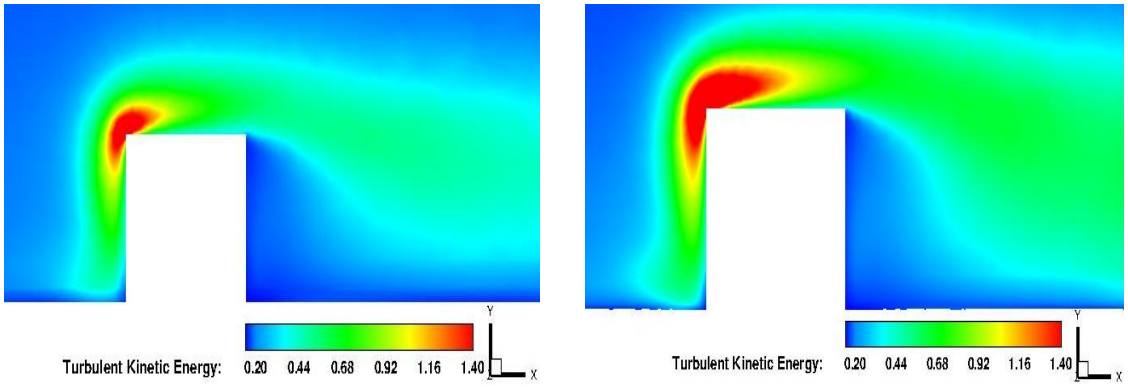

(a) Lower aspect ratio (Case 6) (b) Higher aspect ratio (case 8)

Figure 5.19: Turbulent kinetic energy at plane perpendicular to flow in cubical obstacle (x-y plane, Re=22,000)

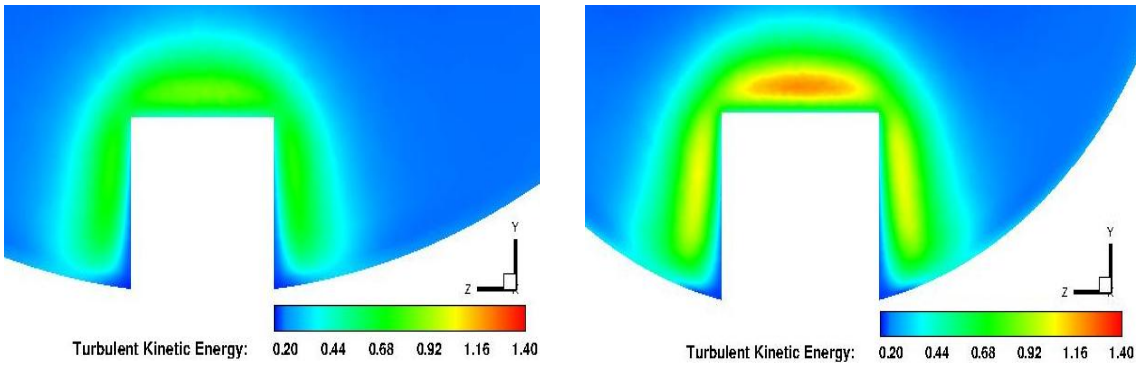

(a) Lower aspect ratio (Case 6) (b) Higher aspect ratio (case 8)

Figure 5.20: Turbulent kinetic energy at plane across the flow in cubical obstacle (z-y plane, Re=22,000)

The distribution of water volume fraction, velocity magnitude and turbulent kinetic energy at vortices region of sidewall and recirculation region behind the cubical obstacle are presented as the regions of interest because of associated change in flow features and will be investigated with line plots. A vertical line is drawn from the pipe base to top of the cubical obstacle at each position; the resulting profile will show the distribution of water volume fraction, velocity magnitude and turbulent kinetic energy along the line. The change in flow features are described below.

Figure 5.21 corresponds to the line plots of water volume fraction distribution along the recirculation region behind the cubical obstacle for lower aspect ratio (case 6) and higher aspect ratio (case 8) with the same value of water volume fraction of 0.3 and Reynolds number of 22,000. It can be seen in figure 5.21 for lower aspect ratio, the recirculation region start from y/H=0.5, at the vortex core, water fraction decrease to 0.29995 at obstacle height y/H=0.38 then finally increase to 0.3007 at the pipe base, while in case of higher aspect ratio, the recirculation region start from y/H=0.95, water start increasing from the vortex core at height y/H=0.8 to height y/H=0.2 then decrease by 0.001 and finally increase to 0.3025 at the pipe base. However, the line plots indicated that more water separate and settle behind the cubical obstacle of higher aspect ratio than the lower aspect ratio because the increase in aspect ratio lead to corresponding increase in area of recirculation region, more water are trap and separate by gravity to pipe base.

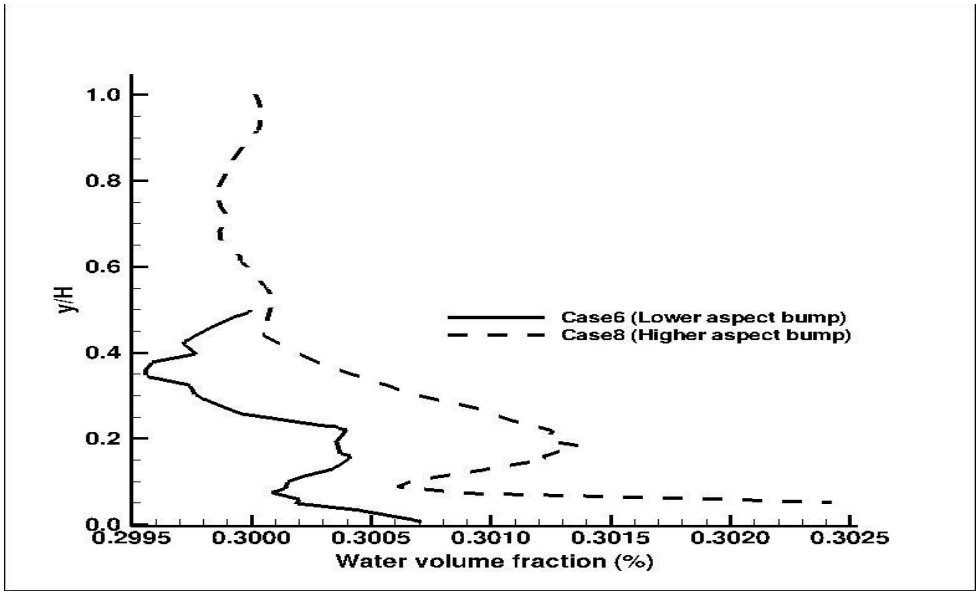

Figure 5.21: Water volume fraction at recirculation region behind cubical obstacle (Case 6 and 8)

Figure 5.22 shows the line plots of water volume fraction distribution profile at vortices region of side wall for lower and higher aspect ratio. It can be seen for lower aspect ratio, the water fraction decrease by 0.0018 from the top to half the height of cubical obstacle and suddenly increase to 0.3008 at the pipe base, in

case of higher aspect ratio, there is slight reduction of water fraction from the top to height y/H=0.6 then water fraction momentarily increase to 0.3025 at pipe base. The results revealed less water fraction are obtained at side wall for case 6 (lower aspect ratio) than case 8 (higher aspect ratio). Hence, the sidewall vortex has an influence on water distribution at pipe base. However, the comparisons of water at the side wall of pipe base with water at pipe base of arch vortex region behind the cubical obstacle suggest that more entrainment of water is found at the side wall due to the primary stage of separation.

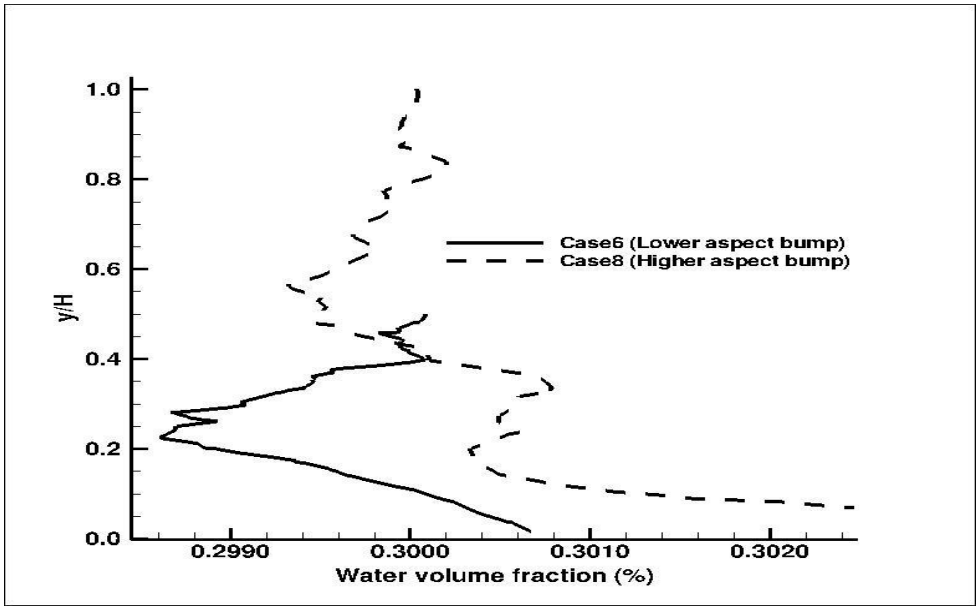

Figure 5.22: Water volume fraction at vortices region of side wall of cubical obstacle (Case 6 and 8)

The velocity profiles shown in figures 5.23 and 5.24 are for recirculation region and vortices region near the side wall which is related to the water volume fraction distribution in recirculation region and vortices region near the sidewall respectively. In figure 5.23 for lower aspect ratio (case 6), the velocity magnitude of 2.0m/s at the top decrease to 0.3m/s at cubical height of y/H=0.2 while for higher aspect ratio, the velocity of 2.6m/s at the top decrease to 0.2m/s at cubical height of y/H= 0.2. It can be deduced from the line plots of velocity magnitude that the flow has developed at recirculation region and the higher

aspect ratio has reduced velocity at pipe base and will likely contain more water. However, the velocity profile indicate water tend to settle down to pipe base because of the reduce velocity.

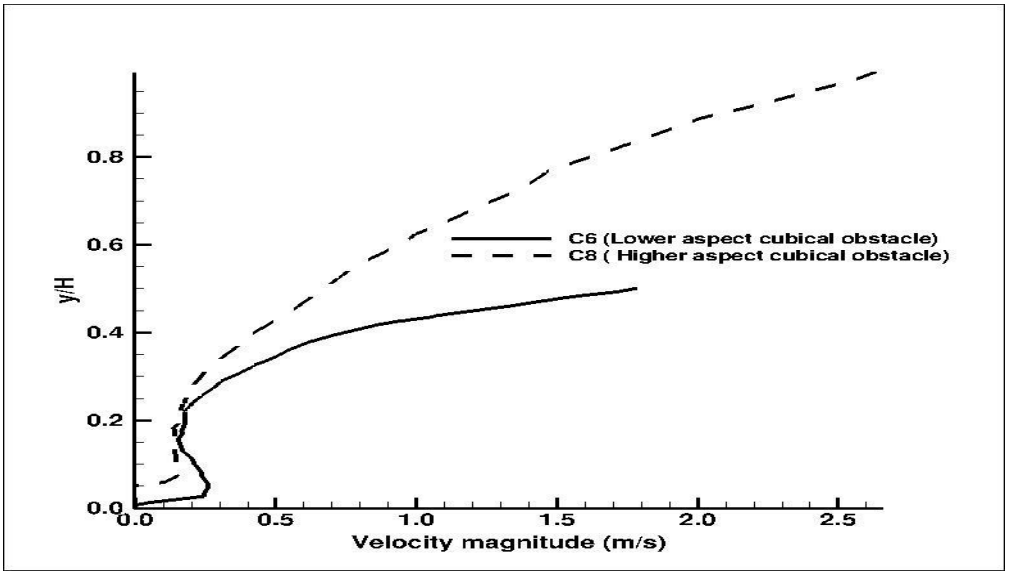

Figure 5.23: Velocity magnitude at recirculation region behind cubical obstacle (Case 6 and 8)

The velocity profile in figure 5.24 indicates similar flow behaviour with the velocity profile in figure 5.23, it can be seen that the profile at vortices region near the sidewall is slightly flat compare with velocity profile in recirculation region. The velocity at the top of cubical obstacle for case 6 (lower aspect ratio) and case 8 (higher aspect ratio) are 2.6m/s and 3.0m/s respectively, which are relatively high compare with the velocity magnitude at recirculation region for case 6 and case 8 as 2.0m/s and 2.6m/s respectively. These analyses suggest that the flow at the side wall of cubical obstacle has high velocity and the velocity reduce as the flow separate and recirculate behind the cubical obstacle. It can be observed that velocity decrease as the fluid mixture move from top to bottom of the cubical obstacle and this situation is favourable to water separation and settlement.

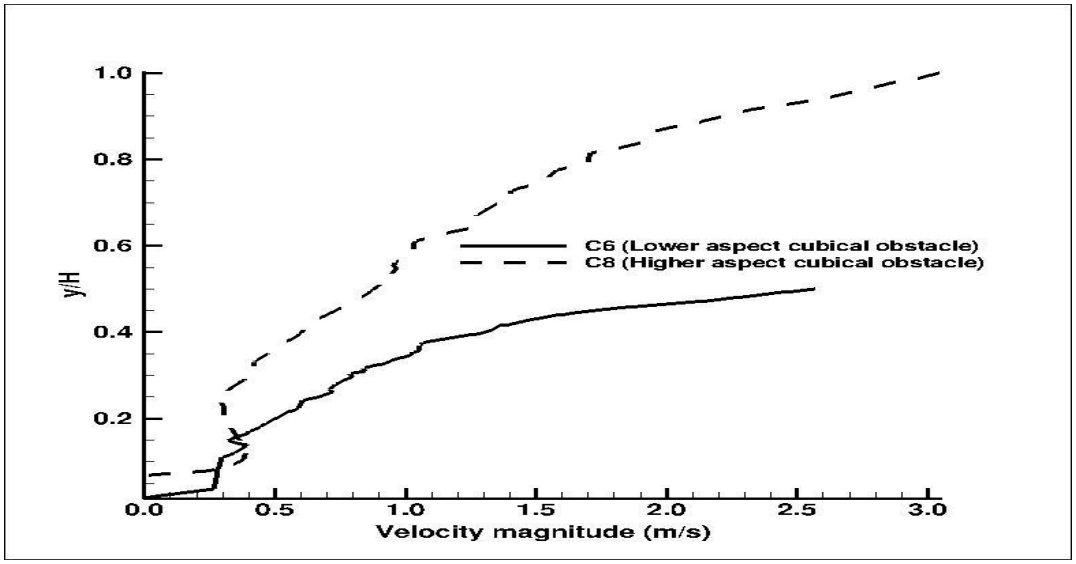

Figure 5.24: Velocity magnitude at vortices region of side wall of cubical obstacle (Case 6 and 8)

Figure 5.25 depicts turbulent kinetic energy at recirculation region behind the cubical obstacle for lower aspect ratio (case 6) and higher aspect ratio (case 8). It can be seen the turbulent kinetic energy for case 6 decreases from vortex core to pipe base which is analogous to velocity magnitude shown in figure 5.23, while turbulent kinetic energy in case 8 shows the maximum turbulent intensity in the vortex core region, where the recirculation is at maximum from then the turbulent kinetic energy decrease downward to zero at pipe wall, this flow behaviour is corresponding to velocity profile and water volume fraction line plots shown in figure 5.23 and figure 5.21.

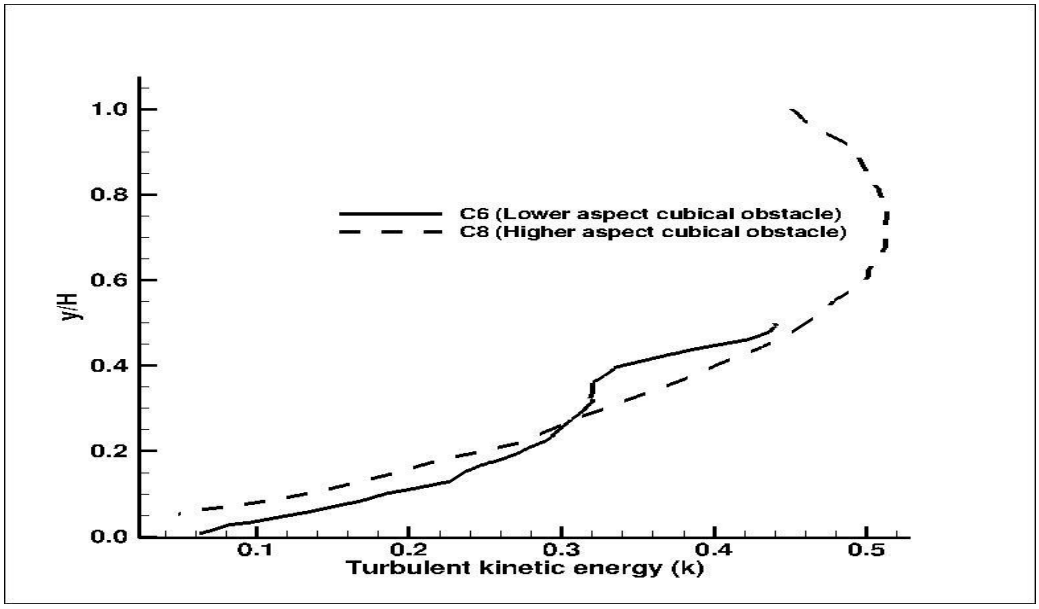

Figure 5.25: Turbulent kinetic energy at recirculation region behind cubical obstacle (Case 6 and 8)

The line plots of turbulent kinetic energy at vortices region near the side wall is presented in figure 5.26 for case 6 (lower aspect ratio) and case 8 (higher aspect ratio). For lower aspect ratio, from the top side of cubical obstacle, the turbulent kinetic energy increase from 0.8 to 1.0 at cubical height of y/H= 0.4 and decrease downward to pipe base, while for higher aspect ratio, from the top side of cubical obstacle, the turbulent kinetic energy increase from 1.2 to 1.4 at cubical height of y/H=0.8 then decreases downward to pipe base. It can be observed the turbulent kinetic energy beside the cubical obstacle of higher aspect ratio (case 8) is relatively high compare with the turbulent kinetic energy of lower aspect ratio (case 6). However, more turbulent intensity and mixing will be encountered in higher aspect ratio compare with lower aspect ratio. Figure 5.26 of turbulent kinetic energy is related to figure 5.24 of velocity magnitude which invariably indicate turbulent kinetic and velocity decrease downward; this will result to water separation and settlement to the bottom of pipe.

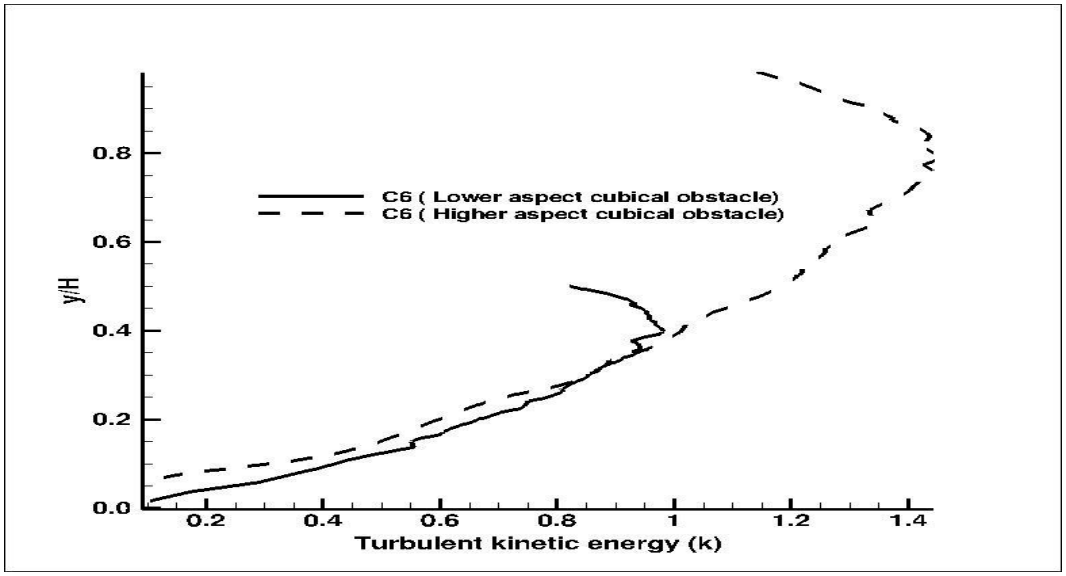

Figure 5.26: Turbulent kinetic energy at vortices region of side wall of cubical obstacle (case 6 and 8)

5.6 Effect of Reynolds number

For the effect of Reynolds number on oil-water flow in pipe with cubical obstacle, the cases with same aspect ratio and same input water volume fraction but difference in Reynolds number will be consider. The analysis will be performed using lower aspect ratio (case 1 and 5) and higher aspect ratio cubical obstacle (case 3 and 7) as shown in table 5.9. A mixture of contour and line plots will be used for the analysis. Figures 5.27 shows contour plots of turbulent kinetic energy on plane perpendicular to flow for cases 1, 5, 3 and 7 respectively. Figure 5.27a (case 1) and 5.27b (case 5) are the lower aspect ratio cases. In figure 5.27b with higher Reynolds number we can see that the region of high turbulence activity is larger at top front face and decrease along the recirculation region behind the cubical obstacle. This suggests that as the Reynolds number is increased, mixing increases in the pipe with cubical obstacle results in lower rates of separation of water from oil in the mixture. Figures 5.27a and 5.27b also disclose more turbulence at the top front side and recirculation region behind the cubical obstacle of high Reynolds number case as compare to the low Reynolds number case.

The increased in turbulent activity of high Reynolds number case will increase water entrainment. In the higher aspect ratio cases shown in figure 5.27c and figure 5.27d, the effect of Reynolds number is very clear. A slight difference is observed when we inspect planes across the flow for higher aspect ratio case (figures 5.28c and 5.28d). The region of high turbulent kinetic energy in these cases are at two lateral side walls and top of cubical obstacle, the turbulent kinetic energy is slightly higher for case 7 (figure 5.28d) than case 3 (figure 5.28c). From figures 5.27a to 5.27d, we can see that as a result of turbulence activities more mixing in the higher aspect ratio case than in lower aspect ratio case. It is reasonable to say that increasing the Reynolds number increases turbulent intensity.

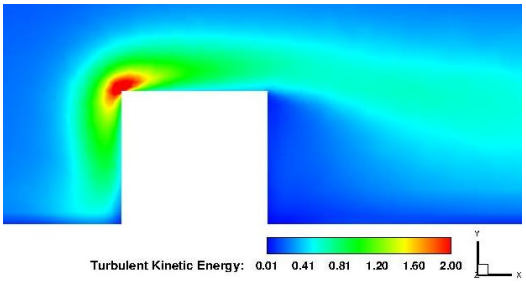

(a) Case 1

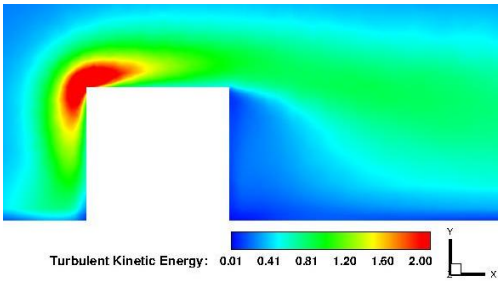

(b) Case 5

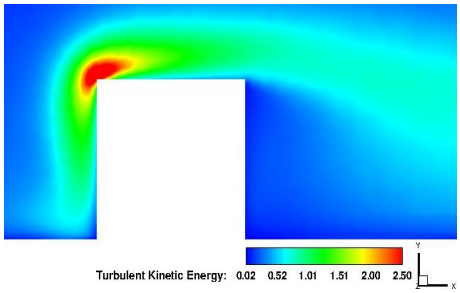

(c) Case 3

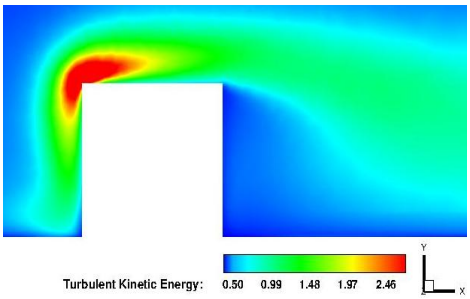

(d) Case 7

Figure 5.27: Turbulent kinetic energy at plane perpendicular to the flow (cases 1, 5, 3 and 7)

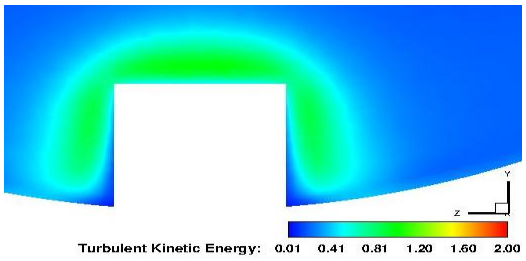

(a) Case 1

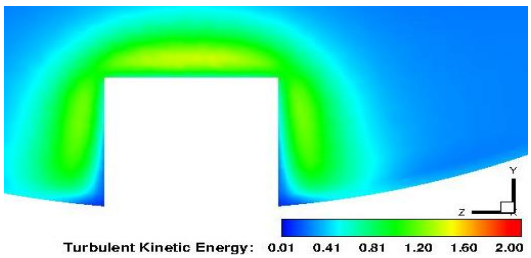

(b) Case 5

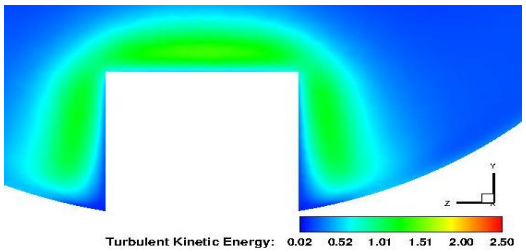

(c) Case 3

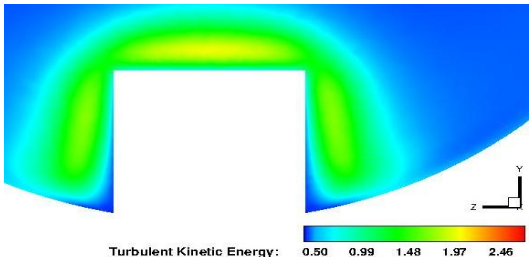

(d) Case 7

Figure 5.28: Turbulent kinetic energy at plane across the flow (cases 1, 5, 3 and 7)

The contour plots of water volume fraction for plane perpendicular and across the flow for case 1, 5. 3 and 7 are shown in figures 5.29 and 5.30 respectively. When we compared figures 5.29a and 5.29b of lower aspect ratio cubical obstacle, the maximum water volume fraction in contact with the pipe wall is about 0.110 for both cases. However, the water wetted area at the bottom front side of cubical obstacle is larger for the low Reynolds number case (figure 5.29a) compared to the higher Reynolds number case (figure 5.29b). Similarly for higher aspect ratio cubical obstacle in figures 5.30a and 5.30b, the water wetted surface area at the bottom front side of cubical obstacle is larger for the low Reynolds number case than for the high Reynolds number case. This is as a result of higher turbulence production and lower water cut. In figure 5.29c and 5.29d for lower and higher aspect ratio cases, the water wetted surface area at the bottom front side of higher cubical obstacle is smaller than for the lower aspect ratio case because of the difference in Reynolds number. Also, there is no significant difference in the maximum water volume fraction in contact with the pipe wall for the higher aspect ratio cases (figures 5.29c, 5.29d, 5.30c and 5.30d).

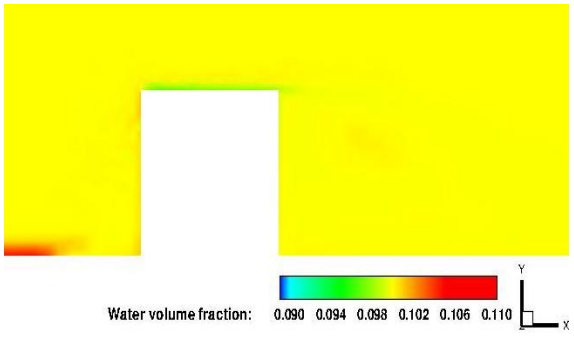

(a) Case 1

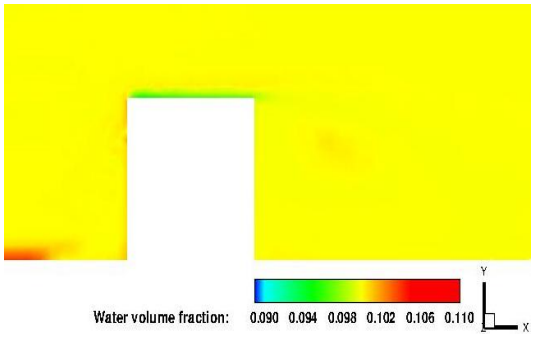

(b) Case 5

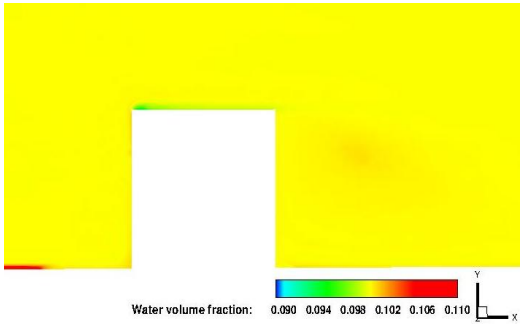

(c) Case 3

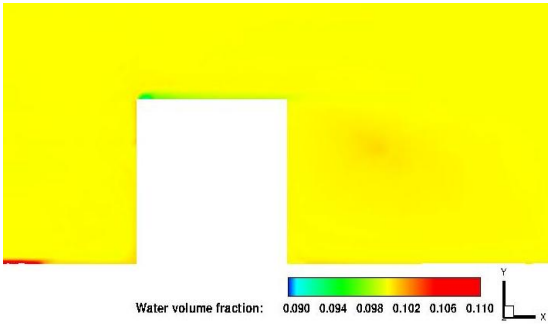

(d) Case 7

Figure 5.29: Water volume fraction at plane perpendicular to flow in cubical obstacle (Cases1, 5, 3 and 7)

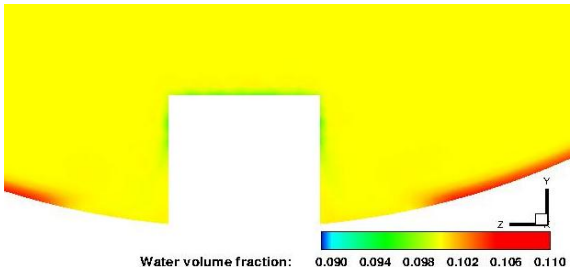

(b) Case 1

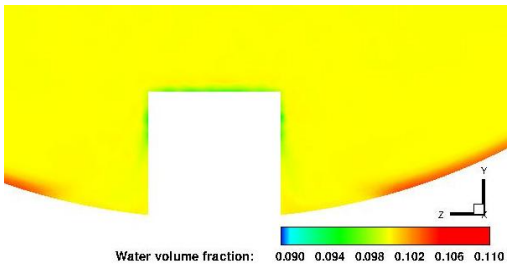

(b) Case 5

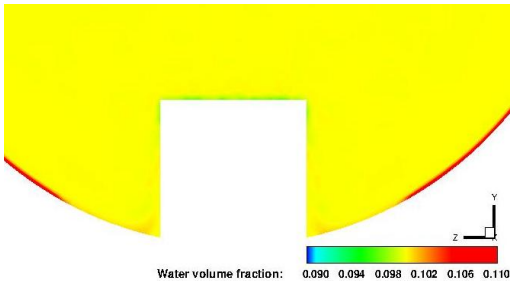

(c) Case 3

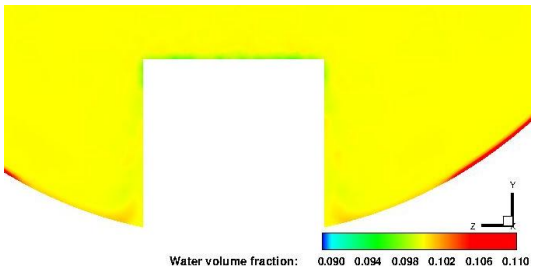

(d) Case 7

Figure 5.30: Water volume fraction at plane across the flow in cubical obstacle (Cases1, 5, 3 and 7)

The line plots of water volume fraction shown in figures 5.31 and 5.32 are for the effect of Reynolds number at recirculation region behind the cubical obstacles and at vortices region near the sidewall respectively. Figure 5.31a displays water fraction profile for lower Reynolds number case 1 (Re=18,500) and higher Reynolds number case 5 (Re=22000) at recirculation region. Along the two profiles, water fraction of 0.1 separate and entered recirculation regions from then decrease to 0.0998 at cubical height of y/H=0.7 then increase to 0.1003 at cubical height of y/H= 0.4 and decrease slightly to height of 0.2 and finally increase to 0.1004 at pipe base. It is observed at vortex core (y/H= 0.7) that water fraction is constant and the two line plots follow the same water distribution trends. However, more water separates and settles for low Reynolds number case 1 (Re=18,500) than higher Reynolds number case 5 (Re=22,000)) because of lower turbulence mixing associated with high water cut in low Reynolds number case.

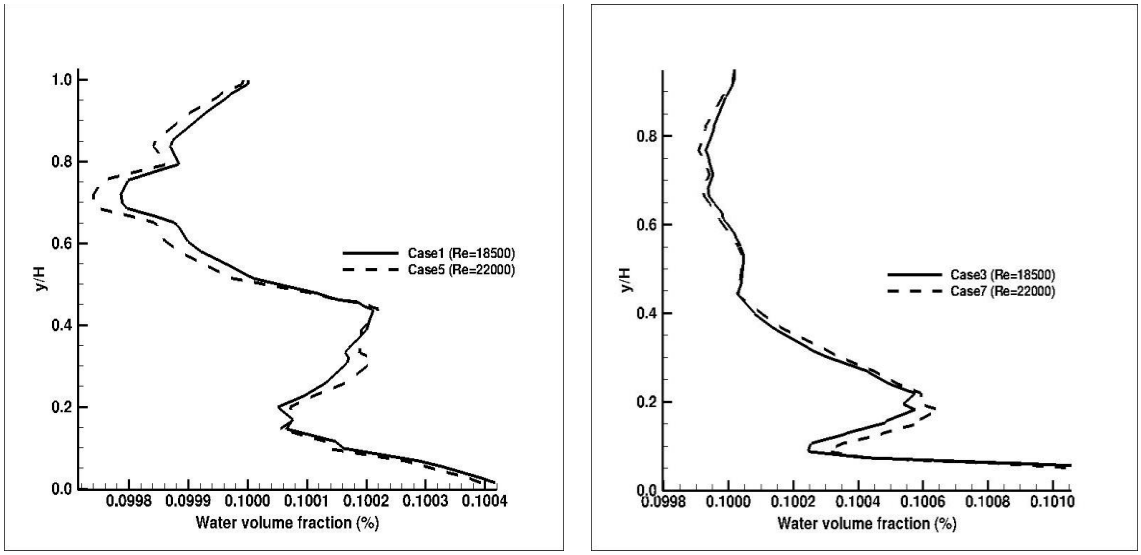

(a) Lower aspect ratio (b) Higher aspect ratio

Figure 5.31: Water volume fraction at recirculation region behind cubical obstacle for cases 1, 5, 3 and 7

Figure 5.31b shows the effect of Reynolds number on water distribution at recirculation region for lower Reynolds number case 3 (Re=18,500) and higher Reynolds number case 7 (Re=22,000). It can be seen from the line plots, water

separate and entered recirculation region at slight higher water fraction volume of 0.1001 and decrease to 0.1 at cubical height of y/H= 0.7, then water increase to 0.1006 at height of y/H= 0.2 and finally water fraction increase to 0.1010 at pipe base. It is observed there is slight difference between water distributions for the two line plots because of difference in Reynolds number. The distribution of water fraction at vortices region beside the sidewall for lower Reynolds number case 1 (Re=18,500) and higher Reynolds number case 5 (Re=22,000) are shown in figure 5.32a, in the line plots, the water fraction separate at high water volume fraction than the input water fraction and decrease to height of y/H= 0.5 then water increase to 0.1003 at pipe base. However, more water separate and settle with case of lower Reynolds number case 1(Re=18,500) than the case with higher Reynolds number case 5 (Re=22,000) and is attributed to high water entrainment by the moving oil in higher Reynolds number case.

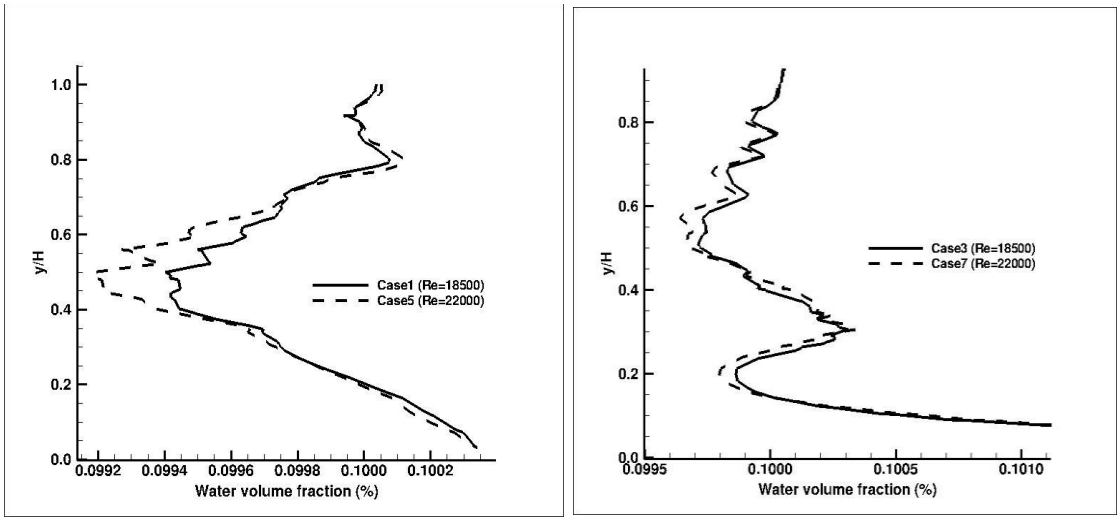

(a) Lower aspect ratio (b) Higher aspect ratio

Figure 5.32: Water volume fraction at vortices region of side wall of cubical obstacle for cases 1,5,3 and 7

The cases with higher aspect ratio at vortices region of sidewall are given in figure 5.32b, the line plots display the effect of Reynolds number for case 3 (Re=18,500) and case 7 (Re=22,000), water separate from the side wall and

decrease to height of y/H = 0.2 and then increase to 0.1010 at cubical height of y/H= 0.1. It is observed that the difference in water fraction separation and settlement between the low and high Reynolds number case beside the side wall is small and it can be ascribed to the initial stage of water separation and settlement.

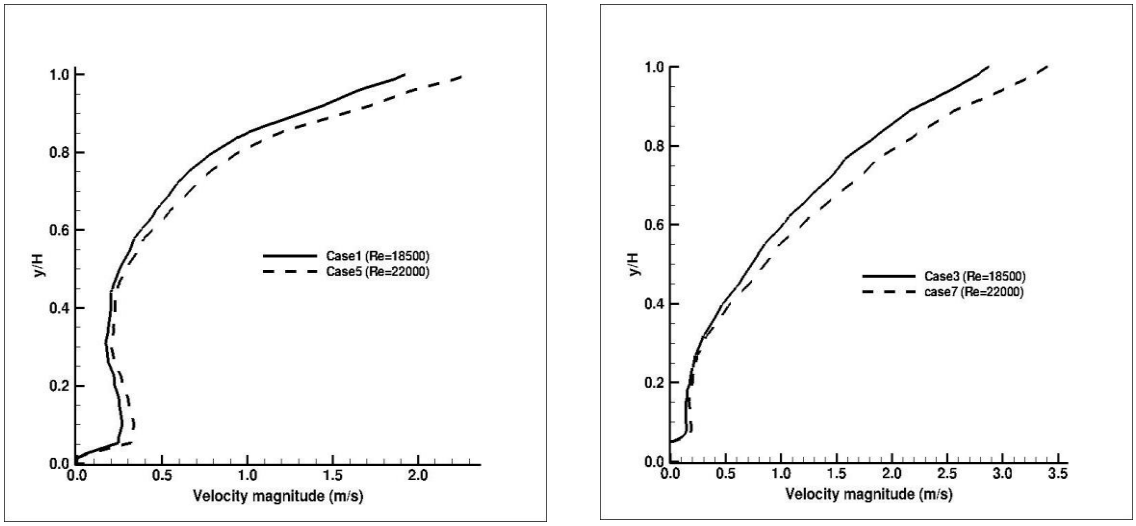

(a) Lower aspect ratio (b) Higher aspect ratio

Figure 5.33: Velocity magnitude at recirculation region behind the cubical obstacle for cases 1, 5, 3 and 7

The effects of Reynolds number on velocity profile at recirculation region behind the cubical obstacles are given in figure 5.33. For lower aspect ratio case in figure 5.33a, the oil and water mixture separates at velocity of 2.0m/s for low Reynolds number case 1 (Re=18500) and at velocity of 2.3m/s for high Reynolds number case 5 (Re=22000). In the two profiles, the velocity decreases downward to pipe base. The velocities difference between the two cases is large from top of obstacles to middle, while the velocities difference at lower height of the obstacles is small. Figure 5.33b is for higher aspect ratio, the velocity is quite high at separation region for the two profiles. However, separation velocity of 3.2m/s is observed for low Reynolds number case 3 and separation velocity of 3.5m/s for high Reynolds number case 7. It can be seen that the flow highly developed and velocities decrease downward to pipe base, this condition is favourable for water settlement.

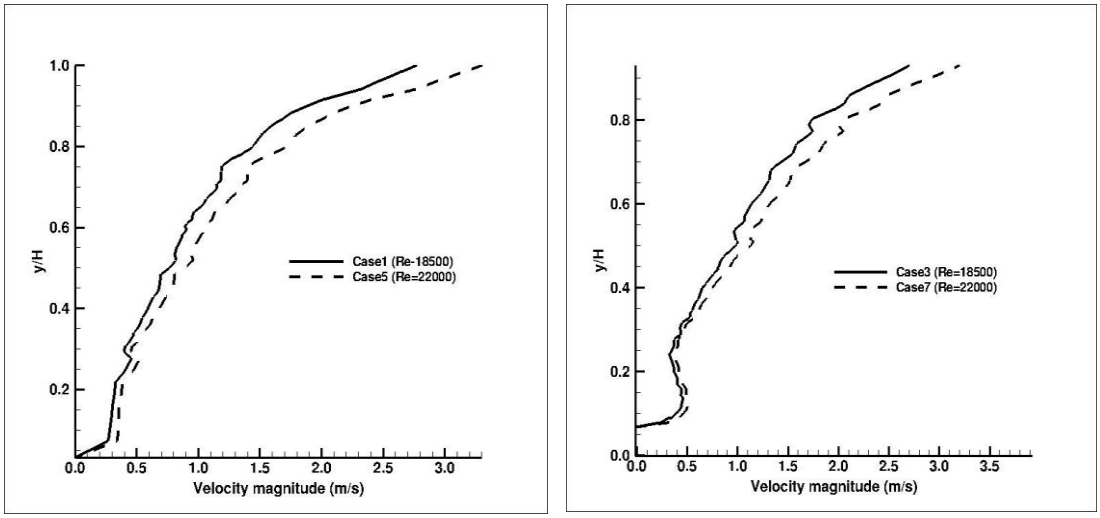

(a) Lower aspect ratio (b) Higher aspect ratio

Figure 5.34: Velocity magnitude at vortices region of sidewall of cubical obstacle for cases 1, 5, 3 and 7

Figure 5.34 shows the velocity profile for lower and higher aspect ratio at vortices region near the sidewall. figure 5.34a shows the effect of Reynolds number on lower aspect ratio. For low Reynolds number case 1(Re=18,500) and high Reynolds number case 5 (Re=22,000), the velocity at separation region of 3.0m/s is observed for low Reynolds number case1 and velocity of 3.5m/s for high Reynolds number case 5. The velocity profile is relatively linear and the velocity decreases downward and the difference between the two velocities profile is evident, Similar line plot trends for velocity profile for higher cubical obstacle are observed with significant difference in maximum velocity at separation region and at the sidewall when compared with lower aspect ratio.

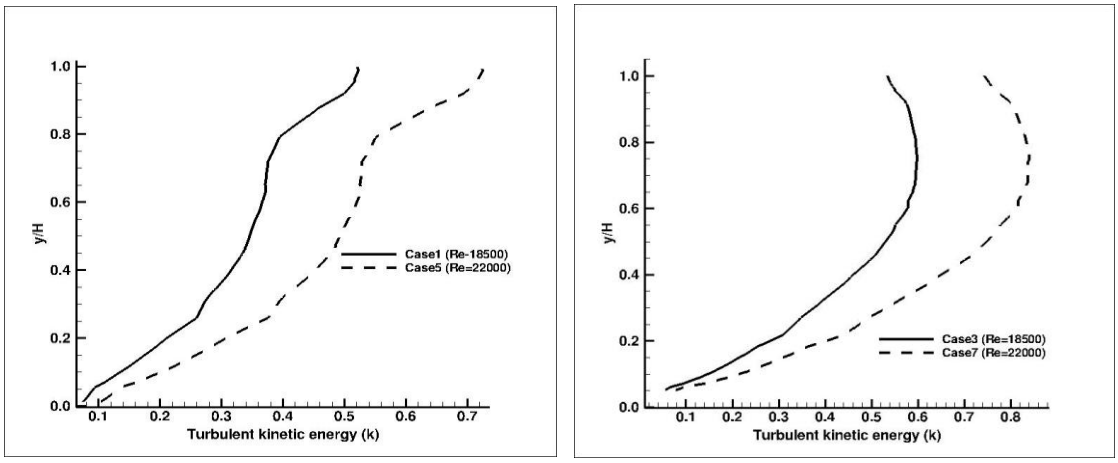

(a) Lower aspect ratio (b) Higher aspect ratio

Figure 5.35: Turbulent kinetic energy at recirculation region behind the cubical obstacle (cases 1, 5, 3 and 7)

The turbulent kinetic energy of low and high Reynolds numbers at recirculation region is given in figure 5.35. The turbulent kinetic energy is maximum at the top of cubical obstacle and decrease downward as shown in figures 5.35a and 5.35b, the turbulent activity is less with case of low Reynolds numbers (case1 and case 3) compared with case of high Reynolds numbers (case 5 and case 7). The turbulent kinetic energy line plots indicate the difference between the two profiles, higher turbulent activity are observed for high Reynolds number cases than the low Reynolds number cases because the high Reynolds number promotes more turbulence mixing.

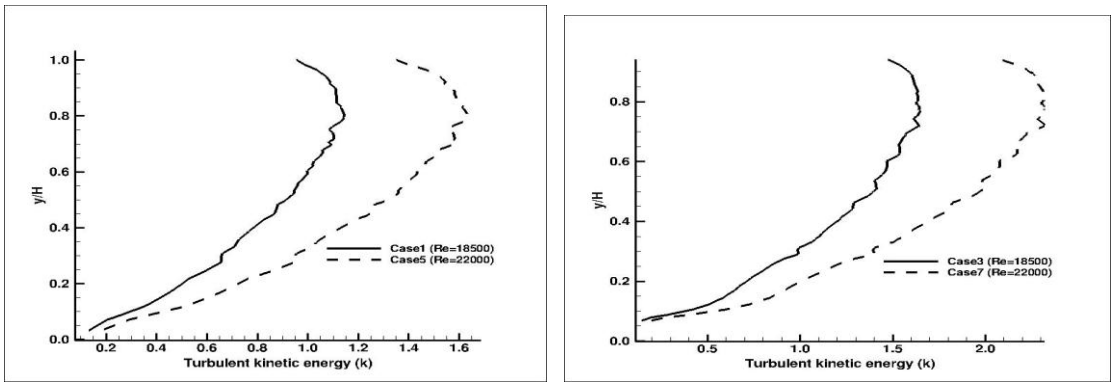

(a) Lower aspect ratio (b) Higher aspect ratio

Figure 5.36: Turbulent kinetic energy at vortices region of sidewall of cubical obstacle (cases1, 5, 3 and 7)

Figure 5.36 displays turbulent kinetic energy at vortice region near the sidewall of lower and higher aspect ratio cases for lower and higher Reynolds number cases. It is observed that the turbulent kinetic energy profiles show the same trend behaviour, the turbulent intensity is higher at top of obstacle and decrease downward, the difference between the turbulent kinetic energy of low and high Reynolds number is quite evident. Figure 5.36a displays turbulent kinetic energy of lower aspect ratio cubical obstacle for case 1 (Re=18,500) and case 5 (Re=22,000). For low Reynolds number case 1(Re=18,500), turbulent kinetic energy increase from 0.8 to 1.0 at cubical height of y/H=0.8 then decrease to 0.2 at the bottom of the pipe. The high Reynolds number case 5 (Re=22,000), turbulent kinetic energy increase from 1.4 to 1.6 at cubical height of y/H=0.8. However, figure 5.36b indicates that higher aspect ratio produces high turbulent kinetic energy in both low and high Reynolds number cases compared with lower aspect ratio cases.

5.7 Effect of input water volume fraction

In order to study the effect of input water volume fraction, the two cases each of lower aspect ratio and higher aspect ratio of cubical obstacle will be examine. The investigation will be done using lower aspect ratio cases (case 1 and case 2) and higher aspect ratio cases (case 7 and case 8) as presented in table 5.9. For the analysis, a combination of contour plots and line plot will be used. Figures 5.37a to 5.37d show contour plots of turbulent kinetic energy on plane perpendicular to flow for cases 1, 2, 7 and 8 respectively. In the lower aspect ratio cases (case 1 and case 2), it can be seen that the higher the input water volume fraction, the lower the turbulence production as shown in figures 5.37a and 5.37b. This is ascribed to water which has higher inertia. As a result, the mixture density of the bulk fluid is denser for the high water volume fraction case than lower water volume fraction. Hence, the turbulent kinetic energy is higher for low water volume fraction case because the amount of energy required to accelerate the oil component of the multiphase mixture is lower as a result the case with more oil results in more turbulence production compared to the case with more water.

Figures 5.38a and 5.38b show plane across the flow which indicates that less turbulence is produced when the input water volume fraction is increased. Higher aspect ratio cases (figures 5.37c, 5.37d, 5.38c and 5.38d) do reveal slight significant difference in turbulence activity. However, in figure 5.38c and 5.38d, the area of high turbulence is slightly higher for the low water volume fraction case compared to the low Reynolds number case shown in figure 5.38a and 5.38b. This flow behaviour has an effect on the rate at which water settles to the area around the cubical obstacle, since less turbulence favours water separation.

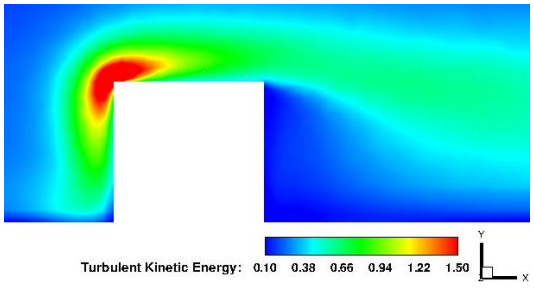

(a) Case1, water fraction=0.1

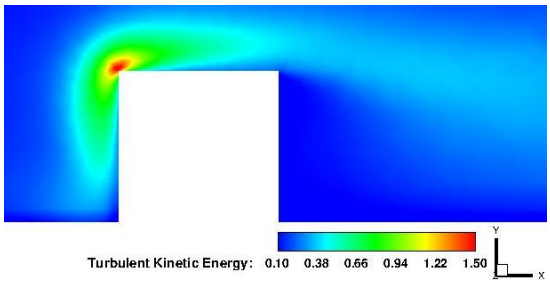

(b) Case 2. Water fraction=0.3

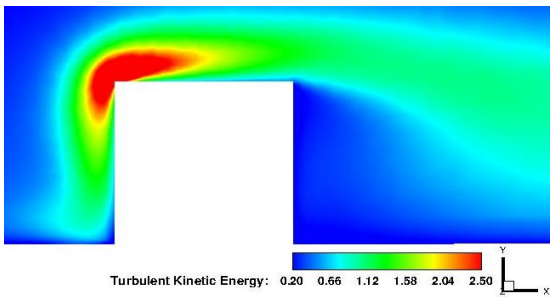

(c) Case 7, water fraction=0.1

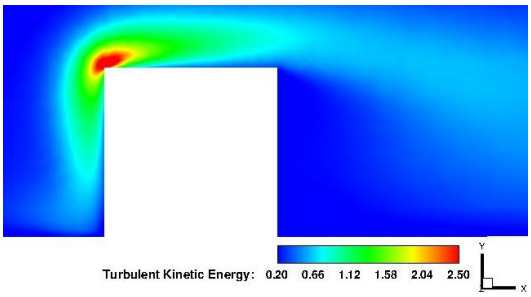

(d) Case 8, water fraction=0.3

Figure 5.37: Turbulent kinetic energy at plane perpendicular to flow in cubical obstacle (Cases 1, 2, 7 and 8)

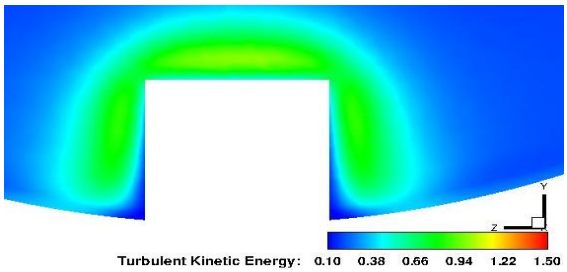

(a) Case1, water fraction=0.1

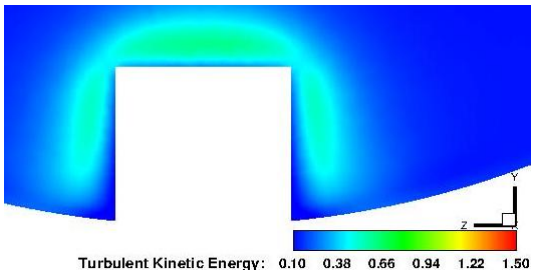

(b) Case 2, Water fraction=0.3

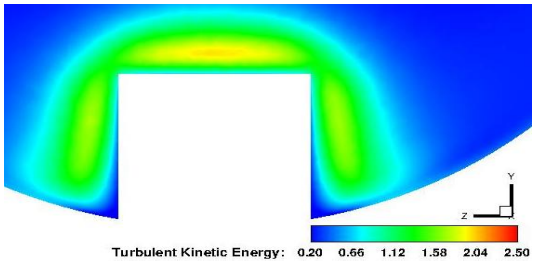

(c) Case 7, water fraction=0.1

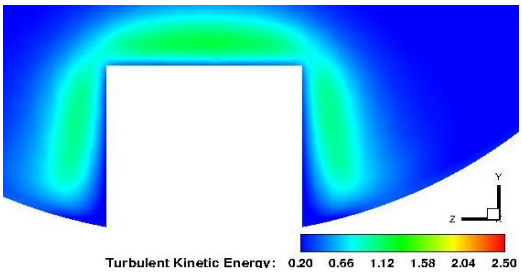

(d) Case 8, water fraction=0.3

Figure 5.38: Turbulent kinetic energy at plane across the flow in cubical obstacle (Cases1, 2, 7 and 8)

The effect of input water volume fraction on oil- water flow in pipe with cubical obstacle is presented in figure 5.39 and 5.40 below. Figure 5.39 is the contour plots of water volume fraction at plane perpendicular to flow for case 1, 2. 7 and 8. When we compare figures 5.39a and 5.39b of lower aspect ratio cubical obstacle with input water volume fraction of 0.1 and 0.3 respectively, the case with high input water fraction (Water fraction=0.3) has large area wetted by water compare with low input water fraction (water fraction=01) while for both cases water bubble appeared at the top of cubical obstacle and at recirculation region behind the cubical obstacle. Similar results can be seen in figures 5.39c and 5.39d for higher aspect ratio cubical obstacle. In all the cases, the maximum water fraction for low input water fraction is 0.110 while for high input water fraction is 0.32.

Figure 5.40 displays contour plots for water fraction at plane across the flow for lower aspect ratio cases (figures 5.40a and 5.40b) and higher aspect ratio cases (figures 5.40c and 5.40d). In the higher and lower aspect ratio cases, large area of pipe wall at the bottom front of pipe are wetted by water more for high input water fraction (water fraction=0.3) compare with low input water fraction (water fraction=0.1) and water bubble tend to concentrate more on cases with low input water fraction at the top and side walls of cubical obstacle and this may be attributed to low turbulence activities because of reduction in bulk density of the oil-water mixture. From this investigation of effect of input water fraction, it can be deduce that increase in input water volume fraction leads to higher rate of water separation from oil and settlement at the pipe base and decrease in input water volume fraction promotes water entrainment in the moving oil which produces less water at the pipe base.

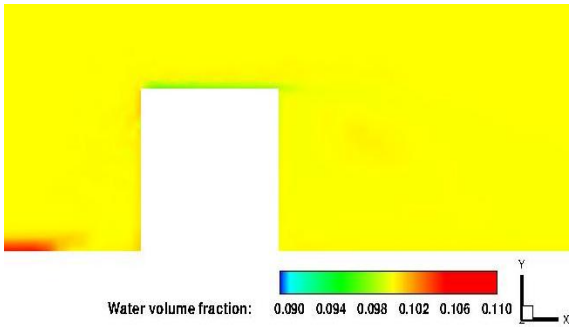

(a) Case1, water fraction=0.1

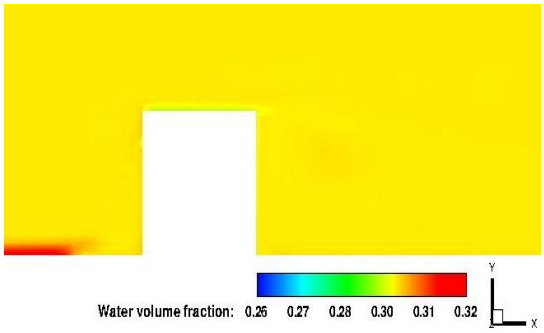

(b) Case 2, water fraction=0.3

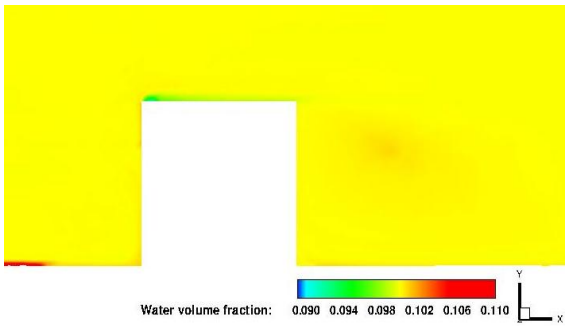

(c) Case 7, water fraction=0.1

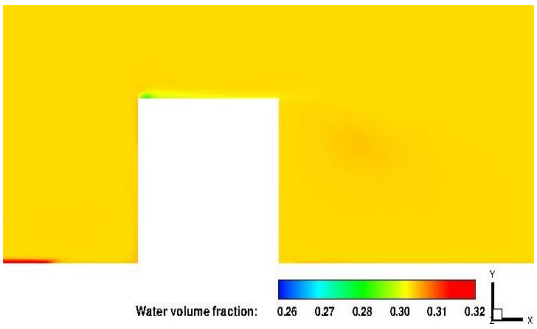

(d) Case 8, water fraction=0.3

Figure 5.39: Water volume fraction at plane perpendicular to flow in cubical obstacle (Cases 1, 2, 7 and 8)

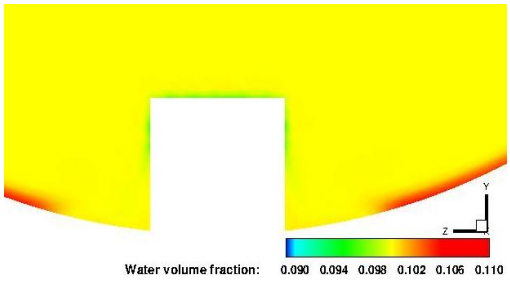

(a) Case1, water fraction=0.1

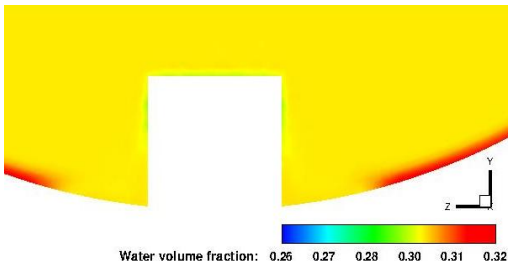

(b) Case 2, water fraction=0.3

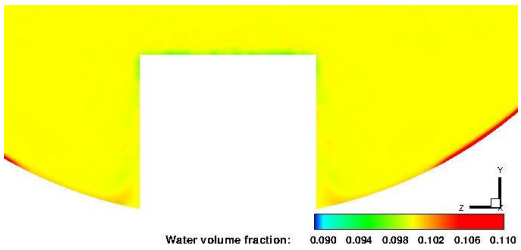

(c) Case 7, water fraction=0.1

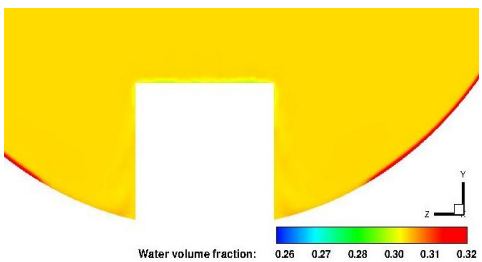

(d) Case 8, water fraction=0.3

Figure 5.40: Water volume fraction at plane across the flow in cubical obstacle (Cases 1, 2, 7 and 8)

The line plots in figures 5.41 and 5.42 show the effect of input water fraction on water separation from oil at recirculation region behind the cubical obstacle and at vortices region beside the sidewall side respectively. Figures 5.41a and 5.41b is the line plots of lower aspect ratio at recirculation region behind cubical obstacle for case 1 (water fraction=0.1) and case 2 (water fraction=0.3) respectively. The line plots indicate the same water distribution pattern, water separate and entered recirculation region, for low input water volume fraction entered at water volume fraction of 0.1 and for high input water fraction at water volume fraction of 0.3. The line plots show the same height of vortex core at cubical height of y/H= 0.7, water fraction at vortex core for low input water fraction is 0.0998 and for high input water fraction is 0.2996, from the vortex core, water increase to cubical height of 0.4 then decrease by 0.0002 to height y/H= 0.2 and finally water increase to 0.1004 at pipe base. Similarly, for high input water fraction of 0.3, water increase from vortex core to cubical height of y/H= 0.4 and decrease by 0.0003 at cubical height of y/H= 0.2 then finally increase to 0.3008 at pipe base. It can be stated that increase in input water volume fraction lead to more water separation and distribution at pipe base of recirculation region, less water are observed at vortex core because of high velocity at the region.

For higher aspect ratio, the effects of input water fraction are shown in figures 5.41c and 5.41d below, water separate and entered the recirculation region behind the obstacle. For low input water fraction (case 7) water separate at water fraction of 0.1 while for high input water fraction (case 8) water separate at water volume fraction of 0.3. The water volume fraction profiles have the same water distribution trends, the vortices core appeared at cubical height of y/H= 0.8. For low input water fraction case (case 7) water increase by 0.0006 to height of y/H= 0.2, and decrease by 0.0004 then finally water increase to 0.1010 at pipe base, while for high input water fraction case (case 8), water increase by 0.0015 at cubical height of y/H=0.2 and decrease by 0.0001 then finally increase to 0.3022 at pipe base. It is observed that the increase in input water fraction leads to water segregates faster and water fraction is higher for

higher aspect ratio case than the lower aspect ratio case because of increase in area of recirculation region behind the cubical obstacle.

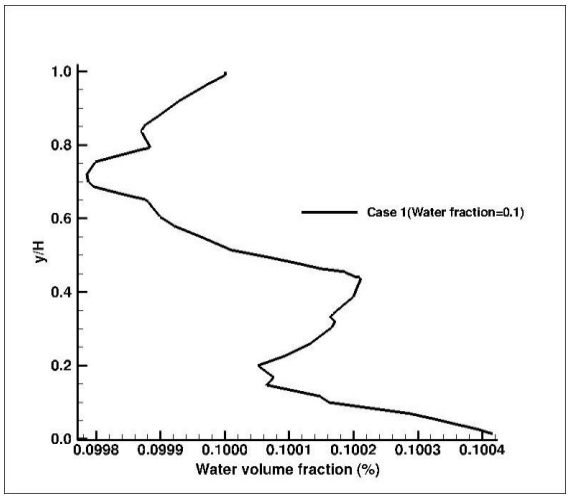

(a) Case 1, lower aspect ratio

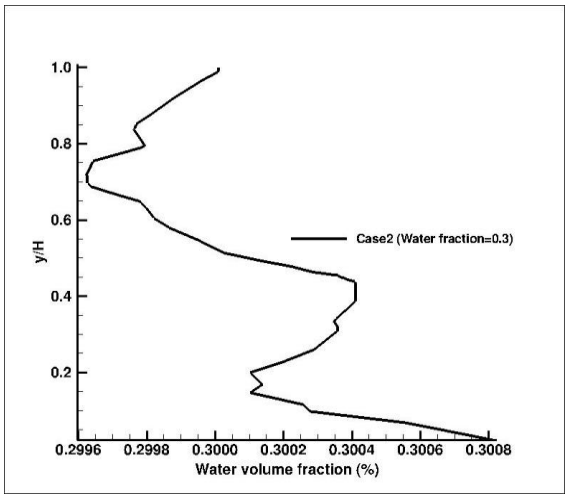

(b) Case 2, lower aspect ratio

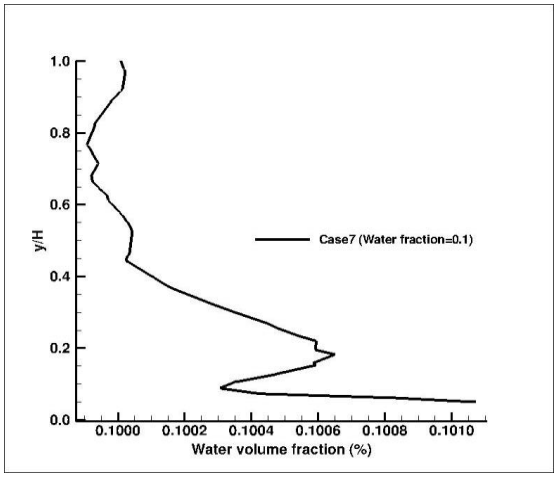

(c) Case 7, higher aspect ratio

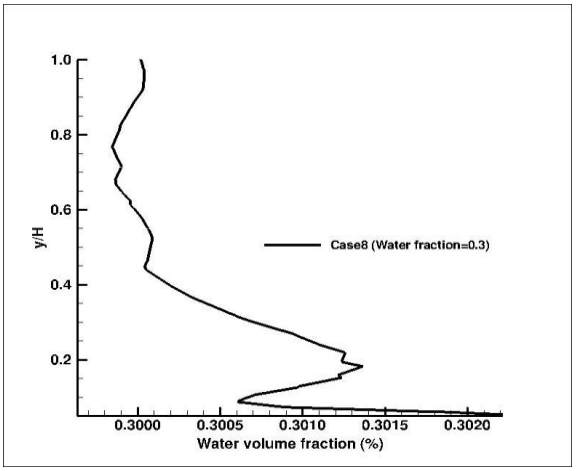

(d) Case 8, higher aspect ratio

Figure 5.41: Water volume fraction at recirculation region behind cubical obstacle (cases1, 2, 7 and 8)

The effects of input water volume fraction at vortices region beside the sidewall are shown in figure 5.42. Figures 5.42a and 5.42b are the line plots for lower aspect ratio case 1(water fraction=0.1) and case 2 (water fraction ratio=0.3) respectively. In the line plots, water separate at high water volume fraction than the input water volume fraction then decrease downward. For low input water fraction case (case 1) water fraction decrease up to height of y/H=0.5 then increase to 0.1004 at pipe base, while for high input water fraction case, water

fraction decrease to cubical height of y/H=0.7 and then increase by 0.0006 at height y/H 0.4 then decrease slightly and finally to 0.3008 at pipe base.

While figures 5.42c and 5.42d are the line plots for effect of input water volume fraction on higher aspect ratio case 7 (water fraction=0.1) and case 8 (water fraction=0.3) respectively. In the water volume fraction profiles, water separate at the side walls at high water fraction than the input water volume fraction from then decrease to cubical height of y/H=0.6 then suddenly increase by 0.0008 to cubical height of y/H= 0.3 for case 7 (water fraction=0.1) and by 0.0015 for case 8 (water fraction=0.3), the two line plots decrease slightly to height y/H=0.2 then finally to 0.1013 and 0.3020 at the pipe base for case 7 and case 8 respectively. It can be seen that water tends to segregate faster for high input water volume fraction case 8 than the low input water fraction case 7.

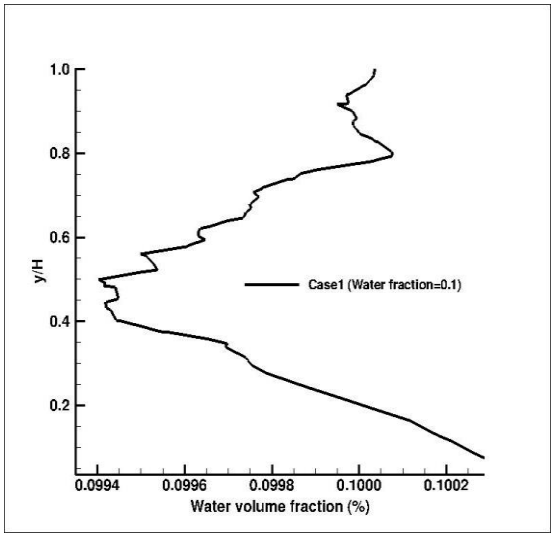

(a) Case 1, lower aspect ratio

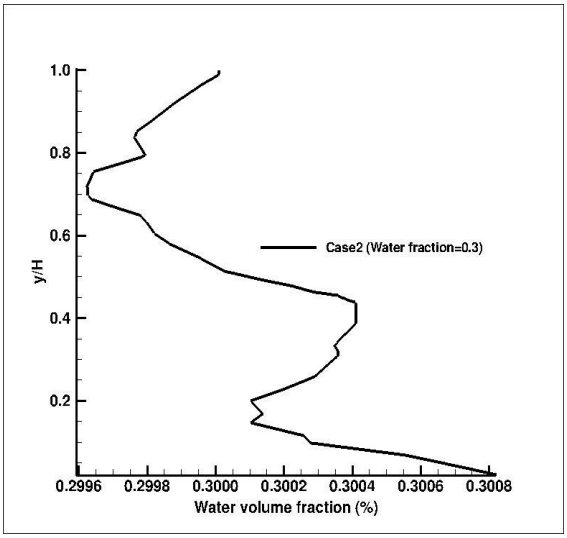

(b) Case 2, lower aspect ratio

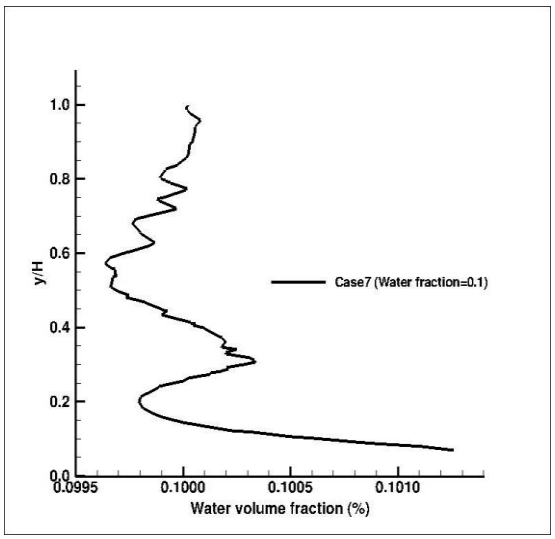

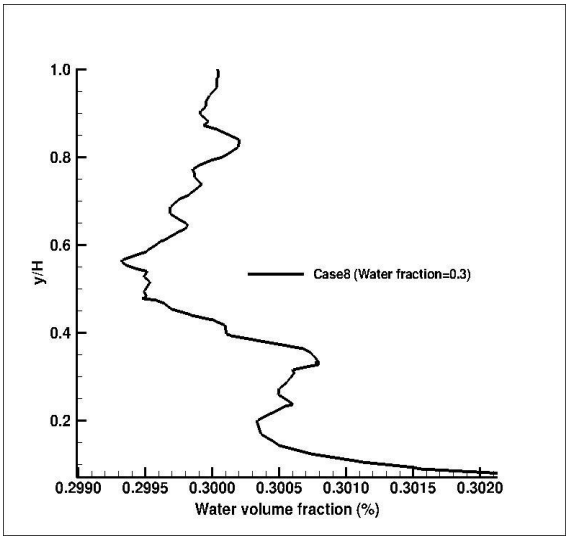

(c) Case 7, higher aspect ratio (d) Case 8, higher aspect ratio

Figure 5.42: Water volume fraction at vortices region of side wall of cubical obstacle (cases 1, 2, 7 and 8)

Figure 5.43 shows the velocity profile at recirculation region behind the cubical obstacle for lower aspect ratio case (figure 5.43a) and higher aspect ratio case (figure 5.43b). In figure 5.43a the case with low input water volume fraction (case 1); the velocity at separation region is high, the fluid separates at velocity of 2.0m/s for low input water volume fraction compared with velocity of 1.5m/s for high input water volume fraction (case 2) and the two velocity profiles decrease downward. For high input water volume fraction of case 2 (water fraction=0.3) the velocity is generally less along the profile line compared with low input water volume fraction of case 1. The higher aspect ratio cases are shown in figure 5.43b (cases 7 and 8), it can be seen that the velocities are generally higher than the lower aspect ratio cases (cases 1 and 2) and the velocity decrease downward from the separation region, the case with low input water volume fraction (case7) the separation velocity is 3.5m/s while the case with high input water volume fraction (case8) the separation velocity is 2.5m/s. However, it can be concluded that the velocity of separation along the line for low input water fraction case has high velocity compared with high input water fraction case; this is attributed to the difference in bulk density of the mixture.

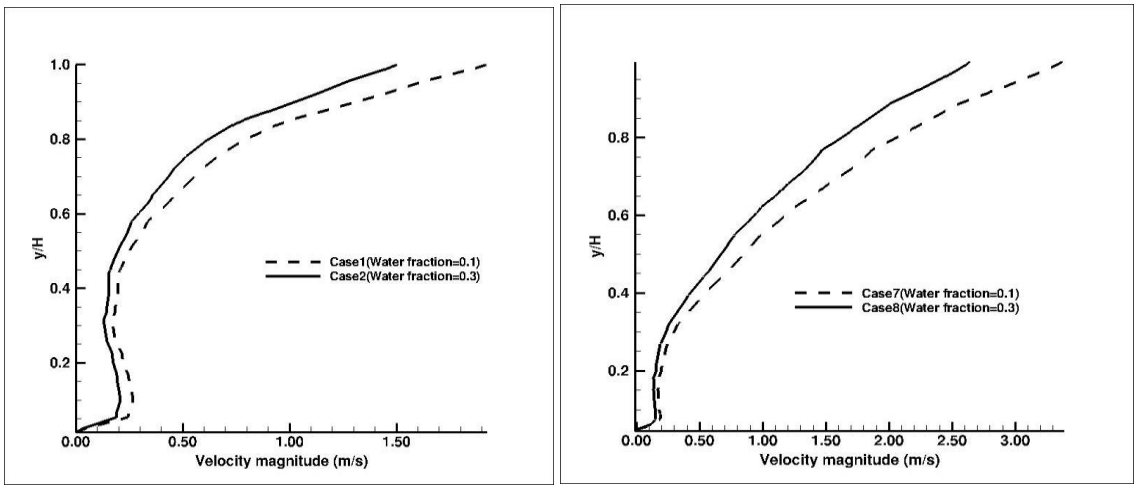

(a) lower aspect ratio (b) higher aspect ratio

Figure 5.43: Velocity magnitude at recirculation region behind the cubical obstacle (Cases 1, 2, 7 and 8)

The effects of input water volume fraction on velocity at vortices region beside the sidewall are shown in figure 5.44. The lower aspect ratios cubical obstacles are shown in figure 5.44a of input water volume fraction of case 1 (water fraction=0.1) and case 2 (water fraction=0.3), water separates at velocity of 2.85m/s and 2.35m/s for case 1 and case 2 respectively. However, the case with low input water fraction (case1) has high velocity of separation and distribution along the line than the case with high input water fraction (case 2) and the velocity decrease downward to pipe base. For higher aspect ratio cubical obstacle shown in figure 5.44b the velocity of separation for low input water fraction case (case7) is 4.5m/s, while for high input water fraction the separation velocity is 3.5m/s. The results show the increase in input water volume fraction lead to decrease in velocity of separation with consequence reduction in velocity distribution along the line from top of obstacle to pipe base.

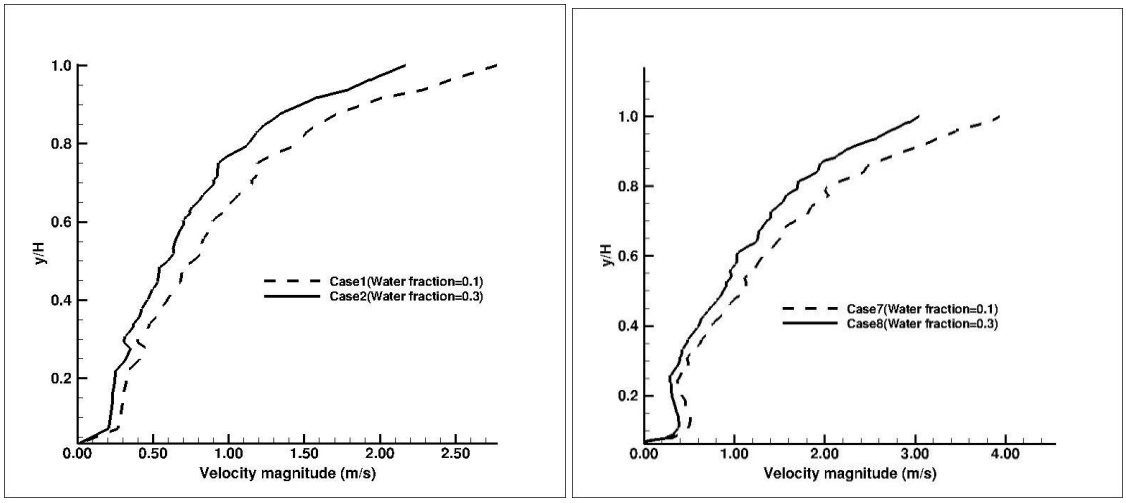

(a) lower aspect ratio (b) higher aspect ratio

Figure 5.44: Velocity magnitude at vortices region of sidewall of cubical obstacle (Cases 1, 2, 7 and 8)

The turbulent kinetic energy at the recirculation region behind the cubical obstacle for lower and higher aspect ratio cases is shown in figure 5.45. It is observed that the turbulent kinetic energy in figure 5.45 is analogous to figure 5.43 of velocity magnitude in which the turbulent kinetic energy is maximum at the separation region and decreases downward to pipe base. For the cases with low input water volume fraction (case 1 and 7) the maximum turbulent kinetic energy appeared at the separation region and at distribution line from vortex core to pipe base compared with cases of high input water fraction (case 2 and 8). However, the turbulent intensity tends to decrease from vortex core to pipe base. For cases with higher aspect ratio, the turbulent kinetic energy tends to be constant at cubical height of y/H=0.7 for both the low and high input water volume fraction cases. However, the turbulent intensity tends to decrease from vortex core to pipe base.

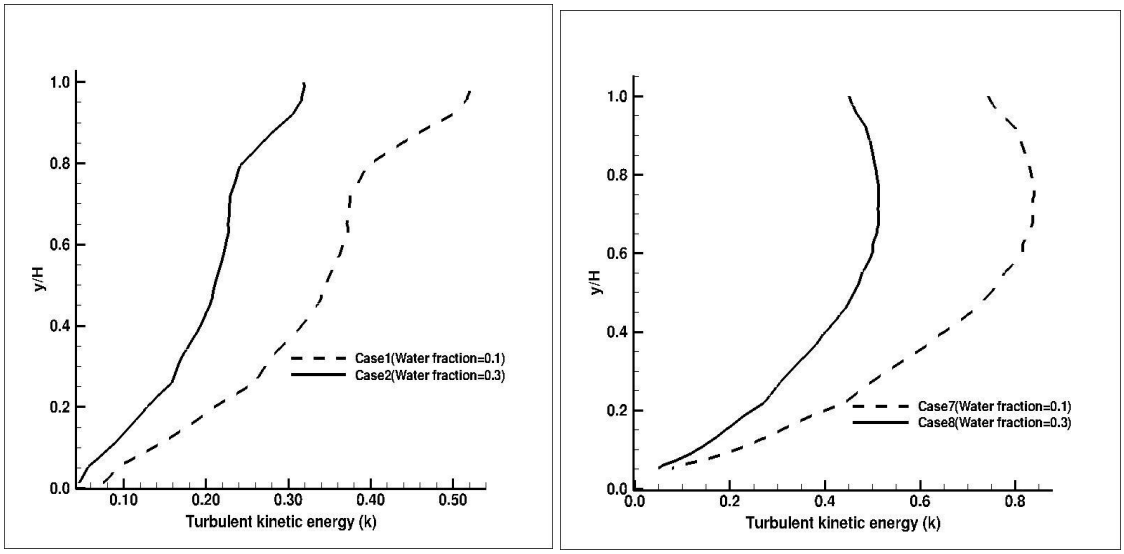

(a) lower aspect ratio (b) higher aspect ratio

Figure 5.45: Turbulent kinetic energy at recirculation region behind the cubical obstacle (Cases 1, 2, 7 and 8)

The turbulent kinetic energy at vortices region beside the sidewall of cubical obstacle is presented in figure 5.46. The difference between the turbulent kinetic energy of the case with low input water fraction (case1 and case7) and the case with high input water fraction (case 2 and case 8) is large. In other words, the turbulent kinetic energy of case with low input water fraction is higher than the case with high input water fraction. In lower and higher aspect ratio cubical obstacles, the turbulent kinetic energy increases from the vortex core to height y/H= 0.8 then finally decrease down to pipe base. More turbulent activities are observed on vortices region of sidewall than the recirculation region behind the cubical obstacle because of entrance effect and initial stage of separation.

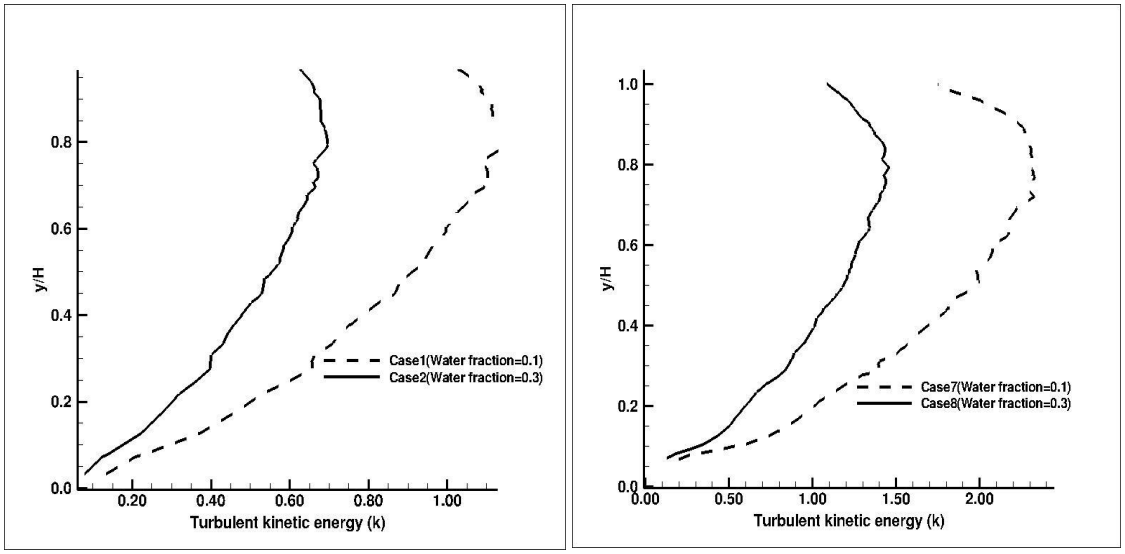

(a) lower aspect ratio (b) higher aspect ratio

Figure 5.46: Turbulent kinetic energy at vortices region of side wall of cubical obstacle (Cases 1, 2, 7 and 8)

Table 5.12 gives the maximum and minimum water volume fraction around the cubical obstacle region for eight simulated cases. The results can be analysing in terms of effect of cubical obstacle aspect ratio, Reynolds number and input water volume fraction. For the effect of cavity aspect ratio on maximum and minimum water distribution in the obstacle region, the maximum water volume fraction of case 1 (lower aspect ratio) and case 3 (higher aspect ratio) are 0.1107 and 0.1202 yielding percentage increase of 10.7% and 20.2% respectively. Similarly, for case 2 (lower aspect ratio) and case 4 (higher aspect ratio) the maximum water volume fraction are 0.514 and 0.90 with percentage increase of 10.7% and 18.2% respectively. The same water volume fraction quantitative trends are observed for case 5 (lower aspect ratio) and case 7 (higher aspect ratio), the water volume fraction increased by 10.2% and 15.3% respectively.

Case Num.	Re_m	Water Volume Fraction	Mixture Velocity	Aspect ratio	Minimum Water Volume Fraction	Maximum Water Volume Fraction	% Increase.
1	18500	0.1	3.2	0.1	0.0758	0.1107	10.7
2	18500	0.3	2.5	0.1	0.2672	0.3322	10.7
3	18500	0.1	3.2	0.2	0.0811	0.1202	20.2
4	18500	0.3	2.5	0.2	0.2443	0.3547	18.2
5	22000	0.1	3.8	0.1	0.0590	0.1102	10.2
6	22000	0.3	2.96	0.1	0.2589	0.3306	10.2
7	22000	0.1	3.8	0.2	0.0843	0.1153	15.3
8	22000	0.3	2.96	0.2	0.2564	0.3429	14.3

Table: Maximum and minimum water volume fraction around the cubical obstacle region

Similarly, for lower aspect ratio of case 6 and higher aspect ratio of case 8, the percentage increases of water volume fraction are 10.2% and 14.3% respectively. However, the quantitative results of water volume fraction revealed that more water settle to bottom around the region of higher aspect ratio cases than the lower aspect ratio cases, this can be attributed to the increase in size of recirculation region and effect of turbulent mixing and action of gravity.

The numerical results of the maximum and minimum water fraction at cubical obstacle region shown in table 4.12 also explained the effect of Reynolds number. For the cases of the same aspect ratio (lower aspect ratio) and constant input water volume fraction of 0.1. For case1 (Re=18,500) and case 5 (Re=22,000). The maximum water fractions are 0.1107 and 0.1102 with percentage increase of 10.7% and 10.2% respectively, while for lower aspect ratio of case 2 (Re=18,500) and case 6 (Re=22,000) yield 10.7% and 10.2% increase in water volume fraction. For higher aspect ratio of case 3 (Re=18,500) and case 7 (22,000), the water volume fraction increased by 20.2% and 15.3% respectively, while for higher aspect ratio of case 4 (Re=18,500) and case 8 (Re=22,000), the water volume fraction increases by 18.2% and 14.3%

respectively. The results for lower and higher aspect ratio indicated that with increase in Reynolds number less water settles down at bottom around the cubical obstacle region and with decrease in Reynolds number more water settles down at bottom around the cubical obstacle region.

The effect of input water volume fraction can be observed with case of the same Reynolds number and aspect ratio. Consider case 1 (input water fraction=0.1) and case 2 (input water fraction 0.3), the maximum water fractions around the cubical obstacle region are 0.1107 and 0.3322 respectively. Similarly for case 3 and case 4, the maximum water volume fractions are 0.1202 and 0.3547 respectively. The quantitative results of the effect of input water volume fraction distribution around cubical obstacle region indicated that increase in input water volume fraction will lead to reduction in mixture velocity and less water entrainment, so more water will separate from oil and settle around the cubical obstacle region.

5.8 Summary of results of oil-water flow in pipe with cubical obstacle

The flow of oil-water in pipe with cubical obstacle presents an interesting flow dynamic characteristic involving oil-water separation, recirculation and separation of water. The oil-water separate from the front, side walls and behind the obstacle which lead to formation of different types of vortices. The core vortex, which is referred to as horse-shoe vortex, was infolds around the cubical obstacle forming wake with two lateral vortices detected at the region of side walls and two arch vortices behind the cubical obstacle. It was observed the size of recirculation region behind the cubical obstacle increases consistently with the size of wake. The distribution of water volume fraction around the cubical obstacle indicated that more water separate and settle at pipe floor in front of obstacle and at vortices region near the side walls as well as at arch vortices region behind the cubical obstacle. It was also found that more water separate and settle for higher aspect ratio compared with lower aspect ratio, the flow structure near the higher aspect ratio revealed additional

vortices. For the flow across the cubical obstacle, there are appearances of eye-vortices at the top of lower aspect ratio obstacle, while eye-vortices were not detected on higher aspect ratio case.

The analysis of effect of Reynolds number on separation and settlement of water was evident. The flow physics revealed that region of high turbulence activity is larger at top front face and decrease along the recirculation region behind the cubical obstacle. It was found that as the Reynolds number increases the rates of water separation from the mixture decreases. At high Reynolds number, there was more turbulence mixing at the top front wall and at recirculation region behind the cubical obstacle compare to low Reynolds number. It was revealed that water wetted area at the bottom front wall was larger for low Reynolds number case than for the high Reynolds number case because of the difference in turbulence intensity.

The analysis showed that from top to bottom of cubical obstacle more water tends to separate and settle for low Reynolds number case because of action of gravity. The oil-water separate at the side walls at high velocity for high Reynolds number case compare with low velocity for low Reynolds number case and the velocity decrease downward from the top of the side walls to pipe base. The velocity of separation for higher aspect ratio was quite higher compared with lower aspect ratio at low and high Reynolds number; these conditions were favourable to water separation and settlement at the pipe base. The turbulent kinetic energy profile at recirculation region behind the obstacle was analogous to velocity profile at recirculation region.

Numerical results of effect of Reynolds number on the vortices beside the sidewalls indicated for low and high Reynolds number cases, water separate at higher water fraction than the input water fraction. The water fraction decrease from separation region to halve the height of cubical obstacle and more water separate from the sidewalls and settle at pipe base with low Reynolds number cases, it was ascribed to the low rate of turbulence mixing and effect of gravity. For cases of higher aspect ratio, the difference between the water separation and settlement for low and high Reynolds number is quite small and it is

attributed to the geometry parameters and the initial stage of flow separation. The difference between the velocity of separation for low and high Reynolds number cases was quite evident and the velocity decrease downward to pipe base. The velocity of separation for higher aspect ratio cases was much higher compared with lower aspect ratio cases. The line plots of turbulent kinetic energy on vortices region at sidewall was directly related to the velocity profile at vortices region. At low and high Reynolds number, the higher aspect ratio cubical obstacles produced maximum turbulent kinetic energy than the lower aspect ratio.

The effect of input water volume fraction on cubical obstacle was investigated, the analysis indicated the higher the input water volume fraction, the lower the turbulence production and hence the turbulent kinetic energy was higher for low input water fraction compare with high input water fraction. The area of turbulence was larger for the low input water volume fraction case because less turbulence favours separation. It was observed that water segregate faster with increase in input water volume fraction and decrease in Reynolds number, water concentrate at the bottom front of cubical obstacle and water bubble are found along the recirculation region behind the cubical obstacle. However, the cases with high input water volume fraction have larger area wetted by water.

Water volume fraction profiles give quantitative measurements of effect of input water volume fraction at recirculation region and at vortices region of sidewall; at the recirculation region water separate and entered the region at the same value of input water volume fraction for both lower and higher aspect ratio cases. For low and high input water volume fraction, the vortex core appeared at cubical height of y/H=0.7 for lower aspect ratio, while it appeared at cubical height of y/H=0.8 for higher aspect ratio. The effect of input water fraction on velocity profile at recirculation region revealed that water separate at high velocity for low input water volume fraction as compared with high input water volume fraction and the velocity decrease downward to pipe base. However, the velocity profile of high input water fraction was lower than the velocity profile of low input water fraction. The results of turbulent kinetic energy profile at

recirculation region are directly related to velocity profile at recirculation region behind the obstacle.

The effect of input water volume fraction at vortices region of sidewall indicated that water separate at high water volume fraction than the input water volume fraction, less quantity of water are found at vortices region of sidewall for lower aspect ratio, while high quantity of water emerged with higher aspect ratio. The velocity profile at vortices region beside the cubical sidewalls show that velocity of separation along the profile was much higher for low input water volume fraction; maximum velocity appeared for higher aspect ratio cases. In general, increase in input water volume fraction results to decrease in velocity at separation region and along the profile from top of cubical obstacle to pipe base. The turbulent kinetic energy profiles at the vortices region of the sidewall are analogous to velocity profiles at vortices region. For low and high input water volume fraction cases, the turbulent kinetic was high at separation region and decrease downward to pipe base. The low input water volume fraction case has maximum value of turbulent kinetic energy as compared with high input water volume fraction case because of reduction in bulk density of oil-water mixture.

6 CONCLUSIONS AND FUTURE WORK

Numerical simulations of three dimensional fully dispersed oil-water flows in pipe with pipe deformation (cavity and scale sediments) have been carried out. The current numerical simulations signify an initial stage to describe the oil-water separation phenomenon due to corrosion cavity and scale sediments build-up in horizontal pipeline. The challenging part of oil-water flow in pipe with corrosion cavity and scale sediments was selection of representatives' geometries for corrosion cavity and scale sediments, no exact geometries data available for corrosion cavity and scale sediments, the investigation focussed on model geometries.

The corrosion cavity and scale sediments were modelled with rectangular cavity and cubical obstacle respectively oriented perpendicular to the pipe flow, because the model geometries will favour separation and will restrict the number of parameters for analysis. The oil-water flow in horizontal pipeline with cavity and cubical obstacle were investigated for input water volume fraction of 0.1 and 0.3 and Reynolds number of 18,500 and 22,000 based on literature survey conducted. Configuration of 16 cases were suggested due to computational requirements. The results were interpreted in terms of effect of Reynolds number, input water volume fraction and geometry aspect ratio. Trends will be explored resulting to improved understanding of the effect of pipe wall deformations under ranged of conditions and the amount of water volume fraction in contact with the pipe wall which was directly linked to pipe corrosion.

The numerical results showed that cavity aspect ratio (shallow and deep cavity) has influenced in changing the velocity, water volume fraction and turbulent kinetic energy at the centre of pipe, distortion appeared at the centre of pipe, more distortion was found for deep cavity than the shallow cavity. In deep and shallow cavity, water volume fraction from the inlet increased towards the cavity due to gravitational and entranced effect, the flow separated from the leading edge of the cavity result to recirculation and separation of water from oil. In the

cavity region, the analysis revealed that the deeper the cavity the higher the amount of water settles at the cavity base.

The results of effect of Reynolds number on cavity flow revealed that the increase in Reynolds number leads to reduction in water volume fraction in contact with the pipe and cavity walls because of water entrainment by the moving oil. Conversely, decreased in Reynolds number resulted to increase in water volume fraction. Analysis of effect of input water volume fraction showed that the increase in input water volume fraction increases the amount of water separates from the oil-water mixture which leads to higher percentage of water volume fraction in contact with pipe and cavity walls. The cases with deep cavity with high input water volume fraction have the maximum water volume fraction in contact with cavity walls.

Parametric computation was performed in order to modify the turbulence models at fully turbulence region and viscosity region, whereby new adjusted turbulent viscosity was formulated and coded with damping function to address the distribution of water volume fraction at pipe wall surfaces. The results revealed that there was less reduction of water volume fraction at walls surface and the water volume fraction was smoothly distributed at pipe and cavity wall.

The numerical results of oil-water flow in pipe with cubical obstacle revealed that the oil and water separated from cubical obstacle and formed different types of vortices; sidewall vortices, horse-shoe vortices and arch vortices. The size of recirculation region behind the cubical obstacle increased consistently with the size of wake. The analysis on the plane perpendicular and across to the flow showed similarities with oil flow experimental visualisation as observed by Martinuzzi and Tropea (1976). The distribution of water fraction near the cubical obstacle indicated that more water separate at vortices region of sidewall and at arch region behind the cubical obstacle.

The effect of Reynolds number showed that for high Reynolds number cases, there was more turbulent mixing at cubical obstacle front walls and at recirculation region behind the cubical obstacle as compared with low Reynolds

number cases. Water wetted area at the front wall was larger for low Reynolds number than the high Reynolds number. On the plane across the flow, there was no significant difference for the turbulent kinetic energy and the maximum water volume fractions for low and high Reynolds number cases.

The analysis at recirculation region behind the cubical obstacle showed maximum turbulent activities appeared for high Reynolds number cases. It was observed from vortex core of recirculation region; more water tends to separate and settle for low Reynolds number cases. The velocity profile at recirculation region indicated that water separated at higher velocity for higher aspect ratio cases at low and high Reynolds numbers. On the vortices region of sidewalls, water separated at high water fraction than the input water fraction for both low and high Reynolds number cases. Water volume fraction decreased from separation region to halve the height of obstacle and then increased to pipe base. Velocity of separation for higher aspect ratio case was much higher compared with lower aspect ratio case and the velocity decreased downward to pipe base. The turbulent kinetic energy profile was directly related to the velocity profile. Higher aspect ratio cubical obstacle produced maximum turbulent kinetic energy at the vortices region of side wall.

Numerical solution of effect of input water volume fraction showed the higher the input water volume fraction, the lower the turbulent production, the area of turbulence was larger for the low input water volume fraction. The cases with high input water volume fraction have large area wetted by water, the percentage increase for lower and higher input water volume fraction was 10% and 20% respectively. These indicated that water segregated faster with increase in input water volume fraction and decrease in Reynolds number.

The results on recirculation region revealed that water separates at the same value of input water volume fraction and entered the recirculation region, while water separates at high velocity for low input water volume fraction as compared with high input water volume fraction. Turbulent kinetic energy profile was directly related to velocity profile at recirculation region. Analysis of effect of input water volume fraction at vortices region of sidewall indicated that water

separates at high input water volume fraction than low input water volume fraction. The velocity profile showed the velocity of separation was much higher for low input water volume fraction; the turbulent kinetic energy was high at separation region and then decreases downward to pipe base.

From the computational results of oil-water flow in pipe with deformation (cavity and cubical obstacle), it is reasonable to conclude that the pipe deformation contributed greatly in changing the flow features and increasing the water volume fraction in contact with pipe and cavity walls and around the cubical obstacle region which is directly related to internal pipe corrosion. The investigation will be useful in pipeline design in enhancing the corrosion prediction models and will further improve the performance and safety of pipeline operation. However, based on the computational results obtained and the complexity of multiphase modelling, the following future work can be recommended on oil-water flow in pipe with deformation:

- Further research could be performed on different range of input water volume fraction and Reynolds numbers.
- Further numerical computation should be conducted on different model geometries or different aspect ratios including the effect of valve, T-junction and stud on oil-water flow in pipe.
- Further improvements in grids resolution at contact points and wall boundary conditions could give better results.
- Future work could be extended to large eddy simulation (LES) as alternative turbulent modelling approach to achieve more accurate results.
- Further modification on turbulence models to address the mixture viscosity and mixture density might give better results.

REFERENCES

Abdulkadir, M. and Hernandez-Perez, V. (2010), “The effect of mixture velocity and droplet diameter on oil-water separation using computational fluid dynamics,” *World academy of science, engineering and technology,* Vol. 61, pp. 35-43.

Anderson, J. D. (1995), Computational fluid dynamics: The basic with application, McGraw-Hill Inc.

Andreini, P. A., Beretta, A., Ferrari, P and Galbiati, L. (1997), “Horizontal oil-water flows in small diameter tubes,” *Int. comm. heat and mass transfer*, Vol. 24 (2), pp. 223-229.

Angeli, P. and Hewitt, G. F. (1998), “Pressure gradient in horizontal liquid-liquid flows,” *International journal of multiphase flow*, Vol. 24, No. 7, pp. 1183–1203.

Angeli, P. and Hewitt, G. F. (2000a), “Flow structure in horizontal oil-water flow,” *International journal of multiphase flow*, Vol. 26, No. 7, pp. 1117–1140.

Angeli, P. and Hewitt, G. F. (2000b), “Drop size distributions in horizontal oil-water dispersed flows,” *Chemical engineering science*, Vol. 55, No. 16, pp. 3133-3143.

ANSYS Fluent User’s Theory Guide (6.3 Documentation).

Arirachakran, S., Oglesby, K.D., Brill, J.P. (1989), An analysis of ail-water flow phenomena in horizontal pipes. *MSc Thesis*, University of Tulsa.

Ayello F., Chong, L., Xuanping, T., Jiyong, C and Srdjan, N. (2008), “Determination of phase wetting in oil-water pipe flows,” *NACE corrosion conference and Expo,* paper No. 08566, pp. 5-7.

Bernard and Wallace (2002), Turbulent flow: Analysis, Measurement and Prediction, Willey.

Brauner, N. (2002), “Modelling and control of two phase flow phenomena: Liquid-liquid two phase flow systems,” *School of engineering*, *Tel-Aviv University,* Tel-Aviv 69978, Isreal.

Brinkman, H. C. (1952), “The viscosity of concentrated suspensions and Solutions,” *Journal of chemical physics,* Vol. 20, pp. 571.

Cavaleiro, A., Carlos Oliveira, J and Brett, M. A. (2000), “Influence of sputtering conditions on corrosion,” *Corrosion science*, Vol.42, pp.1881-1895.

Charles, M., Govier, G. W., Hodgson, G. W. (1961), “The horizontal flow of equal density oil-water mixtures,” *Canadian Journal of chemical engineering*, Vol. 39, pp. 27-36.

Colebrook, C. F. (1978), “Turbulent flow in pipes, with particular reference to the transition region between the smooth and rough pipe laws,” *Journal institute of civil engineering*, Vol. 11, pp. 133-156.

Cox, A. L. (1985), A study of horizontal and downhill two-phase oil- water flow. *M.S. Thesis,* The University of Texas.

Duckler, A. E, Wicks, M., Cleveland, R. G. (1964), “Frictional pressure drop in two-phase flow,” AIChE J. Vol. 10 (1), pp. 44-51.

Elseth, G. (2001), An experimental study of oil / water flow in horizontal pipes. *PhD Thesis*, The Norwegian University of Science and Technology, Porsgrunn.

Fairuzov, Y. V., Arenas-Medina, P. (2000), “Flow pattern transitions in horizontal pipelines carrying oil- water mixtures,” *Journal of energy resources. Technol- Trans.ASME*, Vol. 122, pp. 167-175.

Fairuzov, Y.V. (2000), “Numerical simulation of transient flow of two immiscible liquids in pipeline,” *AIChe Journal*, Vol. 46, No. 7, pp. 1332–1339.

Ferziger and Peric. (2002), Computational methods for fluid dynamic, Springer.

Govier, G. W. and Aziz, K. (1977), The flow of complex mixtures in pipes, Huntington, N.Y: R.E. Krieger Pub, pp. 290–291.

Konan, G. K. (2009), CFD Analysis of Recirculation induced oil- water separation phenomenon. *Msc Thesis,* Cranfield University, Department of Aerospace Sciences, Cranfield University, UK.

Guzhov, A., Grishin, A. D., Medredev, V. F and Medredeva, O. P. (1973), "Emulsion formation during the flow of two immiscible liquids in a pipe," *Neft Khoz.* Vol. 8, pp. 58-61 (in Russian).

Hebie Z. (1997), Steel Pipe Manufacturing Corporation, Hebei province, China.

Hinze, J. (1956), "Fundamental of the hydrodynamic mechanism of splitting in dispersion process," *AICHE*, Vol. 1. No 3, pp. 289-295.

Hirt, C. W., Nichols, B. B. (1981), "Volume of fluid (VOF) method for the dynamics of free boundaries," *Journal of computational physic*, Vol. 39, pp. 201-225.

Hopkins, P. (2004), "The assessments of corrosion in pipelines," *Pipeline pigging and intergrity management conference*-Amsterdam, The Netherland, May 17-18 2004, pp. 5.

Hui, G., Han-yang, G., Lie-jin, G. (2003), "Numerical study of stratified oil-water two-phase turbulent flow in a horizontal tube," *Journal of heat and mass transfer*, Vol. 46, PP. 749-754.

Hussain. S. A., Xu, X. Y and Hewitt, G. F. (2008), "Water local volume fraction on oil-water dispersion," *Journal of Applied fluid mechanics*, Vol. 1 No. 2, pp. 57-66.

Hussein, H. Martinuzzi R. (1996), "Energy balance for turbulent flow around a surface mounted cube placed in a channel," *Phys. Fluids*, Vol.8 (3), pp. 764-780.

Issa R. I. (1988). “Prediction of turbulent, stratified, two-phase flow in inclined pipes and channels,” *Int. J. Multiphase flow,* Vol. 14 (1) pp. 141-154.

Koseff, J.R. and Street, R. L. (1984), “On end wall effects in a lid-driven cavity flow,” *J. fluids eng*. Vol. 106, pp. 385-389.

Krajnovic’, S., David. L. (2001), “Large eddy simulation of the flow around a three dimensional bluff body,” *AIAA 2001-0432, 39th AIAA Aerospace Sciences Meeting and Exhibit,* Reno, Nevada, 8-11 January.

Kumar, A., Hartland, S. (1985), “Gravity settling in liquid-liquid dispersions,” *Canadian journal of chemical engineering*, Vol.63, No.3, pp. 368-376.

Laflin, G. C. Oglesby, K. D., (1976), An Experimental study on the effect of flow rate, water fraction and gas-liquid ratio on air-oil-water flow in horizontal pipes. *B.Sc Thesis*, Univeristy of Tulsa.

Launder and Sandham. (2002), Closure Strategies for Turbulence and Transitional Flows. *Cambridge University Press*, England.

Launder B. E., Spalding D. B. (1972), Lectures in Mathematical models of turbulence, *Academic press*, London.

Lawson N.J., Atvars, K., Knowles, K and Ritchie, S. A. (2009), “Experimental and Computational Investigation of an open Transonic Cavity Flow,” *Journal of aerospace engineering* Vol. 223(G4), pp. 357-368.

Lockhart, R. W., Martinelli, R. C. (1949), “Proposed correlation of data for Isothermal two-phase, two-component flow in pipes,” *Chemical engineering programme*. Vol.1, pp. 39-48.

Lovick, J., Britol, R., Angeli, P. (2000), “Pressure drop and hold-up in liquid-liquid flows*,” Int. symp. On multiphase flow and transport phenomena, Antalya, Turkey,* pp. 548-555*.*

Lovick, J., Angeli, P. (2004), “Experimental studies on the dual continuous flow pattern in oil-water flows,” *Int. Journal of multiphase flow*. Vol 30, pp. 139-157.

Malhotra A. (1995), Study of two and three-phase flows in large diameter horizontal pipeline*, Msc Thesis*, College of Engineering and Technology, Ohio University, USA.

Malinowski, M.S. (1975), An experimental study of oil-water and air-oil-water flowing mixtures in horizontal pipes. *MS Thesis*, University of Tulsa.

Mandal T. K., Chakrabarti D. P (2007), “Oil water flow through different diameter pipes-similarities and differences,” *Trans IChemE, part A.*

Martinuzzi, R., Tropea, C. (1993), “The flow around surface-mounted, prismatic obstacles placed in a fully developed channel flow,” *Trans. ASME, J. fluid eng*. Vol. 115(1), pp. 85-91.

Mathew, R. S. (2008), Report of offshore technology conference presentation. *NACE international oil and gas production*.

Meinders, E and Hanjalic (1999), “Vortex structure and heat transfer in turbulent flow over a wall-mounted metric of cubes,” *Int.J. Heat Fluid flow*, Vol. 20, pp. 255-267.

NACE international resource center (2005), Some safety consideration for pipelines, 1440 South Creek Drive, Houston, TX, USA. Available at http://www.events.nace.org/library/corrosion/localised/shapes (accessed 13th June, 2011)

Nadler, M., Mewes, D. (1997), “Flow induced emulsification in the flow of two immiscible liquids in horizontal pipes,” *International Journal of multiphase flow*, Vol. 23, pp. 55-68.

Oglesby, K.D. (1979), An experimental study on the effect of oil viscosity, mixture velocity and water fraction on horizontal oil-water flow. *MS Thesis*, University of Tulsa.

Osarobo F.O. (2010), Phase separation of oil-water flow in a pipe bends. *Msc Thesis*, Department of Aerospace Science, Cranfield University, UK.

Ping, T., Jian, Y., Jinyang, Z., Guofu, O., Shizheng, H., Jianju, Y., Leong, W. and Yanbao, M. A. (2009), "Erosion-corrosion failure of REAC pipes under multiphase flow," *Front energy power eng., China*, Vol. 3, No. 4, pp. 389-395.

Pope, S.B. (2000), Turbulent flows, Cambridge University Press, England.

Rashmi, G. W., Thomas, S. Y., Choong, S. A., Hussain, M. K and Chuah, T. G. (2009), "Numerical study of dispersed oil-water turbulent flow in horizontal tube," *Journal of petroleum science engineering*, Vol.65, No3-4, pp. 123-128.

Rockwell, D., Linj, J-C. (2001), "Organized oscillations of Initial turbulent flow past a cavity," *AIAA Journal*. Vol.39, pp. 1139-1151.

Rodrigues, O. M. H., Oliemans, R.V.A. (2006), "Experimental study on oil water flow in horizontal and slightly inclined pipes," *International Journal of multiphase flow*, Vol.32, pp. 323-343.

Russel, T., Hodgson, G. W., Govier, G. W. (1957), "Horizontal pipeline flow of mixtures of oil and water," *Journal chemical engineering*, Vol. 37, pp. 9-17.

Schiller, L., Naumanni, Z. (1935), Z. ver. Deutsch. Ing., 77, 318.

Scott, G. M. (1985), A study of two-phase liquid-liquid at variable inclination. *M.S. Thesis*, The university of Texas.

Sheryl M. G., Dewar, G. W., Wroblewski, D. E. (2004), "Experimental investigation of the flow characteristics within a shallow wall cavity for both laminar and turbulent upstream boundary layers," *Experimental in fluids*, Vol.36, pp. 791-804.

Simmons, M. J. H., Azzopardi, B. J. (2001), "Drop size distributions in dispersed liquid-liquid pipe flow," *International Journal of multiphase flow*, Vol. 27, pp. 843-859.

Simonin, O., Viollet, P. L. (1990), “Modelling of turbulent two-phase jets Loaded with discrete particles,” *Proceedings of international seminar on phase interface phenomena in two-phase flow.* ICHMT Belgrade, pp. 259-269.

Sirpa K., Abo A. (1996), “On the mixture model for multiphase flow*,” Mikko Manninen and Veikko Taivassalo*, ESPOO.

Soleimani, A. Lawrence, C. J. and Hewitt, G. F. (2000), “Spatial distribution of oil and water in horizontal pipe flow,” *SPE journal*. Vol.4, No 4, pp. 394-401.

Soot, P. M. (1971), A study of two-phase liquid-liquid flow in pipes. *PhD Thesis,* Oregon State University.

Trallero, J. L. (1995), Oil-water flow patterns in horizontal pipes, *PhD Thesis*, University of Tulsa.

Trallero, J. L., Intevep, S. A., Sarica, C. and Brill, J. P., (1997), “A study of oil-water patterns in horizontal Pipes,” *Journal of multiphase flow*, pp. 165-172.

Valle, A. (1997), “Pressure drop, flow pattern and slip for two phase crude oil-water flow: experiments and model predictions*,” Int. Symp. On academy of liquid-liquid two phase flow and transport phenomena.*

Valle, A., Kvandal, H. (1995), “Pressure drop and dispersion characteristics of separated oil-water flow,” *Proceedings of the 1st International symp. on two-phase flow modelling and experimentation*, Rome, Italy.

Valle, A., Utvik, O. H. (1997), “Pressure drop, flow pattern and slip for two-phase crude oil-water flow,” *Proceeding of Int. Symp.on liquid-liquid two phase flow and transport phenomena,* Antalya, Turkey, pp. 63-74.

Vuong, D. H., Zhang, H. Q., Sarica, C. and Li, M. (2009), “Experimental study on high viscosity oil/water flow in horizontal and vertical pipes,” *SPE Annual technical conference and exhibition, Louisiana USA*. SPE 124542, pp. 1-10.

Wang, L.-Y., Wu, Y.-X., Zheng, Z-C., Guo, J., Zhang, J and Tang, C. (2008), “Oil-water two-phase flow inside T-junction,” *Journal of hydrodynamics*, Vol. 20, No. 2, pp. 147–153.

Xu, X.-X. (2007), “Study on oil–water two-phase flow in horizontal pipelines,” *Journal of petroleum science and engineering,* Vol. 59, No. 1–2, pp. 43–58.

Yang, L., Azzopardi, B. J. (2007), “Phase split of liquid- liquid two-phase flow at a horizontal T-junction,” *International Journal of multiphase flow*, Vol. 33(2), pp. 207-216.

Yao H., Cooper, K. R., Raghunthan, S. (2004), “Numerical simulation of incompressible laminar flow over three-dimensional rectangular cavities,” *Journal of fluids engineering*, Vol. 126, pp. 919 -926.

Zigrang, D.J. and Sylvester, N.D. (1985), “A review of explicit friction factor equations,” *Journal of energy resources technology*, Vol. 107, No. 2, pp. 280 – 283.

APPENDICES

Appendix A : Validation Grid Generator

The following GAMBIT journal has been generated in order to automate mesh generation for the validation studies:

```
$pipelength=9

$piperadius=0.0243/2

$inletcellsize=0.004

$targetmeshsize=1000000

$blfirst=0.001

$blrows=4

$blgrowth=1.1

vertex create coordinates 0 0 0

vertex create coordinates 0 $piperadius 0

vertex create coordinates 0 0 $piperadius

face create "inlet" center2points "vertex.1"

"vertex.2" "vertex.3" circle

blayer create first $blfirst growth $blgrowth total
0.00198598

rows $blrows transition 1 trows 0 uniform

blayer attach "b_layer.1" face "inlet" edge "edge.1" add
```

```
face mesh "inlet" triangle size $inletcellsize

$facemesh=ELEMCOUNT("inlet",t_fa)

$pipewallcellsize=$pipelength/($targetmeshsize/$facemesh[1
])

default set "MESH.INTERVAL.SIZE" numeric $pipewallcellsize

volume create translate "inlet" vector $pipelength 0 0
withmesh

physics create "inlet" btype "VELOCITY_INLET" face "inlet"

physics create "wall" btype "WALL" face "face.3"

physics create "outlet" btype "OUTFLOW" face "face.2"

export fluent5 "angeli.msh"
```

Appendix B : C Language Code For Computing The Turbulent Viscosity Of Water-Oil Flow

The following C language code has been generated in order to modify the turbulent viscosity of oil-water flow

```
DEFINE_TURBULENT_VISCOSITY (turbulent_viscosity_mixture_damping,
cell_index, mixture_thread)
{
 int id_oil = 0, id_water = 1;

 Thread *thread_OIL, *thread_WATER;

 real turbulent_viscosity_water_in_oil, VOF_OIL, VOF_WATER,
RHO_OIL, RHO_WATER, mu_OIL, mu_WATER, mu_mixture;
 real rho_mixture, turbulent_kinetic_energy,
epsilon_dissipation_rate, Cmu;
 real raxis[ND_ND], Eta, ReEta, Amu, A1, fmu;

 turbulent_kinetic_energy = C_K(cell_index, mixture_thread);
 epsilon_dissipation_rate = C_D(cell_index, mixture_thread);

 Cmu = M_keCmu;
 Eta = C_CENTROID(raxis,cell_index,mixture_thread);

 thread_OIL = THREAD_SUB_THREAD(mixture_thread,id_oil);
 thread_WATER = THREAD_SUB_THREAD(mixture_thread,id_water);

 VOF_OIL = C_VOF(cell_index,thread_OIL);
 VOF_WATER = C_VOF(cell_index,thread_WATER);
```

```
 RHO_OIL = C_R(cell_index,thread_OIL);
 RHO_WATER = C_R(cell_index,thread_WATER);

 mu_OIL = C_MU_L(cell_index,thread_OIL);
 mu_WATER = C_MU_L(cell_index,thread_WATER);

 rho_mixture = VOF_WATER*RHO_WATER+VOF_OIL*RHO_OIL;
 mu_mixture  = VOF_WATER*mu_WATER+VOF_OIL*mu_OIL;

 ReEta =
rho_mixture*sqrt(turbulent_kinetic_energy)*Eta/mu_mixture;

 Amu = 0.0165;
 A1 = 20.5;

 fmu = (1.0-exp(-Amu*ReEta))*(1.0-exp(-
Amu*ReEta))*(1.0+(A1/ReEta));

 turbulent_viscosity_water_in_oil =
fmu*Cmu*rho_mixture*(turbulent_kinetic_energy*turbulent_kinetic_
energy)/epsilon_dissipation_rate;

 return (turbulent_viscosity_water_in_oil);
}

/* END OF THE UDF CODE */
```